Compositional, mechanical and transport properties of carbonate fault rocks and the seismic cycle in limestone terrains:

A case study of surface exposures on the Longmenshan Fault, Sichuan, China

Jianye Chen

Utrecht University
and
Institute of Geology, China Earthquake Administration

No. 076

Members of the dissertation committee:

Prof. dr. M.R. Drury
Utrecht University, The Netherlands

Prof. dr. Chris Marone
Pennsylvania State University, United states of America

Prof. dr. Teng-Fong Wong
State University of New York at Stony Brook, United States of America
and
The Chinese University of Hong Kong, HongKong SAR, China

Prof. dr. Shengli Ma
Institute of Geology, China Earthquake Administration, Beijing, China

Dr. Giulio di Toro
Istituto Nazionale di Geofisica e Vucanologia, Rome, Italy

The research was carried out at:
Institute of Geology, China Earthquake Administration
(A1#, Huayanli, Dewai Ave., Chaoyang dist., P.O.Box 9803, Beijing,100029, China)
and at the
High Pressure and Temperature Laboratory, Faculty of Geoscience, Utrecht University
(Budapestlaan 4, 3584 CD Utrecht, The Netherlands)

Printed by: Gildeprint

ISBN/EAN: 978-90-6266-388-0

Compositional, mechanical and transport properties of carbonate fault rocks and the seismic cycle in limestone terrains:

A case study of surface exposures on the Longmenshan fault, Sichuan, China

Samenstellings-, mechanische en transporteigenschappen van carbonaat breuk gesteenten en de seismische cyclus in kalksteen terreinen: Een case study van ontsluitingen langs de Longmenshan breuk, Sichuan, China
(met een samenvatting in het Nederlands)

Proefschrift

ter verkrijging van de graad van doctor aan de Universiteit Utrecht op gezag van de rector magnificus, prof.dr. G.J. van der Zwaan, ingevolge het besluit van het college voor promoties in het openbaar te verdedigen op woensdag 11 maart 2015
des ochtends te 10.30 uur

door

Jianye Chen

geboren op 19 september 1983
Songzi/Hubei, China

Promotoren**:** **Prof. dr. C.J. Spiers**
Prof.dr. X.S. Yang

Dit proefschrift werd (mede) mogelijk gemaakt met financiële steun van het State Key Laboratory of Earthquake Dynamics (LED2010A03) en het Netherlands Center for Solid Earth Science (ISES), beurs 2013-103.

Table of Contents

Summary

Destructive earthquakes are common in tectonically active regions dominated by carbonate cover rocks. Examples that have received much attention include the Mw 5 to 6.5 events that regularly occur in regions such as the Corinth Rift zone and the Italian Apeninnes. The catastrophic Wenchuan earthquake (Mw 7.9) that struck Sichuan, China on 12 May, 2008, also affected a section of carbonate cover terrain. In that event, coseismic surface rupture occurred over a distance of 240 km along the Longmenshan fault zone (LFZ). Here, the long central to northern segment of the main rupture zone is dominated by carbonate strata. Numerous studies have focused on characterizing the compositional, transport and mechanical properties of silicate fault rocks, with many models being proposed for dynamic fault frictional and rupture processes, but little data are available on carbonates to date, especially regarding the evolution of carbonate fault rock properties during the seismic cycle. In **this thesis**, I report on the properties of fault rocks collected from two carbonate-rich surface exposures on the LFZ surface rupture, with the aim of determining how carbonate(-rich) fault rocks differ from other rock types, and addressing how these properties control the dynamics of earthquake faulting occurring in carbonate sequences. I address the structural and compositional properties of the materials collected (Chapter 2), their transport and high-velocity frictional properties (Chapter 3), and their low-velocity frictional and healing properties (Chapters 4 and 5). Fault friction and healing properties are initially quantified in the framework of the well-known rate-and-state friction (RSF) approach. In Chapter 6, however, a new microphysical model is established to explain and quantify the rate-and-state friction (RSF) behavior observed in our experiments without resort to the classical RSF laws .

In **Chapter 1**, the motivation and scope of the study are outlined. Current knowledge of the internal structure and geochemical features of seismogenic fault zones is summarized. Previous experimental studies on high-velocity frictional and transport properties of fault rocks, as well as numerical modeling work on coseismic fluid pressurization, are addressed. The need for experimental work on the frictional and healing behavior of both natural and simulated carbonate fault rocks is also summarized. The aims of the present research are thus motivated at the end of this chapter.

In **Chapter 2**, I report on variations in the mineralogical, geochemical and isotopic ($\delta^{13}C$, $\delta^{18}O$) composition of fault rocks sampled in transects across the two surface exposures studied on the Longmenshan (LFZ) surface rupture. The enrichment/depletion patterns, element partitioning and a very large implied volume loss (> 90 vol.%) found are quite different from those characterizing faults in granites and clastic sedimentary rocks, and can be explained by a mass removal model involving dissolution and advective transport

enhanced by pressure solution. Increasing enrichment in smectite toward the principal slip surface was observed. Illitization of the black gouges on the principal slip surfaces, caused by coseismic frictional heating, was found in both exposures studied. Results imply that coseismic de-watering reactions can be expected to be extensive at depth, and possibly helped generate excess pore pressure assisting dynamic slip weakening during the Wenchuan Earthquake. I propose that coseismic frictional heating, along with the effects of post-seismic hydrothermal fluids, controlled the formation, transformation and distribution of smectite and illite within the fault cores of the carbonate fault zone studied.

In **Chapter 3**, the high-velocity frictional properties and the transport properties of the fault rocks collected from the southernmost exposure studied in Chapter 2 are investigated, to gain a better understanding of dynamic weakening and fluid pressurization mechanisms that operate during seismic fault motion. High-velocity friction experiments revealed that slip weakening is more pronounced for water-dampened gouge than dry gouge, indeed pointing to thermal pressurization. The fault core gouge studied has a very low permeability ($<10^{-21}$ m^2 at 165 MPa effective pressure) and is surrounded by fault breccia with permeability of 10^{-19} to 10^{-17} m^2, grading into less permeable, fractured country rocks. The fault zone thus exhibits a "conduit/barrier" structure. We numerically modeled coseismic slip weakening including thermal pressurization and dehydration/decarbonation, basing our calculation on measured transport and high-velocity frictional properties, and on the slip history inferred for the Wenchuan earthquake. The results indicate that thermochemical pressurization played a key role in causing dynamic slip weakening, while maintaining temperatures below 600 °C. Interestingly, enough heat was generated to remove and thermally pressurize the interlayer water from smectite in the fault core gouge, contributing to a pore pressure rise of ~ 6 MPa. The dramatic weakening predicted offers a compelling explanation for the large coseismic displacement and slip acceleration observed in the study area.

In **Chapter 4**, slip nucleation and interseismic strength recovery on carbonate faults is simulated by exploratory, low-velocity frictional and healing experiments, performed on (simulated) gouge samples prepared from carbonate breccia adjacent to the LFZ fault core material. Experiments, consisting of sequential "velocity stepping" (VS-seq1), "slide-hold-slide" (SHS) and "velocity stepping" (VS-seq2) stages, were performed to study the frictional healing behavior of carbonate fault gouge, and the effects of healing on the velocity dependence of friction, at 20–140 °C and at 50 MPa effective normal stress. Dry experiments show classical or Dieterich-type healing behavior, characterized by a transient peak in friction after each hold period with no effects of SHS testing on steady-state friction.

By contrast, wet tests show 1) an increase in apparent steady-state friction upon resliding after a hold period, and 2) a pronounced increase in the friction rate dependence parameter, ($a–b$), after the SHS stage. The latter promotes velocity strengthening slip above 80 °C where velocity weakening is observed in dry samples. These aspects of "non-Dieterich-type" healing behavior have not been reported previously for carbonate gouges. The observed effect of SHS-testing on ($a–b$) has never been reported. Our findings suggest that, under in-situ hydrothermal conditions, interseismic fluid-assisted deformation processes can significantly promote fault restrengthening causing slip stabilization. If the results apply to active faults in carbonate terrains, they have important implications for understanding how the extent of the seismogenic zone and how earthquake magnitude may evolve with repeated cycles of natural seismicity and interseismic healing.

In Chapter 5, we expand on the preliminary experiments of Chapter 4, investigating the frictional and healing of simulated carbonate fault gouges derived from carbonate breccia and natural gouge sampled from the LFZ. The same experimental strategy (VS-seq1, SHS-seq, VS-seq2) and experimental conditions (20–140 °C and 50 MPa effective normal stress) were employed. The breccia-derived material was chosen to obtain a simulated gouge with a chemically unaltered fault rock composition, appropriate for studying (recurrent) rupture nucleation at depth, while gouge-derived samples were used to represent altered fault core material present at shallow depths (< 7 km) on the LFZ segment studied. The experimental results confirmed the observation reported for breccia-derived material in Chapter 4. In dry experiments, we observed classical "Dieterich-type" healing behavior and zero dependence of (quasi) steady-state friction, on SHS or VS history. By contrast, experiments performed on breccia- and gouge-derived samples under hydrothermal conditions were characterized by "non-Dieterich" healing behavior, featuring a permanent or at least persistent increase ($\Delta\mu_r$) in (quasi) steady-state friction coefficient upon re-sliding after hold periods. An increase in the velocity dependence parameter, ($a–b$), after SHS testing was also observed. The transient peak frictional healing ($\Delta\mu_{pk}$) observed in the hydrothermal experiments was found to be composed of a "Dieterich" component ($\Delta\mu_w$) plus the persistent change in steady-state friction ($\Delta\mu_r$). Further analysis suggests that the "non-Dieterich-type" healing seen in our wet experiments was related to enhanced solution transfer processes, occurring during hold periods. Our findings indicate that under hydrothermal conditions, fluid-assisted healing processes such as pressure solution can strongly promote fault strength recovery rates, especially in clay-rich fault gouges. When applied to natural earthquakes in carbonate terrains, this suggests that the shallow portion of a fault with phyllosilicate-rich cores can heal at rates much higher than previously recognized. At the same time, the

observed increase in (a–b) implies that the upper limit of the seismogenic zone may progressively migrate to deeper crustal levels. Both aspects have important implications for understanding how earthquake magnitude and aftershock distributions may evolve with repeated cycles of natural seismicity and interseismic healing in carbonate terrains.

In **Chapter 6**, a mechanism-based microphysical model is developed for quantitatively describing the frictional and healing behavior of carbonate fault gouge, assuming that the frictional behavior seen in lab experiments is controlled by competing processes of intergranular slip versus contact creep by pressure solution. By solving two controlling equations that are derived from kinematic and energy/entropy balance considerations, and using standard creep equations for pressure solution, we simulate typical lab-frictional tests, namely "velocity stepping" and "slide-hold-slide" test sequences, for velocity histories and environmental conditions employed in experiments on the breccia-derived gouges reported in Chapters 4 and 5. The modeling results capture all of the main features and trends seen in the experimental results, including both steady-state and transient aspects of the observed behavior, with reasonable quantitative agreement. To our knowledge, ours is the first mechanism-based model that can reproduce full RSF-like behavior without recourse to the RSF laws. Since it is microphysically based, we believe our modeling approach can provide a much improved framework for extrapolating friction data to natural conditions, in studies of the seismic cycle not only on the LFZ but on active faults in carbonate terrains in general.

Finally, **Chapter 7** summarizes the main conclusions of the thesis and considers several important implications of the results obtained. This chapter and the thesis as a whole is concluded with a summing up of remaining questions and suggestions for further research. One major conclusion drawn concerns the importance of thermochemical pressurization in dynamic weakening processes of the Wenchuan earthquake. Another important finding is that we observed "non-Dieterich-type" healing behavior, characterized by persistent increase in steady-state frictional strength, and a healing-induced stabilization effect, i.e. an increase in (a–b), for carbonate(-rich) rocks sheared at hydrothermal conditions. A key contribution for the future is that a microphysical model was developed that can reproduce the steady-state, transient and healing behavior of any granular fault gouge undergoing competing effects of granular/cataclastic flow and diffusive mass transfer.

Chapter 1

Introduction

1.1 General motivation and scope of this study: Earthquakes in carbonates

Destructive, relatively shallow earthquakes are commonplace in tectonically active carbonate terrains, nucleating within, and/or propagating through the thick carbonate cover sequences that typically dominate the upper crust of such regions (e.g. *Collettini et al.*, 2014). Examples include the 1995 Mw 6.2 Aigion earthquake in Greece (hypocentral depth 7.2 km, *Bernard et al.* (2006)), the 1979 Mw 5.8 Norcia earthquake (6 km, *Cello et al.*, 1998), the 1997-1998 Mw<6.0 Colfiorito seismic sequence (5-7 km, *Olivieri and Ekström*, 1999), and the 2009 Mw 6.3 L'Aquila earthquake (9.5 km, *Chiarabba et al.*, 2009) in the Italian Apennines. A much larger event, affecting a wide awathe of carbonate-dominated terrain in northern half of the rupture trajectory, is the catastrophic 2008 Mw 7.9 Wenchuan earthquake in Sichuan, China (11 km hypocentral depth in the north segment, *Xu et al.*, 2009; *Zhao et al.*, 2010). Besides the propensity for shallow natural earthquakes in carbonates, induced seismicity tends to be more common in carbonate reservoirs (*Chen and Talwani*, 1998), statistically speaking, than in clastic sedimentary rocks (*Ma et al.*, 2012), possibly pointing to some special attributes of carbonate systems (cf. *Verberne et al.*, 2010).

In the Apennines range (Italy), both seismological and geological evidence has shown that carbonate rocks are present at the hypocentral depths characterizing both present day earthquakes and major historical earthquakes (*Chiaraluce*, 2012; *Bullock et al.*, 2014). Some of these earthquake ruptures have propagated all the way to surface, with aftershocks occurring as shallow as ~ 2 km, as observed after the L'Aquila earthquake in 2009 (*Chiarabba et al.*, 2009). The relatively shallow nature of such events means that they are often highly damaging even when the moment magnitude is moderate. In the case of L'Aquila earthquake, more than 300 people were killed, 1500 injured and 19 billion Euro worth of damage was caused. To improve seismic hazard evaluation in tectonically active carbonate terrains, such as this, the physical and chemical properties of carbonate fault rocks that control active fault behaviour are attracting increased attention - in relation to both earthquake nucleation and rupture propagation (e.g. *Han et al.*, 2007; *De Paola et al.*, 2011; *Smith et al.*, 2011; *Scuderi et al.,* 2013*; Verberne et al.*, 2013a and 2013b). Nonetheless, compared with fault zones developed in other rock types, e.g. in granitic and metamorphic rocks, as in the case of the Median Tectonic line in Japan (*Wibberley and Shimamoto*, 2003), or in clastic sedimentary rocks like the Chelungpu fault (*Tanaka et al.*, 2001), the properties of carbonate-hosted fault rocks are still poorly known.

Turning to the devastating Mw 7.9 Wenchuan earthquake, this struck the densely populated Sichuan province, China, on May 12, 2008, killing more than 80,000 people and injuring more than 370,000. The earthquake occurred on the Longmenshan thrust belt

(Figure 1.1a), producing a 240 km long surface rupture (*Xu et al.*, 2009) and yielding an average stress drop of 18 MPa, i.e. double that characteristic of a typical continental interior earthquake (*Zhang et al.*, 2009). As a major thrust belt marking the foreland of the Tibetan Plateau (Figure 1.1b), the Longmenshan fault zone (LFZ) was only subjected to minor deformation of no more than 1 mm/yr (Figure 1.1b) and had not experienced a devastating earthquake for at least 2700 yrs before the Wenchuan earthquake (*Zhang*, 2013). Geological and trenching profiles across the LFZ after the Wenchuan event revealed that a long (middle-to-north) segment of the surface rupture zone is dominated by carbonate sequences (*Fu et al.*, 2008; *Cao et al.*, 2011; *Li et al.*, 2014; see an example in Figure 1.2), with the largest coseismic displacement of ~ 11 m occurring in this segment (*Zhang et al.*, 2010). Inversion of the spatio-temporal rupture process of the earthquake indicated that the coseismic slip predominantly fell into the upper 10 km on this segment (*Zhang et al.*, 2009; *Zhao et al.*, 2010; Figure 1.3). High-precision relocation studies showed that aftershocks occurred in the area, characterized by magnitudes up to Ms 5.2 and focal depths of ~ 10 km (*Zhang et al.*, 2008). Stratigraphic analysis showed the original thickness of carbonate strata affected in the northern segment of the rupture, which are from Sinian to

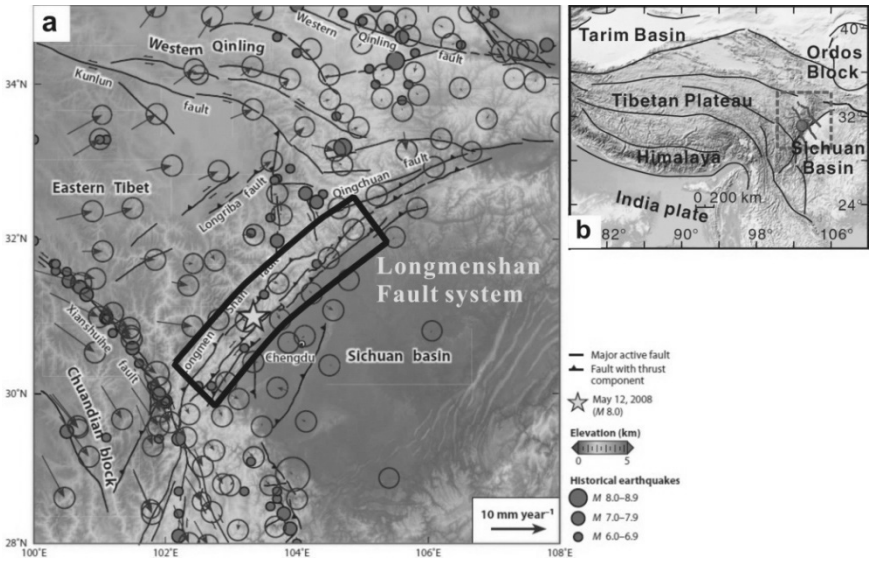

Figure 1.1 Regional tectonic map of the Longmenshan region (after Zhang et al., 2010). a) Active tectonic map of the Longmenshan thrust fault system. GPS velocity vectors are relative to the South China block. Major active tectonic terrains are denoted by their names. Historical earthquakes with magnitude greater than 6.0 are added. b) Geological map of Tibetan Plateau and surrounding area.

Middle Triassic in age, is about 4000 to 7000 m. Deep gas wells drilled in this areas also showed that carbonates dominate down to at least 7560 m (*Cao et al.*, 2011). Seismic reflection profiles further revealed the sedimentary strata persist down to at least 9 km (*Jia et al.*, 2010; *Cao et al.*, 2011). All these pieces of evidence suggest that the extensive carbonate sequences seen at the surface may be present even at the depth where rupture nucleated, and anyway hosted most of the trajectory followed by the rupture process. Against this background, one may ask if the earthquake dynamics in this region is related to the host rock. To answer this question, and to fill the knowledge gap that exists regarding the properties of carbonate fault rocks in general, laboratory studies of these properties of carbonate-hosted fault rocks are necessary.

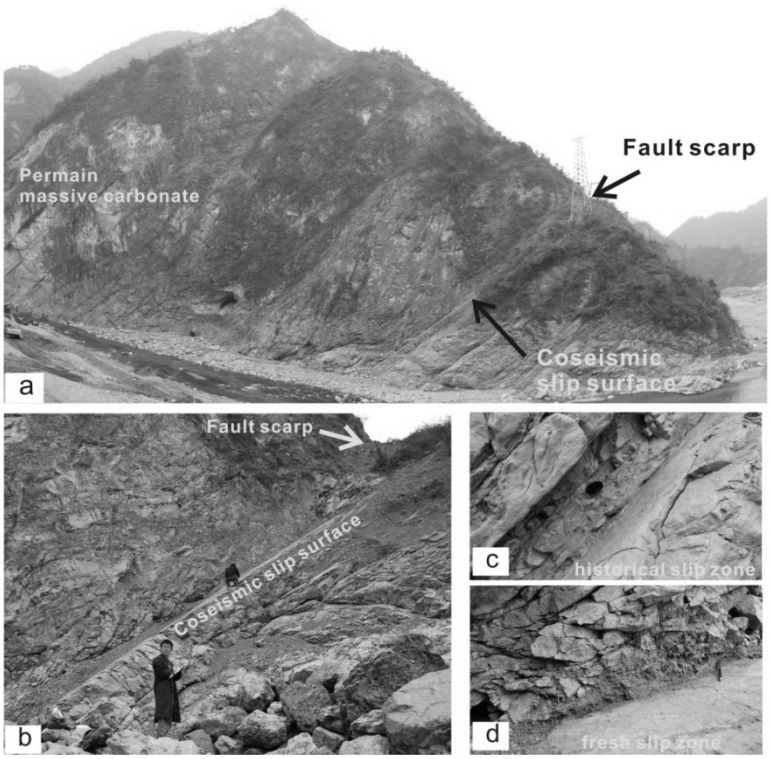

Figure 1.2 Photographs showing a) a typical carbonate outcrop associated with the Wenchuan earthquake. b) A coseismic displacement of 0.5 m occurred in this site (Hou et al., 2012), creating a bed-parallel slip surface extending for at least 20m. We could find both c) well-cemented historical and d) fresh slip zones, characterized by narrow cores (<0.5m) and thin gouge layers (<1mm). (*GPS: 104°16'50"E and 31°38'51"N*)

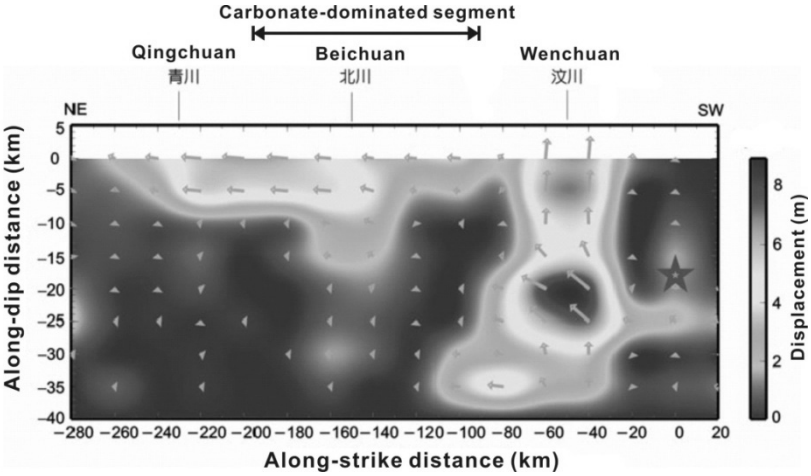

Figure 1.3 Slip direction and slip distance on the fault plane of the Yingxiu-Beichuan fault that ruptured during the Wenchuan earthquake (from Zhao et al., 2010). The star represents the initiation point of the rupture.

In this thesis, I report the results of an experimental study of the compositional, transport, frictional and healing properties of fault rocks focusing on samples collected from surface exposures on the carbonate segment of the coseismic rupture zone of the Longmenshan fault. Implications regarding earthquake nucleation, dynamic slip weakening and fluid transport as well as fault architecture evolution during seismic cycle of the Longmenshan fault zone (LFZ) and of active faults in carbonates in general are considered. In addition, a microphysically based model for describing frictional and healing behavior of granular fault gouge is developed, which succeeds in reproducing the steady-state and transient frictional behavior observed in our experiments, providing an alternative explanation to the classical rate-and-state friction laws.

1.2 Structure and composition of carbonate fault zones

The structure of major faults at upper and mid-crustal depths can generally be divided into three principal zones: the fault core, the surrounding damage zone and the host rock (*Caine et al.*, 1996). The fault core, where most of the displacement is accumulated, is generally characterized by comminuted rocks, such as fault gouge, which are typically subject to geochemical and mineralogical alteration during both co- and post-seismic periods (*Kerrich et al.*, 1984; *Hickman et al.*, 1995; *Solum et al.*, 2006; *Chen et al.*, 2007; *Ishijawa et al.*, 2008; *Hirono et al.*, 2008; *Schleicher et al.*, 2009). Investigation of fault zone composition provides insight into fault strength, fluid flow and fluid-rock interaction.

Extensive studies have been performed on fault zones cutting crystalline and clastic sedimentary rocks (e.g., *Goddard and Evans*, 1995; *Boullier et al.*, 2004). Using bulk rock chemical analysis, *Goddard and Evans* (1995) concluded that fluids passing through fault zones react with the fault rock, dissolving and transporting soluble cations away. Such an effect can change fault rock volume, insoluble content and isotopic composition, as well as transport and mechanical properties (*Labaume et al.*, 2004; *Chen et al.*, 2007; *Molli et al.*, 2010; *Pili et al.*, 2002, 2011; *Chen et al.*, 2013a and 2013b). Similarly, fluid-assisted mineralogical changes may cause fault weakening and reactivation (e.g., *Chester et al.,* 1993), in particular when clay minerals are formed (e.g., *Wintsch et al.*, 1995; *Vrolijk and van der Pluijm*, 1999). Fault gouges are often enriched in clay minerals with respect to the host rock, as seen in the cores of seismogenic faults such as the San Andreas fault (*Lockner et al.*, 2011). However, relatively little work has been done on the geochemical signature of carbonate-hosted fault rocks.

The work that has been done on natural carbonate faults suggests that the internal structure of carbonate fault zones is strongly influenced by chemical processes associated with fluid channeling and fluid-rock interaction (e.g., *Faulkner et al.*, 2003; *Labaume et al.*, 2004; *Janssen et al.*, 2005; *Billi*, 2005; *Agosta and Aydin*, 2006; *Molli et al.*, 2010) and by coseismic thermal-hydrological- mechanical- chemical processes. Geological signatures of seismic slip are rare (*Sibson and Toy*, 2006), except in carbonate-hosted faults where carbonate minerals dissociate at temperatures lower than those required for producing friction melt (*Rowe et al.*, 2012; *Chen et al.*, 2013a; *Tesei et al.*, 2013; *Fondriest et al.*, 2012; *Bullock et al.*, 2014; *Collettini et al.*, 2014). Recent high-velocity friction studies on laboratory faults showed that a large increase in temperature is experienced by carbonate fault rocks on the slip surface at coseismic rates, leading to decomposition of the carbonate components (e.g. *Han et al.*, 2007; *De Paola et al.*, 2011). However, the associated mineralogical change, as observed in laboratory (e.g. *Han et al.*, 2007), is unlikely to be preserved in nature. Signatures for such decarbonation process include geochemical effects (i.e. “isotopic fractionation”, *De Paola et al.*, 2011, and “high-temperature fluid inclusion”, *Ujiie et al.*, 2008) and characteristic, residual textures (i.e. “gritty dolomite”, *Rowe et al.*, 2012, “skeletal crystals”, *Collettini et al.*, 2013). Besides these indicators for thermal decarbonation, “mirror slip surfaces” (*Siman-Tov et al.*, 2013; *Fondriest et al.*, 2013) formed in high velocity friction experiments and seen in many active carbonate faults, have recently been proposed to record seismic slip events, though similar fearures have also been observed to form in low velocity experiments (*Verberne et al.*, *accepted*). Micro- and nano-scale investigations of the principal slip zone of natural and experimental mirror slip surfaces in

carbonates suggest that different deformation processes operate during different stages of natural seismic cycles and laboratory friction experiments, including plastic deformation such as pressure solution (e.g. *Tesei et al.*, 2013). To attach meaning to the microstructures observed in such slip zones, it is crucial to understand the mechanisms that produce them in carbonate fault rocks, such as thoses that ruptured during the Wenchuan earthquake.

Phyllosilicate-rich fault rocks have also attracted much attention (*Morrow et al.*, 1992; *Tembe et al.*, 2010; *Carpenter et al.*, 2011; *Zhang and He*, 2013; *Den Hartog et al.*, 2013), due to the widespread occurrence of phyllosilicate-bearing faults in different tectonic settings, and also to their roles in controlling the earthquake dynamics of rupture nucleation and propagation (e.g. *Verberne et al.*, 2010; *Tesei et al.*, 2012; *Ikari et al.*, 2013; *Den Hartog et al.*, 2013). Recent studies have revealed that clay minerals can be enriched in carbonate-hosted faults, especially in fine-grained fault cores (e.g. *Hou et al.,* 2012; *Chen et al.*, 2013; *Bullock et al.*, 2014; *Viti* et al., 2014). Studies of trenches and boreholes along the LFZ have shown that the principal slip gouges are indeed enriched in clay components (e.g. *Zhang et al.*, 2013; *Li et al.*, 2013). Many mechanisms have been proposed to cause the enrichment of phyllosilicates in fault zones, including the above mentioned thermally induced mineralogical alteration (*Vrolijk and van der Pluijm*, 1999), extensive rock-fluid interactions (e.g. *Labaume et al.*, 2004; *Molli, et al.*, 2010; *Chen et al.*, 2013a) and pressure solution (*Gratier et al.*, 2011). Previous work on carbonate-phyllosilicate rocks is limited to field and (micro)structural analyses, shedding light on the role of phyllosilicates in controlling the deformation mechanisms operating in carbonate faults (*Bullock et al.*, 2014; *Viti* et al., 2014). However, experimental studies concerning mechanical properties of carbonate-phyllosilicate rocks have only been performed at room temperature (*Tesei et al.*, 2012). Accordingly, the mechanism(s) dominating the formation of phyllosilicate rich zones in carbonate faults is at present not clear. Moreover, considering the widespread presence of such zones, it is also important to understand the role of the phyllosilicates in influencing the mechanical properties of carbonate-rich fault rocks, especially at in-situ hydrothermal conditions.

1.3 Dynamic slip weakening in carbonate fault zones

Slip weakening is one of the fundamental processes leading to the generation of large earthquakes (e.g. *Scholz*, 2002). In view of large coseismic displacement and stress drop associated with the Wenchuan earthquake (*Xu et al.*, 2009; *Zhang et al.*, 2009), dynamic slip-weakening mechanism(s) must have played a major role in controlling the rupture behavior (for a review see *Niemeijer et al.*, 2012).

1.3.1 High-speed friction behavior: lack of data on wet systems

Several thermally-activated slip weakening mechanisms have been proposed in the literature to account for low frictional strength of faults during earthquake propagation. These include flash heating (*Rice*, 2006), thermal pressurization (*Lachenbruch*, 1980; *Rice*, 2006), frictional melting (*Hirose and Shimamoto*, 2005), gel formation (*Di Toro et al.*, 2004), thermal decomposition (*Han et al.*, 2007), nanoparticle lubrication (*Han et al.*, 2010), and elastohydrodynamic lubrications (*Brodsky and Kanamori*,2001). Some of these mechanism are expected to be important in carbonate rocks, such as nanoparticle lubrication (*Han et al.*, 2010; *Reches and Lockner*, 2010), decarbonation (*Han et al.*, 2007) and fluid pressurization (*De Paola et al.*, 2011). We note that most previous high-velocity friction experiments were performed at dry conditions. However, under natural earthquake conditions, faults are expected to be subjected to water-saturated conditions. Technical challenges related to pore fluid confinement have hindered the investigation of the role of water in high-velocity experiments that reproduce natural earthquake slip velocities. Those which have been done indicate that thermal pressurization was the dominant mechanism controlling the slip weakening of water-saturated gouge sample (e.g. *Faulkner et al.*, 2011), whereas for bare rocks, the presence of water could accelerate or inhibit the dynamic (frictional) weakening process, depending on the host-rock composition (*Violay et al.*, 2013). With the limited data presently available, it is not practical to estimate the real situation in the rupture propagation processes associated with Wenchuan earthquake. Against this background, it is important to investigate the dynamic frictional behavior of samples collected from the principal slip zone of the Wenchuan earthquake under water-saturated conditions and using sliding velocities simulating the full range of seismic deformation conditions associated with the Wenchuan earthquake.

1.3.2 Coseismic thermochemical pressurization

Theoretical studies have focused on thermal pressurization (TP) as an important slip-weakening mechanism, at both the rupture nucleation (*Segall and Rice*, 2006; *de Lorenzo and Lpddo*, 2010) and coseismic slip (*Lachenbruch*, 1980; *Mase and Smith*, 1985; *Rice*, 2006) stages of an earthquake. The principle of TP is that the pressure of pore fluid, trapped inside a slipping fault, builds up due to frictional heating, thus reducing the effective normal stress acting on the fault plane and hence the shearing resistance of the fault (*Lachenbruch*, 1980). TP can cause additional effects such as increased slip distance (*Rice*, 2006) and an increase in rupture velocity (*Bizzarri and Cocco*, 2006). On the other hand, as

addressed above, growing natural and laboratory evidence suggests that chemical alteration of the sliding material, e.g. by dehydration or decarbonation reactions, at coseismic slip rates must also be taken into account regarding earthquake rupture propagation. Thermochemical pressurization (*Brantut et al.*, 2010) can affect pore pressure via the release of fluid mass (*Brantut et al.*, 2008; *Famin et al.*, 2008; *Ferri et al.*,2010; *Hirono et al.*, 2008; *Sulem and Famin*, 2009), and/or via reaction enthalpy changes (*Brantut et al.*, 2011), i.e. in addition to conventional TP. However, few experiments have yet been successful in verifying coseismic TP (*Ujiie et al.*, 2011; *Sumem et al.*, 2004; 2005), not to mention the influence of reactions upon it.

Lab experiments can only be used to obtain the properties of fault zone materials and to test models of the complex interactions that determine fault behavior. They cannot directly simulate in-situ dynamic faulting behavior. Therefore a key aim of experiments must be to characterize the different processes that can operate, so that these processes can be included in complex numerical models that can then be tested against experiments with well controlled boundary conditions. If validated in this way, such models can in turn be applied to model rupture nucleation and propagation behavior in nature. Recent numerical modeling studies using lab-constrained properties of fault rocks are now leading to an improved understanding of coseismic TP and reaction processes, and of their influence on fault rupture propagation (e.g. *Tanikawa and Shimamoto*, 2009; *Sulem and Famin*, 2009). Beyond the scope of high-velocity experimental studies, it is therefore important to model the coseismic slip inside a fluid-saturated fault zone including thermochemical pressurization and thermally induced reaction, using lab-derived fault rock properties, and the slip history associated with the Wenchuan earthquake.

1.3.3 Transport properties of Wenchuan earthquake fault rocks

Beside dynamic friction coefficient(s), one of the key factors that control fluid pressurization processes is the transport properties of the principal fault gouge (*Rice*, 2006). Statistical analysis (23 in total) has indicated that fault gouges found in almost all active fault zones have permeability lower than 1×10^{-18} m^2 (*Chen and Yang*, 2012), favoring the widespread occurrence of thermal pressurization. However, statistical analysis also indicates permeability of the fault gouges (at the same effective pressure) can vary by a few orders of magnitude down to 6×10^{-23} m^2 (*Morrow et al.*, 2014), presumably related to the texture and composition of the fault rocks, e.g., load-supporting framework, particle size distribution and clay content (e.g. *Wibberley and Shimamoto*, 2003; *Bernabé et al.*, 2004). However, at present no data are available for Wenchuan earthquake fault, and as far as I know, previous

work was mostly on silicate or synthetic fault rocks, with little data existing for carbonate fault rocks in general.

Permeabilities of the fault gouge and its surroundings are also important in determining the hydrological and sealing conditions of the fault zones (*Chen et al.*, 2013b). Recent study used the fluctuation of water levels in a deep borehole in response to solid-earth tides (*Xue et al.*, 2013) to track the in-situ permeability of the damage zone of the Wenchuan earthquake. These indicate high permeability (~ 10^{-15} m^2) and extremely fast post-seismic decay in permeability for the Wenchuan earthquakes fault zone. Other studies investigating the permeability of fault zones using methods such as (repeated) water injection tests also provide data on fault zone permeability and the post-seismic sealing/healing process for active faults, such as the Nojima fault (*Kitagawa et al.*, 2007), the Chelungpu fault (*Doan et al.*, 2006) and the Nankai accretionary prism (*Boutt et al.*, 2012). In-situ measurements, using drill holes penetrating fault zone at depth, can provide permeability data under ambient temperature and pressure condition. However, the permeability obtained represents the average value for volumes of rock extending from several meters (*Boutt et al.*, 2012) to hundreds of meters (e.g., *Kitagawa et al.*, 2002; *Xue et al.*, 2013) from the borehole. Therefore, they are of limited use in identifying the permeability structure of faults that usually have complex internal structure and lithologic heterogeneity (e.g. *Wibberlley and Shimamoto*, 2003; *Chen et al.*, 2009). Note that the volume of material used in laboratory measurements is in order of 10^{-4} to 10^{-3} m^3, which is much smaller than that involved in a typical in-situ fluid transport measurements (>1 m^3, *Boutt et al.*, 2012). Laboratory measurements of core samples are thus likely to provide lower bounds on the true fault zone permeability. In interpretating the hydrological and sealing behavior of real faults under in-situ conditions, measurements at different scales should be combined. To date, no laboratory data are available for the Wenchuan earthquake fault rocks.

1.4 Low-velocity frictional and healing behavior of carbonate fault rock

Alongside dynamic slip weakening in the high-velocity regime as addressed above, velocity weakening of faults is another fundamental process leading to the generation of large earthquakes (*Scholz*, 2002). As stated before, most of the frictional experiments that have been done on carbonate rocks to date were performed at coseismic slip rates (e.g., *Han et al.*, 2007; *De Paola et al.*, 2011). Only a few studies have addressed the rate-and-state friction (RSF) behavior in the seismic nucleation regime or the underlying microphysical mechanism(s) that lead to stable (aseismic) vs. unstable (seismogenic) slip (*Weeks and Tullis*, 1985; *Olsson*, 1974; *Verberne*, 2010; 2013b; *Scuderi et al.*, 2013). Even fewer studies have

addressed carbonate fault healing and associated strength recovery, though these aspects have been widely studied in relation to both natural (*Li et al.*, 2003; *Marone et al.*, 1995) and laboratory faults (*Dieterich*, 1972;) in silicate rocks, as they strongly affect earthquake nucleation, magnitude and recurrence intervals (e.g. *Ruina*, 1983; *Marone*, 1998a).

Fault healing and associated strength recovery has been widely reported following both natural (*Li et al.*, 1998; 2003) and laboratory earthquakes (e.g. *Wong and Zhao*, 1990). Time-dependent fault strengthening via healing is frequently described, in the framework of the empirical RSF laws proposed by *Dieterich* (1979), using a logarithmic function to describe strength recovery. This is termed Dieterich-type healing and is often observed in room temperature experiments (*Dieterich*, 1972; *Marone et al.*, 1998b). However, fault healing can also result in hydrological sealing of a fault, which can influence internal fluid pressure evolution and hence strength, by inducing fluid over pressurization (*Tenthorey* et al., 2003). Moreover, non-Dieterich-type healing behaviour is becoming increasingly frequently reported in friction experiments, notably at hydrothermal conditions (*Karner et al.*, 1997; *Nakatani*, 1998; *Muhuri et al.*, 2003; *Nakatani and Scholz*, 2004; *Yasuhara et al.*, 2005; *Niemeijer et al.*, 2008). Likely mechanisms causing such healing behaviour have long been anticipated, and include thermally-activated lithification (*Karner et al.*, 1997), mechanical consolidation (*Nakatani*, 1998), solution transfer (*Kanagawa et al.*, 2000; *Nakatani and Scholz*, 2004) and pressure solution (*Yasuhara et al.*, 2005; *Niemeijer et al.,* 2008). However, direct observations of such processes, in particular fluid-assisted healing processes, have been limited to quartz rocks and to rock analogue systems (*Bos and Spiers*, 2002).

There is accordingly much interest in obtaining a better understanding of the frictional behaviour of carbonate fault rocks, especially their rate-and-state dependent frictional behaviour under steady state and non-steady state slip conditions. Of particular interest is the main mechanism controlling healing under in-situ seismogenic conditions, i.e. at elevated temperature and fluid pressure where solution transfer and other thermally activated processes are active. Such information is crucial for modeling the seismic cycle on active faults and for evaluating earthquake recurrence intervals and magnitudes. However, very little data is available on healing processes and rates in carbonate fault rocks (*Tesei et al.*, 2012). In cases such as the LFZ, paleoseismic studies suggest a recurrence interval of ~ 2500 years, which agree with estimates made from the average coseismic displacement of ~ 5 m (*Xu et al.*, 2009) and the background tectonic shortening rate of ~ 1 mm/year (*Zhang et al.*, 2010). Progress beyond such average estimates means that a much better understanding of fault healing processes is needed, notably in carbonates where almost nothing is currently known.

1.5 Microphysical model for RSF friction of granular fault gouge

The RSF laws were originally developed as a phenomenological description of the frictional behavior observed in lab experiments (*Dieterich*, 1979; *Ruina*, 1983; *Linker and Dieterich*, 1992; *Kato and Tullis*, 2001). In previous studies, the empirical RSF laws have been extensively and quite successfully applied to fault mechanisms (e.g. *Marone et al.*, 1998a; *Scholz*, 2002), including quasi-static nucleation (e.g. *Scholz*, 2002), slow-slip motion (*Ampuero and Rubin*, 2008), aftershock activity and restrengthening (*Marone*, 1995; *Chen and Lapusta*, 2009; *Helmstetter and Shaw*, 2009), as well as interseismic creeping processes (*Barbot et al.*, 2008; *Hetland et al.*, 2010). However, these laws can not readily be envisioned in terms of the underlying physics (e.g. *Rice et al.*, 2001). Most work up to now is based on the concept of contact creep, which is widely accepted to be a thermally-activated process operating on the sliding surfaces (e.g. *Dieterich*, 1979; *Estrin and Bréchet*, 1996; *Sleep*, 1997; *Berthoud et al.*, 1999; *Nakatani*, 2001; *Rice et al.*, 2001; *Beeler*, 2004; *Sleep*, 2005; *Putelat et al.*, 2011; *He et al.*, 2013). A simple form of this assumes higher microscopic stresses on contacts than the nominally applied (*Estrin and Bréchet*, 1996). However, the deformation mechanisms involved in a friction phenomena are more complex than pure contact creep. Other mechanisms such as cataclastic/granular flow are expected to be active (e.g. *Marone*, 1998a; *Bos and Spiers*, 2002). Moreover, almost all faults are filled with gouge and the actual physical processes that can be inferred to go on in gouge-filled faults on the basis of microstructural and micro-mechanistic studies need to be addressed (*Sleep et al.*, 2000; *Niemeijer and Spiers,*, 2005; 2007; *Den Hartog and Spiers*, 2013). To more reliably apply the experimentally-derived laws to natural fault zones, and notably to extrapolate them beyond experimental conditions, an understanding of the microphysical mechanisms is required.

There are several critical discrepancies between seismological constraints on RSF behavior associated with earthquakes and lab-derived RSF parameters, in particular regarding the static stress drop and characteristic slip distance associated with seismic events (*Scholz*, 2002). Moreover, lab friction studies can address only limited fault topographies, displacements, experimental durations and P-T conditions, which means that scale issues, and especially processes like dilatation and fluid-rock interaction, cannot be fully taken into account. Without a physical basis accounting for such effects, extrapolation of lab-derived RSF data to nature involves significant, often unknown uncertainties. Besides the difficulties in extrapolating to nature, it has been long recognized that the RSF laws have shortcomings in reproducing laboratory results (e.g. *Beeler et al.*, 1994; *Chester*, 1994; *Marone et al.*,

1995). For instance, at hydrothermal conditions where fluid-assisted mass transfer processes are active, frictional healing may be strongly promoted, with the healing rates measured lying far beyond the log-linear model used in RSF approaches (e.g. *Karner et al.*, 1997; *Nakatani and Scholz*, 2004).

Again, in order to more reliably apply experimental results to natural fault zones, and notably to extrapolate lab data beyond laboratory pressure, temperature and velocity conditions, an understanding of the microphysical mechanisms governing fault frictional behavior is required. A better basis is needed to assess reliability and to underpin modeling of earthquake phenomenon and induced seismicity. Some pioneering efforts have succeeded in predicting the steady-state frictional strengths of fault gouges, using microphysical models established from the inferred deformation mechanisms (*Bos and Spiers*, 2002; *Niemeijer and Spiers*, 2007; *Den Hartog and Spiers*, 2014). However, these models have so far addressed only steady state friction, with transient frictional behavior, i.e. the response to a perturbation in sliding rate, not yet being considered. Ideally, of course, a single model based on the physical processes operating should be sought, which describes steady state, transient and healing behavior, as it is likely that the same physical processes are involved in controlling all of these aspects of frictional behavior. Moreover, an ideal model should apply to different ranges of slip velocity. Different deformation and healing mechanisms are involved in controlling material behavior at different P-T-chemical conditions and at different ranges of slip rates. This also needs to be tied to the different regimes of velocity dependence seen in experiments from low to high (*Shimamoto*, 1986; *Den Hartog et al.*, 2013; *Bar-Sinai et al.*, 2014). Moreover, intrinsic material behavior should be seen as a separate aspect from processes such as fluid pressurization that are influenced by boundary conditions, especially in experiments (*Niemeijer and Spiers*, 2007).

1.6 Aims of this thesis

In view of the research questions and knowledge gaps indentified above, for an improved understanding of earthquake nucleation and rupture propagation with respect to carbonate faults in general, it is necessary to investigate the physical properties of carbonate fault rocks under in-situ seismogenic conditions. In the context of the LFZ and the Wenchuan earthquake, which I take as a case study of major importance in Chinese research efforts on earthquake hazard reduction, I now define the following aims for the present thesis:

1) Determination of the internal structure of representative rupture zone profiles, and of the mineralogical, geochemical and isotopic ($\delta^{13}C$, $\delta^{18}O$) composition of fault rocks across chosen transects of the LFZ. My aim is to construct an integrated

model addressing the coupling between fault activity, fluid migration, mass transport and geochemical evolution that can occur under near-surface conditions in active carbonate fault zones.

2) Experimental determination of key fault rock properties related to coseismic slip-weakening processes, i.e. determination of high-velocity friction coefficients of principal slip zone gouges and of the transport properties of the principal slip zone gouge and its surroundings. The purpose here is to reproduce the coseismic thermochemical pressurization processes that likely occurred during the Wenchuan earthquake, and to investigate how both thermal and associated chemical effects contribute to the coseismic slip-weakening processes.
3) Experimental investigation of the (low-velocity) frictional and healing parameters characterizing carbonate(-rich) fault rocks under hydrothermal conditions, choosing a) simulated gouges derived from carbonate-dominated breccia samples to represent the chemically-unaltered fault rock composition appropriate for studying (recurrent) rupture nucleation and restrengthening at hypocentral depth(s), and b) clay-rich gouge collected from the principal slip zone, for understanding rupture propagation and aftershocks occurring in shallow, altered portions of the fault zone. The purpose here is to help assess whether the specific properties of carbonates contribute to the earthquake asperity inferred to characterize the carbonate segment of the LFZ, and to determine the role played by the propertie of carbonates in controlling aftershock nucleation and interseismic (creep) healing behavior at shallow crustal levels.
4) Development of a microphysical model for the frictional and healing behavior of any granular fault gouge that can undergo deformation by granular flow plus a thermally activated creep mechanism, including for the first time both the steady-state and transient behavior. The aim here is to provide an improved understanding the physics of RSF laws, and for constraining extrapolation of lab-derived frictional data to natural seismogenic conditions in future modeling studies.

These topics are tackled sequentially in Chapter 2-6. Finally, in Chapter 7, general conclusions are drawn and suggestions made for future work.

Chapter 2

Mass removal and clay mineral de/re-hydration in carbonate-rich surface exposures of the 2008 Wenchuan earthquake fault: Geochemical evidence and implications for fault zone evolution and coseismic slip

Jianye Chen, Xiaosong Yang, Shengli Ma, Christopher J. Spiers

Journal of Geophysical Research, 118, 474–496

Abstract

We report variations in the mineralogical, geochemical and isotopic ($\delta^{13}C$, $\delta^{18}O$) composition of fault rocks sampled in transects across the Zhaojiagou and Pingxi exposures of the Wenchuan earthquake or Longmenshan Fault Zone (LFZ), where the gouge-rich fault core and principal slip surface cuts through carbonate-rich strata. Pervasive fluid infiltration was found to modify the mineralogical and geochemical architecture of the fault zones studied. Enrichment/depletion patterns, element partitioning and a very large implied volume loss are quite different from those characterizing faults in granites and clastic sedimentary rocks, and can be explained by a mass removal model involving dissolution and advective transport enhanced by pressure solution. An increasing enrichment in smectite observed toward the principal slip surface, high abundance of elements such as Ba, Mg and F, deposition of minerals like barite and fluorapatite, as well as distinct depletion in ^{13}C in vein material, consistently suggest reactions involving a hydrothermal fluid originating at depth. Illitization of black gouges, caused by coseismic frictional heating, was found to be widespread. We propose that coseismic frictional heating along with the action of post-seismic hydrothermal fluids controlled the transformation and distribution of smectite and illite within the fault core of the LFZ. The coseismic de-watering reactions are expected to have been more extensive at depth, possibly helping generate excess pore pressure assisting dynamic slip weakening during the Wenchuan Earthquake.

2.1 Introduction

The structure of the upper portion of brittle faults can generally be divided into three principal zones: the fault core, the surrounding damage zone and the host rock (*Caine et al.*, 1996). The fault core, where most of the displacement is accumulated, is characterized by comminuted rocks, such as fault gouge, which are typically subject to geochemical and mineralogical alteration during both co- and post-seismic periods (*Kerrich et al.*, 1984; *Hickman et al.*, 1995). Investigation of fault zone composition provides insight into fault strength, fluid flow and fluid-rock interaction. Extensive studies have been performed on fault zones cutting crystalline and clastic sedimentary rocks (e.g., *Goddard and Evans*, 1995; *Tanaka et al.*, 2001; *Boullier et al.*, 2004). However, relatively little work has been done on the geochemical signature of carbonate-hosted fault rocks. That which has been done (e.g., *Kirschner and Kennedy*, 2001; *Faulkner et al.*, 2003; *Labaume et al.*, 2004; *Janssen et al.*, 2005; *Molli et al.*, 2010; *Fondriest et al.*, 2012) suggests that the internal structure of carbonate fault zones is strongly influenced by chemical processes associated with fluid channeling and fluid-rock interaction.

The permeability of fault zones can often be several orders of magnitude different from the host rock (*Wibberley and Shimamoto*, 2003). Fault zones accordingly exert an important control on subsurface fluid flow, acting as conduits for or as barriers to flow, or even fulfilling a combined fault-valve function (*Sibson*, *1990*). Fluids in fault zones are thought to play a key role, in earthquake nucleation and seismic rupture propagation (e.g., *Sibson*, 1973; *Chester et al.*, 1993; *Hickman et al.*, 1995). For example, frictional heating and dehydration of water-bearing minerals can result in fluid pressurization that reduces the effective pressure acting on the fault plane, producing a mechanical weakening (*Brantut et al.*, 2008, 2011). Fluids also play an important role in the chemical and architectural evolution of fault zones. Using bulk rock chemical analysis, *Goddard and Evans* (*1995*) concluded that fluids passing through fault zones react with the fault rock, dissolving and transporting soluble cations away. Such an effect can change fault rock volume, insoluble content and isotopic composition, as well as transport and mechanical properties (*Labaume et al.*, 2004; *Chen et al.*, 2007; *Molli et al.*, 2010; *Pili et al.*, 2002, 2011). Similarly, fluid-assisted mineralogical changes may cause fault weakening and reactivation (e.g., *Chester et al., 1993*), in particular when clay minerals are formed (e.g., *Wintsch et al.*, 1995; *Vrolijk and van der Pluijm*, 1999). Fault gouges are often enriched in clay minerals with respect to the host rock, as seen in the cores of seismogenic faults such as the Chelungpu fault (*Isaacs et al.*, 2007) or the San Andreas fault (*Lockner et al.*, 2011), where smectites are the most abundant clay minerals. Lastly, high temperature fluids derived from coseismic heating may interact with fault rocks,

changing isotopic ratios (*Kirrich et al.*, 1984; *Ishikawa et al.*, 2008). These ratios are expected to record the *in-situ* precipitation environment and to provide better indications of the origin of the fluid phase (*Wang et al.*, 2010) than elemental abundance.

Alongside these observations on natural fault rocks, the manner in which mineral reactions interact with the faulting process has recently been observed experimentally. Alteration processes such as the smectite-illite transformation have been shown to result from coseismic frictional heating (*Hirono et al.*, 2008; *Kuo et al.*, 2009). Coseismic mineral decomposition processes, such as dehydration of smectite or gypsum (*Ferri et al.*, 2010; *Brantut et al.*, 2011), dehydroxylation of kaolinite, and decarbonation of calcite or siderite (*Hirono et al.*, 2006; *Han et al.*, 2007; *Tanikawa et al.*, 2007) have also been demonstrated experimentally, corroborating, natural evidence for such reactions seen for example in drill cores from the Chelungpu (*Mishima et al.*, 2006; *Hirono et al.*, 2008; *Hamada et al.*, 2009) and Nojima faults (*Famin et al.*, 2008). Experiments are also showing that syndeformational mineral reactions and associated energy consumption may be much more important than previously recognized (*Brantut et al.*, 2011), as well as showing how reactions induced by frictional heating liberate fluid into the pores, building up pore pressure that may lead to dynamic stress reduction (e.g., *Ferri et al.*, 2010).

Against this background, examining the mineralogical and chemical composition of fault rocks can be expected to yield key insights into the characteristics of the fluid associated with faulting, as well as into the rock-fluid interaction processes that influenced the faulting mechanism. In this paper, we report mineralogical (bulk composition and clay portion) and geochemical (major and trace elements) variations measured in transects across two surface exposures of the 2008 Wenchuan earthquake rupture within the Longmenshan Fault Zone (LFZ), where the main slip surface cuts through carbonate-rich rocks. We document major mass/volume loss and element mobility in the fault rocks studied. A model describing the volume changes resulting from fluid-rock interaction in carbonate-rich fault zones is proposed. We also determine the stable isotope ($\delta^{13}C$ and $\delta^{18}O$) ratios characterizing the fault rocks from one site, by investigating the fault-related carbonate minerals. We go on to test models for isotopic evolution based on a decarbonation versus a water-rock interaction mechanism. In addition, the origin of the clay minerals within the fault zone and their role in the faulting process are discussed. It is argued that black gouge found at the sites studied was formed by illitization of smectite due to frictional heating and that the fluid released may have assisted dynamic rupture at shallow levels during the Wenchuan Earthquake.

2.2 Study area and methods

2.2.1 The study area and key exposures

The Longmenshan fault system constitutes of three parallel sub-faults. From West to East, they are the Maoxian-Wenchuan, Yinxiu-Beichuan and Guanxian-Jiangyou faults (Figure 2.1). The catastrophic Wenchuan earthquake (M_s 8.0) of 12 May 2008, occurred on the Yinxiu-Beichuan fault, producing a 240 km long surface rupture (*Xu et al.*, 2009). In this study, two exposures on the north segment of this fault are systematically investigated, the Zhaojiagou (ZJG) and Pingxi (PX) exposures. Both the principal coseismic slip surface at the ZJG and PX exposures cut though carbonate or carbonate-rich layers. Previous studies of microstructure, permeability, grain size distribution, frictional properties and magnetic properties of the fault rocks at the two localities (*Fu et al.*, 2008; *Han et al.*, 2010; *Chen et al.*, 2011; *Yao et al.*, 2011; *Yang et al.*, 2012) show similar characteristics that may represent common features along much of the LFZ, at least along the north segment where similar internal structure and lithologies are involved in the fault.

2.2.2 Field methodology

To determine the internal structure and composition of the fault zone, transect sampling was employed at the two exposures. A roughly 50-cm-thick surface layer was removed to eliminate weathered rock. Samples were then collected at a spacing of less than 0.5 m across the exposed fault zone. Typical country rocks were also collected. Sampling density was reduced to ~1 cm near the principal slip surface. Oriented gouge samples from the main slip zone (MSZ) were collected for petrographic analysis. They were recognized as very fine grained, tacky, clay-rich material exhibiting ductile behavior when wet. This material was easily distinguishable from the surrounding rocks by its appearance, feel and color. The surrounding damage zone, characterized by an increased density of crushed or fragmented grains and fractures relative to the host rocks, was divided into a highly damaged zone (HDZ) and a weakly damaged zone (WDZ). The fault core, with a width of several decimeters (*Billi*, 2005), was recognized and defined as the combined HDZ and the fault gouges. The WDZ is defined by the portion of transect extending from the outside edge of the fault core (HDZ and the fault gouges) to the point at which the rock is marked by the appearance of bedding. This correlated with a notable decrease in fracture density and degree of alteration, as well as changes in the dominant deformation pattern.

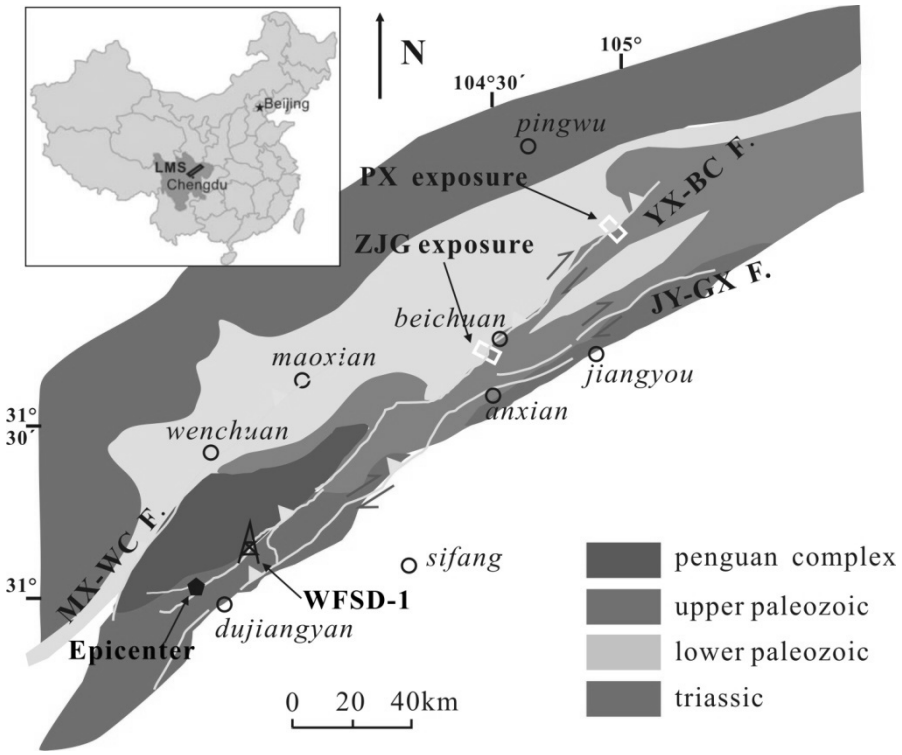

Figure 2.1. Location of the studying area and regional geological map of the Longmenshan (LMS) fault system, consisting of three fault zone, the Jiangyou-Guanxian fault (JY-GX F.), Yingxiu-Beichuan fault (YX-BC F.) and Maoxian-Wenchuan fault (MX-WC F.)

2.2.3 Laboratory analyses

Only fresh samples were selected for mineralogical and geochemical analysis. X-ray diffraction (XRD) was used to determine relative mineral content, including semi-quantitative analysis for clay minerals. Unoriented, hand-powdered bulk samples were scanned over a 2θ range of 3° to 45° with CuK-α radiation (0.15418 nm), at a scan rate of 2°/minute with step width of 0.02°, employing a Dmax 12kW X-Ray power diffractometer (45 kV and 100 mA). Bulk powder samples gave a first evaluation of the relative amounts of bulk clays, whose proportion was further verified by analyzing the clay-sized portion (< 2 μm). This was separated by centrifugation. One-milliliter slurry samples of clays and distilled water were air-dried on glass slides and scanned over a 2θ range of 2.5° to 15°. Ethylene glycol was used to detect the swelling components with 2θ coverage of 2.5° to 30°. Heating the samples to 550 °C also helped distinguish kaolinite from chlorite. For this, a 2θ coverage of 2.5° to 15° was used. The method of semi-quantitative analysis of clay minerals

followed *Syunnan* (1981) and *Lin et al.* (1992).

For comparative purposes, identical samples to those used for XRD analysis were also used for geochemical analysis. About 50 grams of crushed sample material was powdered in an agate ball mill to less than 200 mesh grain size, and then analyzed by X-ray fluorescence (XRF) spectrometry for major and minor oxides, including SiO_2, Al_2O_3, $Fe_2O_3^T$, K_2O, MnO, MgO, CaO, Na_2O, TiO_2 and P_2O_5, using a Magix-pro2440 X-ray fluorescence machine. The FeO content of the samples was determined by titration using $K_2Cr_2O_7$ after being digested by H_2SO_4+HF (*Rao and Govil*, 1995). Volatile components were measured by thermogravimetric analysis (*Tanaka et al.*, 2001): primarily water (presented as "H_2O") was determined by baking the samples at 110 °C and recording the weight increase of 100 % sulfuric acid in a chamber connected to the baking vessel. Weight loss after ignition at 1000 °C for 3 hours was also measured and presented as loss on ignition (LOI) data. Content of CO_2 was measured by nonaqueous titration (*Johnson et al.*, 1985). The weight ratio of major elements, minor elements, H_2O and LOI were combined and normalized to 100 wt. %. As for trace elements, the samples were first digested using distilled HF+HNO_3 in Teflon vessels and the percentages of trace elements were then determined using inductively coupled plasma mass spectrometry (ICP-MS) employing a Thermoelemental X7 analyzer. Sample-digesting procedures, analytical precision and accuracy of ICP-MS analyses are the same as described by *Li et al.* (2006). All geochemical tests were conducted at Hubei Geological Research Laboratory.

In order to quantify the element transfer and volume loss/gain within the LFZ, correlation analysis and the isocon method were applied (*Grant*, 1986; *Tanaka et al.*, 2001). The isocon approach involves plotting element concentration in an altered sample (or mean of a group of altered samples) against an unaltered reference precursor, in a "Grant-type plot" (*Grant*, 1986). Elements that are immobile should be dispersed along a straight line passing through zero. These elements are usually high field strength elements, because they are expected to be less mobile or fully immobile in fluid-rock interaction and weathering processes (*Goddard and Evans*, 1995). In our study, TiO_2 as the most used reference elements (e.g., *Tanaka et al.*, 2001; *Chen et al.*, 2007) was chosen as the immobile proxy defining the isocon line, along which elements that are neither gained nor lost during alteration will fall. The slope of this line defines the net mass change of the altered sample. To quantify corresponding volume changes, grain densities were measured by pycnometry. Average densities of the host rocks, of material from the high damaged zone and from the main slip zone are listed in Table 2.1.

For the ZJG exposure, carbon and oxygen isotope analyses on fault-related calcite

(breccia fragments, matrix and vein material) were performed. Powdered samples were obtained by microdrilling the hand specimens. Breccia fragments refer to fragments with diameter bigger than 1.5 mm so that drilling can be performed on individual particles. Matrix represents portion of the specimen in which the fragments is smaller than 0.5 mm. After dissolving in 100% H_3PO_4, the CO_2 gas released was collected for mass spectrograph analysis, employing the MAT 253 isotope-ratio mass spectrograph machine at the Institute of Geology, Chinese Academy of Geological Sciences. The isotopic compositions measured are reported in the δ-notation permil (‰) with a precision of ±0.2 ‰, using the V-PDB standard for $\delta^{13}C$ and the V-SMOW standard for $\delta^{18}O$, respectively.

Table 2.1. Average bulk and trace element composition along with grain densities of the host rocks (HR), rocks from the highly damaged zone (HDZ) and the main slip zone (MSZ) of the ZJG and PX exposures

Exposur	ZJG						PX					
	HR(5	RS	HDZ(4	RS	MSZ(2	RS	HR(4	RS	HDZ(4	RS	MSZ(4	RS
Na_2O	0.03	0.28	0.14	0.34	0.14	0.01	0.06	0.23	0.04	0.26	0.05	0.17
MgO	0.56	0.16	5.18	0.82	3.65	0.29	17.58	0.09	4.20	0.31	3.16	0.18
Al_2O_3	0.78	0.17	7.25	0.22	16.24	0.09	0.80	0.29	6.02	0.16	11.03	0.23
SiO_2	1.90	0.23	24.36	0.20	53.80	0.08	11.83	0.31	44.92	0.07	62.01	0.02
P_2O_5	0.03	0.00	0.10	0.37	0.16	0.14	0.14	0.42	0.30	0.23	0.47	0.42
K_2O	0.21	0.24	1.86	0.25	3.37	0.05	0.18	1.13	1.64	0.18	2.96	0.37
CaO	53.44	0.01	28.73	0.25	5.56	0.44	27.47	0.16	18.55	0.21	2.98	0.45
TiO_2	0.04	0.32	0.32	0.22	0.62	0.05	0.05	0.21	0.30	0.14	0.54	0.20
MnO	0.01	0.00	0.05	0.29	0.04	0.00	0.20	0.37	0.87	0.23	1.64	1.05
Fe_2O_3	0.13	0.10	1.80	0.32	3.75	0.12	0.44	1.19	2.62	0.11	5.41	0.14
$Fe_2O_3^T$	0.24	0.24	2.72	0.24	6.03	0.08	0.52	1.00	2.64	0.11	5.46	0.15
H_2O	0.41	0.10	2.09	0.20	4.15	0.04	0.60	0.38	1.96	0.16	3.66	0.06
CO_2	42.15	0.00	26.94	0.14	6.12	0.46	40.08	0.12	17.61	0.12	2.88	0.51
LOI	42.63	0.01	29.25	0.11	10.27	0.29	40.97	0.11	20.34	0.09	7.78	0.16
$Trace^T$	0.07	0.10	0.16	0.26	0.26	0.07	0.19	0.37	0.87	0.24	2.27	0.51
Be	0.07	0.36	1.25	0.27	2.61	0.10	0.30	0.46	1.69	0.08	3.16	0.20
Sc	1.10	0.62	7.07	0.23	13.65	0.01	2.95	0.48	5.72	0.10	10.82	0.10
Cr	0.74	0.36	31.69	0.27	72.37	0.08	88.58	0.48	45.78	0.37	120.1	0.37
Co	1.42	0.06	7.85	0.25	14.58	0.03	3.22	0.43	16.20	0.43	47.38	0.56
Ni	16.13	0.07	22.68	0.14	39.99	0.10	46.34	0.52	198.2	0.54	261.7	0.88
Cu	2.51	0.14	20.62	0.68	26.71	0.08	23.20	0.23	44.10	0.31	93.50	0.53
Zn	4.82	0.40	32.99	0.21	81.35	0.09	8.51	0.25	268.9	0.21	351.2	0.67
Rb	13.87	0.36	108.58	0.30	204.5	0.13	8.40	0.35	71.02	0.08	131.2	0.36

Pb	2.19	0.39	10.97	0.39	14.74	0.06	13.45	0.30	26.57	0.24	40.00	0.12
Th	1.23	0.42	8.68	0.24	16.04	0.02	2.11	0.32	7.99	0.09	13.72	0.25
U	0.45	0.18	1.94	0.33	3.19	0.05	12.78	0.29	26.92	0.27	16.66	0.24
Sr	256.7	0.26	148.45	0.42	61.61	0.18	258.7	0.09	225.0	0.24	129.6	0.60
V	6.03	0.13	44.82	0.24	103.0	0.09	315.9	0.33	271.2	0.26	543.2	0.67
Zr	15.55	0.31	75.92	0.17	138.9	0.10	31.79	0.35	65.55	0.17	117.80	0.03
Nb	1.42	0.12	6.73	0.35	12.87	0.05	1.56	0.26	6.16	0.10	11.41	0.13
Ba	188.1	0.10	334.7	0.25	836.7	0.18	699.5	1.12	6160	0.29	1.87E4	0.57
Hf	0.55	0.18	2.39	0.16	4.33	0.13	0.80	0.32	1.85	0.11	3.57	0.07
F	156.4	0.10	661.6	0.39	852.2	0.03	465.6	0.45	1172	0.02	1849	0.11
B	4.73	0.29	56.61	0.50	127.1	0.01	12.27	0.54	54.38	0.05	132.9	0.40
Sn	0.43	0.49	1.39	0.27	3.36	0.06	0.31	0.15	1.34	0.05	3.30	0.64
Density	2.73		2.67		2.60		2.72		2.67		2.62	

Major element data is in wt. %, trace element data is in ppm and density is in g/cm^3.

The figures in brackets are the number of samples for averaging. RSD is relative % of standard deviation (normalized by average value).

2.3 Characterization of the Longmenshan fault rocks: results of the ZJG transect

2.3.1 Character of the exposure

The ZJG exposure is located 3 km southwest of Beichuan city (Figure 2.1). The fault zone exposure at this site was ~ 8 m wide and the coseismic slip offset was ~ 6.5 m thrust motion (*Xu et al.*, 2009). The fault here strikes at an azimuth of 45° and dips 64 - 78° to the NW (Figure 2.2). The hanging wall protoliths consist of fine sandstones and carbonates, while the foot wall is sandstone. The principal slip surface cuts through the carbonate layers. Different types of fault rocks occur across fault zone. From West to East, they are (1) fractured limestone, (2) weakly-cemented coarse breccias, (3) coarse breccias, (4) weakly-foliated fine breccias, (5) gray and dark black gouge, (6) weakly-foliated fine breccias, (7) coarse breccias, and (8) fractured sandstone.

The internal structure of the fault zone is relatively simple. Only one principal slip zone can be found and no branches exist. The width of the fault core is extremely narrow (~ 20 cm), consisting of ~ 2cm-thick gray gouge in the center and weakly foliated yellowish crushed breccias besides (Figure 2.2b and 2.2c). An even thinner black gouge layer (~ 3 mm) is developed adjacent to the gray gouge. The black gouge was harder and less tacky than the gray one. The non-clay fault rocks were progressively cemented towards the fault center. As shown in Figure 2.2b, 2-5 cm-thick vein material occurred at the margins of the gouge zone. Occasionally the gouges were partially cemented to form ultracataclasite.

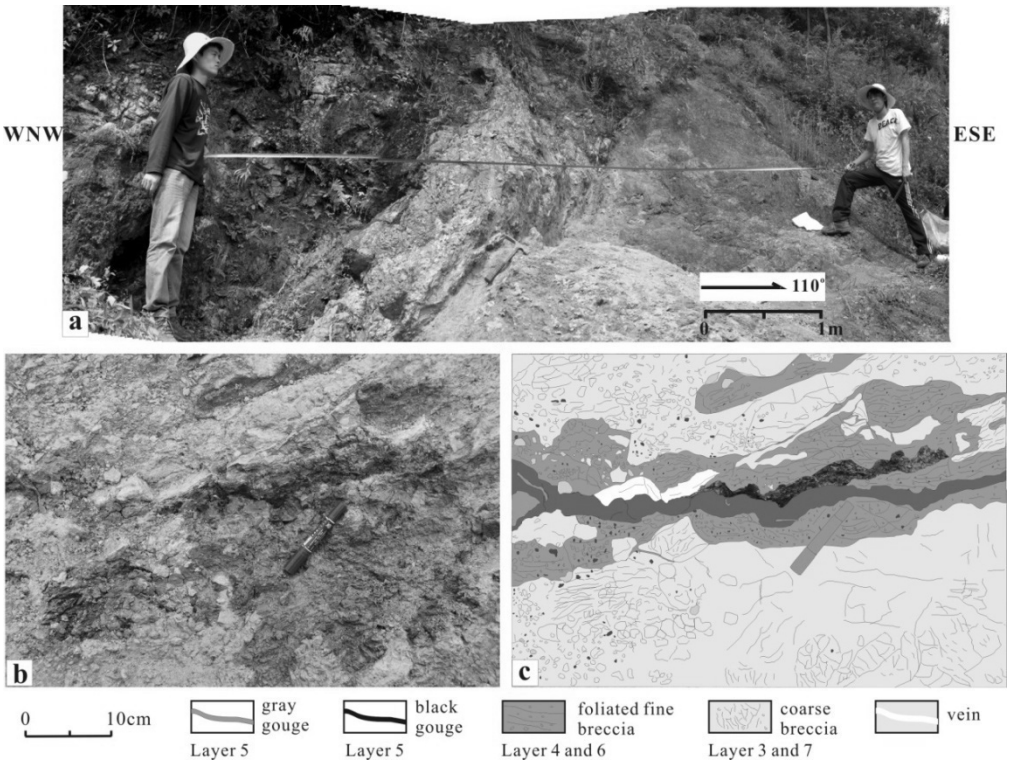

Figure 2.2. (a) Outcrop, (b) fault core structure and (c) the interpretive sketch of the ZJG exposure on the LFZ (GPS location is 31°48'22.44"N, 104°25'57.61"E).

2.3.2 Mineralogical results

Mineralogical analyses were performed on 29 samples across the ZJG exposure. Data on major and trace mineral composition are presented versus logarithmic distance from the principal slip surface in Figure 2.3. The black gouge is defined as the zero position. XRD analysis identified quartz, dolomite, calcite and feldspar as major minerals. The content of quartz was found to increase and that of carbonates and feldspar to decrease towards the principal slip surface, and feldspar fell below detection in the MSZ. Approaching the principal slip surface, the clay content of bulk samples also increases remarkably, with a peak value of 34% for the gray gouge.

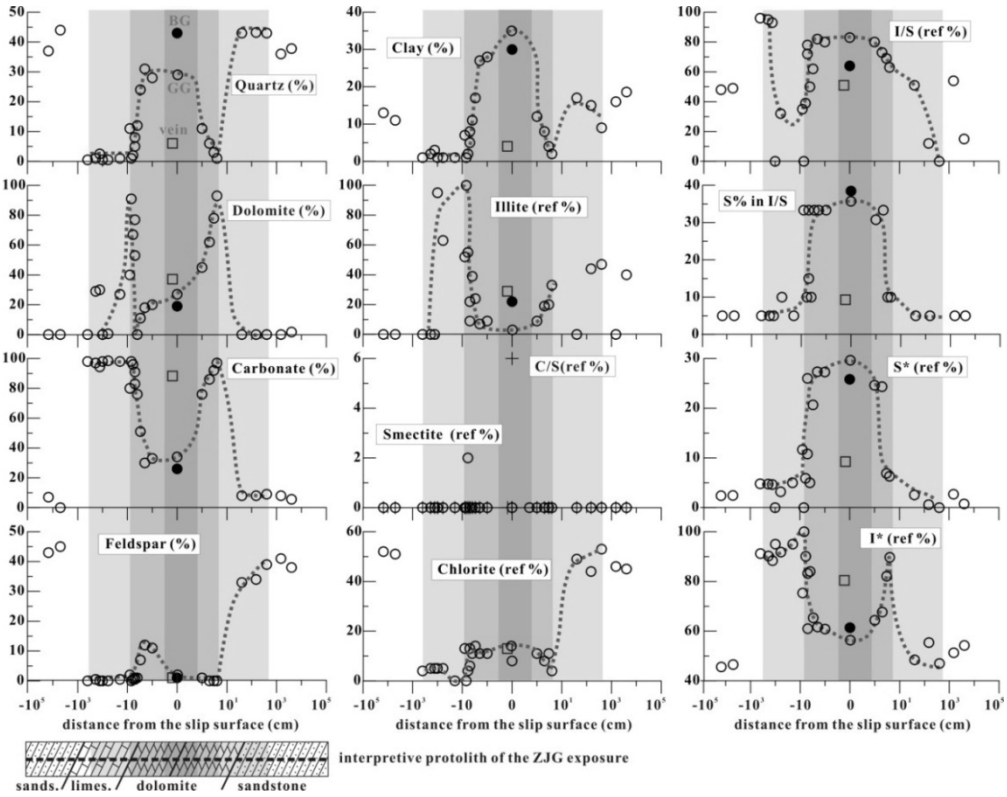

Figure 2.3. Variation in bulk and clay mineral (<2 μm) composition across the ZJG exposure of the LFZ. Different shaded domains, from light to dark, indicate the weakly damaged zone, the highly damaged zone and the main slip zone, respectively. The dashed lines are the interpretive varying trends. Two data points are exhibited at x = 0, representing the gray gouge (GG) and black gouge (BG). The latter is denoted by solid circles. The squared-symbols represent the veins besides the gouge samples. The content of an individual clay mineral is presented in reference content (ref %) accounting for the total clay. S is total content of smectite (S*=smectite + smectite contained in I/S), while I* is total content of illite (I*= illite + illite contained in I/S).*

Clay minerals in the < 2 μm fraction of samples from the ZJG exposure were identified as mainly illite, mixed layers of illite-smectite (I/S) and chlorite, with no detectable smectite (one exception with 2%). As shown in Figure 2.3, the reference abundance of illite decreased gradually towards the principal slip surface (from 100 % to 3 %) while that of I/S showed the opposite trend (from 33 % to 83 %). Chlorite content in the fault core was less than 10 %, while the foot wall was characterized by much higher chlorite content (~ 50 %). The mixlayer ratio (S%, the percentage of smectite in I/S) also increased notably toward the principal slip surface (from the 5% to 38%). Data on the total content of smectite (denoted by

S* = smectite + smectite contained in I/S) and illite (denoted by I* = illite + illite contained in I/S) are also presented in Figure 2.3, indicating increasing enrichment of total smectite and depletion of illite within the fault core. It is worth noting that the gray and black gouges showed similar mineralogical compositions, except for their clay mineral content. The gray gouge contained slightly less quartz and more clay (Figure 2.3). The black gouge was characterized by higher illite content and less I/S with respect to the gray gouge.

2.3.3 Geochemical results

Bulk sample chemical compositions exhibited continuous variation across the exposure, especially in the fault core (Figure 2.4). The content of SiO_2, Al_2O_3, K_2O, TiO_2, $Fe_2O_3^T$, H_2O and $Trace^T$ (weight percentage of all trace elements) were found to be increasingly enriched towards the principal slip surface, with the highest values for the gray gouge, while CaO, MgO, CO_2 and LOI behaved opposite. Nearly all trace elements showed enrichment in the fault core compared with the surrounding host rocks (Figure 2.5). Within the fault core, all trace elements exhibited progressive enrichment towards the principal slip surface, with Sr as the only exception. This trend was consistent with that displayed by major elements such as Al_2O_3, TiO_2 (Figure 2.4), and also by the bulk clay content (Figure 2.3). Among the trace elements, Ba and F showed relatively high abundance, with maximum values of 920 and 1050 ppm, respectively. The gray gouge and black gouge had almost the same trace element compositions. However, for major elements, the black gouge showed slightly lower content of Al_2O_3, K_2O, TiO_2, and higher content of MgO.

At the ZJG exposure, nearly all elements showed positive correlation coefficients with the content of TiO_2, except for CaO (r = -0.94), MgO (r = -0.36), CO_2 (r = -0.97) amongst the major elements, and Sr (r = -0.66) amongst the trace elements. The samples selected for isocon analysis are denoted in the subplot of TiO_2 of Figure 2.4 and the average elemental abundances of the host rock (HR), the highly damaged zone (HDZ) and the main slip zone (MSZ) are listed in Table 2.1. Grant-type plots (Figure 2.6) showed the following results:

(1) The fault rocks within the HDZ (Figure 2.6a) and MSZ (Figure 2.6b) showed obvious enrichment in nearly all elements analyzed compared to the HR, except for CaO, CO_2 and Sr. Data points for SiO_2, MgO, Al_2O_3, K_2O, $Fe_2O_3^T$, and even H_2O for major elements, and Co, Th, Be, Zr, Zn, V, Nb, Pb, Se, Cu, K, Rb and U for trace elements, as covered by the shading in Figures 2.6a and 2.6b, fall fairly close to the isocon line of TiO_2, exhibiting a consistent enrichment signature and also suggesting a high confidence level of our analysis.

(2) A few elements (i.e. Ba, Ni, Na_2O, P_2O_5, F and Cr) deviate from the isocon line.

(3) As shown in Figures 2.6a and 2.6b, the HDZ is 8.3 times enriched in content of TiO_2 and

the estimated volume loss was 87 % relative to the HR. The MSZ is 15.8 times enriched and the volume loss was 93 %.

(4) The inclination of the isocon line for the MSZ was 1.9 times greater than that for the HDZ (Figure 2.6c), indicating increasing volume loss towards the principal slip center.

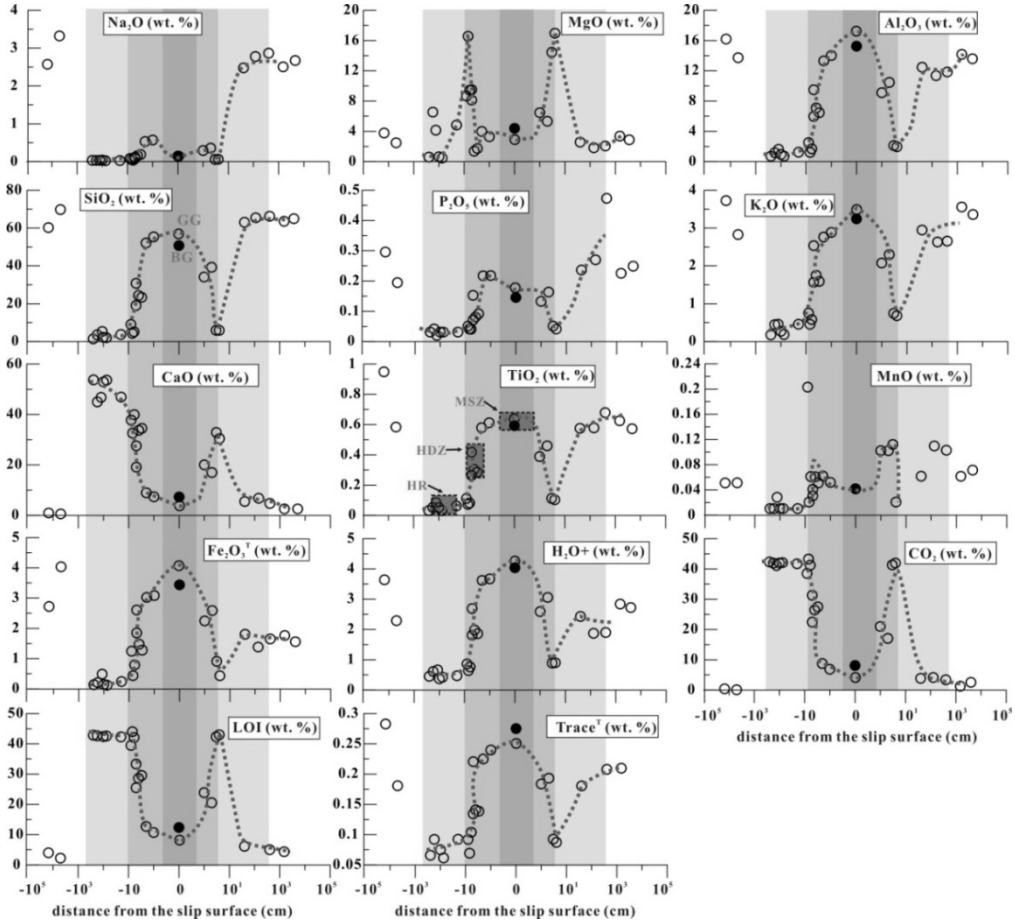

Figure 2.4. Concentration profiles of the bulk elements across the ZJG exposure. The blue dashed squares in the subplot of TiO_2 denote the selected samples for isocon analysis (in Figure 2.6), representing the host rock (HR), the highly damaged zone (HDZ) and the main slip zone (MSZ), respectively. $Trace^T$ = total concentration of trace elements. Other detailed content as in Figure 2.3.

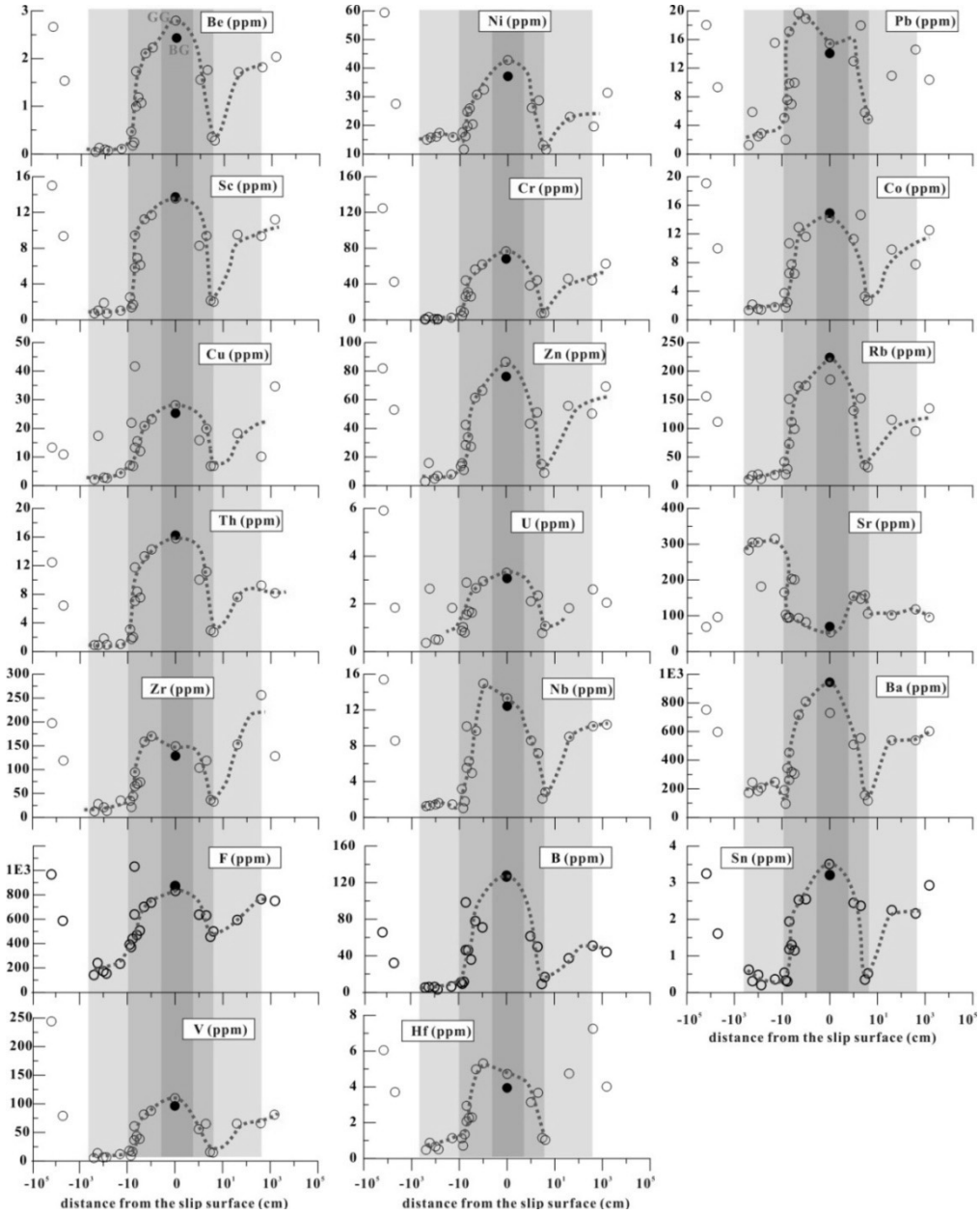

Figure 2.5. Concentration profiles of the trace elements across the ZJG exposure. Other detailed content as in Figure 2.3.

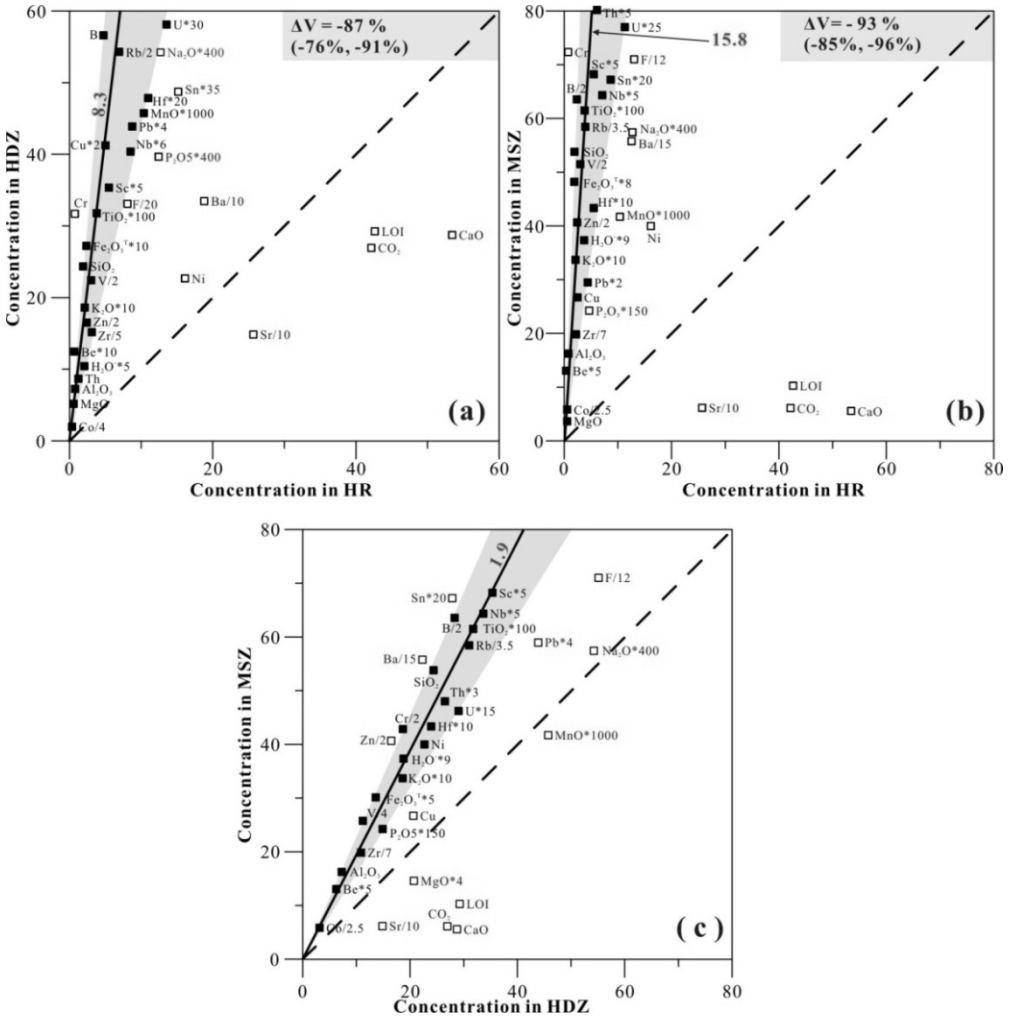

Figure 2.6. Grant-type plots for the host rock (HR) against the highly damaged zone (HDZ) and the main slip zone (MSZ), as well as HDZ against MSZ at the ZJG exposure. Concentrations are noted for major elements in wt. % and for trace elements in ppm, and scaled to the plot. The solid lines are the isocon lines for TiO_2, and the solid symbols (within the shaded area) represent the elements whose compositions are close to the isocon line. The dashed lines are the equilibrium lines, indicating neither enrichment nor depletion. See Table 2.1 for more details of the chemical composition. ΔV (%) indicates the percentage volume loss relative to the HR. The two values in bracket are the volume loss corresponding to the lower and upper bounds of the shaded area.

2.3.4 Isotopic characteristics

Stable isotopic compositions ($\delta^{13}C$ and $\delta^{18}O$) of breccia fragments, matrix and vein

material from the fault core, as well as the country rocks (protoliths) were investigated. As shown in Figure 2.7, the isotopic compositions of the breccia fragments are distinct from that of the matrix and vein material, by a $\delta^{13}C$ value of -4 ‰. Overall, the $\delta^{13}C$ values decreased progressively for breccia fragments, matrix and vein material collected from the same specimen (an example of this trend is denoted by the solid line in Figure 2.7). The lowest $\delta^{13}C$ and $\delta^{18}O$ signature of the fault rocks was shown by vein material ($\delta^{13}C$ = -8.0 ‰ and $\delta^{18}O$ = 19 ‰) located directly adjacent to the fault gouge (Figure 2.2). The values of $\delta^{18}O$ of the breccia fragments (19.7 to 27.8 ‰) are generally greater than that of the matrix and vein material (19 to 21 ‰). The $\delta^{13}C$ and $\delta^{18}O$ values for the breccia fragments displayed a range that is consistent with those plotted in the Figure 2.7 for the protolith in the hanging wall (limestone). The sandstone data (protolith of the footwall) plot far away from both the limestone and fault rock data.

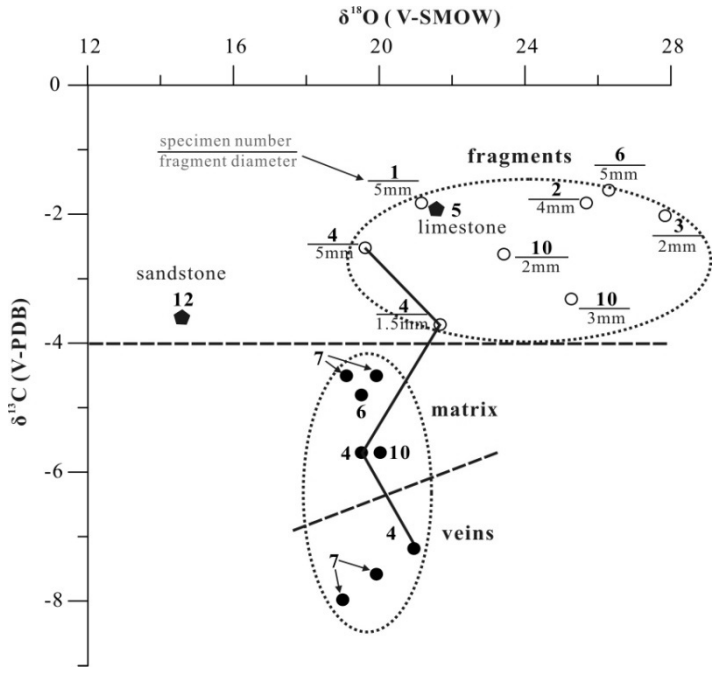

Figure 2.7. Stable isotope compositions ($\delta^{13}C$ and $\delta^{18}O$) of host rocks, breccia fragments, matrix and vein material at the ZJG exposure. The five-cornered stars represent different types of host rocks. The open circles stand for breccia fragments, while solid circles stand for matrix and vein material. Overall, the $\delta^{13}C$ values decreased progressively for breccia fragments, matrix and vein material collected from the same specimen, as denoted by an example in solid line.

2.4 Characterization of the Longmenshan fault rocks: results of the PX transect

2.4.1 Character of the exposure

The PX exposure is located near the northeast terminus of the surface rupture trace (Figure 2.1). The exposure at this site was ~ 9 m wide (Figure 2.8a). The fault plane exhibited slightly reversed inclination, dipping ~ 71^{o} towards the footwall instead of towards the hanging wall. The coseismic thrust and right-lateral shear displacements were ~ 2.0 and 3.0 m, respectively (*Li et al.*, 2010). The rocks surrounding the fault core are fine sandstone. However, field and hand specimen analysis, coupled with petrography indicated that the principal slip of the Wenchuan earthquake must have cut though the carbonate-rich layers. This was further confirmed by the finding that the fault core is enriched in carbonate minerals. Recognizable fragments of limestone are present in the fault breccias in the damaged zone, mixed with sandstone fragments. Tracking along-strike indicated spatial continuity of the internal structure and lithology of the fault zone. From West to East, different types of fault rocks occurred within the fault zone, (1) coarse breccias (> 2.5 m), (2) brownish gouge (15 - 25 cm), (3) gray or dark black gouge (0.5 - 3.5 cm), (4) yellowish gouge (~ 15 cm), (5) black breccias (~ 30 cm) , (6) coarse breccias (1.5 - 2.5 m) and (7) fractured sandstone (> 4.0 m).

The width of the fault core (Layer 2 to 4) is about 40 cm. As shown in Figure 2.8b and 2.8c, the principal slip of the Wenchuan earthquake occurred in Layer 3, which contrasted highly with the surrounding rocks. This was confirmed by continuous slicing analysis. Layer 3 occasionally cut though the brownish gouge (Layer 2) and yellowish gouge (Layer 4), which may record deformation inherited from past fault motion, presumably reflecting repeated earthquakes (*Caine et al.*, 1996). It is interesting that the color of the principal slip gouge varied with thickness. It exhibited a gray color when thick (~ 2.5 cm) and turned black when thinner than 7 mm. As at the ZJG exposure, the gray gouge was wetter, softer and much tackier than the black gouge.

Fragments of vein material were found widespread along the fault core boundaries (Figure 2.8c). On the hanging wall, a manganese-rich layer occurs ~ 3 m away from the slip surface (local people have exploited this as manganese-ore for many years). This was totally black and 15 - 20 cm wide in this exposure. However, its width varies laterally. Its occurrence follows the fault rupture trace for at least ~ 3 km. Mineralogical and geochemical data showed that it is composed of kutnohorite, fluorapatite and quartz, and that the average content of MnO is ~ 21 wt. %.

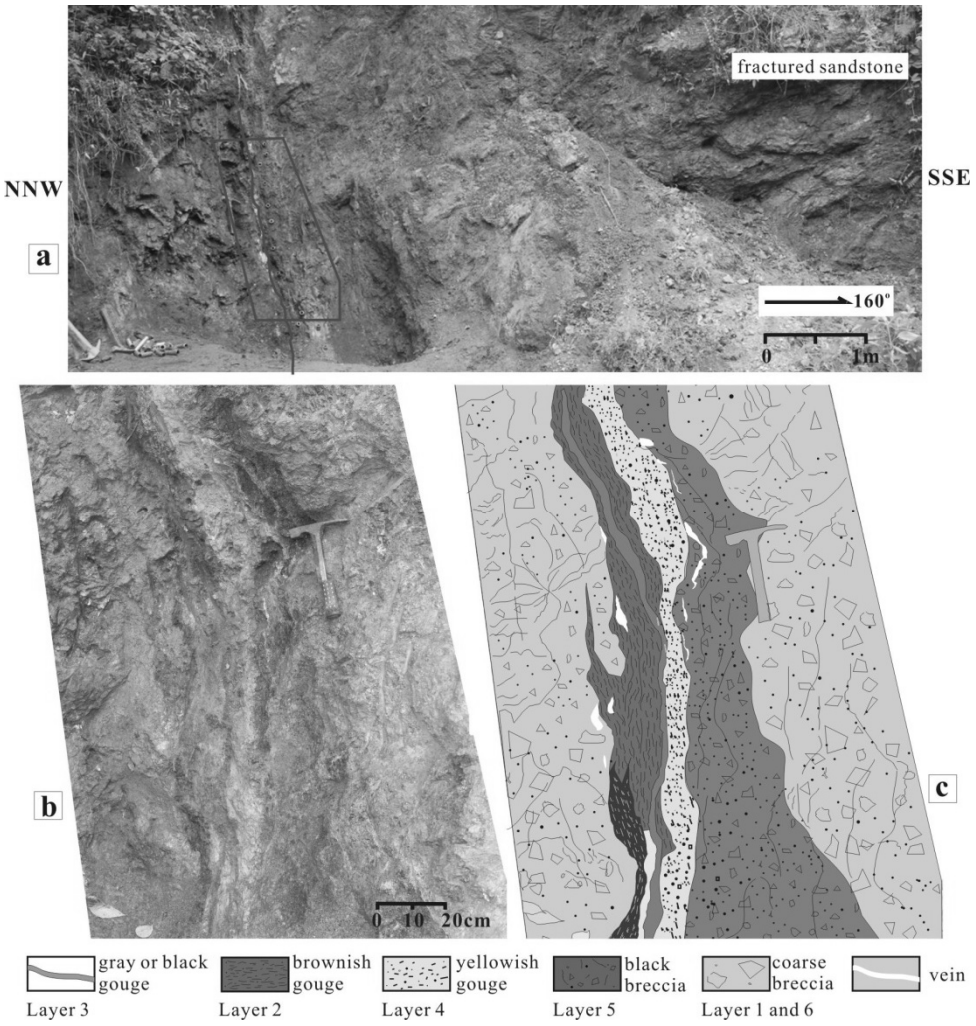

Figure 2.8. (a) Outcrop, (b) fault core structure and (c) corresponding interpretive sketch of the PX exposure on the LFZ (GPS location is 32°17'14.63"N, 104°56'48.54"E).

2.4.2 Mineralogical results

At the PX exposure, 40 samples were collected for mineralogical analysis. XRD analysis identified quartz, dolomite and calcite as major minerals, and K-feldspar, fluorapatite, goethite and gypsum as trace minerals (Figure 2.9). Samples from the fault core contain more carbonate minerals than other portion of the fault zone, demonstrating a carbonate protolith for the fault core. Within the fault core, the content of carbonates decreases while quartz content increases approaching the principal slip surface. Barite was

abnormally concentrated in the fault zone with a maximum value of 6.0 %. The profile showed one barite peak at the fault core boundary and another in the MSZ. Other trace minerals like gypsum and fluorapatite were also enriched at the fault core boundary.

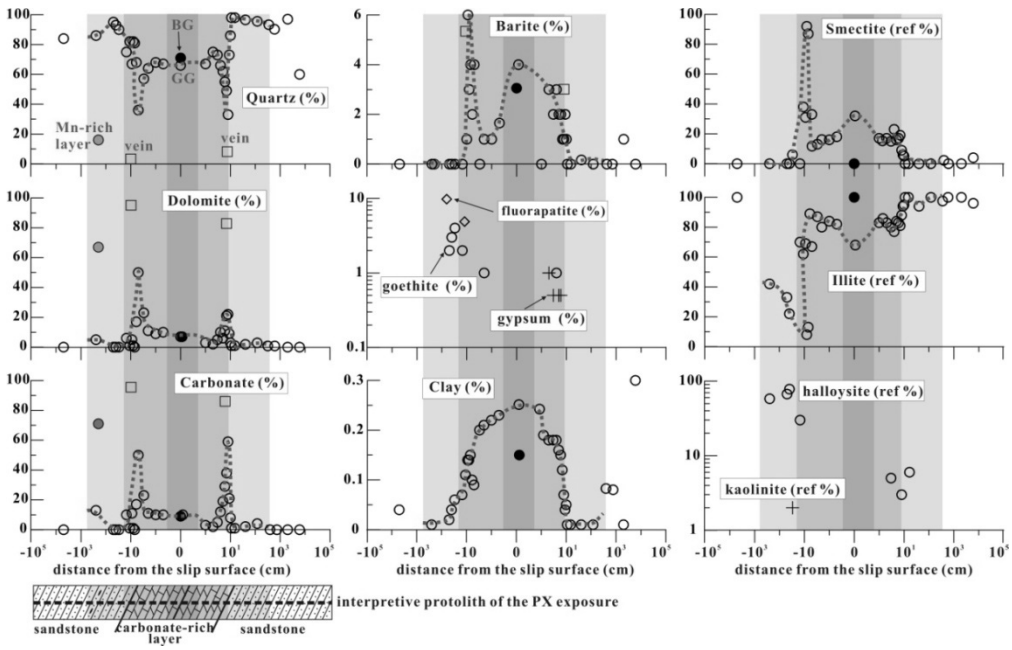

Figure 2.9. Variation in bulk and clay minerals (< 2 μm) composition across the PX exposure. The squared-symbols at the margins of the fault core represent the vein material. Solid circles stand for the Mn-ore layer on the hanging wall. Other detailed content as in Figure 2.3.

The clay content of bulk samples increased notably towards the principal slip surface (Figure 2.9), with a peak value of 25% for the gray gouge. Detailed semi-quantitative analysis showed that the clay minerals at the PX exposure were mainly smectite and illite with minor halloysite (Halloysite is often found near carbonate rocks and it is usually taken as a typical product of hydrothermal alteration (*Kerr*, 1952)). As shown in Figure 2.9, the profile for smectite resembled that of barite. Despite a sharp peak at the hanging wall, smectite showed clear enrichment towards the principal slip surface, while illite exhibited the opposite trend. Halloysite occurred near the margins of the fault core and disappeared below detection in the MSZ. As at the ZJG exposure, the gray gouge and black gouge showed rather different clay composition, even though their bulk mineral compositions were similar to each other. The gray gouge contained slightly less quartz and more clay with respect to the

black gouge. The reference abundances of smectite were 32.0 % for the gray gouge, whereas the black gouge was characterized by the disappearance of smectite. The data of smectite content for the gray gouge seems to match well the trend seen across the entire PX exposure, while the black gouge was far away from that trend.

2.4.3 Geochemical results

Thirty eight samples from the PX exposure were selected for geochemical analysis. As shown in Figure 2.10, the variation profiles of SiO_2, CaO, MgO and CO_2 across the fault zone well match the interpreted carbonate protolith (Figure 2.9), with higher content of CaO, MgO and less SiO_2 in the fault core. This interpretation is consistent with hand-specimen study and petrography, as well as the mineralogical results. As for the variation profile obtained for barite content (Figure 2.9), those for MnO, $Fe_2O_3^T$ and P_2O_5 showed two peaks. With the exception of CaO, MgO, CO_2 and MnO, the profiles for Al_2O_3, K_2O, TiO_2, P_2O_5, $Fe_2O_3^T$, H_2O, and to a lesser extent Na_2O and SiO_2, showed gradual enrichment towards the principal slip surface. Moreover, within the fault core, trace elements like Be, Sc, Rb, Th, Zr, Nb, Hf, F and B exhibited increasing enrichment towards the principal slip surface. In contrast, some elements (Cr, V, U, Sn and Sr) showed gradual depletion towards the principal slip surface (Figure 2.11). The gouge samples displayed anomalous values deviating from the general trends of the fault core, being enriched in Cr, V, U and Sr while depleted in Be, B, Sc, Rb and Th (Figure 2.11). Amongst the trace elements, Ba and F showed anomalously high abundance (with maximum values of 5.4×10^4 ppm and 2.1×10^3 ppm), in accordance with the profiles obtained for barite and fluorapatite content.

At the PX exposure, the concentration of TiO_2 showed positive correlation coefficients with that for Al_2O_3 (r = 1.00), K_2O (r = 0.90) and P_2O_5 (r = 0.42) among the major elements, and for trace elements B (r = 0.86), Be (r = 0.89), F (r = 0.78), Sc (r = 0.97), Rb (r = 0.87), Th (r = 0.95), Zr (r = 0.85), Nb (r = 0.91) and Hf (r = 0.94). Negative correlations were obtained for MgO (r = -0.28), MnO (r = -0.14), CaO (r = -0.4), CO_2 (r = -4.3) and Sr (r = -0.02). The samples selected for isocon analysis are denoted in the subplot forTiO_2 in Figure 2.10. Grant-type plots (Figure 2.12) showed the following features:

(1) As for the ZJG exposure, most elements showed enrichment and the data points fall fairly close to the isocon line, except for major elements MgO, CaO, CO_2 and trace element Sr (Figure 2.12a and 2.12b).

(2) The data points for Zn and Ba fall well above the isocon line.

(3) The HDZ was 6.0 times enriched and the calculated corresponding volume loss was 83% with respect to the HR (shaded area in Figure 2.12a). The MSZ showed 5.1 - 10.7 times

enrichment and a corresponding volume loss of 90 % was obtained (Figure 2.12b).
(4) The inclination of the isocon line of the MSZ was 1.8 times greater than that of the HDZ, indicating a progressive enrichment towards the principal slip surface (Figure 2.12c).

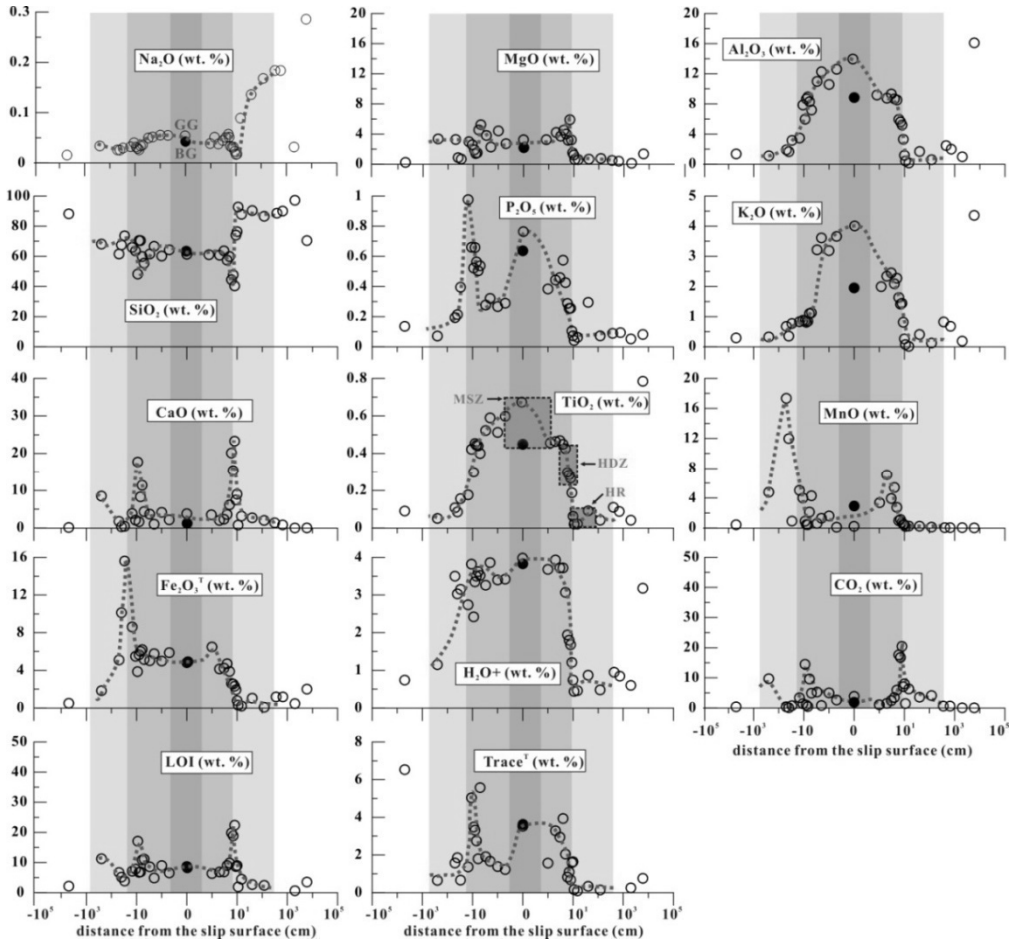

Figure 2.10. Concentration profiles of the bulk elements across the PX exposure. Detailed content as in Figure 2.4.

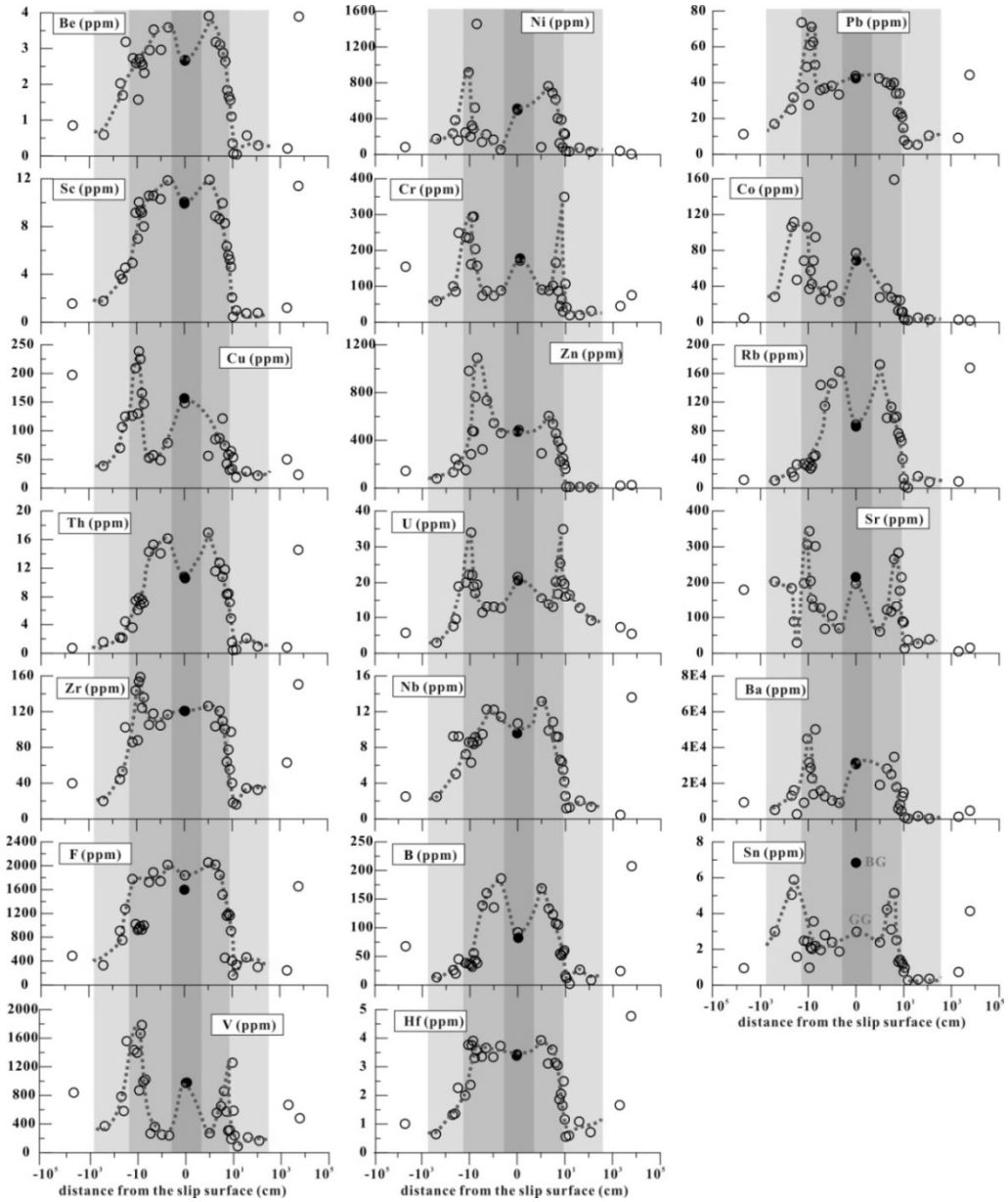

Figure 2.11. Concentration profiles of the trace elements across the PX exposure. Detailed content as in Figure 2.5.

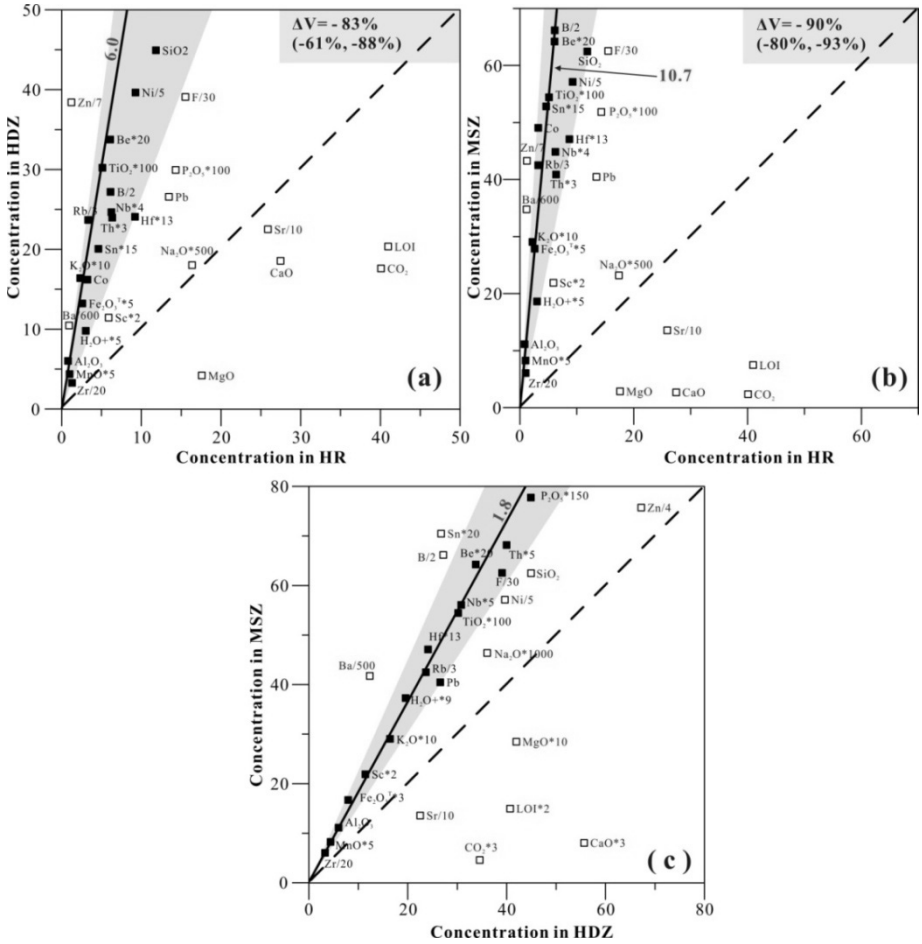

Figure 2.12. Grant-type plots for the host rock (HR) against the highly damaged zone (HDZ) and the main slip zone (MSZ), as well as HDZ against MSZ at the PX exposure. Detailed content as in Figure 2.6.

2.5. Discussion

2.5.1 Mineralogical trends within the LFZ

2.5.1.1 Bulk mineralogical composition

Combining the petrographic and mineralogical results (Figure 2.3 and Figure 2.9), carbonate-rich protoliths are inferred for both the ZJG and PX exposure, at least for the fault core portions. At both locations, the inferred coseismic slip surface has cut through carbonate-bearing layers. Within the fault core, the content of carbonate minerals decreased notably toward the MSZ, while the content of quartz and clay increased. The feldspar content was relatively low (< 3% for PX, < 12 % for ZJG exposure), showing a slight decrease

toward the principal slip surface. The systematic decrease of carbonate mineral content towards the principal slip surface was the most distinctive characteristic of the transects studied. The corresponding reduction in carbonate mineral content normalized to the content at the margin of the fault core, were ~76 % and ~ 75 % for the ZJG and PX exposures, respectively.

At the PX exposure, fluid-derived minerals like gypsum, fluorapatite and barite, were concentrated in the fault rock matrix at the fault core boundary (Figure 2.9), where white vein material also occurred, seemingly having been fractured after formation *in-situ* by precipitation from the fault zone fluid. If this was the case, the vein material (consisting of 94% of dolomite and 5.2% of barite, Figure 2.9) should record information about the fluid composition. The matrix mineral assemblages of gypsum, fluorapatite and barite suggest a typical low-temperature hydrothermal fluid (*Jacobsen et al.*, 1998). By contrast, the vein material at the ZJG exposure is composed of 38% dolomite, 50% calcite and 5% quartz (Figure 2.3), and is exceptionally rich in illite (ref. 30%) compared with nearby material (ref. ~ 9%). The widespread precipitation of dolomite suggests a fluid charged with high concentrations of Mg^{2+} at both exposures, while the enrichment in illite at ZJG can be interpreted as the product of hydrothermal alteration. This is also consistent with the observed enrichment in smectite content towards the slip surface in the fault core (Figure 2.3 and Figure 2.9).

2.5.1.2 The clay assemblage

As shown by the XRD data for the gray and black gouges at both locations (Figure 2.13), these had quite different clay composition, though their bulk compositions were similar. Distinct characteristics of transformation from smectite to illite (PX exposure) or from I/S to illite (ZJG exposure) have been presented. Coseismic frictional heating has been previously proposed as a mechanism capable of producing these mineralogical changes towards illite. The following arguments support this illitization hypothesis (here illitization is taken as a general concept involving reactions including dehydration, dehydroxylation of hydrated smectite and the smectite-illite transformation): (1) The black gouge was identified associated the localized slip zone by field and microscopic analysis (*Han et al.*, 2010). The color and very fine grain size suggested it accommodated large displacement during the earthquake, just like the black gouge observed in the drilling core of the Chelungpu fault (*Hirono et al.*, 2008). (2) The black gouge was always thin (< 7 mm in thickness). This implies high internal strain rate, favoring the frictional heating mechanism. (3) Except for slightly more quartz and less clay, the black gouge had similar mineralogical and chemical

compositions to the gray gouge. On basis of the reaction equation for illitization, smectite + (K^+, Al^{3+}) = illite + (Ca^{2+}, Mg^{2+}) + quartz + water (*Roland and Ola*, 1996), the products contain quartz. This reaction could therefore be responsible for the higher quartz content in the black gouge. (4) High-velocity frictional experiments on the PX fault gouge (*Yao et al.*, 2011) and on other smectite-rich gouge (*Ferri et al.*, 2010) have demonstrated that seismic slip can cause reduction in bulk clay content and in relative abundance of smectite. (5) Halloysite disappeared approaching the principal slip surface (Figure 2.9). Again, this is consistent with frictional heating, as discussed in Section 2.5.3. (6) A few additional measurements of magnetic susceptibility following *Yang et al.* (2012) showed that the magnetic susceptibility of the black gouge was 2.8 - 4 times higher than that of the gray gouge. The magnetic susceptibility values obtained are 13.13×10^{-8} m^3kg^{-1} (black gouge) versus 4.68×10^{-8} m^3kg^{-1} (gray gouge) for the ZJG exposure and 17.56×10^{-8} m^3kg^{-1} (black gouge) versus 4.42×10^{-8} m^3kg^{-1} (gray gouge) for the PX exposure, respectively. This may reflect the formation of ferrimagnetic minerals by thermal decomposition (*Tanikawa et al.*, 2007). (7) The clay content data for the black gouges depart consistently from the overall profiles for the two transects studied (Figure 2.14). This suggests formation by a highly localized mechanism.

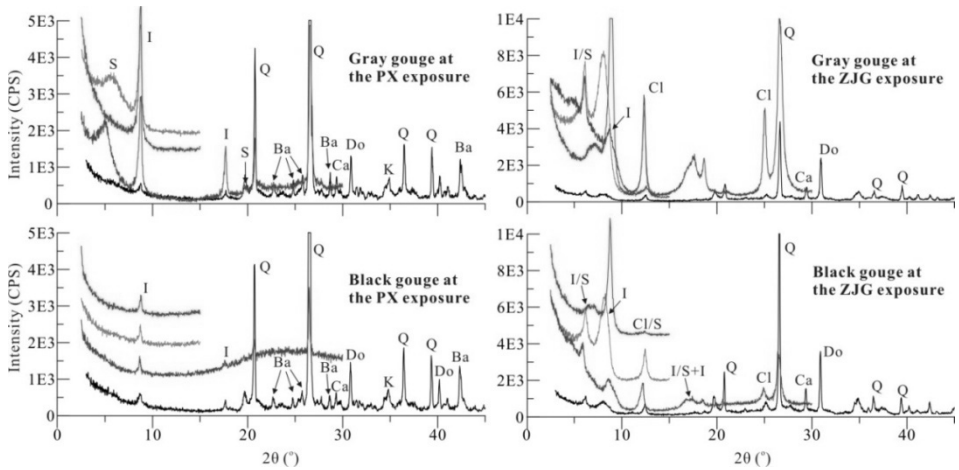

Figure 2.13. X-ray diffraction patterns of the gray and black gouges of the PX and ZJG exposures for identifying the smectite to illite transition. Black lines are the results from the bulk powder samples. Gray, blue and red lines are the results from air-dried, glycolated and heated clay samples (<2 μm), respectively. Q, quartz; Do, dolomite; Ca, calcite; Ba, barite; K, K-feldspar; S, smectite; I, illite; Cl, chlorite; I/S, mixed layers of illite-smectite; Cl/S, mixed layers of chlorite-smectite.

Taken together, all seven arguments point to the black gouge's forming by illitization of the gray gouge. Despite this evidence, we cannot be certain that a coseismic smectite-illite transformation is the cause of the higher abundance of illite observed in the black gouge relative to the gray gouge. This is not only because the transformation involves chemical changes and is expected to be slow (*Huang et al.*, 1993), but also because dehydration or dehydroxylation can cause an apparent rise of illite content. In the coseismic decomposition model, the extent of reaction would be determined by the temperature rise during faulting and by the reaction kinetics. This information can be used to further test the model, as discussed in Section 2.5.3.

Some further, general trends can also be inferred from the clay mineralogy of the transect samples. The results for both the PX and ZJG exposures showed that the smectite and smectite-rich I/S contents gradually increase towards the principal slip surface. Illite behaved the opposite way, increasing in concentration away from the principal slip surface. The gray gouges showed the largest smectite or I/S content relative to the nearby samples (Figure 2.14), and at the ZJG exposure the gray gouge showed the maximum value of S% (Figure 2.3). This smectite enrichment is consistent with that seen in gouge samples (*Xu and Li*, 2010) collected from around 600 m depth in the Wenchuan Fault Scientific Drilling project (WFSD, Borehole-1, located at the southern segment of the Yinxiu-Beichuan fault, as shown in Figure 2.1). Therefore, while illitization occurred in the black gouge, the remainder of the fault core showed smectite enrichment. This observation indicates that the entire fault core underwent a retrograde reaction to form smectite.

One explanation for this smectite enrichment is weathering (*Solum et al.*, 2003). However, if weathering was responsible, the damage zone should be significantly affected too (*Isaacs et al.*, 2007). The damage zone was heavily fractured and showed higher permeability (*Chen et al.*, 2011), hence likely provided a conduit for fluid flow. The brown color (Figure 2.8) and extensive deposition of supergenic minerals (Figure 2.9) consistently indicates surface leaching within the damage zone. The minerals formed include kaolinite and goethite, which are typical weathering products. However, though concentrated in the fine grained fault center, little smectite formed in the damage zone. Moreover, smectite formation requires an interstitial fluid environment rich in Mg^{2+} (*Huang et al.*, 1993). This cannot be supplied by the surface water. Finally, in preparing the exposures for sampling, more than enough surface material was removed to eliminate weathered rocks. Therefore, surface weathering alone does not seem to account for the distribution of smectite observed in the fault rocks. Alteration of pseudotachylite has also been proposed as mechanism of

forming smectite in an active fault zone (*Kuo et al.*, 2009). This is opposed by two arguments. One is that the enrichment of smectite affects the entire fault zone, and that frictional heating could not produce such extensive melting. The other is that the fault core is rich in carbonate minerals (Figure 2.3 and Figure 2.9), so that frictional heating would produce decomposition rather than melting.

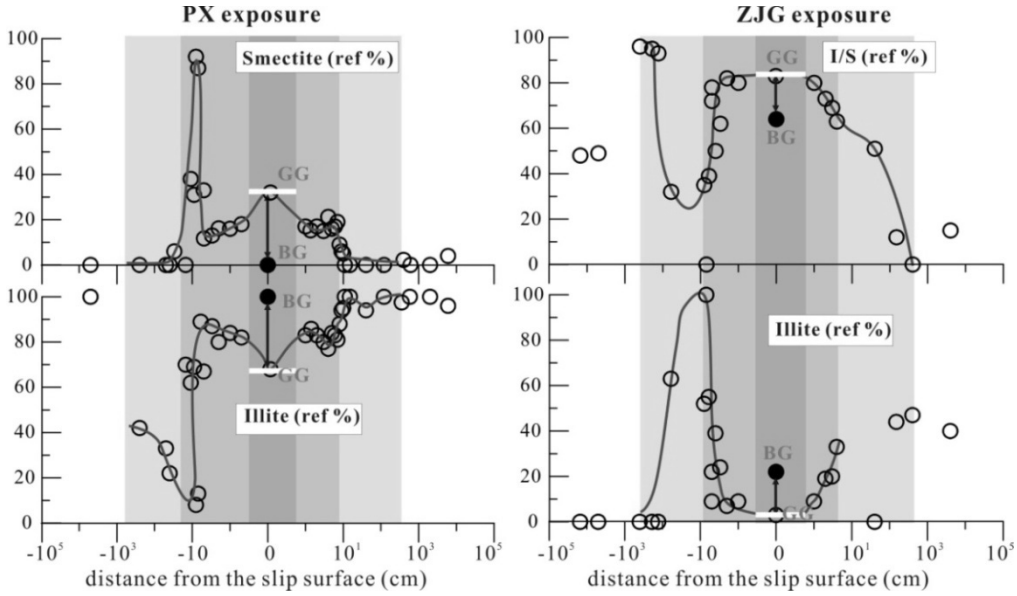

Figure 2.14. Concentration variations of smectite, illite and I/S across the PX and ZJG exposure, showing the enrichment of smectite along the entire transect and the illitization in black gouge.

We propose that in addition to limited weathering, fluid infiltration has played an active role in the transformation of the clay minerals present in the fault rocks in the shallow subsurface, especially in the post-seismic stage. Smectite is a Mg-rich mineral which usually forms following the equation (*Roland and Ola*, 1996), Mg-rich fluid + silicates → Mg-rich phyllosilicate assemblage. In our interpretation, the LFZ fluid was probably rich in Mg^{2+} as discussed in Section 2.5.1.1. Correlation analysis showed that the smectite content is correlated with an abundance of Ba. The profiles obtained for smectite and Ba are also similar, indicating that the formation of smectite may be related to the infiltration of hydrothermal fluid. Retrograde diagenesis of illite to smectite in sedimentary rocks induced by hydrothermal fluids has been well documented (*Zhao et al.*, 1999). Similar observations and interpretations have also been reported for the Chelungpu thrust fault (*Isaacs et al.*,

2007). Moreover, detailed geochemical evidence presented below indicates that the LFZ has experienced extensive hydrothermal fluid infiltration. We infer that frictional heating forming illite followed by the action of post-seismic hydrothermal fluids controlled the mutual transformation between smectite and illite within the LFZ and the final abundances of these minerals.

2.5.2 Fluid infiltration and geochemical trends within the LFZ

2.5.2.1 General geochemical pattern and volume loss

According to the transect variation profiles (Figure 2.4, Figure 2.5, Figure 2.10 and Figure 2.11), the bulk and trace elements investigated can be classified into two broad types characterized by specific trends. The first is one of increasing depletion towards the principal slip surface compared with the host rock (hereafter referred to as D-type). The second is one of systematic enrichment towards the principal slip surface (hereafter referred to as R-type). The relatively immobile, R-type major elements include Al_2O_3, K_2O, TiO_2, P_2O_5, $Fe_2O_3^T$, SiO_2, H_2O and to a lesser extent, Na_2O. Relatively mobile or D-type major elements include CaO, MgO and CO_2, which are all carbonate-related oxides. MnO is not well categorized, but more or less falls in the D-type category. Most trace elements showed immobile R-type behavior, except for Sr. Similar element classifications have been proposed previously (e.g., *Tanaka et al.,* 2001), but the R- and D-type elements in our study are quite different from the classification employed for the granitic (*Goddard and Evans*, 1995) or clastic sedimentary fault zones (*Tanaka et al.*, 2001; *Chen et al.*, 2007), where depletion or enrichment corresponded the overall mobility of elements. It is well documented in these previous studies (*O'Hara*, 1988; *Goddard and Evans*, 1995; *Tanaka et al.*, 2001) that TiO_2, P_2O_5, MnO and Zr are the most immobile oxides, followed by MgO, Al_2O_3 and V, and might therefore be expected to become enriched during geochemical alteration. By contrast, in the carbonate-rich fault zone investigated here, MgO and MnO fall into the mobile D-type category. Sr belongs to the D-type elements, since Sr^{2+} has an ionic radius of 112 pm close to that of Ca^{2+} (99 pm), and can easily replace Ca^{2+} in carbonate minerals.

Summarizing, except for the carbonate-related outliers, the other elemental trends seen along the present transects exhibit increasing concentration towards the principal slip surface. This systematic variation suggests that a single process systematically controlled geochemical evolution. Combined with the petrographic and mineralogical trends (Figure 2.3 and Figure 2.9), we propose that the geochemical trends seen in the LFZ (Figure 2.4, Figure 2.5, Figure 2.10 and Figure 2.11) reflect the loss of carbonates and that the "mass removal" model may account for the observed enrichment signature. This idea is supported by both the

correlation analysis and isocon diagrams of Figure 2.6 and Figure 2.12. The concentration of TiO_2 showed high correlation coefficients (typically greater than 0.85) with R-type elements, but negative correlation coefficients with D-type elements. The R-type elements, such as Al_2O_3, K_2O, SiO_2 and Fe_2O_3 for bulk elements and Be, Sc, K, Rb, Zr, U, Nb, Th and Hf for trace elements, fall fairly close to the isocon line of TiO_2 at both the PX and ZJG exposures (Figure 2.6 and Figure 2.12). Conversely, the D-type elements were well below the isocon line. Some elements exhibited an intermediate state, either reflecting their relatively high mobility (i.e. Na_2O) or perhaps an external contribution via deep fluid activity (i.e. P_2O_5, Ba and F) or effects of adsorption by clay minerals (i.e. Cr and V).

The isocon analysis further revealed that the volume loss at the ZJG and PX exposures was considerable (Figure 2.6 and Figure 2.12). The values at the ZJG exposure were 87 % for the HDZ and 93 % for the MSZ. At the PX exposure, they were 83 % for the HDZ and 90 % for the MSZ. Assuming the unaltered fault core to have a homogenous geochemical composition, the carbonated-related elements (using CO_2 as the proxy and ignoring organic carbon) exhibited an extreme depletion of ~ 80 % for the ZJG exposure (Figure 2.4) and ~ 75 % for the PX exposure (Figure 2.10), in agreement with the depletion degree in carbonate minerals of ~ 76 % for the ZJG exposure (Figure 2.3) and ~ 75 % for the PX exposure (Figure 2.9) as obtained in Section 2.5.1.1. On this basis, the overall volume loss from the LFZ portions studied, at least for the carbonate-rich segment, can be explained by the disappearance of carbonate minerals. The small discrepancy between the volume loss obtained by isocon analysis (Figure 2.6 and Figure 2.12) and the depletion degree in carbonate-related elements (or minerals) may result either from introduction of mass through precipitation to form veins and cements, or from decomposition of other minerals like feldspar (Figure 2.3). The volume loss inferred in our study is much larger than that seen in previous studies of clastic-sedimentary (*Chen et al.*, 2007) or crystalline fault zone (*Tanaka et al.*, 2001). In our study, especially for the fault core portion, the protoliths were carbonate-rich. Carbonate minerals are less resistant to mechanical damage, and more susceptible to dissolution and thermal decomposition, so that they can be easily disaggregated, dissolved and transported away during long-term inter-seismic periods.

Volume gain versus loss implies dilatational or compactional deformation of the zone affected. Based on the geochemically-inferred volume loss of 80 - 90%, the LFZ must have therefore experienced major compaction. Taking the ZJG exposure for example, the width of the HDZ is ~ 18 cm (Figure 2.3), and the isocon analysis revealed a volume loss of ~ 87 %, implying an initial zone thickness of 1.38 m (assuming constant density). Similarly, as the present thickness of the gouge zone is ~ 2 cm, and the volume loss is ~ 93 %, then the initial

thickness should have been ~ 29 cm. Such large thickness changes are of major importance when estimation gouge surface energy and thermal pressurization associated with seismogenic faulting.

2.5.2.2 Mechanism of mass removal: fluid infiltration

The bulk and trace element variation recorded along the PX and ZJG transects clearly indicates significant volume loss within the LFZ. There are three processes that could account for marked reduction in carbonate mineral content: 1) thermal decomposition by frictional heating, 2) chemical dissolution and 3) pressure solution under open system condition. A reduction of inorganic carbon content has been reported for the principal slip zone of the Chelungpu fault (*Hirono et al.*, 2006). This was interpreted as due to thermal decomposition of the carbonate minerals through frictional heating at coseismic slip rates (*Han et al.*, 2007). The higher magnetic susceptibility measured for the black gouge may also suggest formation of ferrimagnetic material by thermal decomposition of iron-bearing dolomite, e.g. kutnohorite (*Mishima et al.*, 2006). In the present study, however, decarbonation is unlikely to have been the mechanism controlling volume loss, though it cannot be ruled out. Decarbonation is unlikely because frictional heating should be localized in a zone of finite width, rapidly decreasing away from the slip zone, and therefore failing to cause extensive decomposition. This is inconsistent with our stable isotopic data as discussed in Section 2.5.2.3.

If fluid infiltration occurred in the LFZ, chemical dissolution would be an important candidate mechanism for removal of carbonate minerals. Even though no pH data are available, on site fluid monitoring at the WFSD-1 and WFSD-2 drilling sites (Figure 2.1) has shown abnormal jumps in concentrations of CO_2 degassing from the fault zone following aftershocks (*Luo et al.*, 2010). After the main Wenchuan earthquake, the soil concentration of CO_2 also displayed conspicuous positive anomalies at several fault scarps along the LFZ (*Zhou et al.*, 2010). On this basis, we infer a relatively acid pH for the interstitial fluid of the fault zone, perhaps facilitating the dissolution of carbonate minerals as the CO_2 pressure drops.

Pressure solution is also an important mechanism in carbonate rocks (*Zhang et al.*, 2010), and could be accelerated in the fault zone due to grain size reduction and/or fluid flow (cf., *de Meer and Spiers*, 1997). Though negligible in the shallow subsurface, pressure solution may be significant at depth in the long-term inter-seismic phase. By examining the Grant-type plots (Figure 2.6 and Figure 2.12), the MSZ displays larger inclinations than the HDZ, further implying that more mobile elements were lost from the slip zone than from the

surrounding, highly damaged rocks. Grain size analysis revealed that the particle size of the fault rocks decreases toward the principal slip surface (*Chen et al.*, 2011). The fine grained signature of the slip gouge (with average particle diameter ~ 4 μm) suggests extremely high surface energy. This would increase the chemical potential hence solubility of the gouge by around 1-10 J/mol ($4\gamma\Omega/d$, where γ is interfacial energy (0.05 - 0.5 J/m^2), Ω is molar volume (~ 2×10^{-5} m^3/mol) and d is grain diameter), as well as increasing fluid-rock reaction rates, in proportion to the surface area. Accordingly, fluid-rock reactions (e.g. dissolution) within the MSZ should be much faster than in the HDZ. Moreover, pressure solution compaction and creep rates are inversely proportional to the particle size cubed (in the diffusion controlled case, see *Zhang et al.* (2010)). On this basis, we interpret the volume strain in the fault rocks to be associated with cataclasis during faulting and the subsequent fluid-rock interaction processes, including mass removal by chemical dissolution and likely compaction by pressure solution (*Gratier et al.*, 2011), though no direct evidence of pressure solution could be observed in these very fine grained materials.

According to previous work (*Chen et al.*, 2011), the fault rocks of the PX and ZJG exposures display moderately high permeability (order of magnitude 10^{-16} - 10^{-13} m^2) at effective pressures below 10 MPa, providing channels for easy fluid flow, which would further enhance fluid-rock reactions and mass removal by undersaturated fluids. On the other hand, the permeability of fault rocks is extremely sensitive to effective pressure so that it would decrease rapidly with increasing depth, implying reduced fluid flux and less mass loss at depth, unless fluid recharge from below could maintain high fluid pressure.

It is important to note here that the volume changes that we report apply to portions of the fault zone that slipped repeatedly in the past. They are not coseismic volume changes but reflect accumulated mass and associated volume loss taking place over many previous earthquake cycles (*Zhang et al.*, 2010). Coseismic rupture can promote such mass removal processes by reducing the grain size and increasing the surface area available for rock-water interaction. The cumulative nature of repeated slip events means that the material seen at the surface has been exhumed from deeper levels. Significantly, the present study area (Western Sichuan, China) is characterized by active uplift and erosion, an active hydrological system and an extremely wet climate. Accordingly, most of the material that we infer was dissolved from fault zone would be easily transported away in both surface and ground water.

Generally speaking, fracturing, fluid infiltration, dissolution and mass removal would result in a reduction of rock strength (*Sibson*, 1973) until a) precipitation of strong mineral phases occurs, expanding the failure envelop (*Sibson et al.*, 1988; *Tenthorey et al.*, 2003; *Hausegger et al.*, 2010) or b) compaction by pressure solution leads to gouge strengthening

(e.g., *Yasuhara et al.,* 2005). In this study, cementation and vein precipitation were well evidenced at both exposures. The fluid-related mineral phases dolomite, barite, gypsum and fluorapatite were widely formed in the fault rocks. Microscopic examination showed different healing textures such as cross-cutting veins, aperture filling and fragment cementation. Like dissolution, cementation and pressure solution are also interfacial processes that are accelerated in fine grained materials with high surface area. This may explain why cemented ultracataclasite occurs adjacent to the main slip zone at the ZJG exposure (Figure 2.2b).

2.5.2.3 $\delta^{13}C$ - $\delta^{18}O$ distribution and related modeling

Stable isotope geochemistry provides hints on the origin of the fluid, the water-rock ratio, and fluid-rock interaction along fault zones (*Molli et al.*, 2010). The distinct differences in $\delta^{13}C$ values observed between the fragments, matrix and veins material in our study (Figure 2.7) suggests that the source of the inorganic carbon cannot be attributed just to remobilization of normal marine sedimentary carbonate (i.e., protolith) whose $\delta^{13}C$ values are ~ -2% (Figure 2.7). With respect to the limestone country rock, matrix and vein material within the fault core studied were depleted in heavy isotopes like ^{13}C. This is expected to result principally from interaction with external fluids depleted in ^{13}C and ^{18}O (*Wang et al.*, 2010) or from other processes such as thermal decomposition (*Shieh and Taylor*, 1969).

According to high-velocity frictional experiments, thermal decomposition of carbonate minerals by frictional heating may be a common phenomenon in natural faulting (*Hirono et al.*, 2006), which could produce significant dynamic weakening (*Han et al.*, 2007). Decomposition leads to the production of CO_2 enriched in heavy ^{13}C and ^{18}O, thus lowering the heavy isotope content of the residual carbonate minerals (e.g., *De Paola et al.*, 2011). Since most samples subjected to isotopic analysis in this study were collected from the fault core, they may have experienced high temperatures, hence decomposition and related isotopic fractionation effects. Using large breccia fragments (> 5 mm, $\delta^{13}C$ = -1.9 ‰ and $\delta^{18}O$ = 26.2 ‰) as an approximation of initial protolith material, isotopic fractionation by thermal decomposition was calculated following the fractionation equation for a closed system, written as $\delta_f = \delta_i + 1000(F-1)\ln(\alpha)$, where i and f denote the initial and final composition, F is the residual component, and α is the fractionation factor (*Sheppard and Schwarcz*, 1970). The results for 400 and 600 ºC (Figure 2.15) indicate that the fractionation trend for pure decarbonation cannot fully explain the observed evolutional trends, so that alternatives should be explored.

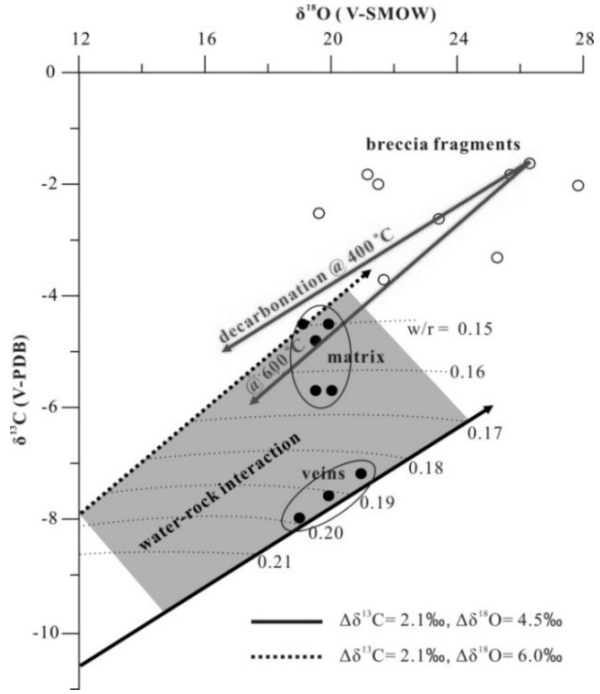

Figure 2.15. Modeling of $\delta^{13}C$ versus $\delta^{18}O$ values obtained from isotopic analyses of the ZJG exposure. The red lines are predicted by theoretical fractionation for decarbonation at 400 and 600 °C. The black lines are the calculated results assuming the vein and partially the matrix material were crystallized from the fluid after exchange equilibrium with the breccia fragments. Other detailed content as in text.

If fluid entering the fault zone is assumed to have had constant isotopic composition (*Hausegger et al.*, 2010; *Molli et al.*, 2010), the relative position of individual data points in the $\delta^{13}C$-$\delta^{18}O$ diagram (Figure 2.7) may relate to variations in the amount of fluid interacting with the sample (*Kirschner and Kennedy*, 2001; *Pili et al.*, 2002, 2011). Large breccia fragments with isotopic values near the protolith interacted with small quantities of fluid. Matrix and vein material with more depleted isotopic values either interacted with larger quantities of fluid, or precipitated from a fluid that had partly retained its original isotopic values. Overall, the isotopic discrepancy between fragments, matrix and vein material may be explained by a model in which: 1) external fluids were involved in the vein precipitation and matrix cementation, and the most ^{13}C-depleted values shown by sparry dolomite adjacent to the principal slip surface reflect their proximity to the hydrocarbon source ($\delta^{13}C$ = -8.0 ‰ and $\delta^{18}O$ = -11.5‰), and 2) the precipitating fluid interacted with the breccia fragments modifying its original isotopic composition. There are several candidate origins of fluid

depleted in ^{13}C. The first is related to organic complexes, which could evolve to yield strongly negative $\delta^{13}C$ values (e.g., -27.6 ‰ in *Hellings et al.* (2001)). However, there is no evidence for organic fluid activity near the ZJG exposure. The second is the contribution of mantle-derived carbon dioxide with $\delta^{13}C \approx$ -5‰ (e.g., *Ballentine and O'Nions*, 1994). This seems unlikely as no mantle-derived features were recognized, and the $\delta^{13}C$ values measured were more negative. The third and most likely possibility is fluid of meteoric origin.

Assuming the veins crystallized from meteoric fluid after reacting exchange equilibrium with the surrounding breccia fragments, mass balance modeling of the isotopic composition of the matrix and vein material can be carried out. At the fluid-fragment interface, cation exchange may take place providing calcium to the solution and promoting equilibrium with respect to the vein material. This means that the ^{13}C and ^{18}O content of veins precipitated from the fluid would be principally determined by differences between the isotopic composition of fluid and that of breccia fragments. Following the mass balance approach by *Zheng and Hoefs* (1993), the governing equations for calculating the ^{13}C and ^{18}O content of vein material precipitated from a fluid after interaction with the fragments, assuming bicarbonate (HCO_3) as the dominant carrier of carbon in the fluid, are:

$$\delta^{13}C^{f}_{vein} = \delta^{13}C^{i}_{HCO_3} + 1000\ln\alpha^{vein}_{HCO_3} + \gamma^{-1}(\delta^{13}C^{i}_{frag} - \delta^{13}C^{f}_{frag}) \quad (2.1)$$

$$\delta^{18}O^{f}_{vein} = \delta^{18}O^{i}_{H_2O} + 1000\ln\alpha^{vein}_{H_2O} + \gamma^{-1}(\delta^{18}O^{i}_{frag} - \delta^{18}O^{f}_{frag}) \quad (2.2)$$

Here i and f denote the initial and final composition, α is the fractionation factor, and γ is the water-rock ratio. In these calculations, we assumed a typical meteoric water composition with $\delta^{13}C^{i}_{HCO_3}$ of -12 ‰ and $\delta^{18}O^{i}_{H_2O}$ of -7 ‰. We also assumed a fluid temperature of 70 °C. The fractionation factors are 1.4‰ for $\delta^{13}C$ of HCO_3-$CaCO_3$ (*Ohomoto and Rye*, 1979) and 20.7‰ for $\delta^{18}O$ of H_2O-$CaCO_3$ (*O'Neil et al.*, 1969). The ranges in isotopic composition in exchanged fragments were 2.1‰ for ($\delta^{13}C^{i}_{frag} - \delta^{13}C^{f}_{frag}$) and 4.5-6.0‰ for ($\delta^{18}O^{i}_{frag} - \delta^{18}O^{f}_{frag}$) (Figure 2.7). As shown in the calculation results presented in Figure 2.15, the model for interaction between breccia and meteoric water can account for the isotopic data characterizing the matrix and vein material. The modeling also indicates water-rock ratio in the range of 0.15-0.20 (Figure 2.7), corresponding to 75-100 g water per kg breccia.

We infer that the ^{13}C-depleted carbonate veins and cements, as well as other fluid-related minerals like barite found in the two sections of fault zone studied, were

probably formed at the post-seismic stage, when deep fluid with excess pressure rose up and interacted with the fault rocks along the fault plane. During this period, healing processes, and the resulting impermeable barrier formed from cemented fault gouge and host rock (*Chen et al.*, 2011), caused a gradual pressure increase in pore fluid entrapped in the damage zone at depth. This led to subsequent frictional failure and the development of a temporarily open system accessible for fluid flow. This alteration between brittle failure and cementation implies a cyclic change between an open and a closed fault zone system, i.e., fault valve behavior (c.f., *Sibson*, 1990).

2.5.3 Clay mineral transitions in the fault gouge and their dynamic effects

The gradual enrichment of smectite (or smectite-rich I/S) towards the principal slip surface, along with the illitization in the black gouge seen in both the study exposures, imply that we should be able to obtain useful information about the faulting mechanism from the *in-situ* clay mineralogy. Though the smectite-bearing upper portion of the LFZ was passively displaced and did not radiate seismic energy, it provides a good illustration of the transition from illite (or illite-rich I/S) to smectite (or smectite-rich I/S) in an active fault zone. This is important for discussing the slip stability of a fault zone containing clayey-gouge (*Brace and Byerlee*, 1966). Smectite is a mineral with one of the lowest coefficients of friction and is usually regarded as an important contributor to coseismic slip weakening (e.g. *Lockner et al.*, 2011). In addition,, the frictional resistance could be further lowered by the introduction of water produced locally by coseismic dehydration of smectite as discussed below.

Coseismic decomposition reactions such as dehydration of serpentine, kaolinite and smectite, have been previously demonstrated in both experimental (*Hirose and Bystricky*, 2007; *Brantut et al.*, 2008; *Ferri et al.*, 2010) and field work (*Hirono et al.*, 2007, 2008; *Hamada et al.*, 2009). For example, *Hirono et al.* (2008) analyzed the clay composition of the Chi-chi earthquake cores and found that the kaolinite and smectite contents were lower in the black gouge than in the surrounding rocks. The dewatering process might have significantly affected the faulting mechanism, since these clay minerals can release water, lowering the fault strength rapidly. In our study, though to a limited extent, illitization has occurred in the black gouges even at the surface. At low pressure condition, smectite begins to lose interlayer water at 110 ^{o}C and illite starts to form at temperatures above ~ 150 ^{o}C (*Saffer and Marone*, 2002). A simple order of magnitude calculation shows that at or just below the ground surface, normal stresses are too low to produce enough frictional heat to transform smectite into illite. A first possibility we offer to explain the observed illitization is that irregularities in the slip surface caused high local normal stress and thus irregular,

increased heat production along the slip surface. This is consistent with the discontinuous nature of the black illitized gouge. The second possibility is that coseismic slip was highly localized. This is probably the reason why illitization only occurred to the thin black layers. An additional possibility is that drastic grain size reduction or comminution within the fault rocks promoted illitization by means of water expulsion and chemical exchange, the reaction kinetics of which are poorly known for nano-particles. We speculate that illitization may become increasingly important at depth because of increased frictional heating, if other factors remain unchanged (*Huang et al.,* 1993). According to the chemical formula of typical smectite ($(Ca_{1/2},Na)_{0.35}(Al,Mg)_2Si_4O_{10}(OH)_2 \cdot nH_2O$, where n is the number of moles of water in one mole smectite) and illite ($(K,H_3O)Al_2Si_3AlO_{10}(OH)_2$), the reaction products of smectite-illite transformation are aqueous silica, Mg^{2+} and water, via the following reaction (*Roland and Ola*, 1996), smectite + feldspar (or pore water) = illite + quartz (or chlorite) + water + cations. The released silica and Mg^{2+} charged pore fluids may migrate along the fault zone during coseismic dilatation (*Goddard and Evans*, 1995) and/or via fault-valve action (*Sibson*, 1990), flushing the fault zone near the surface, promoting new smectite formation at higher levels. Therefore, a self enhancing feed-back mechanism is proposed to explain the features demonstrated above, namely the Mg-rich fluid and the enrichment in smectite.

According to the reaction equation, illitization of smectite involves liberation of a large quantity of water either interlayer water or structural sites. However, a solid volume reduction of 33 - 47 % is also involved since the lattice structure collapses from 150 -190 nm to 100 nm (*Vrolijk and van der Pluijm*, 1999). These two aspects counteract each other in terms of pore pressure change. Synchrotron studies showed that the temperature for smectite dehydration increases with increasing pore pressure (*Huang et al.*, 1994). The positive Clausius-Clapeyron coefficient indicates that the total volume of reaction products was larger than that of the reactants. In addition, the interlayer water is denser than that of the pore fluid (*Hawkins and Egelstaff*, 1980). Taken together, most available evidence favors pore pressure increase during the smectite-illite transformation. Based on this idea, we now carry out calculations to estimate the influence of this dewatering process, induced by frictional heating, on the faulting behavior of the Wenchuan earthquake.

With increasing depth, the higher normal stress should produce more frictional heating. Modeling work on heat production during the Wenchuan earthquake predicts a peak temperature of 600 ºC, with an average temperature of 400 ºC lasting for over 150 s at 600 m depth (*Yang et al.*, 2012). In terms of reaction kinetics, dehydration of smectite is very fast, occurring on a timescale of minutes (*Huang et al.*, 1994; *Hirono et al.*, 2008). Assuming the same clay composition as analyzed on the surface, we can estimate the amount of water

expelled from the gouge and the possible effect on generating excess pore pressure at 3 km depth during the Wenchuan earthquake. Assuming 1 mol of hydrated smectite converts to 1 mol dehydrated material, losing χ mol water and producing a volume reduction of the solid phase of ΔV, the potential pore pressure increment induced by the reaction can be expressed as follows:

$$\Delta p = \lambda(1-\phi)(\frac{\chi M_{H_2O}}{M_{hy}}\frac{\rho_s}{\rho_f} - \Delta V)/S_s \tag{2.3}$$

where λ is mass percentage of hydrated smectite in the gouge, ϕ and S_s denotes porosity and specific storage (Pa^{-1}) of the fault gouge, χ is the number of moles of water released from one mole smectite, M_{H_2O} and M_{hy} are the molar masses of water (18 g/mol) and smectite (366 + n×18 g/mol), ρ_f and ρ_s are densities of fluid (1.0×10^3 kg/m^3) and solid phases (2.61×10^3 kg/m^3). This formula is similar to equation (15) given by *Brantut et al.* (2010). The term $\Gamma = \chi(M_{H_2O}/M_{hy})(\rho_s/\rho_f) - \Delta V$, defined as specific expelled water, is a general expression. For a given dehydration reaction, Γ is a constant, representing the amount of water (vol. %) released. If ΔV is large enough, Γ would be zero. This corresponds to the case in which the overpressure induced by fluid production is compensated by the porosity increase induced by lattice collapse.

In the following, a fully hydrated smectite with three interlayers of water are initially assumed. The cases of losing one, two and three interlayers of water are then explored. The number of moles of water contained in per mole of smectite with one, two and three interlayers of water, are 1.9, 4.5 and 7.16, respectively (*Liu and Lin*, 2005). These figures imply that the χ-values associated with losing one, two and three interlayers of water are 2.66, 5.26 and 7.16, respectively. ΔV can be estimated by considering change of basal spacing (d_{001}) for smectite transferring from one hydration state to another. Smectite has four discrete d_{001} corresponding to its four states, that is, 100 nm for the fully dehydrated state, versus 124, 156 and 188 nm for the hydrated states with one, two and three interlayers of water (*Huang et al.*, 1994 and references therein). This yields ΔV values of 17.0 %, 34.0 % and 46.8 % associated with releasing one, two and three interlayers of water. Substituting the appropriate values of χ and ΔV into the expression above for Γ gives specific expelled water as 8.2 %, 15.9 % and 21.2 %, respectively. The mass content of smectite (λ) can be calculated from the mineralogical results (Table 2.2). *In-situ* porosity (ϕ) and specific storage (S_s) measured on core samples in laboratory were also applied (Table 2.2).

Table 2.2. Estimation of the amount of water expelled by dehydration of interlayer water in smectite [a] and the dynamic effect on generating excess pore pressure [b]

Principal slip gouge	ZJG gray gouge	PX gray gouge
Clay content of bulk sample (wt. %)	34	25
Reference content of smectite (%)	83 ×38%	32
Smectite content (wt. %)	10.7	8.0
Porosity (%) at 3 km	12.8	10.7
Specific storage (Pa^{-1}) at 3 km	1.2×10^{-9}	8.1×10^{-10}
ΔP_f (MPa) by losing 1 layer of H_2O	6.3	7.2
ΔP_f (MPa) by losing 2 layers of H_2O	12.4	14.0
ΔP_f (MPa) by losing 3 layers of H_2O	16.5	18.7

[a] *Smectite here includes pure smectite and smectite contain in I/S. The reference content of smectite in I/S equals to the reference content of I/S multiplied by S%.*

[b] *Calculation were conducted at 3 km depth under an effective pressure of 45 MPa.*

The calculation showed that losing one interlayer of water in smectite generates about 6.5 MPa excess pore pressure over the hydrostatic head at 3 km depth (Table 2.2). This value can increase to 17.5 MPa if the smectite interlayers are fully dehydrated. Such behavior will cause a reduction in effective normal stress acting on the fault plane from 45 MPa to ~ 27.5 MPa. Indeed, our calculation should underestimate the dynamic weakening effect that actually occurred in the Wenchuan earthquake since thermal pressurization is not taken into consideration. On the other hand, the dehydration of smectite is an endothermic reaction (*Hirono et al.*, 2008). Hence, there is a temperature decrease effect during the reaction. Hence, there is consumption of thermal energy during the reaction, which in turn limits the temperature and pore pressure increase. Alongside thermal pressurization, however, this effect is expected to relatively small compared to that of the released of interlayer water. To explore the coseismic thermo-mechanical-chemical process in more detail, numerical modeling coupling the kinetic process of chemical reaction with frictional heating and fluid transportation is needed in the future (*Sulem and Famin*, 2009; *Brantut et al.*, 2010).

A similar treatment to the above can be applied for halloysite, which is concentrated at the margins of the fault core (with maximum content of 3.1 wt. %) while being absent from the slip zone (Figure 2.9). Halloysite has nearly the same chemical composition ($Al_4(Si_4O_{10})(OH)_8.nH_2O$) as kaolinite but contains water interlayers. In terms of lattice structure, kaolinite consists of layers of Si-O tetrahedra and Al-(OH) plates linked by

hydrogen bonds, whereas in halloysite the existence of interlayer water destroys the hydrogen bond, so that the Si-O tetrahedra and Al-(OH) plates must bend to accommodate the change in unit cell dimensions, thus developing a curled or tubular shape. Halloysite therefore forms a natural nano-particulate material and at 50 - 90 °C it dehydrates to kaolinite (*Brindley et al.*, 1952). Considering it is too unstable to survive at depth, we did not take its dehydration into account in our calculation. At shallow depths, however, its dynamic effect on faulting would be considerable as it decomposes at low temperature and the reaction rate is expected to be fast because of the nano-particle size. Furthermore, other reactions like dehydration of gypsum could also occur, but are not included here considering the low content of such phases (Figure 2.9). Finally we should point out that whether these dewatering reactions occurs or not depends upon whether the fault system is drained or undrained. Under drained conditions, even though dehydration can easily occur, the system is relatively open so that excess pore pressure is unlikely to be generated during faulting. By contrast, under undrained or partially drained conditions, dehydration reactions may be prohibited and the effect of dewatering will depend strongly on the transport properties (i.e., permeability and specific storage) of the gouge samples.

2.5.4 Implications for subsurface processes

We will now apply our interpretations of the processes that operated at the two surface exposures studied to construct an integrated, conceptual model synthesizing the coupling between fault activity, fluid migration, mass transport and geochemical evolution that can occur under near-surface conditions in active carbonate fault zones. We assume that the processes inferred at the surface will also occur in the subsurface and reason to what depth they may extend. Our model is represented in Figure 2.16. It assumes cumulative carbonate removal as a key process, so is limited to carbonate-bearing systems. It incorporates the following feathers.

First, the efficiency of carbonate removal is determined by dissolution and advective transport, probably enhanced by pressure solution, especially in compressional tectonic settings. Though the solubility and dissolution rate of carbonate are relatively insensitive to temperature (*Zhang et al.*, 2012), at depths greater than 2.5 - 5 km, porosity and permeability of both fault core and surrounding rock will become strongly reduced due to elevated effective stress (*Wibberley and Shimamoto*, 2003) and thermally activated compaction/healing processes (*Tenthorey et al.*, 2003). This will limit the advective mass removal process. The implication is that the cumulative volume/mass removal phenomenon reported here, and schematically illustrated in Figure 2.16, will only be important in the

upper few kilometers of the crust, where groundwater movement can affect the fault zone. The second feature of our model is cyclic upwelling of hydrothermal fluids originating at depth, notably in post-seismic periods when the fault valve is temporarily opened (*Sibson*, 1990). This results in extensive deposition of characteristic minerals like barite and fluorapatite. Third, hydrothermal fluid probably of recirculated meteoric origin leads to precipitation of carbonate veins and cements, resulting in the observed depletion of ^{13}C in the carbonate-hosted fragments. Fourth, the various cycles of the hydrothermal alteration cause increasing enrichment of smectite toward the principal slip surface. Lastly, the inferred process of smectite illitization and release of interlayer water by coseismic frictional heating, modified by thermal pressurization and endothermic dehydration reaction, cyclically modify the principal slip gouges. This process will of course be limited to the upper 2 - 3 km of the crust where temperatures are low enough for smectite to form in the first place. With increasing depth, the coseismic temperature rise driving the illitization reaction, hence the extent of illitization, can be expected to increase also, because the higher normal stress should produce more frictional heating. The released fluid may be capable of increasing fluid pressure sufficiently to significantly enhance dynamic rupture propagation.

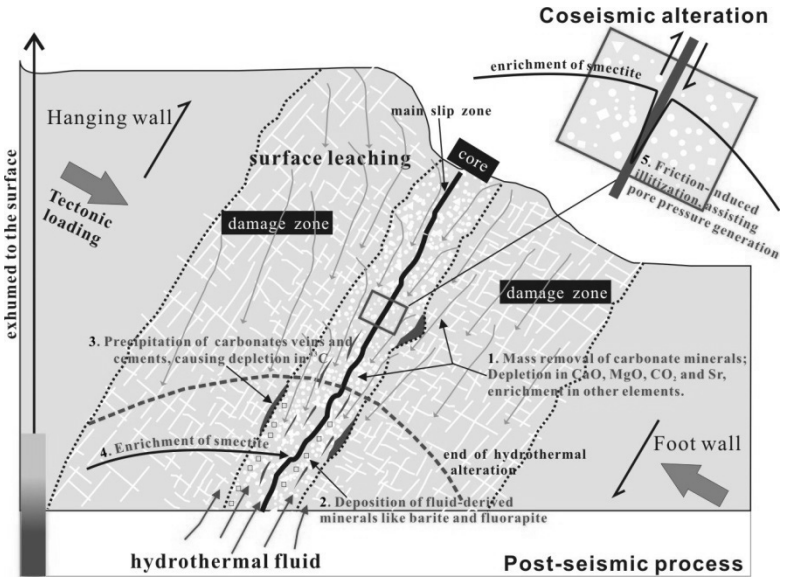

Figure 2.16. Integrated conceptual model illustrating the complete set of mechano-chemical processes inferred to affect the geochemical evolution of the carbonate-rich fault zones studied here and perhaps more generally. Note the five key features of the model.

One key point about this model should be emphasized further. On-going activity of the hydrothermal processes involved (items 2 to 4 in Figure 2.16) should be limited by reactant supply on the one hand and by the healing and sealing of fault permeability on the other. However, paleoseismic studies (*Zhang et al.*, 2010) have revealed that many previous earthquakes have occurred along the LFZ. The active uplift and erosion going on in this area accordingly implies that the material seen at the surface now has been exhumed from the subsurface. It is the cumulative nature of repeated seismic events that explains the large volume loss observed at the sites that we studied. Our model predicts that similar effects should occur in other active, carbonate-bearing fault zones too.

2.6. Conclusions

The main conclusions of this study of the ZJG and PX sites on the LFZ are summarized below.

(1) Mineralogical and geochemical profiles along with the isocon diagrams, as well as isotopic results, consistently demonstrate that pervasive fluid infiltration occurred and altered the chemical architecture of the carbonate-dominated fault zones. Enrichment/depletion patterns, elements partitioning and the large volume loss characterizing the carbonate-rich fault zones investigated are quite different from those characterizing granitic and clastic sedimentary fault zones. A mass removal model, involving dissolution and transportation, likely enhanced by pressure solution creep, is accordingly proposed and can account for the signatures observed in the carbonate-rich fault zone studied.

(2) The increasing enrichment in smectite towards the slip surface, the high abundance of fluid-related minerals and elements, as well as the depletion in heavy isotopes (^{13}C) recognized in the fault zones studied, consistently suggest activity of fluids of hydrothermal origin. Faulting and cementation by deep fluids played a fundamental role in the evolution of the fault zone, with a cyclic change between an open and a closed permeability system during fault evolution. Stable isotope compositions ($\delta^{13}C$ and $\delta^{18}O$) indicate continuous equilibration between protolith-derived breccia fragments and vein material (or cements) precipitated from fluids.

(3) The black gouge found in the studied exposures on the LFZ, is inferred to be the material having accommodated most of the displacement during the Wenchuan Earthquake. Illitization caused by frictional heating has occurred within it. We propose that frictional heating effects along with the action of post-seismic hydrothermal fluids controlled the transformation and distribution of smectite and illite within the fault core of the LFZ. The dehydration of smectite by frictional heating is expected to have been most extensive at

depth. Numerical modeling indicates that excess pore pressures of as much as 17.5 MPa can be generated at 3 km depth by this process, perhaps assisting dynamic slip weakening during the Wenchuan Earthquake.

Acknowledgments. This research was co-supported by the ninth Section (WFSD-0009) of the National Scientific Special Funding of the Wenchuan Fault Scientific Drilling, the State Key Laboratory of Earthquake Dynamics, China Earthquake Administration (LED2010A03), the National Science Foundation (41102130) and the Basic Scientific Funding of Chinese National Nonprofit Institutes (IGCEA1006). We thank Yang Yongxin, Duan Qingbao, Dang Jiaxiang, Yao Lu, Zhang Lei, Hou Linfeng and Yang Tao for their valuable support in the field.

Chapter 3

Importance of thermochemical pressurization in the dynamic weakening of the Longmenshan fault during the 2008 Wenchuan earthquake: inferences from experiments and modeling

Jianye Chen, Xiaosong Yang, Qingbao Duan, Toshi Shimamoto, Christopher J. Spiers

Journal of Geophysical Research, 118, 4145–4169

Abstract

We determined the internal structure and mineral composition of Yingxiu-Beichuan fault zone at the Zhaojiagou exposure and measured frictional and transport properties of the fault rocks collected to gain a better understanding of dynamic weakening mechanisms during seismic fault motion. This fault is a major fault in the Longmenshan fault system that caused the 2008 Wenchuan earthquake. The exposure studied is located midway along the surface rupture, close to where the largest coseismic displacement occurred. High-velocity friction experiments reveal exponential slip weakening from a peak friction towards a steady-state value. Slip weakening is more pronounced for water-dampened gouge than dry gouge, suggesting thermal pressurization. The fault gouge has a very low permeability (< 10^{-21} m^2 at 165 MPa effective pressure) and is surrounded by fault breccia with permeability of 10^{-19} to 10^{-17} m^2, grading into less permeable, fractured country rocks. The fault zone thus exhibits a "conduit/barrier" structure, allowing fluid flow only in the breccia zone. We numerically modeled coseismic slip weakening including thermal pressurization and mineral dehydration/decarbonation, basing our calculation on measured frictional and transport properties, and on the slip history inferred for the Wenchuan earthquake. The results indicate that 1) thermochemical pressurization played an important role in causing dynamic slip weakening, 2) the slip-weakening distance is similar to the seismologically determined values, 3） pore pressures might have exceeded the normal stress, thus maintaining temperatures below 600 °C. Interestingly, enough heat was generated to fully remove and thermally pressurize the interlayer water from smectite, contributing an excess pore pressure of ~ 6 MPa. In addition, we found that the incorporation of state-dependent fluid properties predicts much more efficient fluid pressurization than using constant properties. The dramatic weakening predicted probably offers a compelling explanation for the large coseismic displacement and slip acceleration observed near Beichuan city.

3.1 Introduction

The catastrophic Wenchuan earthquake (Ms 8.0) struck Sichuan, China on 12 May, 2008. Coseismic surface rupture occurred over a distance of 240 km along the northeast-striking Longmenshan fault zone (LFZ), with a maximum vertical offset of ~ 9 m (*Xu et al.*, 2009; *Zhang et al.*, 2010). A maximum displacement of ~ 7.3 m and a corresponding slip rate of 1.25 m/s were inferred from seismological inversion (*Zhang et al.*, 2009). This also yielded an average stress drop of 18 MPa, double that characteristic of a typical continental interior earthquake (*Kanamori*, 1994). The Wenchuan earthquake is the first with such a large magnitude recorded on a high-angle reverse fault within a continental interior (*Zhang et al.*, 2010). Besides high tectonically generated deviatoric stress, a high pore pressure at depth may be required for a reverse fault to yield a mega-earthquake (*Sibson*, 1988). Such pore pressures are only possible if the fault zone is impermeable enough to seal high-pressure fluid within the fault zone (*Faulkner and Rutter*, 2000). A slip-weakening mechanism may also be required to account for the large coseismic displacement observed, which was much higher than experimentally-inferred slip-weakening distances at nucleation slip rates (e.g. *Ohnaka and Shen*, 1999).

Theoretical studies have focused on thermal pressurization (TP) as an important slip-weakening mechanism, at both the coseismic slip (*Lachenbruch*, 1980; *Mase and Smith*, 1985; *Rice*, 2006) and rupture nucleation (*Segall and Rice*, 2006; *de Lorenzo and Lpddo*, 2010) of an earthquake. Other high-velocity slip weakening mechanisms include silica gel lubrication (*Di Toro et al.*, 2004), bulk melting (*Tsutsumi and Shimamoto*, 1997; *Hirose and Shimamoto*, 2005), flash heating (*Rice*, 1999) and nano-particle lubrication (*Han et al.*, 2010; *Reches and Lockner*, 2010). The principle of TP is that the pressure of pore fluid, trapped inside a slipping fault builds up due to frictional heating, thus reducing the effective normal stress acting on the fault plane and hence the shearing resistance of the fault (*Lachenbruch, 1980*; *Mase and Smith*, 1985). TP can cause additional effects such as increased slip distance (*Rice*, 2006) and an increase in rupture velocity (*Bizzarri and Cocco*, 2006).

A growing body of natural and experimental evidence has recently shown that reactions induced by frictional heating may also be more important than the previously realized in producing weakening effects during fault motion (*Hirono et al.*, 2006, 2008; *Han et al.*, 2007; *Hirose and Bystricky*, 2007; *Brantut et al.*, 2008; *Hamada et al.*, 2009; *Ferri et al.*, 2010; *Yamaguchi et al.*, 2011). Aside from the production of minerals that could make faults much weaker than expected from the static mineral assemblage (*Vrolijk and van der Pluijm*, 1999), dehydration reactions (*Brantut et al.*, 2008; *Famin et al.*, 2008; *Ferri et al.*, 2010) may liberate fluid into the pore space, thus building up pore pressure and reducing fault shearing

resistance. On the other hand, some reactions have a strong endothermic effect that can inhibit temperature rise and hence reduce TP effects (*Brantut et al.*, 2011). Few experiments have yet been successful in verifying the coseismic TP process (*Sulem et al.*, 2007; *Ujiie et al.*, 2011), not to mention the influence of chemical reactions upon it. However, numerical modeling has demonstrated that the process is possible (e.g. *Wibberley and Shimamoto*, 2005; *Noda and Shimamoto*, 2005; *Bizzarri and Cocco*, 2006; *Mizoguchi and Shimamoto*, 2008). Recent modeling using laboratory-derived physical properties is now leading to refinement of TP modeling efforts (*Wibberley and Shimamoto*, 2005; *Tanikawa et al.*, 2009) and to improved understanding of the coseismic thermochemical pressurization combing TP and the effect of fluid release due to mineral decomposition (*Brantut et al.*, 2010; *Sulem and Famin*, 2009), and of their effect on rupture propagation.

With those development in understanding of the seismic fault motion, this paper reports mineralogical composition and in situ frictional and transport properties of fault rocks collected from an exposure on the Yingxiu-Beichuan fault, the major coseismic fault in the LFZ that caused the 2008 Wenchuan earthquake. With the lab-constrained fault rock properties, we then numerically model coseismic slip inside a fluid-saturated fault zone including thermochemical pressurization. We performed parametric analysis with respect to a reference case with measured properties to quantify the impacts of different variables on the weakening processes. The results show that the thermochemical processes are likely to control the slip weakening during the Wenchuan earthquake. Our results will be useful in future realistic modeling of the dynamic rupture propagation during the Wenchuan earthquake, thereby in testing how much we understand the origin of the large displacement and slip acceleration behavior observed near our sampling site.

3.2 Geological setting and fault exposure

The Longmenshan fault system constitutes of three parallel sub-faults, Wenchuan-Maoxian, Yingxiu-Beichuan and Guanxian-Jiangyou faults from northwest to southeast (Figure 3.1a). The Wenchuan earthquake activated motion on two of them, with the coseismic surface rupture being denoted by thick black lines. The segment from Gaochuan to Beichuan is shifted eastward by ~ 3 km from the general northeast-striking trend of Yingxiu-Beichuan fault. An enlarged map near Beichuan (Figure 3.1b) shows that the surface rupture trace exhibits a transition from cutting into the Cambrian block to propagating northeast along stratum boundaries. Note that the largest coseismic offset of the Wenchuan earthquake occurred near Beichuan (Figure 3.1c), and that the surface rupture along the fault showed an abrupt jump there, from a vertical offset of 1.7 to 8.6 m, and from a horizontal

offset of 1.6 m to 2.5 m, respectively (*Zhang et al.*, 2010). As shown in Figure 3.1d, the slip rates at various depths exhibited an abrupt acceleration as the rupture approached Beichuan city, and acceleration is also inferred as the rupture propagated from depth upward (*Zhang et al.*, 2009). The fault motion near Beichuan was completed in two stages. One slip event occurs between 36 and 41 s (referred to as "pre-slip") and the other is the main slip, occurring between 48 and 58 s (Figure 3.1e).

In this study, the Zhaojiagou (ZJG) exposure (the southsrnmost exposure studied in Chapter 2), located at ~ 3 km southwest of Beichuan city, was systematically investigated. Located in a cliff (Figure 3.2a), the ZJG exposure is well exposed. The fault here strikes at an azimuth of 45° and dips 64 - 78° to the NW (Figure 3.2b). The principal slip surface cut through carbonate-rich layer. The fault gouge is either black or gray in color and could be distinguishable easily from the amount of visible clasts less than 30 %, following classification of *Sibson* (1977). Surrounding fault breccias were characterized by an increase in the amount of visible clasts and by the development of fractures (Figure 3.2c and 3.2d). Fault zone at this exposure consists of different units. From west to east, they were (1) fractured limestone, (2) cemented coarse breccias, (3) coarse breccias, (4) weakly-foliated fine breccias, (5) gray and black fault gouges, (6) weakly-foliated fine breccias, (7) coarse breccias and (8) fractured sandstone.

The fault core (*Caine*, 1996) is extremely narrow (~ 20 cm), consisting of gray gouge in the center and surrounding weakly-foliated yellowish fault breccias (Figure 3.2c and 3.2d). The thickness of the gray gouge ranges from 10 to 31 mm, with mean of 20 mm and standard deviation of 7.2 mm (15 measurements at an interval of ~ 10 cm). It is interesting that there developed a thin black gouge layer (< 7 mm) adjacent to the gray gouge (Figure 3.2c and 3.2d). These gouges consisted of very fine, tacky, clay-rich material exhibiting ductile behavior when wet. They often branch to the adjacent breccia zone. Figure 3.2e is a photomicrograph under crossed polarized light, showing a slice of specimen (~ 14 mm thick) composed of fault gouge and fault breccia. Further microscopic examination on it revealed that the coseismic slip of the Wenchuan earthquake might be localized. The slip may concentrate in part of the width of the gouge zone (~ 4 mm thick, corresponding to the black gouge in Figure 3.2d), or in an even more localized band (< 1 mm thick, at the left margin of the gouge zone in Figure 3.2e). It is difficult to make sure which was the principal slip zone during the Wenchuan earthquake. Considering the black gouge is not continuous on the exposure, we take evenly-distributed slip as a reference case and the influence of localization on coseismic slip weakening is discussed in detail in section 3.5.4.4.

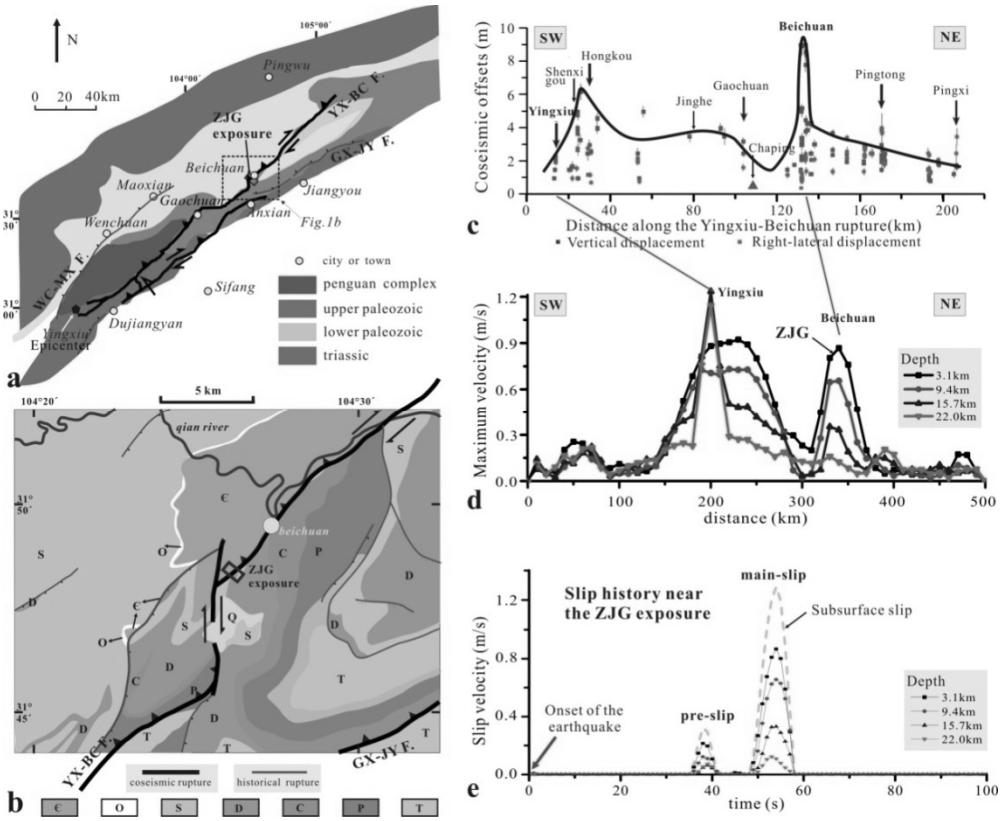

Figure 3.1. Geological setting and slip history of the Wenchuan Earthquake. (a) Location of the study area and regional geological map of the Longmenshan fault system, consisting of three fault zones, the Wenchuan-Maoxian fault (WC-MX F.), Yingxiu-Beichuan fault (YX-BC F.) and Guanxian-Jiangyou fault (GX-JY F.); (b) enlarged geological map near the studying area; (c) coseismic slip distributions of surface rupture along the Yingxiu-Beichuan fault, revised after Zhang et al. (2010) by adding a new data point for Chaping (Hou et al., 2012) and an interpretive envelope curve; (d) maximum slip velocities at various depths along the Yingxiu-Beichuan fault during the Wenchuan earthquake; (e) slip history at a location near the exposure studied at various depths. Notations of symbols for stratum in (b) are Є for Cambrian; O, Ordovician; S, Silurian; D, Devonian; C, Carboniferous; P, Permian; T, Triassic. The data in (d) and (e) is from the inversion results given by Zhang et al. (2009). The slip history presented in (e) is 3.8 km northeast of the exposure studied. To obtain subsurface slip history, we extrapolated the slip history data for 3.1 km depth, derived from the geophysical inversion by Zhang et al. (2009), constraining the total displacement to be equal to that measured at the surface by geological survey (c).

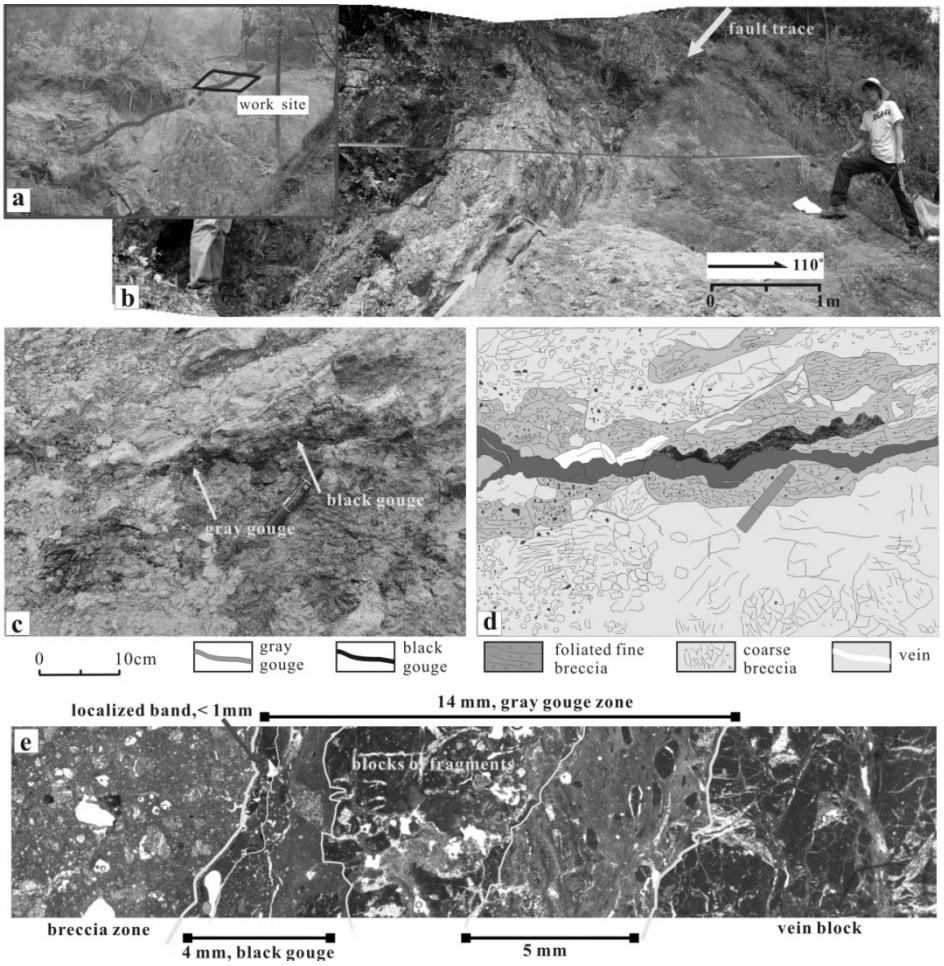

Figure 3.2. Internal structure of the fault zone. (a, b) Photographs of the ZJG exposure, (c) fault core structure and (d) the interpretive sketch. (e) Microstructure of the slip zone. The GPS location is 104°25'57.61"E and 31°48'22.44"N. Note that the exposure is in a cliff so that it's difficult to take a more panoramic view.

3.3 Sampling and experimental methods

3.3.1 Sampling

A roughly 50cm-thick surface layer was removed to eliminate weathered rocks. To provide sufficient data on spatial variation of rock properties to model coseismic slip behavior, the fault gouge and adjacent rocks were carefully sampled. Cylindrical samples used for measuring transport properties were taken by inserting thin-walled (0.1 mm thick) copper tubes with an internal diameter of 20 mm into the exposure and extracting them with the enclosed material. Stainless steel tubes of 22 mm internal diameter were used when the

fault rock was too hard to use copper tube. The cores were transferred into polyolefin heat-shrinkable tubes and then heat-jacketed to protect the cores in cylinder shape. For cohesive rocks like the country rock, hand specimens were collected in the field and coring was done in the laboratory. All the samples were cored parallel to fault surface, except for the gouge sample, which were cored perpendicular to foliation.

3.3.2 Mineralogical analysis

X-ray diffraction (XRD) was used to determine relative mineral content including semi-quantitative analysis for clay minerals. Unoriented, hand-powdered bulk samples were analyzed over a 2θ range of 3°. to 45° at a scan rate of 2°/minute with step width of 0.02°, employing a Dmax 12kW X-Ray powder diffractometer and CuK-α radiation. Bulk powder samples gave a first evaluation of the relative amounts of bulk clays, the composition of which was further verified by analyzing the clay-sized portion. After centrifuging, suspensions of < 2 mm particle size were deposited on glass slides and scanned in the diffractometer. Ethylene glycol was used to hydrate the clay samples so as to recognize swelling components (smectite or illite/smectite mixlayer). Heating to 550 °C helped distinguish kaolinite from chlorite. The method of semi-quantitative analysis of clay minerals followed that of *Lin et al.* (1992).

3.3.3 High Velocity Friction Tests

Friction experiments were conducted at seismic slip rate under both 'dry' (atmospheric humidity) and wet conditions, on the gray gouge and on simulated gouge prepared from the fault breccia. The samples were prepared by lightly tapping in a mortar to produce powder, sieving to a grain size of less than 125 μm, and then oven-drying at 80 °C for 48 h, immediately prior to experimentation. Experiments were conducted using the low-to-high velocity, rotary-shear friction apparatus recently installed at the Institute of Geology, China Earthquake Administration, Beijing (*Yao et al.*, 2013). The apparatus is capable of producing slip velocities ranging from tens of mm/year to seismic slip rates of around a few m/s, but we focused on frictional properties at high slip rate (1.3 m/s). The procedures for experimentation followed *Mizoguchi et al.* (2007). A 1.0 mm-thick (2.3 g) powder layer was sandwiched between a pair of gabbro cylinders of ~ 40 mm in diameter, of which the outer surfaces had been ground with diamond grinding wheel of #150 (100μm) using a cylindrical grinder and the end surfaces had been roughened by grinding with #80 silicon carbide powder (180 μm). A Teflon sleeve was mounted on this sample assembly to prevent gouge loss (Figure 3.3a). An axial force corresponding to the normal stress applied during each

experiment was then imposed on the gouge and maintained for ~ 5 minutes. This is held near-constant (within ~ 1%) by employing a Bellofram cylinder filled with compressed air to serve as a buffer. The gouge was then pre-treated by sliding at a slow rate (1.3 mm/s) for about 15 s, at which point the slip rate was increased instantly to 1.3 m/s to conduct a high-velocity friction experiment at a constant slip rate. Slip rate was incremented instantaneously by changing the gear assembly from intermediate slip rates to high-velocity line without stopping the servo-motor.

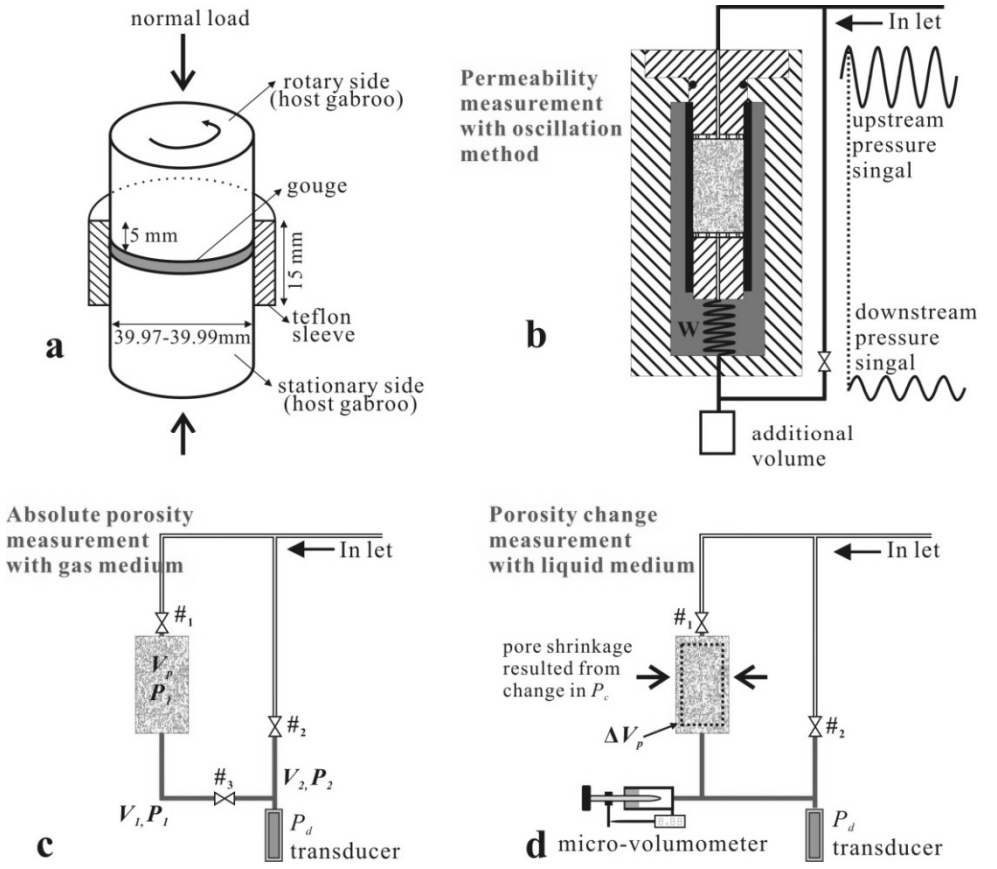

Figure 3.3. (a) Sample assembly of the high-velocity rotary frictional tests; diagrams illustrating (b) permeability measurement using the pore pressure oscillation method, (c) absolute porosity measurement with gas medium and (d) porosity change measurement during each step change in confining pressure.

For wet experiments, 20 wt. % distilled H_2O was added to the gouge layer to fulfill the water-saturated condition using a 0.5 ml syringe. Other procedures were as for dry

experiments. The pore fluid resided within the gouge porosity, enclosed by the gabbro (commercial decorative Indian gabbro, permeability < 10^{-22} m^2) and the poorly-sealed Teflon sleeve, at an unmeasured pressure (likely between 0.1 and 0.65 MPa according to numerical modeling of the experiments, see section 3.6.2), determined by competition between thermal pressurization and leakage past the Teflon sleeve. The effects of heating and decomposition of Teflon sleeves have recently been called into question (*Sawai et al.*, 2012) in high-velocity experiments on gouge samples, because released fluorine probably reacts with the gouge near its outer edge. However, we consider this heating/decomposition effect to be negligible in our experiments, because the (measured) Teflon friction was very low (Figure 3.4a), and because our sample assembly had a larger diameter (~ 40 mm) than most previous studies (~ 25 mm) so that any effects of Teflon decomposition would be volumetrically insignificant (if decomposition occurred at all). Data on torque, axial force, displacement, revolution rate and number of revolution were recorded with a digital data recorder with sampling rates of 2000 Hz. Data processing followed *Togo et al.* (2011).

3.3.4 Transport Properties Measurement

Integrated permeability/porosity measurements were performed using a high pressure fluid flow apparatus, at room temperature and under confining pressure to 180 MPa, using water as confining medium. In a typical measurement, the rubber-tube jacked cylindrical sample with spacers (double layers of steel mesh, #240 and #30, of 0.6 mm thick in total) at its two-ends was inserted inside the vessel, connected to the upstream and downstream reservoirs. Each experiment was initiated by imposing a confining pressure of 10 MPa. The pore fluid system was subsequently evacuated (~ 15 min) and pressurized with nitrogen. The measuring procedure adopted was as follows: (1) determine the absolute porosity of dry sample at an initial effective pressure of P_{e0} using nitrogen as pore fluid, (2) introduce water into the pores by evacuation and saturating the system with distilled H_2O, (3) measure permeability (together with specific storage) using the pore pressure oscillation method at effective pressure P_{e0}, (4) change confining pressure and determine the resultant porosity change, (5) repeat steps 3 and 4 after each step change in confining pressure. In this way, a set of data, including permeability, porosity and specific storage was obtained for a complete confining pressure cycle for each sample. In our tests, the mean pore pressure was set to be around 14 MPa and the confining pressure was first stepped upward from 20 to 180 MPa and then downward.

The pore pressure oscillation method has been described in detail in previous

publications (*Kranz et al.*, 1990; *Fischer and Paterson*, 1992; *Faulkner and Rutter*, 2000; *Bernabé et al.*, 2006), so only a brief description is given here. A sinusoidal oscillating pressure was applied at the upper end of the sample and the response at the downstream end was recorded (Figure 3.3b). The early transient signal was removed and Fourier analysis was carried out to get the amplitude ratio ($0 < \alpha < 1$) and phase delay ($\theta < 0$) between the upstream and downstream signals. Following *Faulkner and Rutter* (2000), permeability (k) and specific storage (S_s) of the sample can be calculated using an iterative method with α and θ as the input data.

Initial porosity (Φ_0) was obtained on basis of the Boyle-Mariotte theory. The effective pore volume (V_p) of the sample was determined based on the balanced pressure (P_3) obtained by connecting two sealed vessels with known internal volume (V_1, V_2) and pressure (P_1, P_2) (Figure 3.3c). If ideal gas behavior is assumed for the N_2 used, we have $P_1(V_1 + V_p) + P_2V_2 = P_3(V_1 + V_2 + V_p)$, so that V_p can be written as $V_2(P_3 - P_2)/(P_1 - P_3) - V_1$. The volume of V_1 and V_2 were calibrated in advance using a series of hard alloy cylinders with holes of various diameters. Porosity was calculated as $V_p / (V_p + V_{gr})$, where V_{gr} is grain volume assumed to be constant. We made this measurement at different pressures up to 3 MPa, but found no dependence of measured porosity on pressure. This means there can be no significant absorption effect. The average value was taken as the initial porosity. Uncertainty in this measurement is below 0.3 %.

A new approach was developed to determine the porosity change at each step-change in confining pressure. In previous studies, pore volume changes were measured by high-precision volumometers with pore pressure being controlled at a constant value (e.g. *Ko et al.*, 1997). In this study, they were evaluated from the fluid pressure change in a closed system (Figure 3.3d), assuming that the entire volume change represents the pore volume change in the specimen, based on the fact that the compressibility of individual grains is much smaller than the bulk compressibility (*Wibberley and Shimamoto*, 2005). In each run, we first closed valve $\#_1$ and $\#_2$ to obtain a closed system, incorporating the core sample and the pipelines connecting the micro-volumometer and the pressure transducer (Figure 3.3d). Confining pressure was then stepped upward/downward from P_{c_i} to P_{c_f}, resulting in shrinkage/swelling of the sample and thus pressurization/depressurization of the pore fluid from P_{d_i} to P_{d_f}, as measured by the pressure transducer. The pore volume change (ΔV_p) can be calculated by integrating B_d^* over the pore pressure change, that is $\Delta V_p = \int_{P_{d\_i}}^{P_{d\_f}} B_d^* dp$, where B_d^* is the sample storage plus the storage of downstream reservoir (B_d). As the most important parameter in processing the data, B_d was precisely determined using the

specially-designated micro-volumometer, composed of a needle valve and a high precision LVDT displacement transducer (Figure 3.3d).

Specific storage can be gained simultaneously with permeability by the pore pressure oscillation method. However, this method may suffer uncertainties (*Bernabé et al.*, 2004; 2006). Alternatively, in poroelasticity theory, specific storage is related to porosity, fluid (β_f) and mineral compressibility (β_m) and drained bulk framework compressibility (β_b) as follows (*Brace et al.*, 1968),

$$S_s = \beta_b + \Phi\beta_f - (1+\Phi)\beta_m \quad (3.1)$$

With the assumption that β_m is negligible in comparison to that of the sample as a whole, β_b can be approximated by finding the pore volume change per unit effective pressure change, and dividing this by the sample volume at the start of each upward or downward pressurization step. This result was an "averaged" compressibility over the P_c range of the step, which was assumed to represent the β_b at the median P_c of the step (*Wibberley*, 2002).

3.4 Experimental Results

3.4.1 Mineralogical Composition

Mineralogical data obtained for the samples investigated are presented in Table 3.1. XRD analysis identified quartz, dolomite and calcite as major minerals, feldspar as minor mineral. Clay minerals in the samples less than 2 μm in size are composed mainly of mixed layers of illite-smectite (I/S), illite and chlorite, with no detectable smectite. Compared with nearby breccia samples, black and gray gouges are abundant in clay minerals and poor in calcite content, and mixed layers of illite-smectite are the dominant clay mineral with percentage of smectite of 36 - 38 %. The thin black gouge, which is considered having accommodated most of the fault motion, has a composition similar to the gray one, except for a higher quartz and illite content (43 % and 6.6 % vs. 29 % and 1 %, Table 3.1).

Table 3.1. Mineralogical composition of fault rocks collected at various distance from the slip surface

Lithology	Distance	Bulk composition					Clay composition (ref. %)			
	(cm)	Q	Fel	Dol	Cal	Clay	It	I/S	Chl	S%
Coarse breccia	-175 [b]	1%	1%	29%	68%	2%	-	95%	5%	5
Yellow fine breccia	-6	2%	1%	67%	29%	2%	39%	55%	6%	10
Thin black gouge [a]	0	43%	1%	19%	7%	30%	22%	64%	14%	38
Gray gouge	0	29%	2%	27%	7%	35%	3%	83%	14%	36
Yellow fine breccia	4	6%	-	62%	24%	8%	19%	73%	8%	33
Gray coarse breccia	60	43%	33%	-	8%	16%	-	51%	49%	5

[a] *The thin black gouge occurs adjacent to the gray zone, and both of them are taken as the slip zone material.*

[b] *Being negative means on the hanging wall.*

Notation of symbols for minerals are Q for quartz; Fel, feldspar; Cal, calcite; Dol, dolomite; It, illite; I/S, mixed layer of illite and smectite; Chl, chlorite; S%, the percentage of smectite in I/S.

3.4.2 High Velocity Friction Data

All friction data were corrected for friction exerted by the Teflon sleeve against the host gabbro block. This was done using the intercepts determined from a set of experiments performed on the material under various normal stresses of 0.4, 0.7, 1.0, 1.59 and 2.19 MPa (Figure 3.4a). Following the method of *Togo et al.* (2011), the Teflon friction was set to evolve with displacement, linearly increasing from zero to peak friction and then exponentially decreasing to steady-state value. Considering the normal stress did not act on the Teflon-gabbro interface, the friction was inferred to be independent of the normal stress imposed.

The dry tests displayed frictional behavior that has been recognized in numerous previous studies of fault material at seismic slip rates. They are characterized by a peak friction followed by dynamic weakening to a steady-state level (Figure 3.4b and 3.4c). The peak (μ_p) and steady-state (μ_{ss}) friction is around 0.65, 0.07 for the gray gouge (Figure 3.4b), and 0.68, 0.28 for the fault breccia sample (Figure 3.4c). Under the normal stresses investigated, 5 to 8 m displacement is required to achieve steady-state slip. The post-peak slip-weakening curves obtained in our experiments (Figure 3.4b and 3.4c) are similar to previous results for fault gouges (e.g, *Brantut et al.*, 2008), as described in the empirical equations proposed by *Mizoguchi et al.* (2007) or *Di Toro et al.* (2011). These equations are equivalent to one another and only differ in how they define the critical slip-weakening distance (d_c). In our study, d_c is defined following *Mizoguchi et al.* (2007), as the distance over which stress drop reduces to 5% of the initial value,

$$\mu_d = \mu_{ss} + (\mu_p - \mu_{ss}) \exp(\ln(0.05)\, d/d_c) \tag{3.2}$$

Here μ_d is dynamic friction, d is displacement. The Value of μ_p corresponded to the value observed at the peak stress, while μ_{ss} and d_c were determined using the fitting method. The corresponding best fit results for the gouge sample are listed in Table 3.2. The peak and steady-state fiction seem to be only weakly dependent of the normal stress (Figure 3.4e), consistent with previous studies (e.g. *Mizoguchi et al.*, 2007). By contrast, the slip-weakening distance decreases notably with increasing normal stress, which can be fitted empirically by a power law, as labeled in Figure 3.4f.

In the cases of the wet experiments, the natural gouge was characterized by rapid

attainment of steady state, and by little or no dynamic weakening (Figure 3.4b). The steady-state friction was lower than that under dry but otherwise the same conditions. For fault breccia sample, the slip-weakening process is very rapid (Figure 3.4d), with d_c around 0.6 to 2.0 m under the normal stress investigated, much smaller than obtained for the dry samples under the same normal stress (Figure 3.4f). Moreover, no systematic relationship between d_c and normal stress was evident (Figure 3.4f).

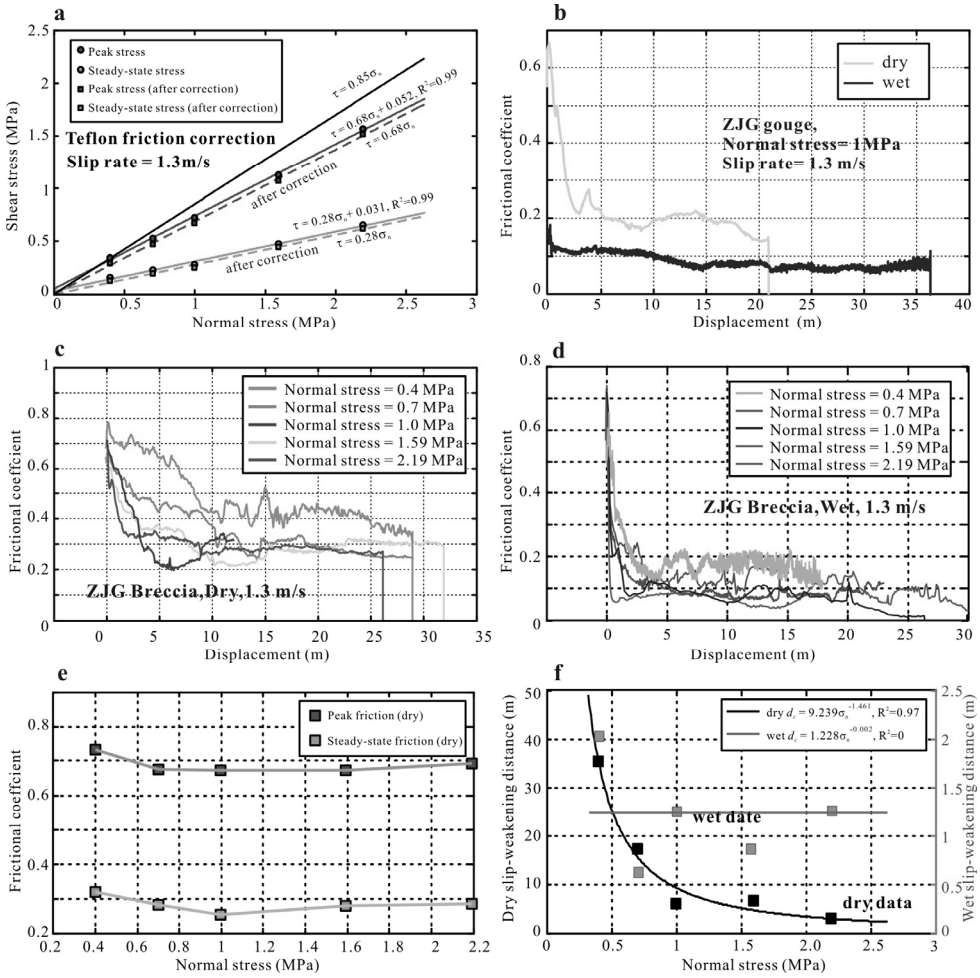

Figure 3.4. High-velocity friction results. (a) An example illustrating Teflon friction corrections by the intercept method; (b) dry and wet friction of the natural fault gouge; (c) dry and (d) wet friction of simulated gouge crushed from the adjacent fault breccia; (e) friction coefficient and (f) slip-weakening distance as function of normal stress for simulated gouge crushed from fault breccia under dry and wet conditions. Data points of (e and f) are derived from (c) and (d).

3.4.3 Transport Property Data

Our logarithmic permeability, porosity and logarithmic specific storage results are plotted against the effective pressure (P_e) in Figure 3.5. The specific storage data is derived from equation (3.1). The permeability curves show a rapid decrease as P_e increases to 165 MPa, while the curves along the downward pressurization path show a slight increase as P_e is reduced from 165 to 30 MPa, followed by a rapid increase as 7 MPa is approached. The permeability of different fault rocks can vary by up to 5 orders of magnitude under the same P_e. The permeability of individual samples can be reduced by 2 to 4 orders of magnitude by an increase in P_e from 7 to 165 MPa. The gray gouge has the lowest permeability (as low as 7.3×10^{-22} m^2 at P_e of 165 MPa) compared with the other fault rocks, which have permeability greater than 1.0×10^{-19} m^2, except for the micro-fractured limestone. The permeability of the country rock (intact limestone) at P_e of ~ 10 MPa is close to the detection level (1.0×10^{-22} m^2) of our experimental configuration, so we did not run a complete P_e-cycling test on it.

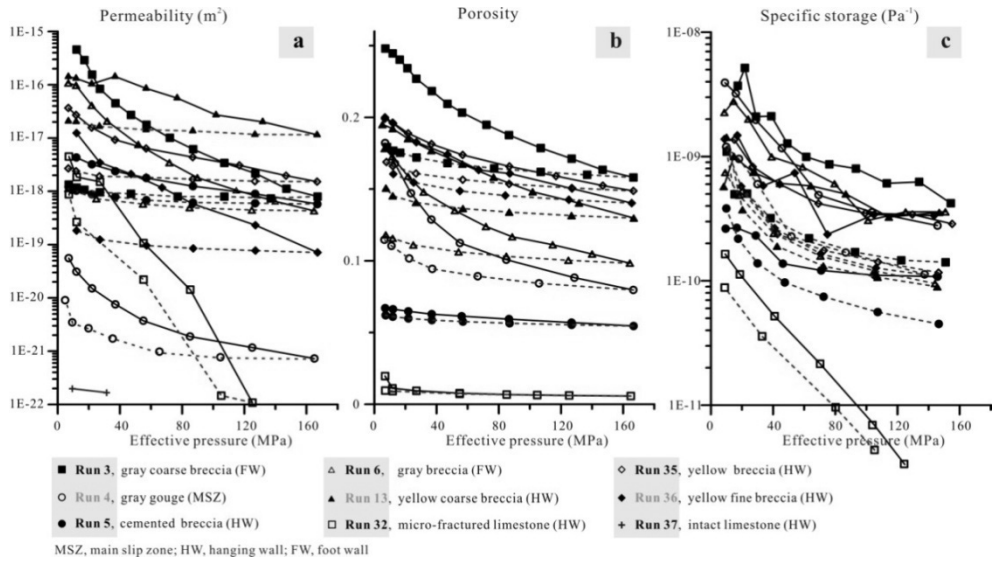

Figure 3.5. Transport property results. (a) Permeability, (b) porosity and (c) specific storage of various fault rocks collected from the ZJG exposure. Solid black and dashed blue lines indicate the upward and downward pressurization paths, respectively. Specific storage is given by using fluid compressibility of 4.3×10^{-10} Pa^{-1} (Fine and Millero, 1973). Results of the hanging wall rocks (Run 4, 13 and 36) are used for numerical modeling and the detailed fitting equations are given in Table 3.2.

Table 3.2. Measured mineralogical, frictional and transport properties of fault rocks for numerical modeling

Parameters	*Sym.*	*Values or functions*	*Units*
		Content of reacting components	
Smectite content of gouge [a]	ω_{sm}	*10.7 %*	*wt. %*
Dolomite content of gouge	ω_{do}	*27 %*	*wt. %*
Smectite content of adjacent fine breccia	ω_{sm}	*1.9 %*	*wt. %*
Dolomite content of adjacent fine breccia	ω_{do}	*62 %*	*wt. %*
Smectite content of coarse breccia	ω_{sm}	*0.4 %*	*wt. %*
Dolomite content of coarse breccia	ω_{do}	*0*	*wt. %*
		Frictional parameters	
Peak friction of dry gouge	μ_p	*0.65*	
Steady-state friction of dry gouge	μ_{ss}	*0.17*	
Slip-weakening distance of dry gouge [b]	d_c	$4.0 \times P_e^{(-1.17)}$	*m*
		Transport properties	
Permeability of fault gouge (Run 4) [c]	k^u	$9.85 \times 10^{-19} P_e^{(-1.3939)}$	m^2
	k^d	$2.31 \times 10^{-20} P_e^{(-0.7189)}$	m^2
Porosity of fault gouge (Run 4)	Φ^u	$0.325\ P_e^{(-0.2661)}$	
	Φ^d	$0.143\ P_e^{(-0.1141)}$	
Compressibility of fault gouge (Run 4)	β_b^u	$5.43 \times 10^{-8} P_e^{(-1.0773)}$	Pa^{-1}
	β_b^d	$1.66 \times 10^{-8} P_e^{(-1.0752)}$	Pa^{-1}
Permeability of adjacent fine breccia (Run 36)	k^u	$7.82 \times 10^{-18} \exp(-0.02829(P_e-1))$	m^2
	k^d	$4.15 \times 10^{-19} P_e^{(-0.3532)}$	m^2
Porosity of adjacent fine breccia (Run 36)	Φ^u	$0.196 \exp(-0.002153(P_e - 1))$	
	Φ^d	$0.182\ P_e^{(-0.05120)}$	
Compressibility of adjacent fine breccia (Run 36)	β_b^u	$4.24 \times 10^{-9} P_e^{(-0.5485)}$	Pa^{-1}
	β_b^d	$6.28 \times 10^{-9} P_e^{(-0.8351)}$	Pa^{-1}
Permeability of coarse breccia (Run 13)	k^u	$1.80 \times 10^{-16} \exp(-0.01642(P_e-1))$	m^2
	k^d	$3.19 \times 10^{-17} P_e^{(-0.1991)}$	m^2
Porosity of coarse breccia (Run 13)	Φ^u	$0.195 \exp(-0.002555(P_e-1))$	
	Φ^d	$0.164\ P_e^{(-0.04571)}$	
Compressibility of coarse breccia (Run 13)	β_b^u	$3.77 \times 10^{-9} P_e^{(-0.5072)}$	Pa^{-1}
	β_b^d	$1.88 \times 10^{-8} P_e^{(-1.2581)}$	Pa^{-1}

[a] *The content of smectite is calculated by multiplying the clay content by the relative content of I/S and by the percentage of smectite (S%) within I/S, with values being given in Table 3.1.*

[b] *Slip-weakening distance (d_c) is extrapolated to the targeted effective stress by a power-decay equation, in which P_e is effective pressure in unit of MPa and the decay coefficient is from yellow breccia sample.*

[c] *Superscript "u" and "d" denote upward and downward pressurization path. The evolution of k as a function of pore*

pressure change (Δp) at a given depth (with initial effective pressure of P_{e0}) is calculated as $k(\Delta p) = k^d(P_{e0} - \Delta p)/k^d(P_{e0}) \times k^u(P_{e0})$ (see explanation in text). Similar formula also applies for the evolution of porosity, $\Phi(\Delta p) = \Phi^d(P_{e0} - \Delta p) - \Phi^d(P_{e0}) + \Phi^u(P_{e0})$. Specific storage is given as $S_s(\Delta p) = \beta_b^d(P_e) + \Phi(P_e)\beta_f - (1 + \Phi(P_e))\beta_m$, where P_e equals to $P_{e0} - \Delta p$. Note that, the equations for transport properties only apply for P_e ranging from 5 to 165 MPa. The properties at low P_e are obtained by extrapolation of low pressure data (5 - 15 MPa) using the exponential law.

Initial porosities (at P_e of 7 MPa) range between 2.1 % and 25 % for the different rocks across the fault zone. Similar to permeability, the fault gouge sample shows rapid decay with increasing P_e (Figure 3.5b). The micro-fractured limestone displays the lowest porosity (0.7 % at P_e of 165 MPa), which is followed by the cemented breccia (5.5 %) and the gray gouge (8.0 %). The specific storage curves are clearly separated between the upward and downward pressurization paths (Figure 3.5c), and the curves are roughly parallel to each other. This results from the bulk framework compressibility (see equation (3.1)), which has much smaller value along the downward pressurization path relative to along the upward one. Initial values of specific storage range between 1.8×10^{-10} Pa^{-1} to 5.3×10^{-9} Pa^{-1}. Most specific storage values fall in the range of 5.0×10^{-11} to 5.0×10^{-9} Pa^{-1}. The fractured limestone shows the highest pressure sensitivity, and its value falls below 1.0×10^{-11} Pa^{-1} under 100 MPa.

Fluid flow simulation requires empirical equations reflecting the relationship between transport properties and depth (or effective pressure). The slopes of all curves become gentler with increasing effective pressure, implying declining pressure sensitivities with depth. To describe this, an exponential law (*David et al.*, 1994) in form of $X = X_0 \exp(-q(P_e - 1))$ and a power law (*Shi and Wang*, 1986) in form of $X = X_0 P_e^{-r}$ have been used to fit these data. Here X represents transport properties such as permeability, porosity and framework compressibility; X_0 is the value at P_e of 1 MPa; q and r are material constants indicating pressure sensitivity. Which relation was adopted for individual materials depends on the goodness of fit. Most of the data in Figure 3.5 do not plot on straight lines described by the exponential law, particularly for the gouge sample, the data of which fits favorably well with the power law, consistent with the previous studies on clay-rich samples (*Shi and Wang*, 1986; *Mizoguchi et al.*, 2008). Fitting results used for modeling are presented in Table 3.2.

3.5 Numerical Analysis of Coseismic Thermochemical Pressurization

During an earthquake, frictional heating generated in the slip zone will induce a temperature rise and thus a pore pressure rise, as well as possible activation of chemical reactions. In the following, we report numerical modeling of the coseismic slip-weakening

process, treating the slip zone as infinite in extent and including thermochemical effects. We use local slip history data for the Wenchuan earthquake and lab friction data to compute the heat source. We use measured *in-situ* transport properties and previous data on reaction rate constants for quantifying the decomposition reactions. Strongly state-dependent thermodynamic properties of pore fluid are also incorporated into our models.

3.5.1 Governing Equations

The coupled equations for energy and fluid mass conservation that govern the coseismic slip process are well established (*Lachenbruch*, 1980; *Noda and Shimamoto*, 2005; *Rice et al.*, 2006). Coseismic chemical reactions have also recently been incorporated (*Sulem and Famin*, 2009; *Tanikawa et al.*, 2009; *Brantut et al.*, 2010), yielding the following description of this highly-coupled system:

$$\frac{\partial T}{\partial t} = \frac{K}{\rho c}\frac{\partial^2 T}{\partial x^2} + \frac{Q_{so}}{\rho c} + \frac{Q_{si}}{\rho c} \tag{3.3}$$

$$\frac{\partial p}{\partial t} = \frac{1}{S_s}\left(\frac{\partial}{\partial x}\left(\frac{k}{\eta}\frac{\partial p}{\partial x}\right)\right) + \frac{\phi(\alpha_f - \alpha_m)}{S_s}\frac{\partial T}{\partial t} + \frac{\Omega_{de}}{S_s} \tag{3.4}$$

In equation (3.3), T is temperature, t is time, K is thermal conductivity, ρ is bulk density, c is specific heat capacity, Q_{so} is the heat source per unit volume generated by frictional heating, and Q_{si} is the heat sink per unit volume by chemical reactions. In equation (3.4), p is pore pressure, k, Φ and S_s are intrinsic permeability, porosity and specific storage, respectively. Further, η is dynamic viscosity of fluid, α_f and α_m are the thermal expansivities of the fluid and individual grains, respectively, and Ω_{de} is fluid generation rate per unit volume by chemical reactions.

The symbols, their definitions and corresponding values of variables involved are listed in Table 3.2 and Table 3.3. Important points in relation to the governing equation are stated below:

(1) Frictional work done by an earthquake can be distributed amongst frictional heating (*Rice*, 2006), chemical reactions (e.g. *Hamada et al.*, 2009) and grain comminution (*Ma et al.*, 2006). In the absence of appropriate fracture energy data, only the former two facts are considered in our modeling. Uniform shearing rate within a slip band is assumed and the heat production rate is then given by

$$Q_{so} = \tau\dot{\gamma} = \mu_d(\sigma_n - \overline{p})\frac{V}{W} \tag{3.5}$$

where $\dot{\gamma}$ is shear rate, V is slip velocity and W is thickness of slip band. As pointed out by *Sulem et al.* (2007), the gradient of shear resistance (τ) induced by coseismic slip acceleration is relatively small (in orders of 10^{-2} MPa/m), so the variation of τ within a slip band can be neglected and mechanical equilibrium can be assumed. The shear resistance is thus taken as linearly proportional to the mean effective normal stress ($\sigma_n - \overline{p}$) inside the slip band (*Sulem et al.*, 2007; *Brantut et al.*, 2010), and set to be zero for overshooting cases ($\overline{p} > \sigma_n$). The heat consumed by chemical reactions is expressed as

$$Q_{si} = \sum \frac{\omega(1-\phi)\rho_s \Delta H}{M} \frac{\partial \xi}{\partial t} \tag{3.6}$$

Here $\sum$ represents summation of all involved reactions. The term ΔH represents the molar enthalpy change of reaction (KJ mol^{-1}) and is negative when endothermic, ω and M are the wt. % content and molar mass of the reactant contained in the gouge sample, ρ_s is the average density of solid minerals, ξ is the accumulative reacted mass fraction of the reactant through time and its time derivative $\partial\xi/\partial t$ expresses the reaction kinetics.

(2) Besides thermal effects, some chemical reactions influence evolution of pore pressure by fluid mass production through dehydration or decarbonation ($\Omega_{de} = \Omega_{dehy} + \Omega_{decar}$). Reactions can also involve volume change in the solid phases. For example, dehydration of smectite can produce a solid volume reduction up to 47 % (*Vrolijk and van der Pluijm*, 1999). Such reduction is associated with lattice collapse and is expected to yield porosity change in bulk rocks (*Wong et al.*, 1997). Assuming 1 mol hydrate converts to 1 mol dehydrate, losing χ mol water and producing a volume reduction in solid phase ΔV, the effective fluid generation rate can be expressed as,

$$\Omega_{de} = \sum \omega(1-\phi)\left(\frac{\chi M_{H_2O}}{M_{hy}} \frac{\rho_s}{\rho_f} - \Delta V\right) \frac{\partial \xi}{\partial t} \tag{3.7}$$

where M_{H_2O} and M_{hy} are the molar masses of the pore fluid (H_2O) and the hydrous mineral, respectively, and ρ_f is the density of the pore fluid. In this expression, evolutional porosity is considered. Aside from this, such an expression is similar to that proposed by *Brantut et al.* (2010) for a general chemical reaction. Except for the coupled thermal effect, equation (3.4) is similar to the equation of *Wong et al.* (1997) for dehydration system. The decarbonation reaction is treated in a similar way, giving an effective fluid release rate,

$$\Omega_{decar} = \sum \omega(1-\Phi)\left(\frac{\chi M_{CO_2}}{M_{car}} \frac{\rho_s}{\rho_{CO_2}} - \Delta V\right) \frac{\partial \xi}{\partial t} \tag{3.8}$$

where M_{CO_2} / M_{car} is ratio between the molar mass of CO_2 and the carbonate minerals, and ρ_{CO2} is the density of CO_2 in fluid phase (Figure 3.A1). Note that once CO_2 is generated, the pore fluid will become a CO_2-H_2O binary system. In our modeling, we treated the CO_2 and H_2O phases separately, since volumetric contraction due to mixing is only a few percents, according to the model given by *Hu et al.* (2007). The effect of the increased density of the mixture was simulated by adjusting ΔV in equation (3.8). In addition, dynamic dilatancy due to fault surface irregularities or damage production can cause an instantaneous rise in porosity (*Samuelson et al.*, 2009). However, this effect is expected to be most marked at the early stage of slip and can be simulated by reducing ambient pore pressure (*Rice et al.*, 2006).

(3) Various chemical reactions have been reported to have occurred during fault motion, including dehydration, dehydroxylation, metamorphic transformation of clay minerals (e.g. *Hirono et al.*, 2008), decomposition of organic material (*Ikehara et al.*, 2007) and carbonate minerals (*Smith et al.*, 2011). The kinetics of chemical reactions is commonly expressed by relations of the form

$$\partial\xi / \partial t = f(\xi)\kappa(T) \tag{3.9}$$

where $f(\xi)$ is kinetic function determined by the active reaction mechanism (Table 3.3). Temperature dependent reaction rate is adopted following an Arrhenius law, $\kappa(T) = A\exp(-E_a/RT)$, where A is the rate constant (s^{-1}), E_a is the activation energy for the reaction ($KJmol^{-1}$) and R is gas constant (8.31 $JK^{-1}mol^{-1}$). The effect of pressure and fluid chemistry on reaction kinetics is neglected because no data are available.

3.5.2 Representative Parameter Values

Only the parameters to which the model is particularly sensitive are discussed here. Reaction kinetics determines to what extent a reaction can occur in a given time. Mineralogical analysis revealed abundant smectite-rich I/S in the gouge sample. As a candidate for dehydration, smectite contained in I/S is treated chemically the same as pure smectite, which, unless otherwise stated, is assumed to carry one interlayer of H_2O in the unit lattice cell. Losing it can cause a volume reduction of 19.4 %, dictated by the change of basal spacing (d_{001}) from the hydrated to dehydrated state (d_{001} are 100 and 124 nm, respectively; *Huang et al.*, (1994)). The reactions of smectite dehydroxylation and transformation from dehydrated smectite to illite are assumed to cause no solid volume change, considering tiny difference in their densities (Table 3.3). A first-order kinetic function is adopted for

dehydration and dehydroxylation, $f(\xi) = 1 - \xi$ (*Bray and Redfern*, 1999). Since both the solid and solution phases are involved in the reaction of smectite-to-illite transformation (e.g. uptake of K^+ from aqueous phase), the kinetic law is complex and expressed as $-dS/dt = \bar{A}\exp(-E_a/RT)(K^+)S^2$ (*Huang et al.*, 1993), where S is relative molar fraction of smectite in the I/S, $\bar{A}$ is the frequency factor given as 8.08×10^{-4} $s^{-1}M^{-1}$ and (K^+) is concentration of potassium (M) present in aqueous solution. To express uniformly as a function of ξ as equation (3.9), S is substituted by $S_0(1-\xi)$, where S_0 is the initial relative molar fraction of smectite. This gives $f(\xi) = (1-\xi)^2$ and $A = \bar{A}(K^+)S_0$. In our modeling, S_0 is 36 % from the mineralogical results (Table 3.1) and (K^+) is 5.4×10^{-2} M, as measured for the interstitial fluid chemistry of the Triassic Xujiahe group at ~ 2016 m depth in Wusheng, Sichuan by *Zhou* (1993). Substituting these values into the expression of A gives a value of 1.57×10^{-5} s^{-1}. Besides I/S changes, XRD analysis also identified dolomite as a major mineral. Dolomite begins to decompose at 550 °C (*Han et al.*, 2007), and the products are Ca-calcite + periclase or lime + periclase (*De Paola et al.*, 2011). In view of the high content of dolomite and the large temperature buffering effect of the endothermic process of decarbonation reaction (*Sulem and Famin*, 2009; *Brantut et al.*, 2011), decarbonation in our study is taken as referring in particular to the reaction $CaMg(CO_3)_2 \rightarrow CaCO_3 + MgO + CO_2$. The kinetic function used is $f(\xi) = (1 - \xi)^{2/3}$ (*Criado et al.*, 1995) and ΔV is assumed to be 24 % on basis of the mass reduction in solid phases. All reactions involved and related kinetic parameters are summarized in Table 3.3.

Table 3.3. Kinetic models and parameters of reactions involved in this study [a]

Reactions	$f(\xi)$	ΔH	A	E_a	χ	ΔV	References
Dehydration of smectite	$1 - \xi$	-43	553	32.2	2	19.4	*Bray and Redfern* (1999); *Noyan et al.* (2008)
Dehydroxylation of smectite	$1 - \xi$	-132	8.8	50.7	1	0	*Tanikawa et al.* (2009); *Noyan et al.* (2008)
Smectite-to-illite transformation *	$(1- \xi)^2$	-100	1.57×10^{-5}	117.2	0	0	*Huang et al.* (1993); *Brantut et al.*(2010); *Zhou* (1993)
Decarbonation of dolomite	$(1 - \xi)^{2/3}$	-178	2.68×10^{7}	187	1	24.0	*Criado et al.* (1995)

[a] *ξ, the reacted fraction; $f(\xi)$, the reaction function; ΔH, molar enthalpy change of the reaction in unit of KJ mol^{-1}; A, the reaction rate constant in unit of s^{-1}; E_a, the activation energy in unit of KJ mol^{-1}; χ, the mole number of fluid that could be lost by a certain reaction for 1 mole reactant; ΔV, solid volume reduction (%) caused by the reaction.*

Frictional and transport properties of the fault gouge are further key parameters deciding the TP effect (*Wibberley and Shimamoto*, 2005). Dynamic friction is set to evolve with displacement following the laboratory-derived empirical equations for dry samples presented in Table 3.2. In doing this, it is assumed that no significant TP effect occurred in our dry experiments (*Tanikawa et al.*, 2012). This is later supported by numerical modeling of our high-velocity experiments (section 3.6.2). The applied normal stress in our friction experiments was much lower than the effective normal stress expected *in-situ* during fault motion, which on the basis of previous modeling studies (*Tanikawa et al.*, 2009) is thought to lie in the range from initial effective pressure to a nearly unconfined condition. Fortunately, the peak and steady-state friction are not sensitive to normal stress in the range investigated here (Figure 3.4e). Also, as a first-order estimate, the slip-weakening distance can be extrapolated to high normal stress using the decay equation given in Table 3.2, while for low normal stress (< 0.4 MPa), it is set to be constant. Transport properties, including permeability and porosity are set as function of effective pressure (P_e) as in Table 3.2. We took the dependences on increasing and decreasing pressure from our results (Figure 3.5), assuming that the sensitivity of these quantities to decreasing P_e from the initial P_e value imposed is independent of that value. Previous P_e-cycling experiments (*Faulkner and Ruther*, 2000; *Noda and Shimamoto*, 2005) have shown that this is a reasonable assumption. Specific storages derived from the depressurization curves (the dashed lines in Figure 3.5c) were used, considering similar evolutional trend in effective pressure for a TP process (*Wibberley and Shimamoto*, 2005). See detailed expressions of these properties at a given depth in the notation of Table 3.2. Note that the dynamic friction data were obtained under constant normal stress (without confinement) and the transport property data were obtained under hydrostatic loading (without non-hydrostatic loading), therefore the stress states do not exactly correspond to one another or to the in-situ condition investigated in our modeling. Of course, each set of the data by itself is quite relevant to the problem at hand.

The rate of fluid transport out of the fault zone is also dependent on the evolution of pressure and temperature (PT) through changes in fluid properties. For example, with increasing temperature, pore fluid becomes less viscous, facilitating fluid transportation. In fact, the PT conditions during faulting can vary over a large range, and the pore fluid may even undergo phase changes (*Tanikawa et al.*, 2009; *Sulem and Famin*, 2009) as well as changes in gas phase solubility (*Sabirzyanov et al.*, 2003). The fluid properties can correspondingly undergo large changes (Figure 3.A1). To model the *in-situ* situation more realistically, state-dependent fluid properties (SDFP), i.e. density, compressibility, thermal expansivity and viscosity, are introduced. These properties are interpolated as functions of

PT and from the basic thermophysical properties database of water (see Appendix 3.A for details). The values of specific heat capacity and thermal conductivity are from *Tanaka et al.* (2006) (Table 3.4).

Table 3.4. Parameters used in the modeling

Parameter	Symbol	Value [a]	Units	Reference
Slip velocity	V	SH	ms^{-2}	*Zhang et al.* (2009)
Time span of slip	t_s	22	s	*Zhang et al.* (2009)
Slip band thickness	W	20 (0.3 - 20)	mm	Measurement in this study
Specific heat capacity	c	800	$Jkg^{-1}K^{-1}$	*Tanaka et al.* (2006)
Heat conductivity	K	2	$Wm^{-1}K^{-1}$	*Tanaka et al.* (2006)
Thermal gradient	dT/dz	21	$°Ckm^{-1}$	*Mori* (2010)
Bulk density	ρ	2.5×10^3	kgm^{-3}	Measurement in this study
Solids density	ρ_s	2.7×10^3	kgm^{-3}	Measurement in this study
Fluid density	ρ_f	SDFP (or 1.0×10^3)	kgm^{-3}	NIST
Dynamic viscosity	η	SDFP (or 1.26×10^{-4})	Pas	NIST (or *Rice* (2006))
Thermal expansivity of fluid	α_f	SDFP (or 5.0×10^{-4})	K^{-1}	NIST (or *Fine and Millero* (1973))
Compressibility of fluid	β_f	SDFP (or 4.3×10^{-10})	Pa^{-1}	NIST (or *Fine and Millero* (1973))
Thermal expansivity of grains [b]	α_m	2.2×10^{-5}	K^{-1}	*Bayer* (1973)
Compressibility of grains [c]	β_m	1.2×10^{-11}	Pa^{-1}	*Birch* (1966)
Hydro-/lithostatic pressure	λ	0.4 (0.1- 0.5)		

[a] *Values in brackets are used for parametric analysis. SH, from inferred slip history by seismological inversion; SDFP, state-dependent fluid properties (Appendix 3.A); NIST, from website http://webbook.nist.gov/chemistry/fluid/*

[b] *The coefficient of thermal expansivity of quartz was used in place of that of the minerals contained in fault rocks.*

[c] *The compressibility of mica was used in place of that of the minerals contained in fault rocks.*

3.5.3 Modeling Strategy

A laterally infinite and homogeneous, plate-like planar fault model is used, assuming that all quantities, including frictional and hydraulic properties of the fault rocks, change only in the direction normal to the fault plane. In accordance with the real fault structure (Figure 3.2c), a symmetric geometrical model is constructed, consisting of the central fault gouge (2 cm-thick), the adjacent fine breccia zones (9 cm-thick for each side) and the coarse breccia zones (40 cm-thick for each side) outside. As illustrated in Figure 3.6f, the geometrical model is meshed into 608 elements in total, 32 of which occupy the gouge zone.

Boundary and initial conditions are set as below. We take zero-flux boundaries for the fluid and temperature fields. The fault model is sufficiently wide to be "infinite" relative to

the temperature and fluid fields, with respect to the time span investigated. Uniform hydrostatic initial condition, unless otherwise stated, is assumed by letting λ (the ratio of pore pressure to lithostatic pressure) to be 0.4. Uniform initial temperature is assigned on basis of the local geothermal gradient (Table 3.4). As shown in Figure 3.2c and 3.2d, two kinds of gouge occur in the fault center, the gray gouge and the thin black gouge. Mineralogical and chemical analyses (*Chen et al.*, 2013a, Chapter 2) have revealed the black gouge to be the material having accommodated most of the coseismic displacement and having formed from the gray gouge. Therefore, the gray gouge is taken as the initial material before the Wenchuan earthquake. Initial mineral composition of the gray gouge, the fine and coarse breccia zone is set according to the XRD data for these materials (Table 3.2).

The slip history computed from wave shape inversion of seismological data (*Zhang et al.*, 2009) is used to specify the heat source. The nearest inversion result is 3.8 km northeast of the exposure studied. The subsurface slip history is extrapolated from the data for 3.1 km depth, constraining the total displacement to be equal to that measured at the surface by geological surveying (Figure 3.1c). The slip histories at various depths were linearly interpolated from the curves given in Figure 3.1e. Our modeling addresses a time interval totaling 2500 s from the onset of the slip. In accordance with the real slip history (Figure 3.1e), the time step is set to be 0.05 s in the first 25 s (coseismic stage) and is then changed to 0.5 s for the post-seismic stage.

The coupled partial differential equations (PDEs) describing energy balance, fluid mass transport and chemical reactions are solved using the finite element software-Comsol (version 3.5), solving simultaneously for all dependent variables including pore pressure (p), temperature (T) and normalized chemical concentrations (ξ). In other words, all these variables are iterated sequentially until the accumulated (global) error meets both the relative and absolute tolerations represented by the error in each time step. The mean pore pressure inside the slip ($\overline{p}$) has also been taken into the iteration. In each iteration step, it is calculated by integrating the pore pressure over the slip band width and dividing it by the width of the slip band. Nonlinear parameters, i.e. permeability, porosity, specific storage, friction, d_c and reaction constants, are taken into the iteration procedure as well. Finally, the linear equations (in form of $Ax=b$) assembled from all the coupled PDEs and boundary conditions are solved using a linear-system solver (UMFPACK), which uses the nonsymmetric-pattern multifrontal method and direct LU factorization of the sparse matrix A.

3.5.4 Numerical Results

Our modeling approaches calculate the evolution of pore pressure, temperature and reactant concentration through time as a function of distance from the slip surface. Dynamic friction and dynamic shear stress are computed versus displacement. The weakening efficiency ($\mu_d(\sigma_n - \overline{p})/\mu_p(\sigma_n - p_0)$), defined as dynamic shear stress divided by initial shear resistance, depends on the evolution of both the friction and the mean pore pressure inside the slip zone. Evolution of the latter is further controlled by the interplay between thermal pressurization of fluid trapped in pores, fluid mass liberation from reactions and fluid loss by drainage from the heated zone, whereupon we evaluate the contribution of these terms of $\frac{\phi(\alpha_f - \alpha_s)}{S_s}\frac{\partial T}{\partial t}$, $\frac{\Omega_{de}}{S_s}$ and $\frac{1}{S_s}(\frac{k}{\eta}\frac{\partial^2 p}{\partial x^2})$ separately. To understand energy partitioning during fault motion, heat production by friction ($Q_{so}/\rho c$), heat consumption by endothermic reactions ($Q_{si}/\rho c$) and thermal diffusion ($\frac{K}{\rho c}\frac{\partial^2 T}{\partial x^2}$) are evaluated also. The time integral of each term is computed as well. To illustrate the interplay between frictional heating and fluid pressurization, local pore pressure at the slip surface are plotted against temperature (referred to as p-T curve). Representative results are presented in the following (Figure 3.6).

3.5.4.1 The Reference Case

First, we show results of the reference case (referred to as "*Ref*"), in which slip is evenly distributed in a 20 mm-thick gouge zone located at 3 km depth, with ambient temperature of 83 °C, confining pressure of 75 MPa and initial pore pressure of 30 MPa. Other parameters are as for the representative values set in section 3.5.2. Allowing for two stages of slip, a total displacement of 5.6 m was achieved in 22 s (Figure 3.6a). The shear stress first drops from 29.3 to 16 MPa in the pre-slip stage and then further to 1.1 MPa by the end of the slip (Figure 3.6b). The shear stress continues to decay when the friction attains steady state (Figure 3.6b), suggesting involvement of extra weakening mechanism besides frictional weakening of the fault material. By the end of the slip, the maximum temperature on the slip surface reaches 431 °C (Figure 3.6c). The pore pressure closely approaches the lithostatic pressure, but it decays rapidly away from the slip surface (Figure 3.6d). Smectite contained in the gouge has fully lost its interlayer water by the end of the slip (see the curve for material at 10 mm away from the slip surface in Figure 3.6e) and dehydroxylation occurs to a limited degree. Snapshots of the fluid pressure and temperature fields in time are also presented (Figure 3.6f and 3.6g). The shape of the pore pressure profiles versus distance from the slip surface is sharper than that for the temperature field, suggesting lower

efficiency in fluid diffusion than heat transport. Our calculations further show that the pore pressure builds up mostly due to the TP effect (Figure 3.6h). Dehydration of smectite yields a pore pressure rise of ~ 6 MPa, while fluid diffusion away from the slip zone is almost negligible (Figure 3.6h). In energy partitioning, reactions and heat diffusion only take up a negligible portion of the frictional work produced by the earthquake, and diffusion begins to become significant effect to dictate the temperature evolution after the earthquake (Figure 3.6i).

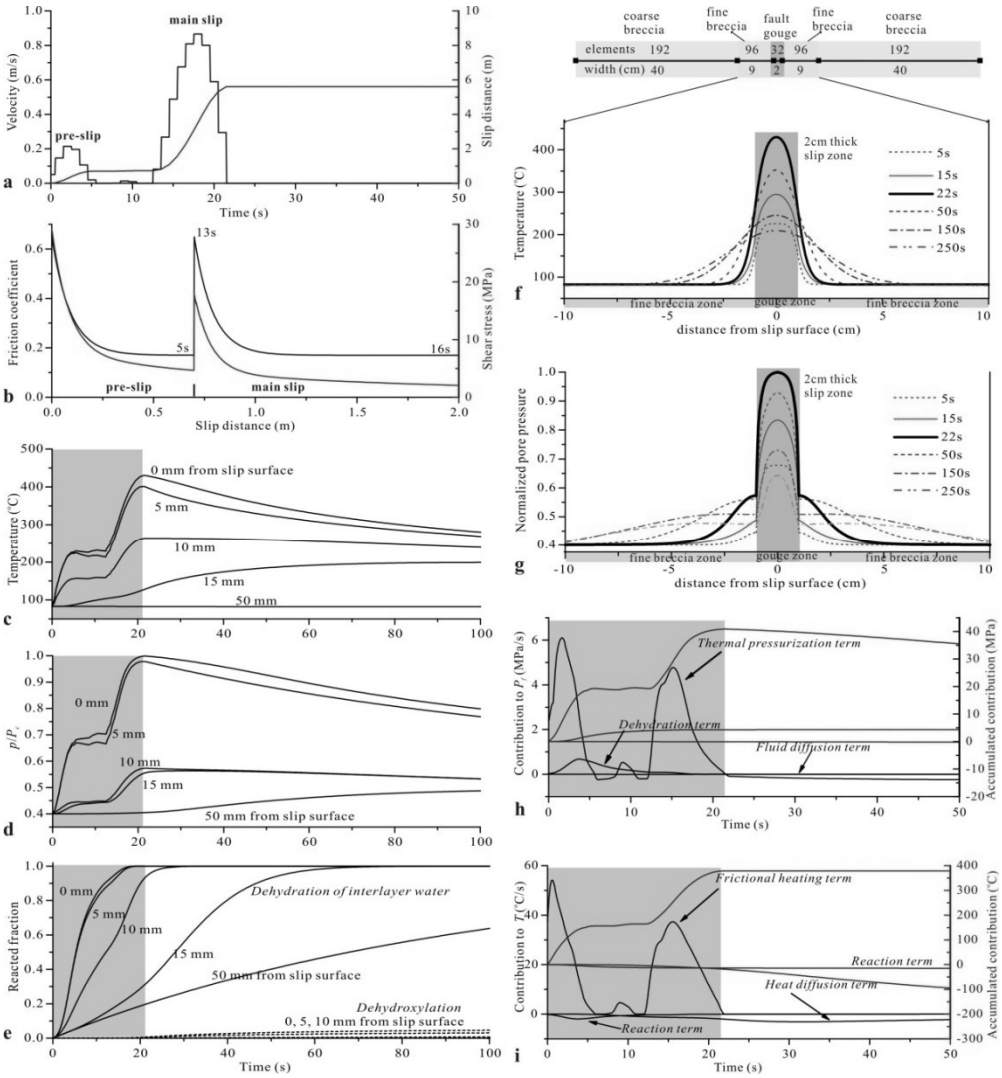

Figure 3.6. Modeling results of the reference case ("Ref"). (a) slip velocity and accumulated displacement with time; (b) the evolution of friction coefficient and shear stress as slip distance; the evolution of (c) temperature, (d) normalized pore pressure and (e) reacted fraction of reactants with time at various distances from slip surface; snapshots of the distribution of (f) temperature and (g) normalized pore pressure across the fault core; (h) contribution to the temperature rise by thermal pressurization, dehydration and diffusion, respectively; (i) contribution to the pore pressure build-up by thermal pressurization, dehydration and diffusion, respectively. The conditions implied in "Ref" are explained in the text. The shaded areas in (c), (d), (e), (h) and (j) denote the time span of the Wenchuan earthquake, and those in (f) and (g) represent the gouge zone. Simulations are performed on the fault model consisting of the central gouge zone, the fine breccia zone and the coarse breccia zone (upper panel of f). To show details at the central portion, the temperature and pore pressure profiles presented (f and g) only include the gouge zone and the fine breccia zone.

3.5.4.2 Effects of Chemical Reactions

In order to gain an insight of the potential effect of chemical reactions in the framework of a rapid slip event on a fault, we model the following cases: 1) the reference case without chemical reactions; 2) the reference case but without considering solid volume reduction due to reaction; 3) the reference case without thermal pressurization. These cases are referred to as "*Ref* || *no_react*", "*Ref* ||ΔV_0", "*Ref* || *no_TP*", respectively. The p-T curve of "*Ref* || *no_react*" is similar to that of the standard *"Ref"* case (Figure 3.7). If "ΔV_0" is assumed, the maximum temperature is reduced by 49 °C in comparison with that reached in *"Ref"*. The p-T curve of "*Ref* || ΔV_0" exhibits a rapid increase in pore pressure at the very first stage of slip. Due to rapid reduction in effective normal stress, the fault becomes weaker, i.e. the shear stress is 3 MPa smaller than for *"Ref"* after the pre-slip. In case of "*Ref* || *no_TP*", excess pore pressure can only be generated by reactions. As shown in Figure 3.7, dehydration of smectite first causes a pore pressure rise of 6 MPa. As the temperature approaches ~ 600 °C, dolomite starts to decompose, resulting in a rapid build-up of pore pressure until it significantly exceeds the lithostatic pressure. The ultimate temperature rise is limited to sit below 897 °C. This shows that in our study chemical reactions can limit temperature rise, not so much because they are endothermic, but because of the release of fluid which causes reduction in effective normal stress.

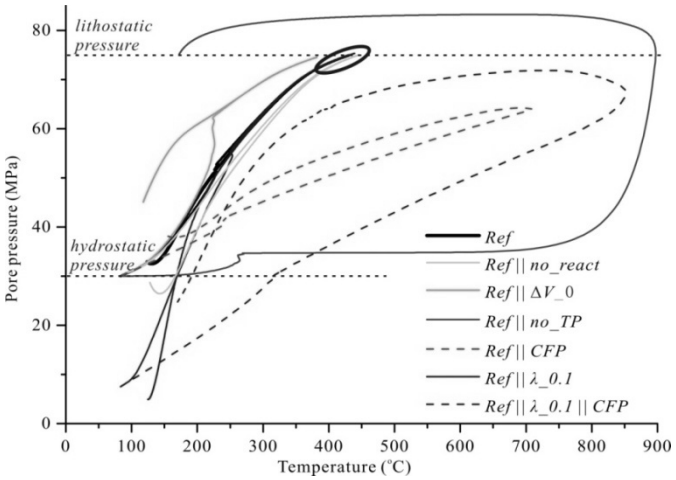

Figure 3.7. The computed p-T curves at the slip center in different cases. "Ref", reference case; "Ref || no_TP", reference case without thermal pressurization; "Ref || no_react", reference case without chemical reactions; "Ref || ΔV_0", reference case without considering solid volume reduction due to reaction; "Ref || CFP", reference case but using constant fluid properties (CFP); "Ref || λ_0.1", reference case except for λ of 0.1 being used; "Ref || λ_0.1 || CFP", reference case but using CFP and λ of 0.1.

A chemical reaction can only occur to a significant extent after sufficient temperature rise causes adequate thermal activation of the reaction rate. To allow for extensive occurrence of reactions, we investigated the case "*Ref || λ_0.1 || CFP*", where "*CFP*" signifies constant fluid properties. As discussed in section 3.6.3, low λ-value and the use of CFP mean more frictional heat can be produced. Here, in this case, a maximum temperature of 872 °C is achieved (Figure 3.7). Despite full dehydration of smectite, dehydroxylation of smectite and decarbonation of dolomite occur to extents of 71 % and 34 %, respectively (Figure 3.8a). These chemical reactions cause a pore pressure rise of as much as 18 MPa, compared with 46 MPa by thermal pressurization (Figure 3.8b). In terms of energy partitioning, the energy taken up by these endothermic reactions is also comparable with that by diffusion (Figure 3.8c). As shown in Figure 3.7, the p-T curves of "*Ref || λ_0.1 || CFP*" and "*Ref || no_TP*" are characterized by a distinct hysteresis signature, that is, the depressurization curves are well above the pressurization curves. We infer this is caused by extra fluid mass released by chemical reactions. Since the reactions involved are all irreversible, they will not stop until the temperature falls below the threshold or all the reactants are consumed. This means that even though fluid pressurization becomes fully efficient so that no frictional heating can be produced any more, the de-watering or

de-gassing reactions will continuously provide fluid mass to the pore space, causing a prolonged increase of pore pressure. We emphasize that chemical reactions can help overshoot the normal stress acting on the fault plane, and that such overshooting is impossible to occur in cases with TP only. That is because frictional heating will stop only if the pore pressure reaches the lithostatic pressure. In this sense, TP can only lead to pore pressure closely approaching the lithostatic pressure, but never exceeding it. Note that once overshoot occurs, the equation used for fluid flow cannot accurately describe the system any longer because of possible non-Darcy flow.

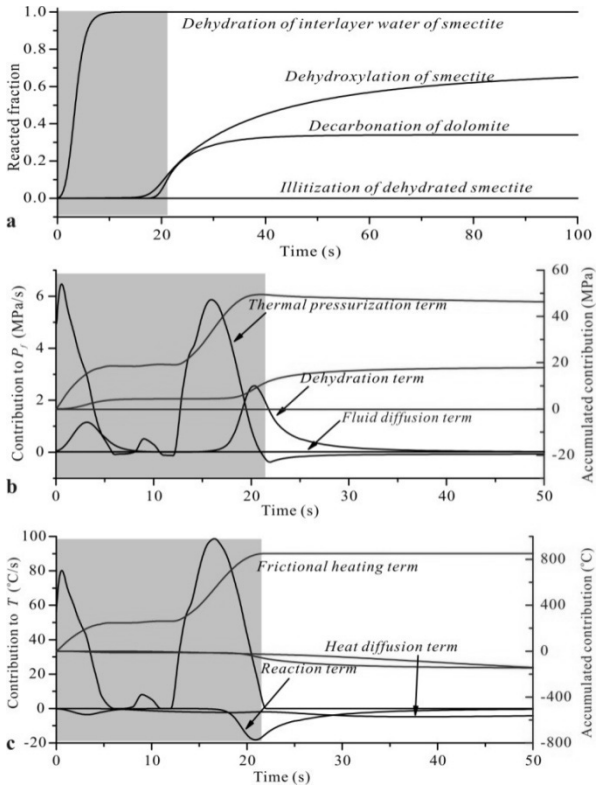

Figure 3.8. Modeling results of a case with extensive chemical reactions. (a) The evolution of reacted fraction of different reacting substances with time; (b) the pore pressure and (c) energy partitioning along with time. The results are from the case of "Ref || λ_0.1 || CFP". The shaded areas denote the time span of the Wenchuan earthquake.

3.5.4.3 Effect of Initial Pore Pressure

The initial pore pressure inside fault zone can vary greatly at depth. In order to test its influence on TP efficiency, we conducted modeling with λ-values of 0.1, 0.2, 0.3 and 0.5

(referred to as "*Ref* || *λ_0.1*", "*Ref* || *λ_0.2*", "*Ref* || *λ_0.3*" and "*Ref* || *λ_0.5*"). Larger temperature rise is expected for lower λ-value, because more energy is required to build up pore pressure to reach the overpressured condition under which frictional heating stops. However, the modeling results unexpectedly show that the p-T curves for various λ cases gradually converge as slip progresses (as marked in an ellipse in Figure 3.7). The maximum temperatures exhibit subtle increase from 425 to 439 °C when λ decreases from 0.5 to 0.1. We infer this strongly relates to the introduction of state-dependent fluid properties (SDFP). Actually when CFP is used, as shown in Figure 3.7, a prominent difference will be produced for various λ-values (compare "*Ref* || *CFP*" and "*Ref* || *λ_0.1* || *CFP*"). Considering the limited contribution by diffusion and reaction (Figure 3.6h), the slope of the p-T curve can roughly represent the coefficient of thermal pressurization of the system (Λ), expressed as (α_f - α_m)Φ/S_s. Because α_f tends to decrease with pressure in low temperature regime (Figure 3.A1), higher TP efficiency should be expected for smaller λ-values. As slip continues, the difference of pore pressure in various λ cases will get smaller and smaller until Λ become identical to each other.

3.5.4.4 Effect of Slip Band Thickness

Field observations (Figure 3.2c) in combination with microscopic analysis on the natural and lab-sheared gouges suggested that coseismic slip might be localized (Figure 3.2c and 3.2e). Candidate values of the slip band thickness, W, are 20 mm if slip was distributed evenly in the entire gouge zone, and ~ 7 mm if to represent the black gouge, and $W < 1$ mm to represent the micro-scale localization. Therefore, the effect of slip band thickness, ranging from 0.3 to 20 mm has been investigated (Figure 3.9). We let slip be localized at one margin of the gouge zone (Figure 3.10a) resembling the real fault structure (Figure 3.2c and 3.2e), and the mesh grid was refined to make sure more than 12 elements occupied the localized shear band. Due to the asymmetric distribution of transport properties relative to the shear band, the pore pressure exhibits asymmetric profiles (Figure 3.10a). The breccia zone directly in contact with the shear band has higher pore pressure compared with the other side. This is in agreement with a previous study investigating the influence of asymmetric permeability structure on fluid pressurization in response to frictional heating (*Vredevoogd et al.*, 2007). In the case of a 7 mm-thick slip band, the effect of "localization" is not conspicuous, producing a p-T curve similar to that of the "*Ref*" case. In contrast, the case of "*Ref || 0.5 mm-thick slip band*" exhibits much higher temperature and pore pressure increase, and the p-T curve thus differs strongly from that of the "*Ref*" case. Varying W (Figure 3.9) indicates that if the slip band is thicker than 2 mm, the maximum temperature achieved falls

in a small range, i.e. from 431 to 471 °C. On the other hand, if W is smaller than 1 mm, the temperature rise is very sensitive to W (Figure 3.9). In other words, there exists a critical slip band thickness, W_{cr}, above and below which the TP shows contrasting behavior. This suggests that the variation in W can dramatically affect the overall efficiency of TP, and hence lead to significant heterogeneity in the degree and rate of slip-weakening along the fault plane.

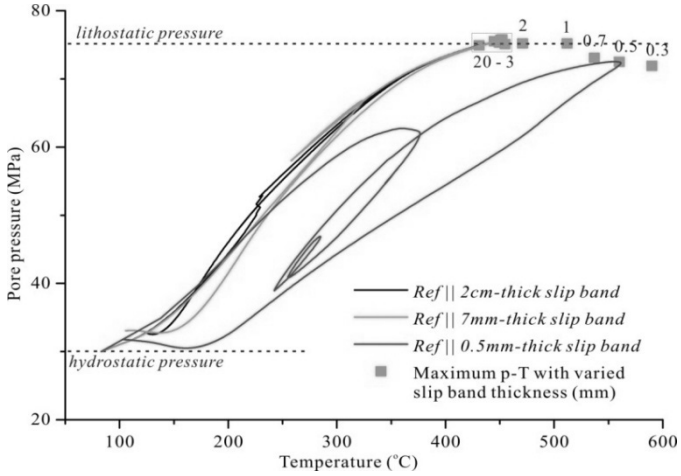

Figure 3.9. The computed p-T curves at the slip center in cases of slip localization.

Theoretical studies suggest that TP efficiency depends strongly on the rate of propagation of the slip-induced fluid pressure pulse relative to the slip displacement (*Lachenbruch*, 1980; *Mase and Smith*, 1985). The characteristic length of hydraulic diffusion during an earthquake L_f is $(t_s k/(\eta S_s))^{1/2}$, where t_s is time span of an earthquake. According to our measurements, the gouge sample has a permeability of 1.0×10^{-21} m^2 and specific storage of 4.0×10^{-10} Pa^{-1} at 3km depth. Substituting these values into the above formula gives an L_f of 0.66 mm. The W_{cr} value obtained (1 - 2 mm) is coincidently equal to ~ 2 times of L_f. If the shear band is thinner than W_{cr}, loss of pressurized fluid out from the heated zone can no longer be neglected. Temperature rise within the shear band is thus facilitated by more efficient fluid escape. As shown in Figure 3.10b, for a 0.5 mm-thick shear band, the evolution of pore pressure is controlled by competition between TP and fluid diffusion outside the shear band (Figure 3.10b). Likewise, for the temperature field, heat transport almost balances frictional heating (Figure 3.10c). By contrast, if W is much larger than W_{cr}, the slip event can be taken as an "adiabatic and undrained" process (*Rice*, 2006). In this case,

the hydrothermal diffusion terms in equation (3.3) and (3.4) can be neglected, and evolution of temperature against pore pressure during a fault shearing can be then simplified as $\Delta T = \Lambda^{-1}\Delta p$, if assuming no chemical reactions (*Lachenbruch*, 1980; *Rice*, 2006). Therefore, on a first order approximation, the temperature rise is expected to be proportional to the potential increase of pore pressure, in agreement with the modeling results that the cases with W ranging from 2 to 20 mm show similar temperature rises (Figure 3.9).

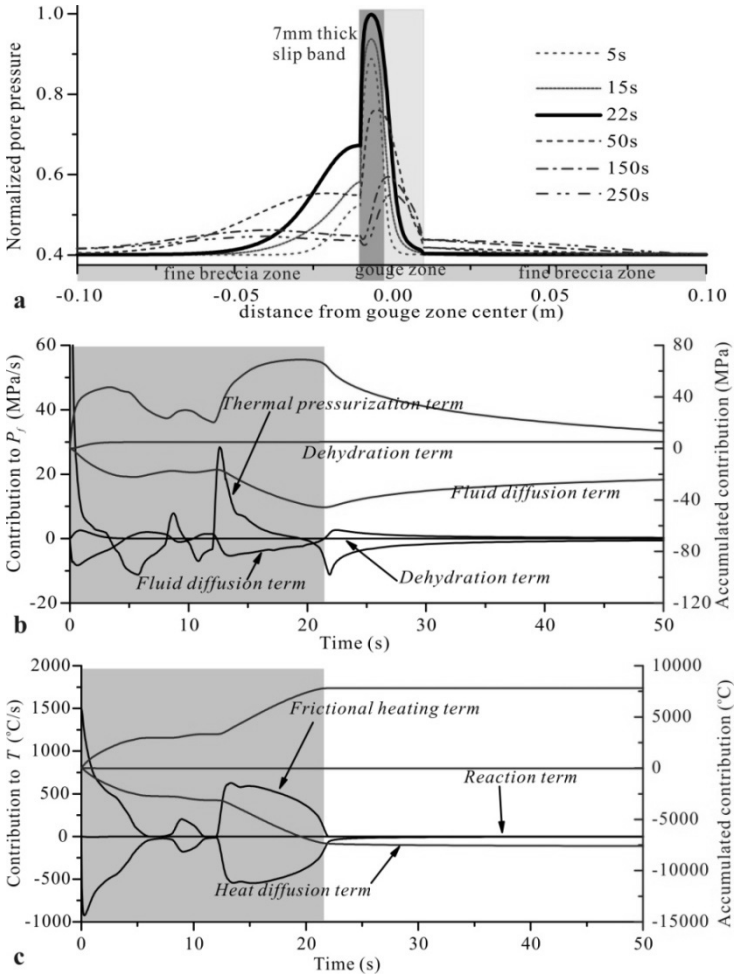

Figure 3.10. Modeling results of cases with slip localization. (a) Snapshots of the profile of normalized pore pressure across the fault core in the case of "Ref || 7 mm-thick slip band". (b) Pore pressure and (c) energy partitioning in the case of "Ref || 0.5 mm-thick slip band". The shaded area in (a) represents the gouge zone and the dark part signifies the localized slip band. The shaded areas in (b) and (c) denote the time span of the Wenchuan earthquake.

3.5.4.5 Effect of Depth

We also modeled coseismic TP processes at various depths (1-7 km). The fault gouge collected in the exposure studied is rich in smectite-rich I/S, which can survive dehydration to depths over 7 km, as evidenced by deep oil-well drillings (*Pollastro*, 1993). The variation in the absolute content of smectite with depth was neglected here, but its effect on modeling results has been evaluated by varying the hydration state of smectite phase used in the modeling (see section 3.6.3). The slip history at depth is interpolated from the surface rupture offsets and the seismological inversion results (Figure 3.1e). At deep conditions, the increased normal stress implies that more frictional heat can be generated, while the fault rocks are expected to be more impermeable. Indeed, as shown in the Figure 3.11, calculation results indicate that the weakening effect is more efficient at depth. The maximum pore pressure attained is close to lithostatic pressure when the depth is greater than 2 km. Overshooting occurs at depths greater than 4 km. The maximum temperature attained is facilitated by the larger increase in pore pressure possible at greater depth, from 306 °C at 1 km depth to 642 °C at 7 km depth in our calculations. The contrast between results for various depths is much bigger when using CFP as discussed later in section 3.6.2.

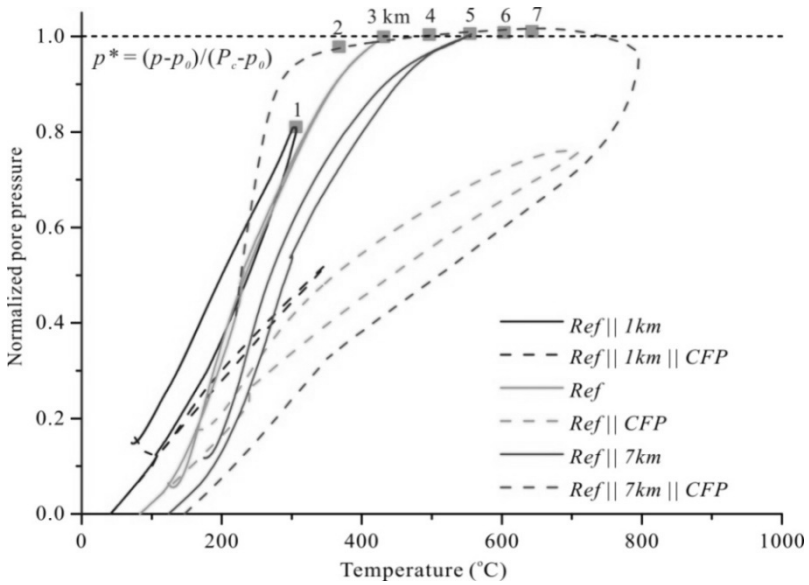

Figure 3.11. The computed p-T curves at slip band center at various depths. Solid and dashed lines indicate the modeling results using SDFP and CFP, respectively. The blue squares denote the pore pressure and temperature

conditions by the end of the slip event. For comparing purpose, the pore pressure is normalized by the initial pore pressure and lithostatic pressure as the formula labeled above.

3.5.4.6 Effect of Branching Slip

Slip surfaces branching off the gouge zone and cutting into the surrounding breccia rocks are commonly observed on the outcrop scale, not only at the ZJG (*Yang et al.*, 2012) but also at other exposures (e.g. *Togo et al.*, 2011; *Hou et al.*, 2012) along the LFZ. To explore the effect of slip branching into the branches, we replaced the central gouge zone in our reference model with a fault breccia zone. The frictional and transport properties (Run 3 in Figure 3.5) of the coarse breccia were used.

Figure 3.12 compares the temperature rise for slip in the gouge zone versus slip in the breccia zone. Much higher temperatures are achieved in the latter case, even causing extensive melting (1000 °C is set as threshold for melting). To compare the effect of fluid pressurization on dynamic slip-weakening, we plot the evolution of normalized effective pressure inside the slip band along with displacement (Figure 3.13), instead of shear resistance, to exclude the contribution from the evolution of μ_d. The results show that the reduction in effective pressure in the breccia zone is 20 % less than that in the gouge zone (between "*Ref*" and "*Ref || breccia*" in Figure 3.13). Because of rapid fluid escape, the result even displays transient recovery in the interval between the two slip events (Figure 3.13). Moreover, the p-T curves exhibit much more gradual increase of pore pressure with temperature in comparison with slip occurring in an impermeable gouge zone, implying a lower efficiency of TP (Figure 3.14). The comparative modeling results suggest that slip branching into the breccia zone can play an important role in determining the spatial distribution of pore pressure generation during an earthquake. Splaying of ruptures into surrounding breccia zones or into a permeable subsidiary fault will prevent excess pore pressure generation. Therefore, like variations in W, slip branching behavior may also cause heterogeneity of TP along the fault plane, thus influencing dynamic fault motion.

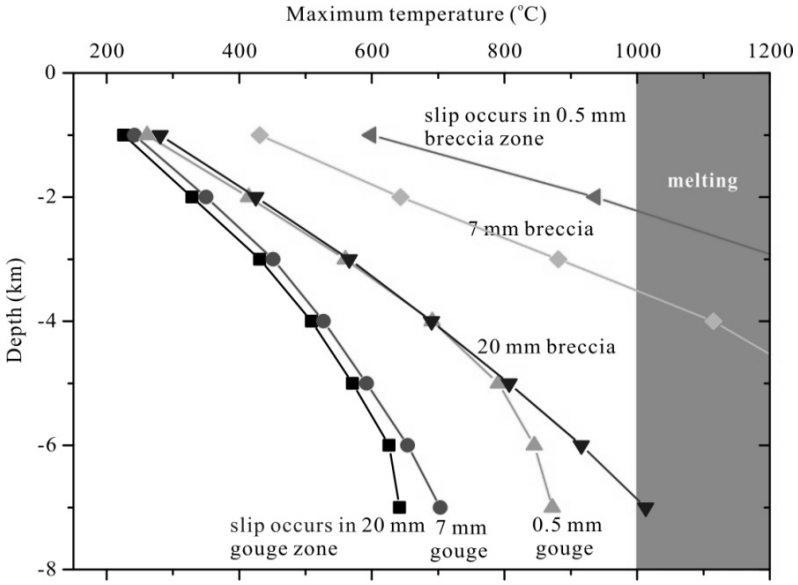

Figure 3.12. Comparison of the maximum temperature in cases when slip occurs in a gouge zone versus in the surrounding breccia zone. Suppose heating to 1000 °C could cause local melting. The effect of slip band thicknesses (0.5, 7 and 20 mm) is also investigated.

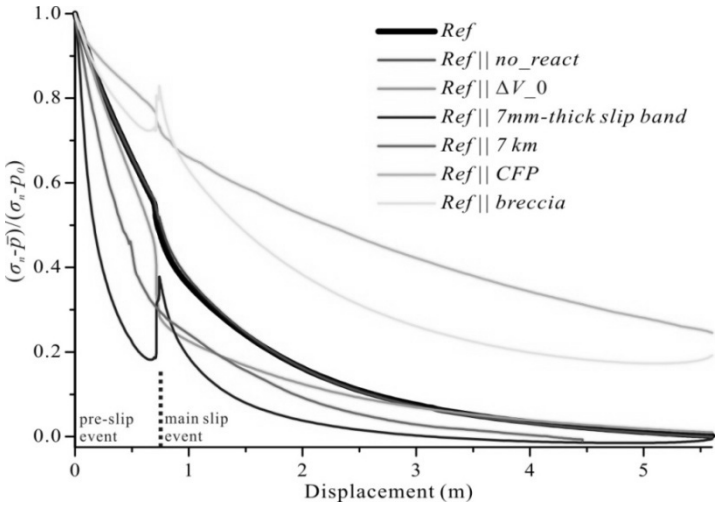

Figure 3.13. Evolution of normalized effective pressure along with displacement in various cases. "Ref", reference case; "Ref || no_react", reference case without chemical reactions; "Ref || ΔV_0", reference case without considering solid volume reduction due to reaction; "Ref || 7 mm-thick slip band", slip occurring in a localized shear band of 7 mm thick; "Ref || 7 km", slip occurring at 7 km depth; "Ref || CFP", reference case but using constant fluid properties (CFP); "Ref || breccia", slip branching into a surrounding breccia zone.

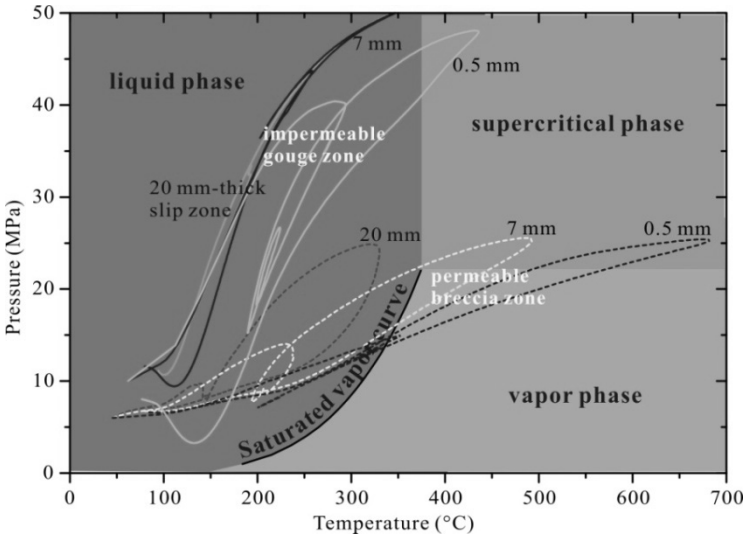

Figure 3.14. Comparison of p-T curves in cases when slip occurs in a gouge zone versus in a breccia zone. The calculations are at 2 km depth for slip in a gouge zone and at 1.2 km depth for slip in a breccia zone. In both cases, the initial pore pressure is set 0.2 of the lithostatic pressure. Note that since our modeling here does not consider phase changes of water, the portion of curves passing through the saturated vapor curve should be treated with caution - because once the p-T state of pore water meets the saturated vapor curve, it will begin to vaporize. The considerable enthalpy change involved in this process can inhibit the temperature rise (Brantut et al., 2011). At the same time, vaporization strongly promotes pore pressure rise because water vapor has much lower density than that of liquid water. However, once vaporization occurs, the fluid flow enters the two-phase regime, which is beyond the capability of our finite element framework.

3.6 Discussion

Our laboratory and numerical results have revealed several issues that require explanation and/or further analysis. They are as follows. (1) The transport properties of the fault rocks investigated show significant variability with effective pressure and with rock types. How can these data refine our understanding of the fluid flow pattern in the Wenchuan earthquake fault zone? (2) The dry and wet samples display distinctly different slip-weakening behavior at seismic slip rates. What does this discrepancy imply? (3) Our numerical modeling shows that the highly-coupled thermal-hydrological-mechanical-chemical processes during fault motion are of great importance in influencing the coseismic slip-weakening behavior. What is the sensitivity of this weakening to the various controlling factors? How did these processes influence

coseismic rupturing on the Wenchuan earthquake fault?

3.6.1 Hydrological Architecture of the Fault Zone

The discussion here is based on our transport properties data obtained for samples taken across the fault zone, as measured in the upward pressurization path. As shown by the results of these measurements (Figure 3.5), the central gray gouge and micro-fractured limestone at the margin of the fault zone have the lowest permeability. They are below 2×10^{-18} m^2 at P_e higher than 20 MPa. By contrast, the fault breccias surrounding the gouge zone have much higher permeability, greater than 5×10^{-19} m^2 at the P_e-value investigated. The cemented breccia and micro-fractured limestone near the fault margin show the lowest porosity and specific storage values (Figure 3.5b). They decrease to un-measurable levels in the intact country rock. The gouge sample studied also has relatively low porosity, especially at P_e-value above 30 MPa. Therefore, the transport properties across the fault zone at the ZJG exposure take on a typical "conduit/barrier" binary structure as proposed by *Caine et al.* (1996). This is in agreement with a previous study performed using nitrogen as fluid medium under low pressure conditions (*Chen et al.*, 2011), and also with the permeability structure revealed in other active fault zones (*Mizoguchi et al.*, 2008; *Tanikawa et al.*, 2009). The implication is that the fault fluid is mainly stored in the porous damaged zone, and its flow is constrained between the barriers of fault gouge and country rock. Thus, the hydrological architecture of the LFZ shows strong a macro-anisotropy, thereby fluid flow is easy in the direction parallel to the fault plane.

The variations in transport properties across the fault are presumably related to the contrast in structural and material properties of the fault rocks, e.g., load-supporting framework, grain size distribution and clay content. The micro-fractured limestone has very low porosity, and its permeability and specific storage is extremely sensitive to effective pressure (Figure 3.5). This can be explained by the crack-dominated structure. The gouge sample, consisting of very fine grains with average diameter of 4 μm and containing a large percentage of clay minerals, has a typical matrix-supported structure and low porosity (Figure 3.2d), which could strongly reduce the fluid transport efficiency with increasing effective pressure (*Bernabé et al.*, 2004). In contrast, the fault breccias show a clast-supported framework structure which is relatively resistant to compaction, thus exhibiting less sensitivity to effective pressure (Figure 3.5).

As a final note on the hydrological architecture of the fault zone, it is expected that low permeability is required in and around the fault zone in order to maintain the high P_f needed to nucleate a high-angle thrust rupture (*Sibson et al.*, 1988; *Zhou and He*, 2009) at a mid

crustal depth (*Zhang et al.*, 2010). At that depth, the low-friction minerals found at the surface (e.g. smectite, I/S) are unlikely to exist and hence are unlikely to have played a dominant role over p_f in determining rupture behavior at depth. However, our lab measurements showed quite high permeability for the coarse fault breccias of the damaged zone. We believe this can be explained by the following reasons. (1) The fault rocks investigated have undergone severe fault motion and damage during the Wenchuan earthquake. They were sampled ~ 11 months after the Wenchuan earthquake, hence more likely reflecting the hydrological architecture of the fault zone in the post-seismic stage. (2) Fluid-involved mechanisms such as precipitation, cementation and pressure solution, can help heal the fault rocks at depth in a long term. Just like the cemented breccia zone on the hanging wall of the exposure studied, the samples in this zone are composed of fine matrix and scattered fragments, whereas they are well cemented and rare macro-fracture can be seen in it (strictly, this kind of rock should be termed cataclasite). We infer their formation has recorded deformation inherited from past fault motion, presumably by repeated earthquakes and by fluid-assisted healing in long-term interseismic periods. However, these are out of the reach of this study.

3.6.2 Thermal Pressurization in the High-velocity Experiments

The friction behavior for water-dampened samples is characterized by rapid slip-weakening and by lower steady-state frictional strength (Figure 3.4d) than the dry samples (Figure 3.4c). For the fault gouge, in particular, the dynamic weakening process is completed in the very first stage of slip (Figure 3.4b). This can be explained as pressurization of pore water by frictional heating provided both the gouge material and the sealing capacity of the Teflon sleeve contribute to restricting fluid flow. Similar weakening behavior has been reported for natural fault gouge (*Ujiie et al.*, 2011), landslide surface gouge (*Ferri et al.*, 2010) and simulated gouge samples (*Faulkner et al.*, 2011), and was explained as a TP process in these studies also. Conspicuous dilation, observed in our wet experiments, supports this viewpoint. Moreover, much smaller d_c values have been obtained in our wet experiments (0.6 - 2.0 m, Figure 3.4d) than in our dry experiments (2 - 35 m, Figure 3.4c). This implies an extra slip-weakening mechanism associated with the presence of water. The lack of a systematic relationship between d_c and the applied normal stress under wet conditions can be explained by fluid pressurization of the pore water, which leaked in an unreproducable manner, from run to run, due to the poor sealing capacity of the Teflon sleeves.

To test whether TP can explain the dramatically different frictional behavior observed

between wet and dry experiments, a finite element (FE) model for simulating the high-velocity experiments was constructed. The FE approach is the same as used for fault slip modeling, but employed 2-D axisymmetric geometry and appropriately rewritten partial differential equations. Initial and boundary conditions, as well as detailed parametric settings of the model are addressed in detail in Appendix 3.B. The dry friction data (Figure 3.4b) were imported to specify the heat source, given as $Q_{so} = \tau\dot{\gamma} = 2\pi\varpi r\mu_{dry}(\sigma_n - \overline{p}(r))/W$. Here ϖ is rotation rate (s^{-1}), r is the distance from the rotation axis, μ_{dry} is dry friction, σ_n is the normal stress imposed and W is the gouge layer thickness. The friction between the rotary wall rock and Teflon sleeve is an additional heat source, which can be calculated from the Teflon friction correction data (Figure 3.4a). Unlike our planar fault model, the vertically-averaged pore pressure ($\overline{p}$) is function of r ($\overline{p}(r) = \int_{-W/2}^{W/2} p(r,z)dz/W$). The calculated result is then compared with the measured wet friction data. If TP is the only mechanism responsible for weakening in the wet experiments, the calculated equivalent friction (μ_{eq}), defined as

$$\mu_{eq} = \frac{\int_0^R \mu_{dry}(\sigma_n - \overline{p}(r))2\pi r^2 dr}{\int_0^R \sigma_n 2\pi r^2 dr} \tag{3.10}$$

should be identical to that observed in wet experiment. Here, μ_{wet} is the measured wet friction and R is the radius of the host gabbro cylinder. The modeling results (Figure 3.15) show that the equivalent friction (marked by μ_{eq_TP}) agrees well with the measured wet friction (marked by μ_{wet}), in particular at steady-state. The slip weakening distance is reduced from 4.0 m in the dry case to less than 2.0 m. However, for the first few seconds, μ_{eq_TP} peaks to a value well above μ_{wet}, and is followed by a much dramatic slip-weakening than that seen in the wet experiment. The most obvious explanation for this discrepancy is initial compaction by grain comminution at the onset of slip. The axial shortening observed at the onset of slip supports this viewpoint. To examine this further, the initial pore pressure was assumed to increase by an amount of 0.1- 0.2 MPa due to initial compaction. An increase of 0.2 MPa was sufficient to decrease the equivalent peak friction by ~ 0.15 ($\mu_{eq\_TP\&CP}$ in Figure 3.15), bring the overall trend of the equivalent friction close to the measured wet friction curve. A second possible explanation is the change in sealing capacity of the Teflon sleeve. In the simulations, water is allowed to permeate freely through the interface between the Teflon sleeve and the host gabbro. This is what happens when the Teflon sleeve has expanded after running for a few seconds. However, at the onset of slip, the Teflon sleeve could have partially sealed the pore pressure, causing an initial spike in pore pressure in the initial stage of motion.

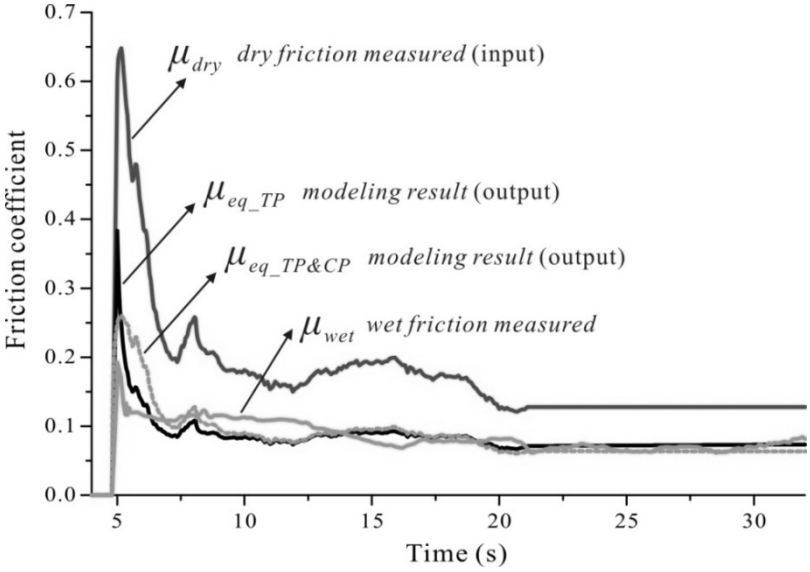

Figure 3.15. Comparison of the measured dry and wet friction data versus equivalent frictional strength derived from modeling. In the modeling, the dry friction data (μ_{dry}, red line) was imported to specify the heat source, the calculated equivalent friction (μ_{eq}) was compared with wet friction observed (μ_{wet}, yellow line). μ_{eq_TP} (dark line) corresponds to the case that thermal pressurization (TP) is considered, while $\mu_{eq\_TP\&CP}$ (blue line) corresponds to the case that both TP and initial compaction (initial pore pressure was assumed to increase by 0.2 MPa) have been taken into account. Note that, the dry friction data only lasted to 23s, and has been extrapolated to 32.7s, assuming constant friction after 23s.

Under dry conditions, even though dehydration of smectite releases some water, our dry model shows that the effect of pressurization of free fluid by frictional heating can be neglected. Detailed settings of the model for the dry case are given in Appendix 3.B. The results show that vaporization of water lost from the smectite occurs at the very beginning of slip (0.2 s after slip), and that ~ 2/3 of the outer radius of the gouge layer reach the critical temperature for vaporization during the dry run. In spite of this, the pore pressure rise by less than 0.1 MPa (1/10 of σ_n) due to high compressibility and easy escape of the low viscosity pore gases. The weakening effect caused by vaporization of dehydrated water is thus small. As a first approximation, our dry friction data can therefore be used to calculate the heat source in modeling coseismic slip at depth. The dynamic stress drop observed can then be explained by flash heating (*Goldsby and Tullis*, 2011), even though thermal decomposition of the carbonate minerals present (*Han et al.*, 2007) cannot be fully ruled out (Table 3.1). The

conclusion drawn from our high-velocity experiments is that TP is an important process in thin layers of wet fault gouge at coseismic slip rates, and exerts a strong control on the magnitude of slip weakening and on d_c.

3.6.3 Role of Coseismic Thermochemical Processes and Implications for the Wenchuan Earthquake

Our numerical analyses, which incorporated the measured physical and chemical properties of the local fault rocks, is believed to provide a realistic way of modeling the main features of the faulting process of the 2008 Wenchuan earthquake. The results indicate that TP should have occurred extensively at depth and effectively reduced the dynamic shear resistance during the Wenchuan earthquake. The most crucial parameter determining dynamic rupture propagation, acceleration and the energy partitioning inside the fault zone during earthquakes (*Ida*, 1972; *Marone et al.*, 2009), is the effective slip-weakening distance (defined as critical distance over which shear resistance drops to the residual level), denoted as D_c. This should be carefully distinguished from the laboratory-derived d_c (Figure 3.4f) which only reflects the weakening caused by the evolution of friction. According to the extrapolation of our experiment results, d_c at 3 km depth (at P_e of 45 MPa) is ~ 0.036 m (Table 3.2), much lower than the seismologically-inferred value of 0.52 m for the Wenchuan earthquake (*Liu and Shi*, 2011). However, TP can first raises d_c to a moderate level of 0.22 m on basis of the empirical equation obtained describing the relation between d_c with normal stress (Figure 3.4f), and then raises it further to the seismological level (~ 0.5) through reducing the effective normal stress acting on the fault plane.

Taken together with previous work, our study demonstrates that chemical reactions, in particular smectite dehydration, may have played an important role in rupture propagation during the Wenchuan earthquake. First, dehydration of smectite is predicted to start at the onset of slip, and the reaction rate is very fast (Figure 3.6). Second, at the ZJG exposure, there is evidence that illitization induced by frictional heating occurred in the thin black gouge during the Wenchuan earthquake (*Chen et al.*, 2013a, Chapter 2). Third, a growing number of studies on surface exposures (*Dang et al.*, 2012; *Hou et al.*, 2012; *Zhang et al.*, 2013; *Chen et al.*, 2013a; *Yao et al.*, 2013) and drilling cores (*Xu and Li*, 2010) have revealed that the enrichment in smectite (or smectite-rich I/S) is a common feature for the Longmenshan fault zone. Although pure smectite is unstable at depths beyond 2-3 km (*Saffer and Marone*, 2003), I/S can survive to depths over 7 km, as evidenced by deep oil-well drilling (*Pollastro*, 1993). Smectite dehydration is therefore expected to have occurred extensively along the Wenchuan earthquake fault up to such depths.

The dynamic effect of smectite dehydration on faulting depends on the content and hydration-state of the smectite in the gouge sample. These will both vary with increasing depth (c.f. data from San Andreas Fault Observatory at Depth presented by *Solum et al.* (2006) and *Lockner et al.* (2011)), but no quantitative constraints are available. The variation of smectite content with depth is not taken into account in our modeling. However, its effect on modeling results has been evaluated by varying the hydration state of the smectite content (10.7 wt. %) measured in the gray gouge (χ in equation (3.7) and Table 3.3). In our modeling, 10.7 wt. % smectite with one interlayer H_2O generates about 6 MPa excess pore pressure (Figure 3.6; Figure 3.8; Figure 3.11). This value increases to 16.5 MPa if three interlayers of water molecules are initially present in the smectite. We consider this to be the maximum effect of smectite dehydration, because both smectite content and hydration-state are expected to decrease with depth. Competing effects (i.e., reaction enthalpy change and solid volume shrinkage) associated with reactions act to affect generation of excess pore pressure as well. For reactions involving clay alteration, the endothermic effect is negligible relative to frictional heating (Figure 3.6i). With high reaction enthalpy, decarbonation can potentially function as an important buffer of temperature rise (Table 3.3; Figure 3.7 and Figure 3.8). However, high temperature (> 600 °C) is required to activate this reaction, and in our modeling it only occurs in cases of highly localized slip (Figure 3.9) or branching slip or at very deep condition (Figure 3.12). Dehydroxylation of smectite starts at ~ 400 °C. Since the reaction rate is slow (Table 3.3), its contribution to coseismic process is limited, though it would occur continuously during the post-seismic stage. The reaction of smectite-to-illite transformation is the slowest of reactions involved. Its effect in terms of fluid pressurization is negligible in all our analyses even when high temperature is achieved. Moreover, volume change in the solid phases has to be taken into consideration, otherwise an overestimation of fluid pressurization will result (Figure 3.7 and Figure 3.13).

Reaction-enhanced TP process would have increased the pore pressure inside the slip zone thereby moderating the temperature rise during the Wenchuan earthquake. Heat generation is facilitated by more efficient fluid escape from the heated zone, either associated with localized (Figure 3.9) or branching slip (Figure 3.12), or to a lesser extent, with the large pore pressure rise possible at depth (Figure 3.11). Typically as in the exposure studied, principal slip gouges in active fault zones usually contain abundant clay minerals (e.g. *Lockner et al.*, 2011) and have very fine grain size (e.g. *Ma et al.*, 2006). Statistic analysis (23 in total) has indicated that fault gouges found in almost all active fault zones have permeability lower than 10^{-18} m^2 (*Chen and Yang*, 2012). These factors tend to inhibit the temperature rise through enhanced fluid pressurization by potential de-watering reactions

(*Yamaguchi et al.*, 2011) and by reducing fluid transportation (*Bernabé et al.*, 2004). Therefore, the now widely accepted concept of TP offers a compelling explanation for the apparent scarcity of pseudotachylite in natural faults (*Sibson*, 1975; *Rice*, 2006; *Sibson and Toy,* 2006). If the hydrous mineral present in a fault zone is abundant enough, melting is unlikely to occur easily since dehydration reactions, occurring at the very start of slip, will effectively slow down heat production (*Brantut et al.*, 2011). Our results thus agree favorably with the assertion that pseudotachylite can only be produced in dry, crystalline rocks, as reported by *Sibson and Toy* (2006).

Coseismic pressurization of pore fluid is a complex process involving interplay between frictional heating, reaction and diffusion. According to systematic parametric analysis (i.e. λ, W and depth; with/without reactions; branching slip), our results show that W and permeability (branching slip) are the most important factors influencing TP efficiency (Figure 3.13), as proposed in previous studies (e.g. *Rice*, 2006; *Sulem and Famin*, 2009). The influence of depth can be attributed mostly to permeability change as well. If a slip zone propagates into a localized band or branches to an adjacent breccia zone or immature splay (Figure 3.13), it will lead to enhancement of fluid escape, partially inhibiting TP as a slip-weakening mechanism. This suggests that branching or localized slip can lead to a pronounced heterogeneity in fluid pressure distribution along the fault, which could result in variations in the degree and rate of slip-weakening, hence influencing the dynamics of fault motion (*Wibberley and Shimamoto, 2005*). Although it is difficult to incorporate along-strike variations in properties (i.e., W and k) of the slip zones into modeling work on the gross slip response, we infer that rupture propagation will be locally controlled by these slip resistant points. In other words, fault branches and localized slip locations may act as seismic asperities. This mechanism can also help explain why the almost complete dynamic strength drop seen in our simulations (e.g. Figure 3.6) is not reflected as a stress drop in natural earthquakes (*Zhang et al.*, 2009).

The coseismic rupture was associated with the largest fault offsets near the exposure studied (Figure 3.1c). Friction experiments at seismic slip rates revealed relatively low friction for the gouge sample (Figure 3.4). However, there is not much difference from the gouges sampled from other segments along the LFZ, e.g. the Pingxi exposure at the northeast terminus (*Yao et al.*, 2013), the Hongkou exposure close to the epicenter (*Togo et al.*, 2011), or the Chaping exposure in the central segment (*Hou et al.*, 2012). The acceleration of slip from depth upward (Figure 3.1d) suggests the coseismic motion was not passively pushed from depth, and there must be an extra mechanism allowing acceleration. We propose that fluid pressurization within fluid-saturated fault zone may have been responsible for this. First,

as stated above, our friction experiments on wet gouge samples and numerical analysis indicate that the reaction-enhanced TP would have occurred easily at the ZJG exposure, and the modeling results are in broad agreement with seismological observations. Second, previous modeling work (*Mizoguchi and Shimamoto*, 2008) has demonstrated that TP is an important slip-weakening mechanism when the permeability of fault gouge is lower than 10^{-18} m^2. Third, the efficiency of TP that occurred near the ZJG exposure is expected to be higher than elsewhere along the LFZ. This is because the gouge sample of the ZJG exposure shows so far the lowest permeability (7.3×10^{-22} m^2 at P_e of 165 MPa) in comparison with four other gouges along the LFZ. They are 2.6×10^{-20}, 4.3×10^{-20}, 1.7×10^{-19} and 9.2×10^{-19} m^2 for Pingxi, Jinghe, Hongkou and Shenxigou exposures, respectively (see their locations in Figure 3.1c). Recall that TP is not only dependent upon the permeability of the slip zone, but also upon other factors such as slip band thickness. To exclude the influence of other factors, thorough experimental and modeling work needs to be done on other locations. On the basis of our findings, we propose a new approach to seismic-hazard assessment in the future. TP efficiency whereby should be incorporated in. Such an approach cannot predict the spatio-temporal distribution of nucleation site, but can provide an evaluation of the response of a fault (or segment) to the earthquake rupture if an earthquake has already nucleated. Though accuracy cannot be declaimed and possibility for validation of our model is elusive, our work does provide a basic method for evaluating TP efficiency.

Further, our modeling work shows that the local PT conditions inside the slip zone can vary through a large range during faulting, so that the pore fluid may even undergo multiple phase changes, from the liquid to supercritical states as well as existing in the gaseous form (Figure 3.14). Accordingly, the fluid properties can vary by up to two orders of magnitude (Figure 3.A1). There are indeed several competing factors associated with evolving fluid properties that influence TP efficiency. It is therefore difficult to say whether the introduction of state-dependent fluid properties (SDFP) facilitates TP or not. We conducted modeling with SDFP and CFP (constant fluid properties) separately (Figure 3.7; Figure 3.11) to evaluate the potential impact of fluid properties on TP efficiency. Basically, in the cases of SDFP, the pore pressure can build up more rapidly than for the cases of CFP. The temperature increases, though, when assuming CFP are much larger than assuming SDFP (Figure 3.7; Figure 3.12). The results indicate that the variation of fluid properties during faulting have played a crucial role that can strongly influence slip processes and likely did strongly affect the evolution of the Wenchuan earthquake, much more so than the previously realized.

3.7 Conclusions

The coseismic slip associated with the Wenchuan earthquake has been systematically investigated based on the combined experimental and modeling work, and considering the effects of a range of thermal- hydrological-mechanical-chemical processes within the slip zone. Main conclusions are summarized below.

(1) High-velocity friction experiments revealed low steady-state friction for both fault breccia and central fault gouge samples collected from the exposure studied. The wet results are characterized by rapid slip weakening and by lower friction than the dry results, suggesting the presence of friction-induced fluid pressurization in thin layers of wet gouges.

(2) The gouge samples show the lowest permeability and low porosity compared with the fault rocks from the surrounding damaged zone, such as coarse fault breccias. The intact country rocks also have low permeability, even below the detection of our experimental configuration. The hydrological profile across the fault zone thus exhibits a typical "conduit/barrier" binary structure, with fluid flow being constrained to occur in the highly damaged zone on each side of the central gouge.

(3) Numerical modeling of coseismic slip using the measured fault rock properties and seismological data on slip rate and displacement, indicated that thermochemical pressurization played an important role during the Wenchuan earthquake, with dynamic stress reduction being strongly enhanced by increase of pore pressure due to frictional heating, and with calculated slip-weakening distance being consistent with the seismologically-inferred level. Overshooting of lithostatic pressure by pore pressure generation might have occurred at depth, limiting temperature development to values less than 600 °C. There was more than enough heat generated to fully dehydrate the interlayer water in smectite, which can contribute an excess pore pressure of ~ 6 MPa. Fluid pressurization within the slip zone can help explain the large coseismic displacement and slip acceleration observed near Beichuan city. We propose TP should be considered in future seismic-hazard assessment.

(4) Slip wedging into a localized fault or splaying into a surrounding breccia zone will lead to enhanced fluid loss, partially inhibiting the TP process. We speculate that the locations where localized or branching slip occurs will behave as strong portion of the fault that may act as seismic asperities. There exists a critical thickness, W_{cr}, which is approximately equal to 2 times the characteristic hydrological diffusion length. If the coseismic slip band is thicker than W_{cr}, major TP weakening is possible.

(5) State-dependent fluid thermophysical properties are newly introduced in this work. Their use shows fluid pressurization to be much more efficient than when these properties

are taken as constant and equal to the values for a reference state. The changes in temperature and pressure conditions that occur in fault core during fault motion allow the pore fluid to undergo multiple phase changes. The corresponding changes in fluid properties may play a determining role in earthquake dynamics, and are much more important than the previously realized.

Appendix 3.A: the State Dependent Thermophysical Properties of Water

Within the PT range of our modeling, the fluid properties, i.e., thermal expansivity, density, viscosity, compressibility, can vary significantly (Figure 3.A1). In an attempt to model the situation more realistically, we employ state dependent fluid properties, with pure water as a proxy for the natural pore fluid. To avoid data singularity at the phase boundaries, the p-T graph is divided into three domains on basis of the three-phase diagram (Figure 3.14): Domain I-supercritical phase: $p \geq 22.06$ MPa and $T \geq 373.9$ °C; Domain II-liquid phase: $T < 373.9$ °C and above the saturated vapor curve; Domain III-vapor phase: $p < 22.06$ MPa and below the saturated vapor curve. The database of thermophysical properties of water downloaded from the National Institute of Standards and Technology (NIST, http://webbook.nist.gov/chemistry/fluid/) is then fitted employing a 5-order polynomial. It is expressed as $Y(T, p) = \sum_{i=0}^{4}\sum_{j=0}^{4} A_{ij} T^i p^j$, where T is temperature in unit of °C, p is pore pressure in MPa, Y is dependent variable such as density and A_{ij} is the corresponding coefficient matrix.

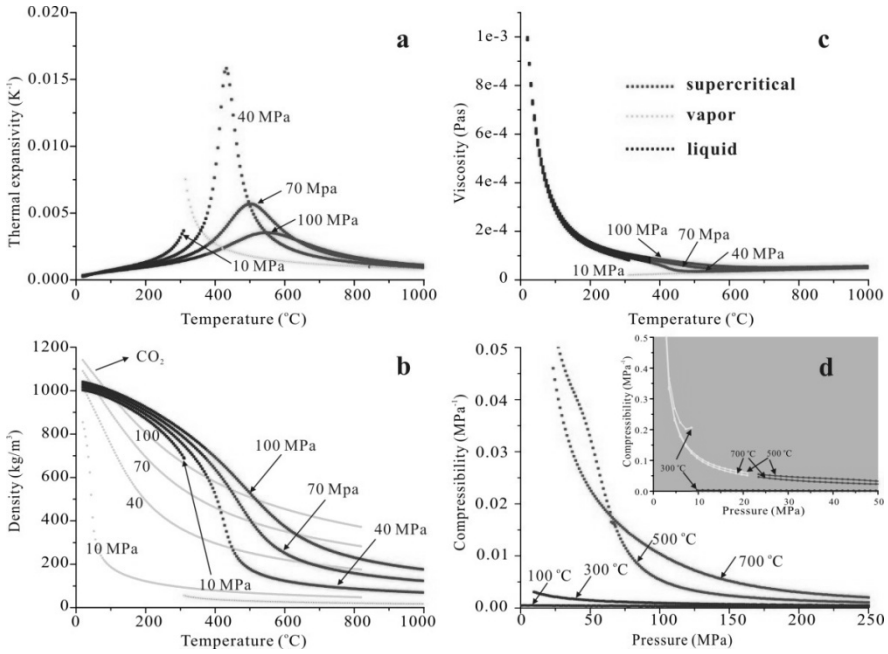

Figure 3.A1. State-dependent thermodynamical properties of pure water, including (a) thermal expansivity, (b) density and (c) dynamic viscosity as functions of temperature, as well as (d) compressibility as a function of pressure. The insert plot in (d) is the enlarged graph for low pressure part. Density of pure CO_2 is also presented in (b).

Appendix 3.B: Model Settings for Simulating the High-Velocity Experiments

A finite element (FE) model was constructed for simulating high-velocity experiments under both dry and wet conditions. Model geometry, meshing, boundary conditions and detailed settings for key parameters were as follows,

(1) The sample assembly (Figure 3.3a) was represented using a 2-D axisymmetric FE geometry, consisting of the gouge sample, the wall-rock cylinders, the Teflon sleeve, the sample grips and the loading shaft. The geometrical model was meshed self-adaptively using triangular elements (5531 in total).

(2) Gouge friction was the main heat source (Figure 3.4b). Friction between the rotary wall rock and Teflon sleeve is an additional heat source, calculated from the Teflon friction correction data (Figure 3.4a). The boundaries of the loading frame were assumed to be at a fixed temperature of 20˚C, and the temperature of surfaces exposed to air was assumed to evolve following Newton's cooling law. The thermal conductivities of the gouge and gabbro host rock were measured using a TK04 Thermal Conductivity Meter (TeKa, Germany). Specific heat capacities of the wall-rock and gouge sample were calculated from specific

heat of the constituent minerals and their mass fraction.

(3) Permeability, porosity and specific storage values for the gouge sample were based on extrapolations from our experimental data (Figure 3.5), neglecting damage induced by preparation and shear of the gouge. The wall rock (Indian gabbro) is practically impermeable ($\sim 1\times10^{-22}$ m^2). The sealing capacity of the Teflon ring is assumed to be negligible. The initial pore pressure was set at atmospheric, unless otherwise stated.

(4) The composition of the fault gouge was based on our XRD data (Table 3.1).

(5) The properties for pore gases (in dry experiments) were assumed to be represented by data for nitrogen, as obtained from the NIST website. The liquid-vapor phase transition was also considered, as this can promote pore pressure increase and inhibit temperature rise. For the dry experiments, we assumed that once the temperature reaches the critical temperature for vaporization, the smectite interlayer-water will be released as water vapor. The enthalpy change associated with the phase transition is simulated by increasing the enthalpy of the reaction by an appropriate amount. The contribution of water vapor to the pore pressure generation rate was calculated from equation (3.7), using the density of water vapor as download from NIST. When modeling the wet experiments, vaporization is ignored as a first approximation (because the resultant two-phase flow is beyond the capability of the present FE framework), yielding a minimum TP effect.

Acknowledgement: This research was co-supported by the National Science Foundation (41102130), the Basic Scientific Funding of Chinese National Nonprofit Institutes (IGCEA1006) and the ninth Section (WFSD-0009) of the National Scientific Special Funding of the Wenchuan Fault Scientific Drilling. Thanks to Yongxin Yang, Jiaxiang Dang, Lu Yao and Lei Zhang for their support in the field. Yong Zhang is thanked for providing the coseismic slip results from wave shape inversion. We also thank T.-f. Wong and another anonymous reviewer for their constructive comments, which greatly improved this manuscript.

Chapter 4

Interseismic re-strengthening and stabilization of carbonate faults by "non-Dieterich" healing under hydrothermal conditions

Jianye Chen, Berend A. Verberne, and Christopher J. Spiers

Submitted to Earth and Planetary Science Letters

Abstract

Friction experiments, consisting of sequential "velocity stepping", "slide-hold-slide" (SHS) and "velocity stepping" stages, have been performed to study the frictional healing behavior of carbonate fault gouge, and the effects of healing on the velocity dependence of friction, at 20 – 140°C and at 50 MPa effective normal stress. Dry experiments show classical Dieterich healing characterized by a transient peak in friction after each hold period, with no effects of SHS testing on steady-state friction or velocity dependence. By contrast, the wet tests show 1) an increase in apparent steady-state friction upon resliding after a hold period, and 2) a pronounced increase in the velocity dependence parameter, $(a - b)$, after the SHS stage. While the first of these "non-Dieterich-type" healing effects has been observed in previous hydrothermal experiments on simulated quartz gouges, it has not been reported previously for carbonate gouges. The observed effect of SHS-testing on $(a - b)$ has never been reported. Our findings suggest that, under in-situ hydrothermal conditions, interseismic fluid-assisted deformation processes, such as pressure solution, can significantly promote fault re-strengthening in carbonates and can cause slip stabilization. If the results are applicable to active faults in carbonate terrains, they have important implications for understanding how the extent of the seismogenic zone, and how earthquake magnitude and aftershock distributions, may evolve with repeated cycles of natural seismicity and interseismic healing.

4.1 Introduction

Most moderate to large earthquakes occurring in the continental crust nucleate in crystalline basement at depths of ~ 10 – 25 km, i.e. in the brittle-plastic transitional region for silicate rock types (*Sibson et al.*, 1982). As a result, most experimental work has focused on characterizing frictional properties relevant to these materials under the corresponding P-T-Stress conditions (e.g. *Dieterich*, 1972; *Byerlee*, 1978; *Blanpied et al.*, 1995; *Marone*, 1998b; *He et al.*, 2007). However, in tectonically active regions dominated by carbonate cover lithologies, destructive earthquake ruptures commonly nucleate and/or propagate at shallower depth, i.e. in the upper 5 - 15 km of the crust (*Mirabella et al.,* 2008*; Valoroso et al.,* 2013). Examples include the 1995 Mw 6.2 Aigion earthquake in Greece (hypocentral depth 7.2 km, *Bernard et al.* (2006)), the 2009 Mw 6.3 L'Aquila earthquake in Italy (9.5 km, *Chiarabba et al.* (2009)), and the 2008 Mw 7.9 Wenchuan earthquake in China (11 km for the north segment, *Xu et al.* (2009)). Some of these earthquake ruptures propagated all the way to surface with aftershocks occurring as shallow as ~ 1 km (*Chiarabba et al.*, 2009). Recent experimental studies (e.g. *Verberne et al.*, 2010) have shown that shallow seismicity is likely to be promoted in such terrains because carbonate fault rocks are a) strong (friction coefficient of ~ 0.7) and b) prone to unstable slip at relatively low effective normal stresses (e.g. 50 MPa) and temperatures (≥ 80 °C). For this reason, and because of the need for improved seismic hazard evaluation in carbonate terrains such as those mentioned above, the frictional properties of carbonate faults are attracting increased attention in relation to earthquake nucleation and rupture propagation (e.g., *Han et al.*, 2007; *De Paola et al.*, 2011; *Smith et al.*, 2011; *Violay et al.*, 2013; *Verberne et al.*, 2013a and 2013b). Specific points of interest include the frictional strength of carbonate fault gouges, their rate-and-state dependent friction (RSF) behavior and the underlying microphysical processes that control in-situ fault friction. To date, however, data on carbonate fault friction remain sparse, especially regarding the effects of fluids at in-situ, seismogenic, P-T conditions, where solution-transfer and other thermally-activated processes operate. Most experiments that have been reported have been conducted at coseismic slip rates (e.g., *Han et al.*, 2007; 2010; *De Paola et al.*, 2011; *Di Toro* et al., 2011), with only a few studies addressing carbonate fault friction in the rupture nucleation regime (*Verberne et al.*, 2013a; *Scuderi et al.*, 2013). In particular, very little is known about the interseismic strengthening or healing behavior of carbonate faults, though such data are crucial for understanding the seismic cycle and its repeat frequency.

In silicate rock systems, fault healing and associated strength recovery effects have been widely investigated in relation to both natural (*Li et al.*, 2003; *Marone et al.*, 1995) and

laboratory earthquakes (e.g. *Wong and Zhao*, 1990; *Karner and Marone*, 2000). These effects strongly influence earthquake nucleation and magnitude, as well as recurrence intervals (e.g. *Ruina*, 1983; *Marone* 1998b). In the classical framework of RSF modeling, frictional strengthening, i.e. healing following cessation of active slip, is treated as increasing linearly with the logarithm of "hold time" (*Dieterich*, 1972; 1979). Such time-dependent fault re-strengthening or "Dieterich-type" healing behavior, is commonly assumed in modeling fault behavior during the seismic cycle. However, the relevance of this behavior to natural faults has recently been questioned on the basis of healing experiments conducted on quartz fault rocks under hydrothermal conditions (*Karner et al.*, 1997; *Olsen et al.,* 1998*; Tenthorey et al.,* 2003; *Nakatani and Scholz*, 2004; *Yasuhara et al.*, 2005; *Tenthorey and Cox*, 2006). These studies have shown that the operation of thermally activated and/or fluid-assisted deformation mechanisms, such as pressure solution, can significantly enhance re-strengthening processes in quartz, far beyond the values predicted by the Dieterich-type log-linear aging law. However, no data are yet available on the potential importance of such effects in carbonates, or on the microphysical mechanisms responsible for healing in carbonates.

In an attempt to fill this knowledge gap, we investigate the slip stability and healing behavior of simulated carbonate fault gouge at temperatures ranging from 20 to 140 °C, at an effective normal stress of 50 MPa, under both dry and wet conditions. Henceforth, we use the term gouge to mean simulated gouge, except where otherwise specified. While the dry experiments show classical Dieterich-type healing behavior (e.g. *Marone*, 1998b) , the wet experiments show "non-Dieterich-type" healing effects, as well as healing-induced changes in the velocity dependence of frictional strength that have never been recognized previously. Our observations cannot be described or explained in terms of standard RSF concepts of healing, and lead to an alternative conceptual model for healing effects in carbonate faults with potentially important implications for seismicity in carbonate terrains.

4.2 Definitions used in this study

The experimental method used here, and in previous work on fault healing, is the slide-hold-slide (SHS) method. This involves imposing a fixed sliding velocity (V) on the simulated fault, at the so-called load point (i.e. the point at which the loading frame is loaded), followed by a stationary hold of duration t_h (the "hold time"), and then by re-shearing at velocity V. In previous work mostly at room temperature, this typically produces "Dieterich-type" healing (DH) behavior, characterized by a log-linear healing law

of the form $\Delta\mu \propto \log(t_h)$, where $\Delta\mu$ is the transient increase in friction coefficient (or healing effect) defined as the difference between the steady-state friction coefficient, measured before (or after) the hold period, and the peak frictional strength associated with reshearing.

However, the more complex "non-Dieterich-type" healing (NDH) behavior observed in many previous, mainly hydrothermal experiments (e.g. *Nakatani and Mochizuki*, 1996; *Karner et al.*, 1997; *Yasuhara et al.*, 2005; *Niemeijer et al.*, 1998; *Tenthorey and Cox*, 2006; *Carpenter et al.*, 2011; *Tesei et al.*, 2012), and reported here, ideally requires a more general terminology, and more general parameters, to describe healing conveniently. In our view, a more general terminology is also needed to avoid confusion between healing-induced changes in steady-state frictional strength, referred to as $\Delta\mu_{ss}$ by some authors (*Karner et al.*, 1997; *Nakatani and Mochizuki*, 1996; *Yasuhara et al.*, 2005), versus a) the transient frictional healing effect ($\Delta\mu$) defined above and b) the difference in steady-state friction coefficient measured in velocity stepping tests (also referred to as $\Delta\mu_{ss}$ by many authors, *e.g. Scholz,* 2002).

In line with this, we define the three parameters shown in Figure 4.1, which allow description of all possible DH and NDH healing responses. In this scheme, $\Delta\mu_{pk}$ is defined as the transient peak strength increase due to healing, measured in terms of the difference between the peak friction upon reshearing and the prehold steady-state friction coefficient. By contrast, $\Delta\mu_w$ is the post-peak frictional weakening, measured as the difference between the peak and the post-hold steady-state friction coefficients. Lastly, $\Delta\mu_r = (\Delta\mu_{pk} - \Delta\mu_w)$, is the residual, healing-induced strengthening, measured as the change in steady-state friction coefficient values observed after vs. before the hold period. Note that in some previous experiments (e.g. *Karner and Marone*, 2001; *Niemeijer et al.*, 2008), post-peak frictional weakening was characterized by a prolonged slip-weakening distance (> 2 mm), over which transient frictional healing was ultimately erased, so that $\Delta\mu_r = 0$. The term "residual strengthening" ($\Delta\mu_r$) defined by us above refers to an increase in apparent steady-state strength that is not erased in the post-hold slip distances investigated, which are incidentally similar to the slip distances of 0.2 – 0.5 mm investigated in most previous SHS work (e.g. *Olsen et al.*, 1998; *Muhuri et al.*, 2003; *Yasuhara et al.*, 2005).

Making use of these parameters and taking into account their characteristics and the way in which they depend on hold time in previous healing studies, we now define the following generically possible categories of frictional healing to facilitate easy description (see Figures 4.1a, 4.1b and 4.1c):

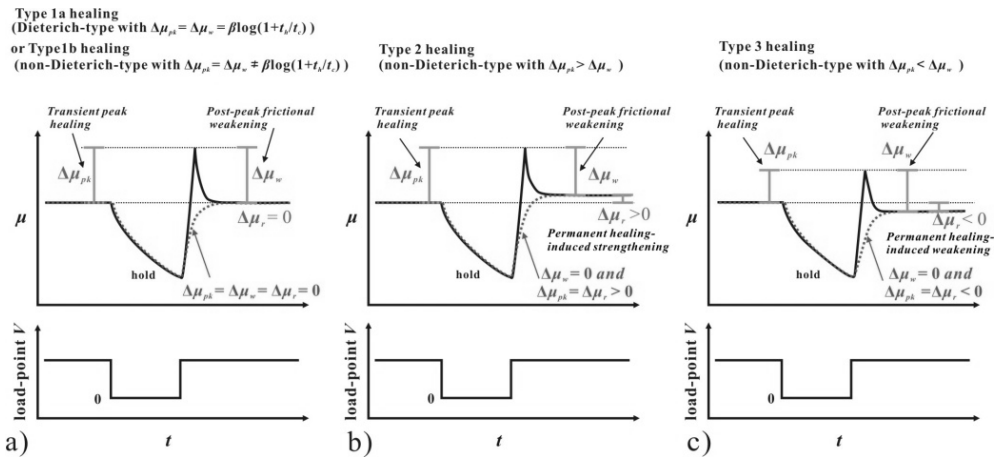

Figure 4.1. Definition of frictional healing parameters obtained in SHS tests, as required to describe all possible phenomenological classes of healing behavior (Dieterich- and non-Dieterich-types, see text). Three main classes of behavior are possible, as shown in (a), (b) and (c), respectively. Note the inequality in Type 1b means that $\Delta\mu_{pk}$ is not well described by a log-linear relationship of the type found by Dieterich (1972), but is better described by other functions, as sometimes reported in the literature (e.g. power law, Coulomb, 1785). The three special cases of healing behavior indicated by the red dotted lines in (a), (b) and (c) are characterized by a zero slip weakening effect ($\Delta\mu_w = 0$). Such behavior has been previously reported, in experiments on wet quartz, mostly at high temperatures (e.g. Olsen et al., 1998), and on dry phyllosilicate-rich gouges at room temperature (Carpenter et al., 2011). See text for details.

1) Type 1 healing. In this type, $\Delta\mu_{pk} = \Delta\mu_w$ and $\Delta\mu_r = 0$ (Figure 4.1a). It can be divided into two subclasses.

Type 1a healing (Classical DH). Here $\Delta\mu_{pk} = \Delta\mu_w = \beta \cdot \log(1+t_h/t_c)$, where t_c is a cutoff time, of the order of 1 second, beyond which the healing shows a log-linear growth, and where $\beta = d(\Delta\mu_{pk})/d\log(t_h)$ is a constant usually referred to as the healing rate (e.g. *Dieterich*, 1972; *Marone*, 1998b).

Type 1b healing (NDH). In this case, the above Dieterich-type log-linear relation is not obeyed, and $\Delta\mu_{pk}$ can be any other function of hold time $f(t_h)$, such as a power law like that proposed by *Coulomb* (1785) and by *Tenthorey and Cox* (2006), or a log-linear law but with much larger cutoff time, e.g. hundreds of seconds as reported by *Nakatani and Scholz* (2004) and *Niemeijer et al.* (2008) (see Figure 4.1a). As shown using the red dotted line in Figure 4.1a, a further variant of Type 1b behaviour can be recognized for which $\Delta\mu_{pk} = \Delta\mu_w = \Delta\mu_r = 0$. This variant has been widely observed, in experiments on ultrafine quartz gouge at high temperature (600 °C) hydrothermal conditions, for

example (*Chester and Higgs*, 1992).

2) Type 2 healing (NDH). In this case, $\Delta\mu_{pk} > \Delta\mu_w$ and $\Delta\mu_r > 0$ (Figure 4.1b). In addition, we may have $\Delta\mu_x = \beta \cdot \log(1+t_h/t_c)$ or any other function of t_h, where $\Delta\mu_x$ represents $\Delta\mu_{pk}$, $\Delta\mu_w$ or $\Delta\mu_r$, and where $\beta = d(\Delta\mu_x)/d\log(t_h)$. A positive $\Delta\mu_r$ has been widely observed in previous studies (*Nakatani and Mochizuki*, 1996; *Karner et al.*, 1997; *Muhuri et al.*, 2003; *Yasuhara et al.*, 2005). A variant of Type 2 behavior, characterized by a permanent change in steady-state friction without slip weakening, i.e. for which $\Delta\mu_w = 0$ and $\Delta\mu_{pk} = \Delta\mu_r > 0$, is shown using the red dotted line in Figure 4.1b. This has been observed by *Olsen et al.* (1998) in quartz-feldspar gouge sheared under hydrothermal conditions at 250 °C.

Type 3 healing (NDH). As a last possibility, $\Delta\mu_{pk} < \Delta\mu_w$ and $\Delta\mu_r < 0$ (Figure 4.1c). As for Type 2 healing, any function of $\Delta\mu_x$ versus t_h could be possible here. Type 3 behaviour has rarely been observed, besides in tests on quartz gouge at low humidity (*Frey and Marone*, 2002). However, the variant for which $\Delta\mu_w = 0$ and $\Delta\mu_{pk} = \Delta\mu_r < 0$, i.e the dotted red line in Figure 4.1c, has been observed experiments on many material, for example quartz gouge (636 °C, *Karner et al.*, 1997) and olivine gouge (400 – 1000°C, *King and Marone*, 2012) tested at hydrothermal conditions, and on a variety of phyllosilicate-rich gouges at room temperature (*Ikari et al.*, 2009; *Carpenter et al.*, 2011; *Tesei et al.*, 2012).

4.3 Experimental Material and Method

The starting material used for our experiments consisted of carbonate fault breccia collected from a surface exposure of the Yingxiu-Beichuan fault, which hosted the devastating 2008 M_w 7.9 Wenchuan earthquake in Sichuan, China. The exposure studied is located ~ 3 km away from the point of the largest surface displacement (~ 11 m, *Zhang et al.*, 2010) associated with the Wenchuan Earthquake, in a region where the coseismic rupture cut through extensive carbonate rocks (*Chen et al.*, 2013a; 2013b, Chapters 2 and 3). A representative sample of fault breccia, taken from this exposure, was brought to the laboratory for crushing, and then sieved using a 35 μm sieve, to produce a simulated fault gouge. X-ray diffraction analyses showed that the simulated gouge consisted of 68% calcite, 29% dolomite, 1% quartz, and 2% clays. The clays were composed mostly of mixed layer smectite-illite (~ 95%) with minor chlorite (~5%). The breccia was chosen as starting material in order to obtain a simulated gouge with a chemically unaltered fault rock composition, appropriate for studying (recurrent) rupture nucleation at depth. A comparison of our results for this material with the frictional behavior of strongly altered clay-rich gouge

representing the dominant fault-core rock at shallow levels (depths up to 7 km, *Chen et al.*, 2013a, Chapter 2) will be made in a future paper (Chapter 5).

We conducted friction experiments on the simulated, breccia-derived fault gouge using the internally heated, pressure-compensated, triaxial testing apparatus plus direct shear assembly described by *Verberne et al.* (2013a and 2013b). The direct shear assembly used in the experiments consisted of a "69" forcing-block configuration specially designed for use in triaxial testing machines (Figure 4.2). For a detailed description, see *Samuelson and Spiers* (2012). The "69" set-up consists of two opposing direct shear blocks, each comprising a half-cylinder with a full-cylindrical base at one end (diameter 35 mm). This geometry has the advantage that the normal stress acting on the gouge layer, sandwiched between two shear blocks, is independent of shear displacement, and equal to the applied confining pressure at all times. Internal pore fluid plumbing provides fluid-access to the shearing surface of each half-cylinder, which consists of a grooved plate of porous (sintered) stainless-steel. These plates provide traction to the sample and ensure uniform access of pore fluid to the sample surfaces.

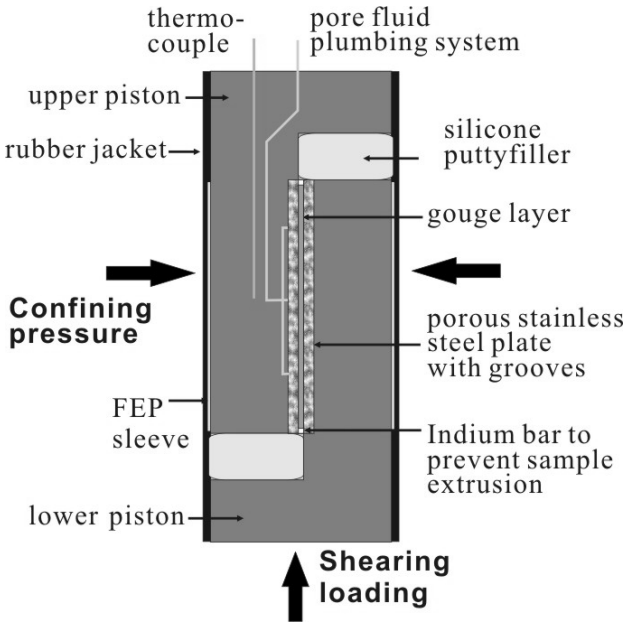

Figure 4.2. Sample assembly used for the present direct-shear experiments performed in a triaxial deformation apparatus.

In preparing each experiment, we mixed ~ 4.5 g of sample power with ~ 1.5 ml

sample-saturated demineralized water, to yield a moldable paste. A specially designed jig allowed for easy emplacement of a 1 mm (± 0.05 mm) thick layer of this gouge paste onto the grooved/porous surface of one of the direct shear blocks. For dry experiments, the sample assembly was dried in an oven at ~ 105 °C for at least 3 hours to remove the added water. The second shear block was then placed on the gouge layer in the "69" orientation (Figure 4.2), and the displacement-accommodating voids at the ends of the gouge layer were plugged with silicone putty enveloped in PTFE foil. Finally, the entire sample assembly was jacketed, first in a thin FEP heat-shrink tube and then using an EPDM rubber sleeve, sealing the latter against the upper and lower shearing block ends with wire tourniquets.

In total, we ran 9 experiments (Table 4.1), comprising three dry and six wet tests, at temperatures (T) of ~ 20 °C, 80 °C and 140 °C, all at an effective normal stress (σ_n) of 50 MPa. Wet tests were performed under drained conditions, using a fluid pressure of 15 MPa and a confining pressure of 65 MPa. Pore fluid pressure was controlled, and sample pore volume changes measured, using a high precision, servo-controlled volumetric pump. Dry experiments were performed with the pore fluid system vented to lab air. As illustrated in Figure 4.2, in each run we applied a total shear displacement of 5 to 6 mm, divided into the following stages: 1) slip at an initially constant "run-in" displacement rate of V = 1 or 10 μm/s, imposed until a steady-state frictional strength was reached, 2) a velocity stepping sequence, 3) a slide-hold-slide sequence, and 4) a final velocity stepping sequence. Each velocity stepping sequence (VS-seq) consisted of switching the load-point displacement rate between 0.1, 1 and 10 μm/s. Slide-hold-slide sequences (SHS-seq) consisted of sliding at a constant velocity (1 μm/s), arresting the load-point displacement for a systematically varied hold time (t_h), followed by resumption of load-point displacement at the pre-hold velocity. For the wet experiments at 80 °C, we also investigated different reshearing velocities (0.1, 1 and 10 μm/s, Table 4.1). In each SHS sequence, we applied 6 – 9 individual hold events, using hold-times that were progressively increased from 35 s to a maximum of 2.35×10^5 s in roughly three-fold jumps. The sliding displacements imposed after each hold were 0.18 – 0.5 mm. One control run was performed on a wet sample at 80°C, implementing three velocity stepping sequences separated first by a single 9-hour and then by a single 4-hour hold-period, and employing an SHS velocity of 1 μm/s. This was done for purposes of comparison with the multi-hold SHS experiments. After testing, representative samples were sectioned and polished, and the microstructure investigated using scanning electron microscopy (SEM).

Table 4.1. List of experiments, conditions and key data.

Experiment	*Type*	*T*	P_c	P_f	V_{SHS}	W_f	ΔW	*Sample behavior*			
								VS-seq1	*SHS-seq*	*VS-seq2*	β_w
Run-14	dry	20	50	atm.	1	0.83	0.17	*s*	type 1a	*s*	0.0086
Run-19	dry	80	50	atm.	1	0.85	0.15	*n* or *w*	type 1a	*n* or *w*	0.0073
Run-20	dry	140	50	atm.	1	0.88	0.12	*w*	type 1a	*w*	0.0060
Run-12	wet	20	65	15	1	0.75	0.25	*s*	type 1a	*s*	0.0117
Run-8	wet	80	65	15	0.1	0.65	0.35	*w* or *n*	type 2	*s*	0.0126
Run-6	wet	80	65	15	1	0.70	0.30	*w* or *n*	type 2	*s*	0.0135
Run-4	wet	80	65	15	10	0.78	0.22	*w*	type 2	*s*	0.0196
Run-22	wet	140	65	15	1	0.70	0.30	*w*	type 2	*cs*	0.0090
Control run	wet	80	65	15	1	0.66	0.33	*w*	type 2	*s*	–

Notation: T (°C) = temperature; P_c (MPa) = confining pressure; P_f (MPa) = pore pressure; V_{SHS} (μm/s) = re-shearing velocity during SHS sequence; W_f (mm) = final thickness of the gouge layer; ΔW (mm) = final thickness change of the gouge layer with respect to an initial thickness of 1 mm (± 0.05 mm); β_w (/decade) = frictional healing rate calculated as $d(\Delta\mu_w)/d\log(t_h)$. The abbreviations "s", "n", and "w" represent velocity strengthening, velocity neutral and velocity weakening, respectively, while "cs" denotes conditionally velocity strengthening behavior, which occurred in the VS-seq2 of Run-22 (see Figure 4.4 for details). Types 1a and 2 healing behavior occurring during SHS testing are defined as in Figure 4.1 and in the text. The single wet control run appearing last in the list was performed with three velocity stepping sequences separated by two SHS events using a single 9-hour and a single 4-hour hold period.

In each experiment, we determined the frictional strength (i.e. the apparent friction coefficient, μ) as a function of displacement from the ratio of the shear stress supported by the sample layer divided by the effective normal stress, assuming zero cohesion. The measured axial displacement was corrected for elastic machine distortion using calibrations obtained from compression tests on a steel dummy of known elastic properties. Calibrations were performed at or near the pressure and temperature conditions used in this study. Using the data obtained in the VS-sequences, the (near) steady-state strength (μ_{ss}) reached before and after each velocity (V) step was employed to determine the friction rate parameter, $(a - b) = \Delta\mu_{ss}/\Delta\ln V$ (*Dieterich*, 1979). At velocities where unstable stick-slip events occurred, the average friction coefficient (i.e. the mean of the maximum plus minimum friction coefficients) taken over all stick-slips occurring at the imposed drive velocity, was taken as the steady-state friction and used to quantify apparent $(a - b)$ values (*Verberne et al.*, 2010).

Positive values of ($a - b$) indicate stable velocity strengthening, while negative values indicate potentially unstable velocity weakening (*Marone*, 1998a). For the SHS-sequences, we determined the frictional healing parameters ($\Delta\mu_{pk}$, $\Delta\mu_w$ and $\Delta\mu_r$) using the definitions given in Section 4.2 (see Figures 4.1 and 4.3 inset). Some of our experiments exhibited minor, near-linear slip weakening behavior, while a few showed minor slip strengthening in some velocity intervals (Figure 4.3). These effects were corrected for, in obtaining changes in (quasi) steady-state friction from our VS and SHS data, by linearly detrending of the data following the approach of *Blanpied et al.* (1995), i.e. by removing the slopes in the data before and after each VS or SHS event (see Figure 4.3 inset). Taking into account errors in internal force measurement (*Verberne et al.*, 2013b), and performing conventional error propagation analysis, the standard errors in a) the absolute friction coefficient (μ), b) the parameters $\Delta\mu_{ss}$, $\Delta\mu_{pk}$, $\Delta\mu_w$ and $\Delta\mu_r$, and c) the frictional rate parameter ($a - b$) determined in our experiments were ± 0.003, ± 0.004 and ± 0.0017, respectively.

In the wet experiments, changes in pore fluid system volume were used to determine changes in thickness of the gouge layer by assuming constant sample surface area (constant shear plane area), and correcting for temperature changes in the fluid exchanged between the sample and the pressure control pump. The error/scatter obtained in determining sample thickness change was about 7 μm. In processing and plotting the volumetric and thickness change data, we employed a second order polynomial smoothing method to reduce noise, yielding an improved resolution of ~ 2 μm.

4.4 Results and Data Analysis

4.4.1 Friction coefficient versus displacement data

All experiments performed are listed in Table 4.1. Typical friction versus displacement curves obtained for dry and wet experiments are illustrated in Figure 4.3, in this case for tests run at 80 °C. All samples showed quasi steady-state frictional strength in the range μ = 0.63 to 0.7, regardless of temperature and sliding velocity. In the dry experiment displayed in Figure 4.3, the VS sequences executed both before and after the SHS-seq displayed velocity neutral or slightly velocity weakening behavior. In the SHS sequence, each SHS event showed mechanical behavior consistent with Type 1a or Type 1b frictional healing behavior, i.e. the steady-state friction coefficient remained unchanged ($\Delta\mu_{pk} = \Delta\mu_w$) after each hold period. By contrast, the healing behavior seen in the wet experiment represented in Figure 4.3 was characterized by a progressive increase in the quasi steady-state friction level attained after each hold, whereby $\Delta\mu_{pk} > \Delta\mu_w$ and $\Delta\mu_r > 0$ (Type 2 healing). Measured relative to background trends in slip weakening, these increases persisted throughout each sliding

stage of the SHS tests on the wet samples (0.18 – 0.5 mm per sliding stage). In the wet control experiment that we performed using long hold periods only (Table 4.1), the increase in quasi steady-state strength attained during subsequent re-sliding persisted for a total displacement of ~ 1.7 mm.

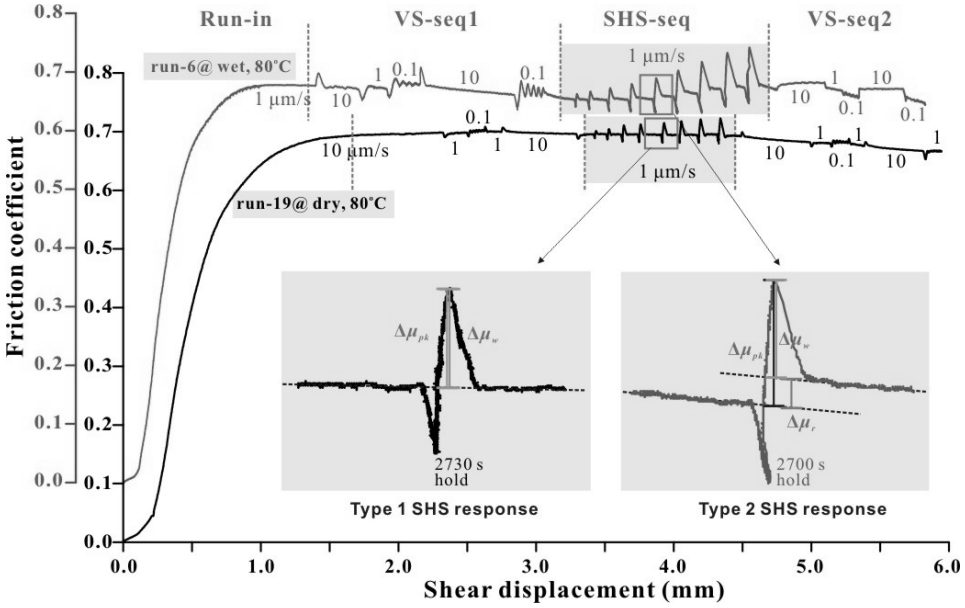

Figure 4.3. Typical friction versus displacement data obtained in the present shearing experiments conducted on dry and wet samples. The data shown here were obtained at a temperature of 80 °C and an effective normal stress of 50 MPa. The wet experiment was performed under a confining pressure of 65 MPa and a pore pressure of 15 MPa. Each experiment consisted of 1) a "run-in" at constant velocity, 2) a velocity stepping sequence (VS-seq1), 3) a slide-hold-slide sequence (SHS-seq), and 4) a second velocity stepping sequence (VS-seq2). The inserts illustrate typical data obtained in individual SHS events. Note how changes in steady-state friction coefficient were obtained from data showing slip weakening (right hand inset).

Alongside the above non-Dieterich-type healing behavior observed during the SHS-seq in the wet experiments depicted in Figure 4.3, of particular interest is that a switch occurred in the velocity dependence of frictional strength before and after the SHS-seq. The first velocity stepping sequence (VS-seq1) showed minor velocity weakening behavior, while velocity stepping after the SHS sequence (VS-seq2) became more stable, generally switching to velocity strengthening (Figure 4.3). This switch did not occur in the dry experiment performed at 80 °C, which showed more or less velocity neutral behavior after the SHS

testing sequence (Figure 4.3). Alongside these observations on samples deformed at 80°C, both dry and wet experiments showed significant effects of temperature on the velocity dependence of friction and on SHS behavior. These effects are addressed below.

4.4.2 Velocity stepping data

The velocity dependence of friction seen in our experiments is examined further now by comparing the friction rate parameter, $(a - b)$, obtained in the VS-seqs executed before and after the SHS-seq, for all experiments, wet and dry. In both the dry and wet experiments, a transition occurred from velocity strengthening to velocity weakening with increasing temperature, as shown in Figure 4.4. In the dry experiments, $(a - b)$ values determined before and after the SHS sequence were indistinguishable, and showed a clear transition from velocity strengthening to weakening at ~ 80 °C (Figure 4.4a). In the wet experiments, $(a - b)$ values determined before the SHS sequence (VS-seq1) were closely similar to those seen in the dry tests, though slightly more scattered, with the transition from velocity strengthening to weakening again occurring at 80 °C (Figure 4.4b). However, the post-SHS velocity stepping sequences (VS-seq2) performed on wet samples showed significantly higher $(a - b)$ values, and much wider variability in $(a - b)$, resulting in velocity weakening being first seen at 140 °C (Figure 4.4b). Thus, our results show that, in wet experiments, implementing an interim SHS-seq leads to an increase in $(a - b)$. In most cases (i.e. velocity steps of 1 – 10 μm/s), this resulted in stable velocity strengthening after the SHS-seq, compared with near neutral or unstable velocity weakening with stick-slips beforehand, implying that SHS testing had a stabilizing effect on frictional sliding in the wet samples (Figure 4.3b, Table 4.1), at least within the displacements investigated here.

4.4.3 Slide-hold-slide results

SHS-seq data from the dry and wet experiments performed at ~ 20, 80, and 140 °C are shown in Figures 4.5a, 4.5b and 4.5c. The frictional healing parameters. $\Delta\mu_{pk}$, $\Delta\mu_w$ and $\Delta\mu_r$, were determined from these data for each individual SHS event, after correction for slip weakening and occasional slip strengthening effects as described in Section 4.3. This approach implicitly assumes that the observed slip weakening or strengthening reflects sample assembly effects, or such as the decrease in load supporting area hence measured strength that occurs in a direct shear experiment, or such as sample thickness changes (e.g. *Frye and Marone*, 2002). That the slip weakening effects seen in our experiments were indeed artifacts of this type is strongly supported by the fact that the rate of change of frictional strength with displacement rapidly approached a constant (slightly negative) value

in the evolution stage following each reshearing event.

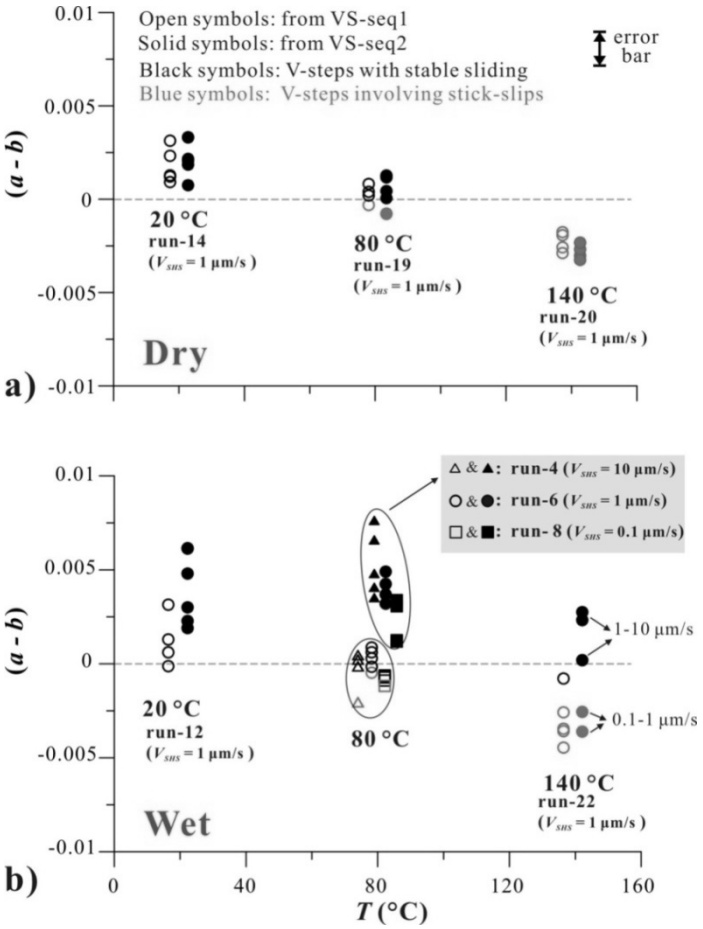

Figure 4.4. Temperature (T) dependence of the friction rate parameter (a – b), determined in velocity stepping sequences performed before (open symbols, VS-seq1) and after (solid symbols, VS-seq2) SHS testing (SHS-seq) in a) dry and b) wet experiments. Circles, squares and triangles at 80 °C in (b) represent (a – b) values obtained in tests employing differing SHS re-shearing velocities (Table 4.1). Note that the individual sequences of (a – b) data obtained at each temperature investigated are plotted at T-values slightly displaced from the corresponding test temperature. This is done for plotting clarity. Some of the (a – b) data (blue symbols), were determined at velocities where stick slip occurred. The mean friction was then used to characterize steady-state friction. Uncertainties in the blue (a – b) data are accordingly expected to be ~ 1.5 times greater than the error bar in (a). The VS-seq2 in Run-22 showed stable, velocity strengthening sliding behavior at velocities stepped between 1 and 10 µm/s, but velocity weakening behavior with stick-slip events at velocities stepped in the range 0.1 – 1 µm/s.

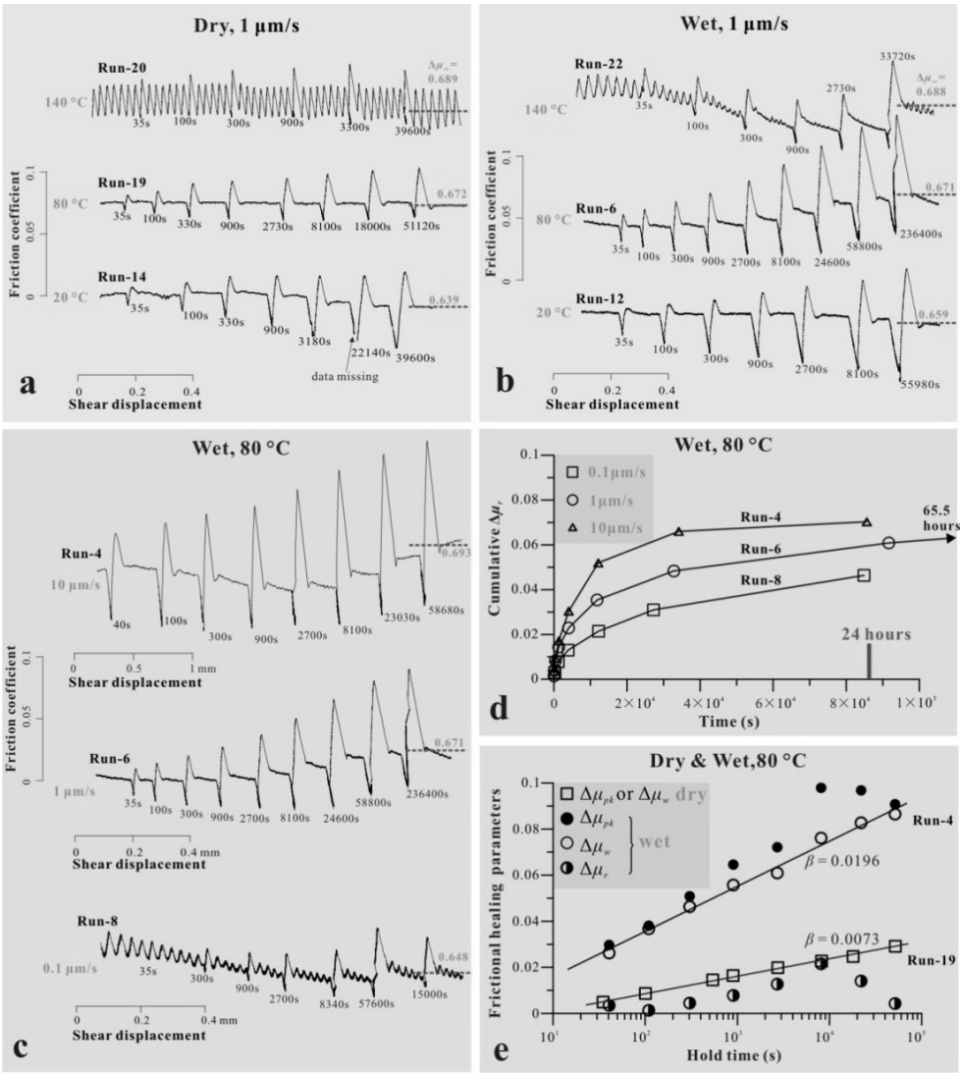

Figure 4.5. Representative results obtained in the present SHS test sequences. Hold times indicted in seconds. a) Friction coefficient versus displacement data for dry samples, at 20, 80 and 140°C, and at a sliding velocity of 1 µm/s . b) Same for wet samples. c) Wet tests at 80 °C but conducted at different reshearing velocities (0.1, 1 and 10 µm/s). d) Cumulative, residual healing-induced re-strengthening ($\Sigma\Delta\mu_r$) as a function of cumulative hold time (denoted as "Time") with data from runs shown in c). Here, the zero cumulative time point (i.e. zero Time) corresponds to initiation of each SHS testing sequence. e) Frictional healing parameters as a function of the logarithm of hold time per individual hold event, for typical dry and wet experiments at 80°C . Note that in run-8 (c and d), the last two hold periods was imposed in reverse sequence by accident.

In all experiments, we observed an increase in healing-induced transient peak strength ($\Delta\mu_{pk}$) with increasing hold time and to some extent with increasing temperature. However, the $\Delta\mu_{pk}$ values, and the extent of stress relaxation during hold, measured in dry experiments were lower in magnitude than in the wet experiments (Figures 4.3 and 4.5b), at the same conditions of hold time, temperature and load-point velocity. The post-peak strength or $\Delta\mu_w$ values obtained in both the dry and wet experiments showed the same trends (Figures 4.5b and 4.5c). As shown in Figure 4.5c, $\Delta\mu_{pk}$ and $\Delta\mu_w$ showed a positive dependence on sliding velocity at otherwise similar conditions, i.e. in wet material sheared at 80 °C. In the dry experiments, $\Delta\mu_{pk}$ and $\Delta\mu_w$ were roughly equal in individual SHS events, yielding a residual strengthening of $\Delta\mu_r \approx$ zero in each case (Type 1a or 1b healing behavior). Positive $\Delta\mu_r$ values (i.e. Type 2 behavior) were seen only in the wet experiments, notably at 80 and 140 °C, where $\Delta\mu_{pk}$ was consistently greater than $\Delta\mu_w$ (Figures 4.5b and 4.5c). In the wet runs at these temperatures, $\Delta\mu_r$ increased rapidly with hold time, for hold times less than ~ 60000 s, then slowing down to approach an asymptotic saturation value, or even decreasing slightly (Figures 4.5b and 4.5c). This "saturation effect" was observed in wet samples tested at both 80 and 140°C, at all re-shearing velocities (V_{SHS}) explored, and is illustrated further in Figure 4.5d, where the cumulative value of $\Delta\mu_r$ is plotted against cumulative hold time for the wet experiments run at 80°C, displaying a positive dependence on V_{SHS}. This, along with Figure 4.5c, clearly demonstrates the positive dependence of all the three healing parameters on load-point velocity seen in wet samples.

The dependence of the three healing parameters, $\Delta\mu_{pk}$, $\Delta\mu_w$, $\Delta\mu_r$, on (non-cumulative) hold event time for a wet sample deformed at 80 °C is illustrated in the plot of Figure 4.5e. The dry result ($\Delta\mu_{pk}$ or $\Delta\mu_w$) at the same temperature is added for comparison. In the dry experiments, the transient peak healing parameter $\Delta\mu_{pk} = \Delta\mu_w$, shows a clear linear relation with log hold time at each temperature investigated, demonstrating Type 1a or classical Dieterich healing (Figure 4.1a). The corresponding healing rates (β-values) obtained slightly decrease from 0.0086 to 0.0060 per decade, in the temperature range 20 – 140 °C (Table 4.1). By contrast, in the wet experiments, $\Delta\mu_{pk}$ exhibits a more complex dependence on t_h (Figure 4.5e). In the wet experiment illustrated in Figure 4.5e, $\Delta\mu_{pk}$ gradually increases to a maximum value at $t_h \approx 10^4$ s and then starts to decrease. However, the post-peak frictional weakening ($\Delta\mu_w$) measured for this sample does show a linear relation with respect to the logarithm of hold time. The same general behavior was observed in the data obtained in all wet experiments except that performed at 20 °C (Table 4.1). The associated healing rates (β_w –values, Table 4.1) for $\Delta\mu_w$ fall in the range 0.009 – 0.0196 per decade, and exhibit a slightly

increasing trend with increasing load-point velocity at fixed temperature (Table 4.1). On this basis, our results for wet samples tested at 80 – 140 °C can be classified as Type 2 healing (Section 4.2) and suggest that the direct healing effect ($\Delta\mu_{pk}$) observed in our wet experiments essentially consists of two components, i.e. a "Dieterich-type" component influencing $\Delta\mu_w$ plus an increase in dynamic friction coefficient ($\Delta\mu_r$ effect) that persists relative to background slip weakening effects, at least for the re-sliding displacements investigated here. In the single wet sample tested at 20 °C, note that $\Delta\mu_r = 0$, corresponding to classical Dieterich-type healing (Figure 4.5b).

Figure 4.6 displays the friction coefficient versus shear displacement data obtained from the wet control run in which three velocity stepping sequences was separated by two SHS sequences with single holds of 9 and 4 hours (Table 4.1). As shown in Figure 4.6a (inset), after the first 9-hour hold period, the quasi steady-state frictional strength increased markedly (VS-seq1 vs. VS-seq2), while a smaller increase occurred after the second 4-hour hold (VS-seq2 vs. VS-seq3). Moreover, a transition from velocity weakening to velocity strengthening occurred immediately after the 9-hour hold period, with velocity strengthening also persisting after the second 4-hour hold.

4.4.4 Volumetric data and microstructural observations

Our method of measuring sample volume changes during deformation from changes in pore fluid volume, means that we have no volume change data for the dry experiments, except for thickness change data (ΔW) based on direct measurement of sample thickness before and after testing (Table 4.1). The mean thickness change (ΔW) measured for dry samples was ~ 0.15 mm, corresponding to ~ 15% porosity reduction (compaction plus any lateral material extrusion). Dry samples showed essentially the same microstructure at all temperature investigated (20 – 140 °C). As illustrated in Figures 4.7a and 4.7b, boundary shear bands developed at the sample margins with a width varying from 50 to 150 μm. These bands are characterized by marked grain size reduction compared with the bulk of each sample, with most particles in the shear bands being less than 1 μm in diameter. By contrast, the main gouge body seen in the dry samples shows a broad grain size distribution with numerous angular clasts similar in size to the coarsest grains present before deformation (Figure 4.7a-c). High magnification, secondary electron imaging of the shear band exhibits a chaotic (no preferred orientation), granular microstructure similar to the gouge bulk, but with much smaller grain sizes (Figure 4.7d).

In the case of the wet experiments, we were able to obtain data on compaction of the gouge layer that occurred during both the VS and SHS testing sequences, as indicated above.

Figure 4.8a exhibits a representative result showing dynamic dilatation/compaction of the entire gouge layer in response to a velocity stepping sequence. Regarding the SHS sequences, significant permanent compaction was recorded, especially during long hold periods, though dynamic dilation upon resliding was not evident (i.e. below the detection limit of ~ 3 μm) (Figure 4.8b). The control experiment featuring two long holds showed large amounts of compaction plus measurable dilatation upon shearing (Figure 4.6b). Typical values of finite thickness change ΔW measured directly for the wet-tested samples lay around a mean of 0.28 mm (0.22 – 0.35 mm, Table 4.1), twice that measured for the dry experiments. Total pore volume changes measured throughout shearing translated to an overall thickness change of

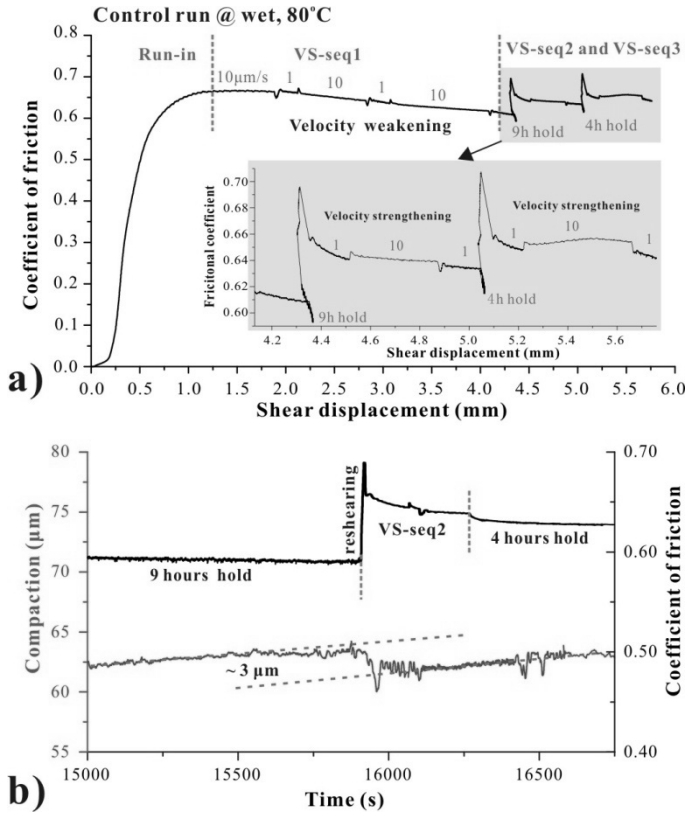

Figure 4.6. Results obtained from a control run in which the SHS sequences were performed for one 9-hour and one 4-hours hold period only, each separating three velocity stepping sequences (VS-seq1-3). a) Coefficient of friction versus displacement. b) Plot of gouge compaction (pore fluid volume reduction) and friction coefficient versus time, showing dynamic dilatation upon reshearing after the 9-hour hold period.

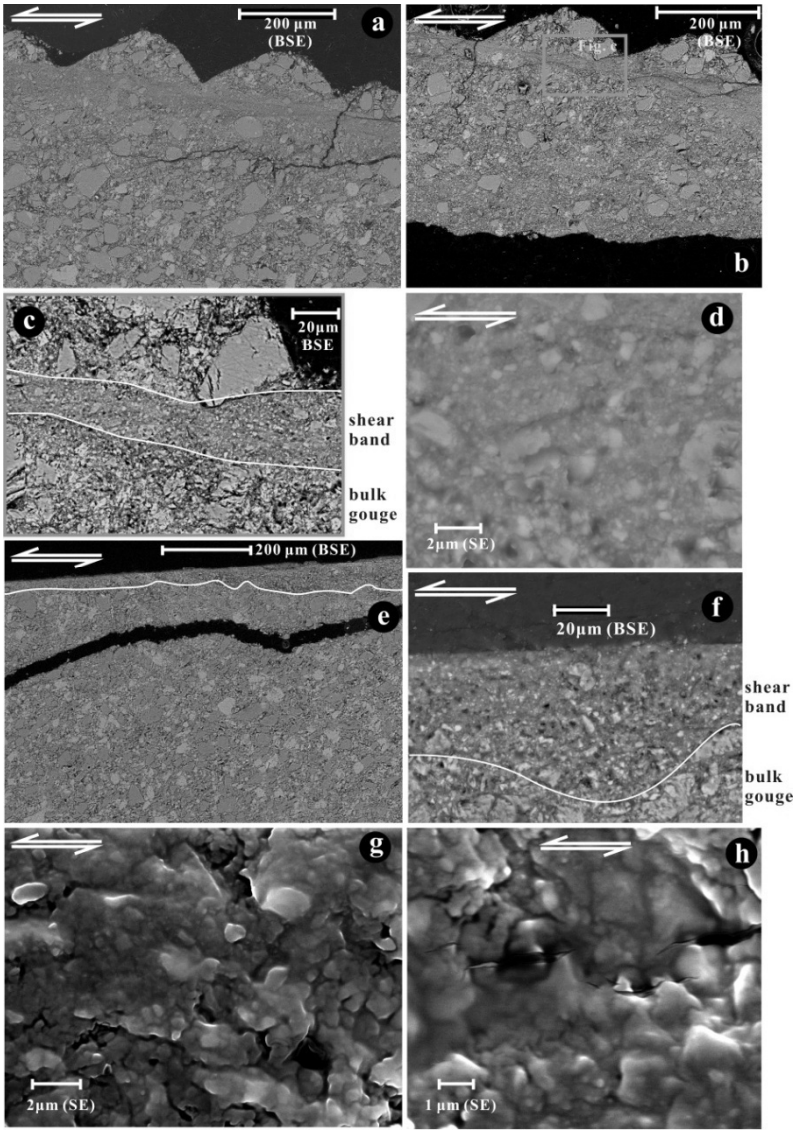

Figure 4.7. SEM microstructures of samples tested dry (a-d) and wet (e-h) at 80 °C. Images a, b, c, e and f were obtained using backscattered electrons. Images d, g and h were obtained from boundary shear zones in wet samples using secondary electrons. Shear sense is as indicated. Note the impression of the toothed sample grips in images (a) and (b) and the sintered appearance of the sub-micrometer-sized grains in (g) and (h). Boundary shear bands are clearly visible in the dry samples (images a-c). They are also visible in the wet samples (e, f), but less clearly, so have been delineated. In (e) and (f), the impressions of the toothed sample grips are not preserved, as the sample surfaces stuck to the grooved piston surface (porous stainless steel, Figure 4.2) when dismantled.

0.075 – 0.16 mm occurring during all stages of deformation. The deformed wet samples show a similar but more uniform microstructure (Figure 4.7e) compared with the dry samples (Figure 4.7a-c). Though visible, the shear bands are less distinct and much denser than those seen in the dry samples (cf. Figures 4.7f-h versus 4.7b-d). The bulk gouge in the wet samples is also finer than in the dry, with a lower proportion of coarse clasts (Figure 4.7e). High magnification secondary electron images showed the shear bands consist of rounded, (sub)micrometer-sized grains that are cemented or sintered together (Figure 4.7g). These sintered aggregates are locally cut by shear-band-parallel cracks that presumably formed during sample unloading or thin-section preparation (Figure 4.7h), suggesting a co-deformational origin of the sintered micro-structure.

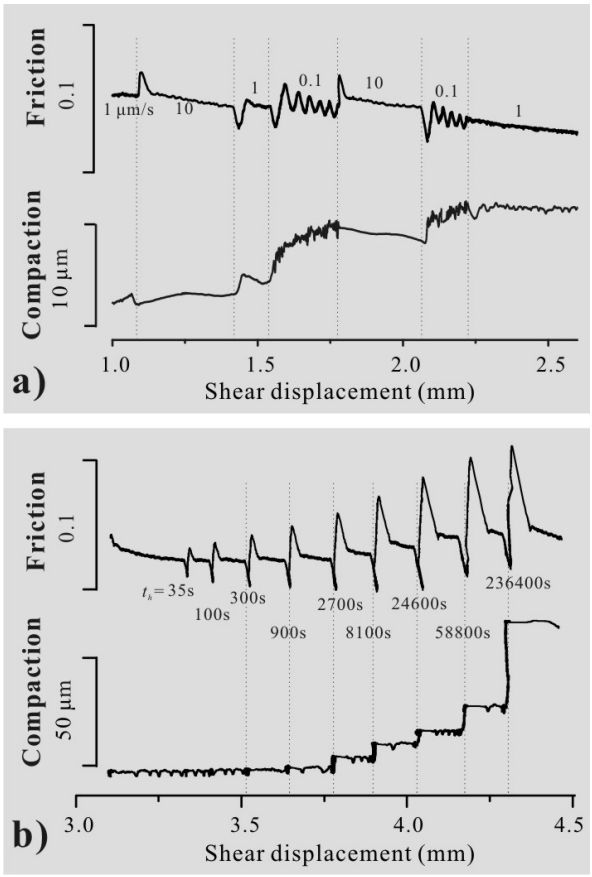

Figure 4.8. Plot of friction coefficient and gouge compaction versus displacement, for the a) VS-seq1 and b) SHS testing sequences performed on a wet sample tested at 80 °C (Run-6). The compaction data was obtained from pore fluid volume changes measured at constant fluid pressure.

4.5 Discussion

4.5.1 Type 1a or Dieterich-type healing in the dry samples

As described above, the SHS stage of our dry experiments showed conventional Dieterich-type (i.e. Type 1a) healing behavior at all temperatures investigated, this being characterized by a linear relation between $\Delta\mu_{pk}$ and log hold time (t_h) and by unchanged steady-state friction before and after each SHS event ($\Delta\mu_r = 0$). This behavior is qualitatively identical to that seen in previous experiments performed on dry quartz and dry granite gouge samples at similar conditions (e.g. *Marone*, 1998b; *Frye and Marone*, 2002). The healing rates obtained in our dry experiments (0.0060 – 0.0086 per decade) are also comparable to those seen in dry quartz and granite gouges. Based on the microstructural (Figure 4.7) and thickness change data (Table 4.1) obtained for our dry samples, we infer that cataclastic grain size reduction and grain rearrangement, leading to granular flow focused in the shear bands found at the boundaries of the samples, were the dominant deformation mechanisms operating during active sliding periods. This is consistent with magnitude of measured compaction being relatively small (Table 4.1). Though we have no direct evidence ourselves, from the conclusions of previous studies addressing Dieterich-type healing (*Dieterich*, 1979), we infer that the mechanisms controlling $\Delta\mu_{pk}$ in our dry SHS testing sequence, likely involved static growth or strengthening of solid-solid contact points, due to indentation creep or surface diffusive transport.

4.5.2 Type 2 (non-Dieterich-type) healing seen in wet samples

The Type 2 or "non-Dieterich-type" healing behavior seen in our wet experiments is a first-time observation for carbonate fault rocks, and the associated slip stabilization effects are novel and interesting. Similar healing behavior, i.e. with $\Delta\mu_r > 0$, has been reported previously but only rarely. Examples include experiments on wet quartz gouge subjected to healing at low (65 °C) (*Yasuhara et al.*, 2005) and high (636 °C) temperatures (*Karner et al.*, 1997), and on wet gypsum at room temperature (*Muhuri et al.*, 2003). *Karner et al.* (1997) performed so-called "hold-slide" experiments in which their gouges were "healed" at high temperature (630 °C) prior to sliding at lower temperature (~ 200 °C). These authors observed an increase in both peak and steady-state friction compared to samples subjected to the same "hold-slide" sequence at 200 °C, i.e. without high temperature treatment. However, the strengthening observed in their experiments, presumably reflected the effects of lithification-induced hardening (*Karner et al.*, 1997) occurring during the hold periods at 630 °C. This likely involved different mechanisms from those operating during sliding at

200 °C, or else the same mechanism but drastically accelerated by the high hold-temperature. In line with our observations (Figure 4.3), the NDH behavior reported by *Yasuhara et al.* (2005) occurred only at elevated temperature. NDH behavior was also absent in the dry control experiment on gypsum reported by *Muhuri et al.* (2003). Unfortunately, neither *Yasuhara et al.* (2005) nor *Muhuri et al.* (2003) reported or analyzed their healing data in a way that can be easily compared with ours. Nonetheless, taking into account their findings as far as possible, we now consider what mechanisms could have played a role in our wet experiments, and how could these explain the Type 2 (non-Dieterich-type) healing behavior observed.

As in the dry samples, the microstructure of our wet samples shows that active displacement was accommodated by cataclastic grain size reduction and flow, focused in localized boundary shear bands. In addition, the sintered/cemented internal microstructure of these bands in the wet samples suggests the operation of a diffusive mass transfer process, such as pressure solution. Previous 1-D compaction experiments on wet granular calcite have also shown that intergranular pressure solution (IPS) is an important deformation mechanism under the P-T conditions investigated here (*Zhang et al.*, 2010). This type of process was inferred to produce enhanced NDH behavior by both *Muhuri et al.* (2003) and *Yasuhara et al.* (2005), on the basis of microstructural evidence, such as crack sealing and pore cementation. In addition, many other studies have demonstrated that solution transfer can significantly enhance healing processes in fault gouges sheared under (hydrothermal) conditions where solution transfer is possible (e.g., *Olsen et al.*, 1998; *Bos and Spiers*, 2002; *Nakatani and Scholz*, 2004; *Niemeijer et al.*, 2008). Frictional re-strengthening in these previous studies was attributed to 1) an increase in intrinsic intergranular cohesive strength (*Yasuhara et al.*, 2005), 2) an increase in cohesive solid-solid contact area within the gouge zone (*Niemeijer et al.*, 2008), or 3) dilatation following fluid-assisted compaction during hold (*Bos and Spiers*, 2002). Any of these three re-strengthening processes could potentially contribute to the transient peak healing effect ($\Delta\mu_{pk}$) seen in our wet experiments at 80 – 140 °C, presumably through their operation within the boundary shear band, and/or the sample body. However, the healing-induced strengthening effect ($\Delta\mu_r$) that we observe is not explained by any of them, as discussed below.

First, in the case of intergranular cohesion, an increase in steady-state friction has been proposed to occur when aggregates of welded grains, formed during hold periods, are forced to move as an assemblage upon reshearing, requiring more mechanical work for dilatation (see Figure 6 of *Yasuhara et al.*, 2005). Evidence for grain aggregation and cementation can be seen in the shear bands in our wet samples (Figure 4.7g, h). However, discrete clusters are

not observed. To examine the viability of this mechanism further, we checked the volumetric data obtained in the control run listed in Table 4.1, in which a long hold period (9 hours) was immediately initiated after the first VS-seq, yielding large transient ($\Delta\mu_{pk}$) and quasi steady-state ($\Delta\mu_r$) healing effects (Figure 4.6a). Transient dilation upon reshearing after this hold was around 4.5 μm settling back to a longer lived baseline effect of ~ 3 μm (i.e. just resolvable by our volumetric pump - see Figure 4.6b). The transient healing effect (i.e. $\Delta\mu_{pk}$) correlates with and is partly explainable by the (smoothed) transient dilatation (dilatation strain × σ_n < $\Delta\mu_{pk}$ × σ_n), perhaps reflecting an effect of the type envisaged by *Yasuhara et al.* (2005). However, the baseline volume increase cannot have been important in determining $\Delta\mu_r$, i.e. in producing the Type 2 healing behavior in our wet experiments at elevated temperatures, because active dilatation was not measured during the steady sliding stages of the experiments. Instead, the samples compacted continuously (see Figure 4.8b).

Static increase in grain contact cohesion or static growth in grain contact area, due to fluid-enhanced indentation creep (IPS), neck growth (*Hickman and Evans*, 1992) or hydrolytic weakening effects (*Frye and Marone*, 2002), without any clustering or other microstructural change occurring during hold or reshearing (as envisaged by *Niemeijer et al.,* 2008), is also unlikely to be the reason for the positive values of $\Delta\mu_r$, hence Type 2 behavior, seen in our wet tests. This is because the enlarged or strengthened contacts would be immediately destroyed when reshearing the gouge layer. Similar reasoning also makes IPS-enhanced compaction, followed by dilatation of pores between individual grains (*Bos and Spiers*, 2002), an unlikely explanation for the observed Type 2 behaviour, as the strength contribution associated with dilation and increased dilation angle falls to zero as the steady-state sliding porosity (or bulk background compaction) is re-established during re-shear. As a result of this, compaction/dilatation can again only contribute to transient peak healing ($\Delta\mu_{pk}$).

A further possibility for explaining the Type 2 healing behavior seen in our wet experiments at 80 – 140 °C is strain localization/delocalization. As proposed by *Sleep et al.* (2000), this can cause changes in frictional strength by altering the strain rate in the active slip zone. However, in the model by Sleep et al., localization/delocalization was only used to explain transient peak healing and the prolonged slip-weakening distance. They assumed that as re-shearing proceeds to steady state, the delocalization return back to the same steady-state level.

Here we propose that the increased dynamic friction ($\Delta\mu_r$) observed in the SHS sequences of our wet experiments at 80 – 140 °C is due to more complex, permanent effects of porosity reduction, occurring in both the shear bands and the gouge body. Our argument is

as follows. First, marked compaction was detected during the hold periods by the precision volumetric pump employed for pore pressure control in the wet tests (Figure 4.8b). This compaction reflects the sum of the sample pore volume change occurring in both the shear band and bulk gouge. Second, porosity reduction by IPS is indicated by the fact that, though both the wet and dry samples had the same initial thickness (1 ± 0.05 mm), the final thickness was much less in the wet samples (~ 0.72 mm) than in the dry samples (~ 0.85 mm). In line with previous evidence for pressure solution in calcite under the present conditions (*Zhang et al.*, 2010), this implies that compaction and porosity reduction by pressure solution must have occurred during the hold periods of our SHS runs, causing an increase in grain-to-grain contact area, contact strength and dilation angle, in both the gouge bulk and boundary shears. The much larger shear stress relaxation that occurred during the hold periods of our wet experiments compared with the dry ones (Figure 4.3 and Figure 4.5a, 4.5b) further supports such a process (*Marone and Saffer*, 2014/2015). We infer that the associated microstructural changes produced a transient increase in frictional strength of the samples that led to the observed peak strength on re-shearing ($\Delta\mu_{pk}$ effect), as interpreted in many previous studies (e.g. *Nakatani and Scholz*, 2004; *Yasuhara et al.*, 2005; *Niemeijer et al.*, 2008). During on-going re-shearing, however, the pre-hold porosity and microstructure were clearly not (fully) restored, as in classical Dieterich healing. Instead, the residual healing effect ($\Delta\mu_r$), seen in our wet samples sheared at 80–140°C, implies that re-shearing was accommodated, presumably in a boundary shear, in gouge material having persistently lower porosity and/or higher contact cohesion, hence persistently higher strength, than the active gouge zone prior to hold.

To achieve such persistent changes in slip zone strength ($\Delta\mu_r$) during post-hold re-shearing, two possible changes in microstructure can be envisaged. One possibility is permanent widening of the principal boundary shear band upon re-shearing (or formation of a new, wider shear band). This would lead to lower shear band strain rates at a given imposed velocity, and hence to more effective internal competition of compaction, by IPS, versus dilatation associated with cataclastic/granular shear flow. The result would be lower steady-state porosity and higher strength. A second possibility is grain size reduction (i.e. grain breakage) occurring within the principal boundary shear upon post-hold re-shearing. This too would lead to an enhancement of compaction by pressure solution relative to dilatation by cataclastic/granular flow, since the rate of pressure solution compaction increases with decreasing grain size (*Zhang et al.*, 2010). We favor this explanation because of the extreme narrowness and submicron grain size of the boundary shear bands seen in our samples (Figure 4.7e-h). Nonetheless, previous microphysical models, based on gouge

deformation by granular flow plus pressure solution, predict increasing steady-state friction with both decreasing particle size and with increasing shear band thickness (*Niemeijer and Spiers*, 2007; *Den Hartog and Spiers*, 2014), so that either explanation seems viable. A quantitative model explaining both the steady-state and transient frictional and healing behavior observed in this study, including healing-induced strengthening, will be developed in a future paper.

Having identified possible origins for $\Delta\mu_r$, and again noting the modest of dilation occurring upon reshear (Figure 4.8b), we propose that the remaining part of the direct healing effect ($\Delta\mu_{pk}$) observed in our wet experiments, i.e. $\Delta\mu_w = \Delta\mu_{pk} - \Delta\mu_r$, reflects changes in contact area and porosity, resulting from more or less irreversible compaction, in combination with reversible static contact growth and/or strengthening, as envisaged in the classical Dieterich model for healing. This is strongly supported by the Dieterich-type healing behavior exhibited by $\Delta\mu_w$ in our data (Figure 4.5e). Hence, our interpretation of $\Delta\mu_{pk}$ in our experiments is that it consists of a Dieterich-type part ($\Delta\mu_w$) related to reversible contact growth and strengthening, plus a non-Dieterich-type part ($\Delta\mu_r$) related to pressure solution compaction, plus a concomitant increase in contact area, all enhanced by permanent grain size reduction or shear band broadening. Similar healing partitioning was previously proposed by *Frye and Marone* (2002) to explain the enhanced healing observed in quartz gouge sheared at relatively high relative humidities at room temperature. In their experiments, water-assisted healing operative at contact junctions was distinguished from an additional compaction-induced strengthening effect, by comparing the results of SHS tests performed with and without normal stress cycling.

4.5.3 Slip stabilization and its cause

In our wet experiments, we observed a clear increase in ($a - b$) after the SHS testing sequence (Figure 4.4). This "fault stabilization" effect was totally absent in dry samples. Previous studies (e.g., *Byerlee*, 1967; *Tullis and Weeks*, 1986; *Wong and Zhao*, 1990) report a similar transition from unstable stick-slip to stable sliding, but this was caused by continued wear with accumulated displacement (*Wong and Zhao*, 1990), especially for slip on initially bare surfaces (*Byerlee*, 1967; *Tulllis and Weeks*, 1986). By contrast, almost all previous experiments on simulated fault gouges show the opposite trend, i.e. from velocity strengthening to velocity weakening with increasing shear displacement (*Dieterich*, 1979; *Marone et al.,* 1990; 1998; *Beeler et al.*, 1996; *Richardson and Marone*, 1999). In our experiments, the stabilization effect was only seen in the wet experiments after the SHS stage, so is unlikely to be due to accumulated displacement. This is confirmed by the control run

(Table 4.1) in which we imposed a 9-hour hold, whereby stabilization occurred immediately after (Figure 4.6a).

An alternative explanation for the stabilization effect that we observed might potentially lie in strain localization/delocalization effects, e.g. of the type proposed by *Sleep et al.* (2000). However, we reject this possibility, because a) the required changes in shear band thickness were not observed in our experiments, compared with runs conducted on calcite by *Verberne et al.* (2013) without a SHS sequence, and b) because in the *Sleep* model strain or strain rate localization/delocalization does not change the value of ($a - b$) (see equation 10, *Sleep et al.*, 2000), but only the frictional strength.

We note here that the stabilization effect seen in our wet experiments at elevated temperatures was always accompanied by Type 2 (NDH) behavior, characterized by a permanent increase ($\Delta\mu_r$) in quasi steady-state friction. As shown in Figures 4.5c and 4.5d, the magnitude of $\Delta\mu_r$ obtained in the SHS-sequences increases with increasing load-point velocity. With reference to Figure 4.9, the increase in ($a - b$) following SHS testing can accordingly be explained by the difference in the accumulated, healing-induced strengthening ($\sum\Delta\mu_r^{V_1}$ and $\sum\Delta\mu_r^{V_2}$) measured at velocities V_1 and V_2. The corresponding change in ($a - b$) can be determined as follows: $\Delta(a-b) = (\sum\Delta\mu_r^{V_2} - \sum\Delta\mu_r^{V_1})/(\ln V_2 - \ln V_1)$.

Based on the data given in Figure 4.5d, the changes in ($a - b$) in our wet samples are ~ 0.0043 for velocity steps of 1 – 10 μm/s, and ~ 0.048 for velocity steps of 0.1 – 1 μm/s. These values are consistent with the increase in ($a - b$) obtained from the VS-sequences performed before and after SHS testing (i.e. with the vertical offset of the VS-seq2 data with respect to VS-seq1 in Figure 4.4b), suggesting that the stabilization effect may be due to the persistent healing-induced strengthening effect discussed above. However, this does not explain the stabilization effect seen at 20 °C, where $\Delta\mu_r$ is more or less zero. Further work is needed to resolve this issue.

4.5.4 Implications

Our SHS observations indicate that standard concepts of frictional healing, as embodied in the log-linear healing effect incorporated in the classic RSF formulation (*Dieterich*, 1972) (i.e. Type 1a healing), need to be modified to describe the interseismic re-strengthening ($\Delta\mu_{pk}$ and $\Delta\mu_r$ behavior) of carbonate-rich fault gouges under hydrothermal conditions where chemically enhanced healing processes such as pressure solution are active. For the same reasons, our results imply that previous estimates of frictional healing rates in simulated

quartz gouges, based on the log-linear fits to dry and room temperature healing data (e.g. *Marone*, 1998b), may significantly underestimate hydrothermal healing rates and magnitudes ($\Delta\mu_{pk}$) that actually apply to the (much longer) interseismic periods of natural faults. It is therefore important to take into account the effects of in-situ conditions and of fluid-rock interaction processes when extrapolating the lab-derived healing rates to natural faults (*cf*. *Nakatani and Scholz*, 2004). In addition, slip associated with aftershocks and changes in fault loading rate may also have important effects on fault re-strengthening processes in nature, which need to be taken into account (Figure 4.7c, *Marone*, 1998b).

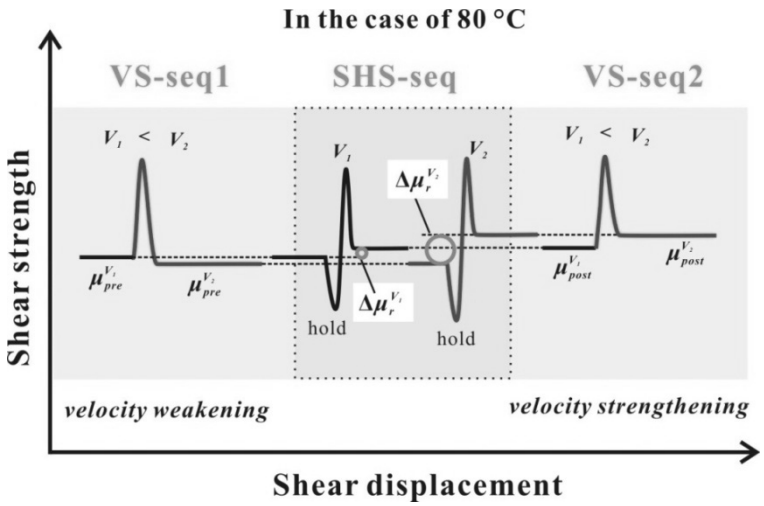

Figure 4.9 Schematic diagram illustrating how "interseismic" healing may cause slip "stabilization", i.e. an increase in (a – b), in the present experiments at hydrothermal conditions (e.g. 80 °C). In line with the "VS-SHS-VS" sequences implemented in our experiments, we infer the following. 1) VS-seq1: the pre-healing steady-state friction coefficients are $\mu_{pre}^{V_1}$ *and* $\mu_{pre}^{V_2}$ *for sliding velocities of* V_1 *and* V_2 ($V_1 < V_2$); *2) SHS-seq: the "interseismic" hold period causes persistent, residual, healing-induced strengthening* ($\Delta\mu_r$), *which accumulates in repeated healing (SHS) cycles and depends positively on active sliding velocity (Figure 4.5d), such that* $\sum\Delta\mu_r^{V_1} < \sum\Delta\mu_r^{V_2}$ *; 3) VS-seq2: the post-healing steady-state friction coefficients here are* $\mu_{post}^{V_1} = \mu_{pre}^{V_1} + \sum\Delta\mu_r^{V_1}$ *and* $\mu_{post}^{V_2} = \mu_{pre}^{V_2} + \sum\Delta\mu_r^{V_2}$. *Note that the SHS-seq presented includes one SHS event for each of the two sliding velocities represented. The change in (a–b) after versus before healing (i.e. SHS testing) can thus be determined from the difference in the accumulated healing-induced strengthening* ($\sum\Delta\mu_r$) *for different velocities, that is from* $\Delta(a-b) = \dfrac{\sum\Delta\mu_r^{V_2} - \sum\Delta\mu_r^{V_1}}{\ln(V_2/V_1)}$. *This scenario applies to the results obtained at 80 and 140 °C, but the behavior seen at 140 °C is more complex due to oscillatory stick-slips.*

In this study on carbonate-rich, breccia-derived sample material (68% calcite, 29% dolomite, 2% clay and 1% quartz), healing rates obtained for $\Delta\mu_w$ (= $\Delta\mu_{pk} - \Delta\mu_r$) in wet samples, at 20 – 140 °C, can be described by a Dieterich-type log-linear fit, yielding β values that fall in the range of 0.009 – 0.0196 per decade, which is higher than the $\Delta\mu_w$ (= $\Delta\mu_{pk}$) healing rates obtained for dry samples, and higher than the reported for dry quartz ($\beta < 0.009$, *Marone et al.* 1998b) or dry phyllosilicate-rich ($\beta < 0.002$) fault gouges (*Carpenter et al.*, 2011; *Tesei et al.*, 2012). Taking into account the residual healing-induced strengthening effect ($\Delta\mu_r$) seen in our experiments (Figure 4.5e), the direct healing effect ($\Delta\mu_{pk} = \Delta\mu_w + \Delta\mu_r$) in carbonate-rich gouge is even higher than predicted from healing rates for $\Delta\mu_w$. Comparison between the healing magnitudes and rates observed in our wet experiments at 20 – 140 °C with those seen in wet quartz under hydrothermal conditions of 65 – 200 °C, is difficult due to the very limited data available for quartz and the different P-T conditions (*Nakatani and Scholz*, 2004; *Yasuhara et al.*, 2005). However, healing in carbonates does seem to be especially rapid. If this applies on the interseismic time scales of major natural faults, then after an earthquake, faults should tend to preferentially regain its strength in segments where carbonate rocks are extensive, at least at the P-T range investigated here.

In addition, our results for carbonate gouge indicate that the "non-Dieterich-type" (Type 2) healing observed under wet conditions can cause an increase in ($a - b$) value. If these results apply to natural faults in carbonates, the implication is that repeated operation of interseismic healing processes, under otherwise unchanging conditions, may tend to stabilize rupture nucleation, assuming that the elastic stiffness of the surrounding rock (K) does not decrease with respect to the critical stiffness ($K_c = \sigma_n(b - a)/D_c$) for unstable (stick-)slip (*Scholz*, 2002), where D_c is critical slip-weakening distance. Other factors that can affect fault slip stability and rupture nucleation, in nature, of course include changes in the tectonically-driven loading rate (*Wong and Zhao*, 1990; *Marone*, 1998b) and the magnitude of local stress perturbations (*Scholz*, 2002).

At the same time, our data for wet samples show that (a–b) decreases with increasing temperature (Figure 4.4b), transitioning from velocity strengthening to weakening with increasing temperature, hence depth. If our results on the effect of healing on (a–b) apply to natural faults, this in turn suggests that, after repeated seismic cycles, the stabilization effect could result in the upper limit of the seismogenic zone migrating to deeper crustal levels in carbonate terrains (Figure 4.4b). In principle, this effect, combined with the enhanced frictional healing effect will tend to promote the occurrence of earthquakes with progressively increasing magnitude in an increasingly narrow depth range. We note, however, we could find no evidence to support the existence of such effects from natural earthquake

records. This absence of such evidence may, of course, reflect preferred operation of other processes, such as initiation/activation of a new, weaker fault plane or principal slip zone at similar crustal level, rather than reactivation of a healed one. If healing of a fault is effective enough via by chemical processes, like cementation (*Chen et al.*, 2013a) or coseismic thermal welding or recrystallization (*Smith et al.*, 2012), the strength of the gouge may exceed the strength of the neighboring fault rocks. Indeed, sub-parallel fault systems are widely observed in carbonate terrains (e.g. *Fondriest et al.*, 2012; *Collettini et al.*, 2014; *Bullock et al.*, 2014), and in the rupture zones associated with Wenchuan earthquake (*Fu et al.*, 2008). Alternatively, broadening of the fault zone could also play a role. That this occurs too is supported by numerous field observations showing that carbonate fault can have fault cores up to 20 m wide (*Billi and Storti*, 2004), characterized by multiple internal slip surfaces and zones (*Collettini et al.*, 2014).

Additional factors that may complicate the evolution of seismicity and the seismic cycle in carbonate terrains include the rapid temperature increase caused by nucleation or propagation of an earthquake rupture (as recently reported for carbonate faults in the laboratory and in nature – see *De Paola* et al., 2011*; Collettini et al.*, 2014; *Bullock et al.*, 2014). Such heating may cause unstable slip at shallow depths that are normally in the velocity-strengthening regime (i.e. T < 80 °C). Moreover, subsequent temperature decay with time and the healing effects ($\Delta\mu_r$) seen in our data, could have important effects on the evolution of (a–b) and hence on aftershock nucleation and distribution with depth (*Chiarabba et al.*, 2009). Studies of 4-D seismological data obtained for earthquakes occurring in carbonate terrains, such as the Apennines, may offer a means of assessing these speculations in future.

4.6 Conclusions

In the present study, we have investigated the frictional stability and healing behavior of a simulated carbonate fault gouge under dry and wet conditions, using a direct shear setup operated within a triaxial testing machine at temperatures in the range 20 – 140 °C and effective normal stresses of 50 MPa. The following conclusions have been drawn.

1) Velocity stepping tests yielded quasi steady-state friction coefficients in the range 0.63 – 0.7, depending on sliding velocity and temperature, in agreement with previous data for wet and dry carbonate gouges. However, SHS testing under hydrothermal conditions showed non-Dieterich-type healing behavior, characterized by a persistent increase in quasi steady-state friction coefficient after hold, superimposed on any background slip-weakening or slip-strengthening trends . This behavior was not seen in dry experiments.

2) Mechanisms previously proposed to explain frictional healing cannot fully explain this persistent, residual increase in quasi steady-state friction coefficient observed here in carbonate gouge under hydrothermal conditions. This healing-induced strengthening is inferred to reflect the frictional behavior of localized principal shear bands, and to be related to enhanced compaction of these bands by internal pressure solution, due to permanent grain size reduction or to shear band broadening upon re-shear (*cf. Sleep et al.*, 2000). Welding-induced dilatation (*Yasuhara et al.*, 2005) does not seem to explain the experimental results well.

3) To the best of our knowledge, our experiments on wet carbonate gouge are the first to show that slide-hold-slide testing, or interseismic healing, can cause changes in slip stability, i.e. an increase in the RSF rate parameter ($a - b$). In our experiments, this increase leads to a concomitant shift in the temperature above which velocity weakening becomes important in wet calcite-rich gouge from around 80°C (as reported by *Verberne et al.*, 2010, , 2013a and 2013b) to above 140°C.

4) If the above stabilization effect seen in the present experiments applies to faults in tectonically active carbonate terrains, it implies a tendency for shift in the upper limit of the seismogenic zone to deeper, warmer crustal levels, following interseismic healing events. This shift, combined with the persistent, residual strengthening effect seen in our healing data, will tend to promote the occurrence of progressively stronger earthquakes at deeper and deeper levels in a gradually shrinking seismogenic zone.

5) In practice, competing processes, such as the initiation of new (weaker) faults, or frictional heating by seismic rupture propagation and the effects of this temperature increase on the propensity for velocity weakening (i.e. on $a–b$), will likely complicate the above picture, through effects on both main shock and aftershock distributions. Future studies of seismicity in carbonate terrains may shed light on whether the effects observed in our experiments do actually play any role in nature.

Acknowledgements: We would like to thank Peter van Krieken and Gert Kastelein for their technical support in maintaining the testing machine. We also benefitted from discussions with A.R. Niemeijer, C. He, L. Zhang and L. Yao. JC was funded by the Foundation of State Key Laboratory of Earthquake Dynamic (LED2010A03) and the Netherlands Center for Solid Earth Science (ISES) grant 2013-103, while BAV was supported by ISES grant 2011-75.

Chapter 5

Effects of healing on the seismogenic potential of carbonate fault rocks: Experiments on samples from the Longmenshan Fault, Sichuan, China

Jianye Chen, and Christopher J. Spiers

Abstract

Numerous studies have focused on characterizing the frictional properties of silicate rocks but little data is available on carbonates, especially regarding the effects of slip and healing history on frictional strength and slip stability in the earthquake nucleation regime. We investigate these effects by means of friction experiments performed on simulated gouges derived from an immature carbonate fault breccia and a clay/carbonate fault-core gouge, collected from a surface exposure of the Longmenshan fault zone (LFZ) which hosted the 2008 Wenchuan earthquake. The experiments consisted of direct shear tests involving sequential velocity stepping (VS), slide-hold-slide (SHS) and velocity stepping stages, and were conducted under a variety of wet and dry conditions at temperatures up to 140 °C and an effective normal stress of 50 MPa. Dry experiments performed on breccia-derived samples showed zero dependence of (quasi) steady-state friction, on SHS or VS history, and were characterized by classical "Dieterich-type" healing behavior. By contrast, experiments performed on breccia- and gouge-derived samples under hydrothermal conditions were characterized by "non-Dieterich" healing behavior. This included 1) an increase in (quasi) steady-state friction coefficient ($\Delta\mu_r$) upon re-sliding after a hold period, and 2) an increase in the velocity dependence parameter, ($a–b$), after SHS testing. The transient peak frictional healing ($\Delta\mu_{pk}$) observed in these experiments was essentially composed of two components – a post-peak strength decrease ($\Delta\mu_w$) that increased linearly with the logarithm of hold time, plus the changes in steady-state friction ($\Delta\mu_r$). Further analysis suggests that the healing behavior seen in our wet experiments was related to enhanced solution transfer processes, occurring during hold periods. Our findings indicate that under hydrothermal conditions, such processes can strongly promote fault strength recovery rates, especially in clay-rich fault gouges. When applied to carbonate terrains, this suggests that the shallow portion of a fault with phyllosilicate-rich cores, as seen in the LFZ, can heal at rates much higher than previously recognized. At the same time, the observed slip stabilization effect, i.e. the increase in ($a–b$), implies that the upper limit of the seismogenic zone may progressively migrate to deeper crustal levels. These effects have important implications for understanding the seismic cycle in tectonically-active carbonate terrains.

5.1 Introduction

In the continental crust, most moderate-to-large earthquakes nucleate on faults at mid-to-lower crustal depths, i.e. at 10– 25 km (*Sibson*, 1982; *Scholz*, 2002). For this reason, studies of rupture nucleation and propagation have focused mainly on characterizing the frictional properties of crystalline basement rocks, such as granite, gabbro and gouges derived from these (e.g. *Dieterich*, 1972; *Byerlee*, 1978; *Fredrich and Evans*, 1992; *Blanpied et al.*, 1995; *Marone*, 1998b; *He et al.*, 2007). However, in tectonically active, carbonate cover terrains, destructive earthquakes often nucleate at shallower levels (e.g. *Chiarabba et al.*, 2009). Recent frictional sliding experiments conducted on simulated calcite(-rich) fault gouges at upper-crustal conditions, have revealed that these materials are both strong (friction coefficient of ~ 0.7) and prone to velocity weakening slip at relatively low temperatures (as low as 80 °C) (*Verberne et al.*, 2013a). This is consistent with the shallow seismicity and shallow upper limit of the seismogenic zone seen in carbonate cover regions (e.g. *Bernard et al.*, 2006; *Chiarabba et al.*, 2009). Destructive earthquakes occurring in such terrains include the 1995 Mw 6.2 Aigion earthquake in Greece (hypocentral depth 7.2 km, *Bernard et al.*, (2006)), the 2009 Mw 6.3 L'Aquila earthquake in Italy (hypocentral depth 9.5 km, *Chiarabba et al.*, (2009)) and the 2008 Mw 7.9 Wenchuan earthquake in Sichuan, China (< 10 km depth in the northern segment, *Zhao et al.*, (2010)). Despite such events, though, very few data are available on the frictional behavior of carbonate fault rocks, and to improve seismic hazard assessment in carbonate terrains, a much better understanding of the frictional properties of natural carbonate fault rocks is needed.

Most of the frictional experiments that have been done on carbonate rocks to date were performed at coseismic slip rates (e.g., *Han et al.*, 2007; *De Paola et al.*, 2011). Only a few studies have addressed the rate-and-state friction (RSF) behavior in the seismic nucleation regime or the underlying microphysical mechanism(s)that lead to stable (aseismic) vs. unstable (seismogenic) slip (*Weeks and Tullis*, 1985; *Olsson*, 1974; *Verberne*, 2010; 2013b; *Scuderi et al.*, 2013). Even fewer studies have addressed carbonate fault healing and associated strength recovery, though these aspects have been widely studied in relation to both natural (*Li et al.*, 2003; *Marone et al.*, 1995) and laboratory faults (*Wong and Zhao*, 1990; *Karner and Marone*, 2000; *Nakatani and Scholz*, 2004) in silicate rocks, as they strongly affect earthquake nucleation, magnitude and recurrence intervals (e.g. *Ruina*, 1983; *Marone*, 1998a, 1998b).

Moreover, while numerous studies have investigated the effects of mineral and fluid composition, environmental conditions and fault displacement on the slip-rate dependence of friction in silicate rocks (see reviews by *Marone* (1998a) and by *Paterson and Wong* (2005)),

we are aware of no work experimentally addressing how the slip rate dependence of friction in either silicates or carbonates evolves with time, especially in (static) interseismic periods. In both experiment and nature, carbonate rocks are well known to exhibit ductile deformation by mechanisms such as crystal plasticity and pressure solution, at lower pressures and temperatures than generally required for similar mechanism to operate in silicate-dominated crustal rocks (*Liu et al.*, 2002; *Spiers et al.*, 2004). At seismogenic depths, where these thermally activated and (or) fluid-assisted deformation mechanisms are expected to operate, faults heal during interseismic periods, as the internal microstructural state of the gouge changes (e.g. *Yasuhara et al.*, 2005; *Niemeijer et al.*, 2008). However, how healing by these processes may affect the velocity dependence of fault friction is virtually unexplored.

Lastly, the effects of phyllosilicates on the frictional and healing properties of carbonate fault rocks needs to be considered. Phyllosilicate-rich fault rocks have long attracted attention (*Morrow et al.*, 1992; *Tembe et al.*, 2010; *Carpenter et al.*, 2012; *Zhang and He*, 2013; *Den Hartog et al.*, 2013), due to their widespread occurrence and role in controlling the dynamics of rupture nucleation and propagation at shallow crustal levels (e.g. *Verberne et al.*, 2010; *Tesei et al.*, 2012; *Ikari et al.*, 2013). It is well known that phyllosilicates can significantly reduce fault frictional strength (e.g. *Tembe et al.*, 2010) as well as and rates of inter-seismic fault re-strengthening (*Bos and Spiers*, 2002; *Carpenter et al.*, 2012). Recent studies of faults, such as that hosting the 2008 Mw 7.9 Wenchuan earthquake (*Hou et al.*, 2012; *Chen et al.*, 2013a), have revealed that clay mineral content can become strongly enriched in carbonate fault cores (see also *Bullock et al.*, 2014; *Viti* et al., 2014), due to extensive rock-fluid interaction (e.g. *Chen et al.*, 2013a; *Bullock et al.*, 2014). This raises the question of how clay minerals influence the frictional and healing behavior of clay/carbonate fault core rocks under in-situ hydrothermal conditions.

In this paper, we expand on previous preliminary experiments (*Chen et al.*, submitted, Chapter 4) with the aim of determining the rate dependence of friction, and the effects of healing upon this, in both dry and wet carbonate and carbonate-clay fault rocks subjected to direct shear at 0.1–10 μm/s, at 20 to 140 °C and at 50 MPa effective normal stress. The samples used were derived from both immature carbonate breccia and clay-rich fault core gouge collected from a surface exposure of the Wenchuan earthquake rupture, Sichuan, China (*Chen et al.*, 2013b, Chapter 3). Our results show marked healing and history-related slip stabilization effects in the presence of water. We consider the microphysical mechanisms responsible for the observed behavior as well as the implications of our results for fault slip, slip stabilization and interseismic strength recovery in tectonically-active carbonate terrains in general.

5.2. Materials and Methods

5.2.1 Sample materials

We collected samples from a surface exposure of the Yingxiu-Beichuan Fault (YBF), a principal branch of the Longmenshan Fault zone (LFZ), which hosted the devastating 2008 Mw 7.9 Wenchuan Earthquake rupture (Sichuan, central China). A 240-km long surface rupture was generated during the Wenchuan earthquake (*Xu et al.*, 2009), with the largest displacement of ~ 11 m occurring on the YBF some 3 km from our sampling site (*Zhang P. et al.*, 2010; *Chen et al.*, 2013a; 2013b). At the exposure studied, the coseismic rupture cuts through extensive carbonate strata, reactivating a ~ 5m-wide fault zone with a typical breccia-gouge-breccia sandwich structure (*Mizoguchi et al.*, 2008; *Hou et al.*, 2012; *Chen et al.*, 2013a). The width of the fault core is extremely narrow, with a 2-cm-thick gouge developed in the center, representing the only principal slip zone that can be found within the fault. Mineralogical analysis revealed increasing enrichment in clay toward the slip zone, from ~ 2% at the margin to 35% in the fault gouge. A detailed description of the exposure and relevant fault rocks is given by *Chen et al.* (2013a, Chapter 2).

In the experiments reported here, a representative clay-rich gouge sample and a typical (clay-poor) breccia sample were chosen as starting material(s). Quantitative X-ray diffraction analyses revealed that the fault breccia mainly consists of calcite (68%) and dolomite (29 %),with minor clay (2%) and quartz (1%). The fault gouge consists of clays (35%, smectite-illite and chlorite), quartz (29%), dolomite (27%) and calcite (7%), with minor feldspar (2%). Simulated fault gouges were produced from both materials by crushing and sieving to produce powders with a grain size (sieve mesh) less than 35 μm. The breccia sample was chosen in order to obtain a simulated gouge with a chemically unaltered fault rock composition, appropriate for studying (recurrent) rupture nucleation at depth, while the gouge sample was used to represent the fault core material developed in the shallow portion of the fault zone (*Chen et al.*, 2013a; 2013b). Where context leaves no ambiguity, the term "gouge" will be used in this paper to cover both simulated and natural gouges.

5.2.2 Experimental apparatus and direct shear sample assembly

All experiments were performed on 1 mm layers of the above-mentioned gouges, sandwiched in a direct-shear sample assembly located within a conventional triaxial testing apparatus. The triaxial machine comprised a pressure vessel and pressure-balanced axial loading piston (see *Verberne et al.,* (2013b)). Confining pressure was applied using an external diaphragm pump, and held constant to within ~ 0.1 MPa of the desired test value,

using an ISCO servo-controlled pump. An internal force gauge, incorporating a differential variable reluctance transformer, allowed measurement of axial force independently of seal friction. In wet experiments, pore pressure was applied and controlled using a three term (P-I-D), high-precision, volumetric servo-pump constructed at Utrecht. During individual wet experiments, pore fluid volume changes determined using this system, were used as a measure of sample compaction or dilatation normal to the shear plane. In experiments at elevated temperature, heating was achieved using a Thermocoax internal furnace, and temperature was controlled using a CAL2300 controller. Sample temperature was measured using a thermocouple located within the direct shear assembly, close to the sample layer (Figure 5.1a). Temperature fluctuations varied within ± 2.0 °C during each experiment.

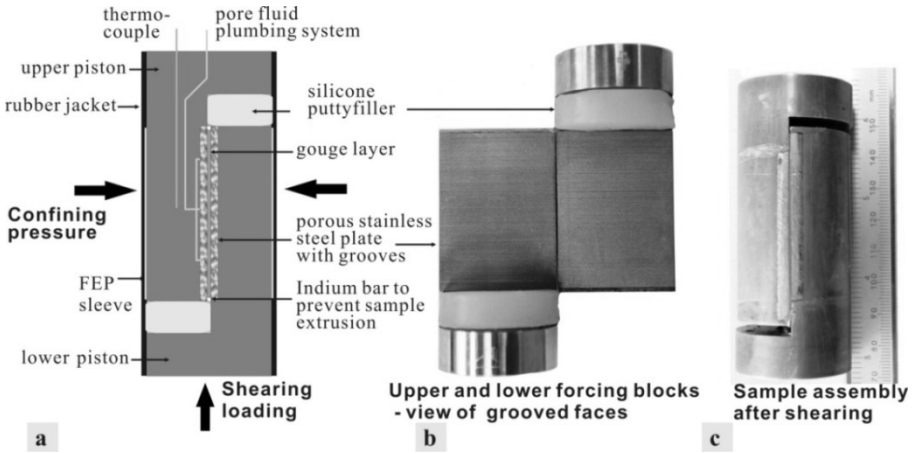

Figure 5.1. Sample assembly used for the present direct shear experiments performed in a triaxial deformation apparatus. a) Cross-section of the sample assembly. b) Upper and lower "69" shearing blocks with grooved plates of porous stainless steel. c) Sample assembly after deformation, with extruded silicone putty filler removed.

The direct shear assembly used in the experiments consisted of a "69" or direct shear forcing block set specially designed for use in triaxial testing machines (Figure 5.1). For a detailed description, see *Samuelson and Spiers* (2012) and *Verberne et al.,* (2013b). The set-up consists of two, opposing, direct shearing blocks, each comprising a half-cylinder with a full-cylindrical base at one end (diameter 35 mm). Besides being easily jacketable, this geometry has the advantage that the normal stress acting on the gouge layer, sandwiched between two shear blocks (Figure 5.1a), is independent of shear displacement, and is equal to the applied confining pressure at all times. Internal pore fluid plumbing provides fluid-access to the shearing surface of each half-cylinder, which consists of a grooved plate of porous

(sintered) stainless-steel (Figure 5.1a). These plates provide traction to the sample and ensure even access of pore fluid to the sample surfaces (Figure 5.1b). The grooves are spark-eroded into the porous plates at a spacing of 200 μm, being 120 μm-wide and 60 μm-deep (Figure 5.1b).

In preparing each experiment, we mixed ~ 4.5 g of sample power with ~ 1.5 ml sample-saturated demineralized water, to yield a moldable paste. A specially designed jig allowed for easy emplacement of a 1 mm (± 0.05 mm) thick layer of this gouge paste onto the grooved/porous surface of one of the direct shear blocks. Initial layer dimensions measured 49 mm in length by 35 mm in width. For dry experiments, the sample assembly was dried in an oven at ~ 105 °C for at least 3 hours to remove the added water. To avoid extrusion of sample material upon shear deformation, 1 mm sections of the sample layer length were removed from the ends of the layer, using a razor blade, and replaced by two soft indium bars measuring 1×1×35mm. In this way, a 47×35×1 mm plate of gouge paste was left, onto which the second shear block was placed (Figure 5.1a and 5.1c). The displacement-accommodating voids (9 mm long) at the ends of the gouge layer were then plugged with silicone putty enveloped in PTFE foil (Figure 5.1b). These plugs "flow" in response to axial shortening of the shear assembly, accommodating the imposed shear displacement with undetectable shear resistance (Figure 5.1c). Finally, the entire sample assembly was jacketed, first in a thin FEP heat-shrink tube and then using an EPDM rubber sleeve of ~ 1.4 mm thickness, sealing the latter against the upper and lower shearing blocks with wire tourniquets.

5.2.3 Experimental procedure

In performing each experiment, the jacketed assembly was first loaded into the pressure vessel and externally pressurized to a confining pressure of ~ 8 MPa. For runs at elevated temperature, we then switched on the furnace and waited for at least 6 hours until a near-constant sample temperature was achieved. Sample temperatures of 20 °C, 80 and 140 °C were employed. As the sample temperature approached the target value, the confining pressure also increased. This was manually maintained below the test value until thermal equilibrium was reached, at which point servo-control of the confining pressure was enabled. Wet experiments were conducted using a confining pressure of 65 MPa, while for dry tests we used 50 MPa. In the case of wet experiments, the pore fluid system was charged by evacuating for ~ 15 minutes, then injecting demineralized water under vacuum. The fluid was subsequently pressurized to a constant value of 15 MPa using the high-precision volumetric servo-pump.

After full P-T equilibration, each experiment was initiated by advancing the loading piston at a constant displacement rate of 1 or 10 μm/s. After reaching steady-state sliding, we conducted, in this order, a "velocity stepping" sequence, then a "slide-hold-slide" sequence, and finally a second "velocity stepping" sequence. The velocity stepping sequences (VS-seq1 and VS-seq2) involved switching the load point velocity between 0.1, 1 and 10 μm/s in 5–6 steps, while the slide-hold-slide sequence (SHS-seq) consisted of 6–9 individual SHS events performed using a single velocity per experiment of 0.1, 1 or 10 μm/s. Each SHS event involved imposing the chosen sliding velocity (V_{SHS}) until a displacement of 0.2 – 0.5 mm was achieved, followed by a stationary hold period of 35 s to 65.5 hrs duration, and then by re-shearing at the same velocity (V_{SHS}). The hold times (t_h) used were typically increased from 35 s to a maximum of 2.35×10^5 s (65.5 hours), in jumps of roughly half an order of magnitude (~ factor 3).

All experiments performed are listed in Table 5.1. They fall into four sets. Three of these correspond to experiments performed on samples prepared from wet fault gouge (Dataset 1), dry fault breccia (Dataset 2) and wet fault breccia (Dataset 3). We did not conduct experiments on dry fault gouge because the smectite components would dehydrate when subjected to elevated temperatures, rendering the results inapplicable to natural conditions. In each of the above sets of experiments, we systematically varied the experimental temperature (T = ~ 20 °C, 80 °C and140 °C), and the reloading velocity employed in the SHS sequences (V_{SHS} = 0.1, 1 and 10 μm/s). Note that, in a few runs, only VS or SHS testing was performed, in the latter case with hold times first increasing and then decreasing (Runs 2 and 4, Table 5.1). One test (Run-11) was performed using a single hold period (5.5 hours), for comparison with the multi-hold experiments. Another test was run using a random hold time sequence (Run-9). This was done to investigate the effect of slip/hold history on frictional healing.

Besides the three sets of experiments addressed above, we conducted a fourth set of control experiments, in which the composition of the pore fluid was varied to gain insight into the nature of fluid-rock interactions occurring (Table 5.1). In three of these experiments, we used NaH_2PO_4 solution (0.01 M) as pore fluid. The presence of phosphate ions in solution is known to slow down the rate of intergranular pressure solution creep (e.g., *Zhang X., et al.*, 2010). In a second set of three experiments, we used silicone oil as a chemically inert fluid. Finally, to test the effect of pore pressure on our wet experiments, an additional experiment was performed on a water-saturated sample drained to atmospheric conditions. In all experiments employing an aqueous pore fluid, since the gouge samples used were fine grained and the time between fluid injection and test initiation were typically 8 hours, we

assume that the pore fluid was close to being saturated with the soluble components of the samples (see also *Chen et al.*, submitted, Chapter 4).

Table 5.1. List of experiments, conditions and key results.

Exp.	T	P_c	P_f	Pore fluid	V_{SHS}	μ_{max}	W_f	Testing type	Healing type	
Dataset 1: Wet gouge-derived samples										
Run-31	20	65	15	sat. water	0.1	0.310	0.75	VS-SHS-VS	Type 3	
Run-27	20	65	15	sat. water	1	0.308	0.65	VS-SHS-VS	Type 1a	
Run-25	20	65	15	sat. water	10	0.309	0.80	VS-SHS-VS	Type 3	
Run-29	80	65	15	sat. water	0.1	0.296	0.60	VS-SHS-VS	Type 2	
Run-26	80	65	15	sat. water	1	0.322	0.75	VS-SHS-VS	Type 2	
Run-30	80	65	15	sat. water	10	0.303	0.65	VS-SHS-VS	Type 2	
Run-32	140	65	15	sat. water	0.1	0.337	0.50	VS-SHS-VS	Type 2	
Run-28	140	65	15	sat. water	1	0.310	0.55	VS-SHS-VS	Type 2	
Run-33	140	65	15	sat. water	10	0.330	0.50	VS-SHS-VS	Type 2	
average						0.314	0.64			
Dataset 2: Dry breccia-derived samples										
Run-15	20	50	atm.	lab air	0.1	0.652	0.80	VS-SHS-VS	Type 1a	
Run-14	20	50	atm.	lab air	1	0.65	0.83	VS-SHS-VS	Type 1a	
Run-3	20	50	atm.	lab air	10	0.68	0.75	VS-SHS-VS	Type 1a/3	
Run-23	80	50	atm.	lab air	0.1	0.70	0.85	VS-SHS-VS	Type 1a	
Run-19	80	50	atm.	lab air	1	0.698	0.85	VS-SHS-VS	Type 1a	
Run-16	80	50	atm.	lab air	10	0.691	0.95	VS-SHS-VS	Type 1a	
Run-1	140	50	atm.	lab air	0.1	0.721	0.90	VS	Type 1a	a
Run-20	140	50	atm.	lab air	1	0.71	0.88	VS-SHS-VS	Type 1a	
Run-18	140	50	atm.	lab air	10	0.693	0.85	VS-SHS-VS	Type 1a	
average						0.688	0.85			
Dataset 3: Wet breccia-derived samples										
Run-5	20	65	15	sat. water	0.1	0.635	0.70	VS-SHS-VS	Type 1a	
Run-12	20	65	15	sat. water	1	0.667	0.75	VS-SHS-VS	Type 1a	
Run-2	20	65	15	sat. water	10	0.66	0.65	SHS(in-/decreasing)	Type 1a	b
Run-8	80	65	15	sat. water	0.1	0.67	0.65	VS-SHS-VS	Type 2	
Run-6	80	65	15	sat. water	1	0.67	0.70	VS-SHS-VS	Type 2	
Run-11	80	65	15	sat. water	1	0.664	0.67	VS-H-VS	Type 2	c
Run-4	80	65	15	sat. water	10	0.68	0.78	SHS(in-/decreasing)	Type 2	b
Run-10	140	65	15	sat. water	0.1	0.65	0.65	VS-SHS-VS	Type 2	
Run-22	140	65	15	sat. water	1	0.682	0.70	VS-SHS-VS	Type 2	
Run-9	140	65	15	sat. water	1	0.695	0.58	VS-SHS-VS	Type 2	d
Run-7	140	65	15	sat. water	10	0.69	0.72	VS-SHS-VS	Type 2	
average						0.669	0.69			
Dataset 4: Control runs on breccia-derived samples										
Run-37	20	65	15	phos.sol.	1	0.708	0.80	VS-SHS-VS	Type 2	e
Run-34	80	65	15	phos.sol.	1	0.672	0.75	VS-SHS-VS	Type 2	e
Run-35	140	65	15	phos.sol.	1	0.628	0.78	VS-SHS-VS	Type 2	e
Run-47	20	50	atm.	silicone	1	0.715	0.85	VS-SHS-VS	Type 1a	f
Run-44	80	50	atm.	silicone	1	0.705	0.85	VS-SHS-VS	Type 1a	f

Run-46	140	50	atm.	silicone	1	0.720	0.85	VS-SHS-VS	Type 1a	f
Run-13	80	50	atm.	sat. water	1	0.645	0.70	VS-SHS-VS	Type 2	g

Abbreviations: T = temperature (°C); P_c = confining pressure (MPa); P_f = pore fluid pressure (MPa); V_{SHS} = load point velocity used during the SHS stages (μm/s); μ_{max}= peak strength of material picked from the friction-displacement curves at a slip rate of 10 μm/s (interpolated where necessary); W_f = final thickness of the gouge layer (mm); VS = velocity stepping; SHS = slide-hold-slide; atm.= atmospheric pressure; phos.sol.= phosphate solution; sat. water = sample-saturated demineralized water.

a. *Occurrence of marked stick slips at all sliding velocities used. Velocity stepping sequence only.*

b. *SHS tests only, in which the hold times used were first applied in a forward (increasing) sequence and then in the reverse (decreasing) sequence (e.g. 35s-100s-300s-900s-2700s-8100s-55800s- 8100s-2700s-900s-300s-100s-35s).*

c. *A run, in which the SHS sequence contained one hold period (5.5 hours) only. This procedure is accordingly referred to as "VS-H-VS".*

d. *A run performed using random hold times (35s-100s-300s-900s-54960s-2700s-6600s-18000s).*

e. *Experiments using 0.01 M NaH_2PO_4 solution as pore fluid.*

f. *Experiments using silicon oil as pore fluid.*

g. *Experiment using a water-saturated sample drained to the atmosphere, i.e. tested wet at zero pore fluid pressure.*

5.2.4 Data processing

For each experiment, we calculated the apparent friction coefficient (μ) as a function of displacement by taking the ratio of shear stress to effective normal stress supported by the gouge layer, assuming zero cohesion. Using the friction vs. displacement data obtained in the VS-seqs and SHS-seqs, we then obtained the frictional rate dependence and healing parameters as follows. Note that the measured axial displacement was corrected for elastic machine distortion using calibrations obtained from compression tests on a steel dummy of known elastic properties.

Starting with the VS data, we used the (quasi) steady-state frictional strength (μ_{ss}) reached before and after each velocity step (V-step) to determine the RSF rate dependence parameter, $(a–b) = \Delta\mu_{ss}/\Delta\ln V = (\mu_{ss}^{V2}–\mu_{ss}^{V1})/ \ln(V_2/V_1)$ (*Marone*, 1998a) (Figure 5.2a). In the case of unstable stick-slips, we took the average strengths at the relevant sliding velocities to obtain apparent ($a–b$) values (Figure 5.2a). We determined ($a–b$) for all V-steps in the range of 0.1↔1μm/s and 1↔10 μm/s. Recall that in the framework of rate-and-state dependent friction modeling, positive values of ($a–b$) indicate intrinsically stable, velocity strengthening behavior, whereas negative values indicate potentially unstable, velocity weakening behavior,

which is prerequisite for unstable stick-slip behavior (*Ruina*, 1983; *Scholz*, 2002).

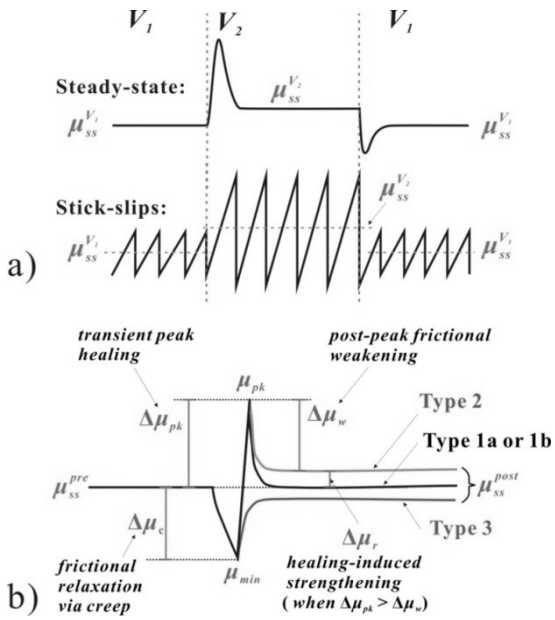

Figure 5.2. a) Terminology for describing the "steady-state" friction coefficient measured in velocity stepping tests, in the cases of stable sliding and stick-slip behaviour. Friction rate parameter (a–b) = (μ_{ss}^{V2}-μ_{ss}^{V1})/ ln(V_2/V_1). b) Definition of frictional healing parameters and classification of healing behavior after Chen et al., (submitted). Note that Type 1 behaviour can be further divided in to 1a (classical Dieterich-type, characterized by log-linear relation between $\Delta\mu_{pk}$ and hold time) and 1b (any other relationship). See Chen et al., (submitted) for details.

For each SHS sequence and constituent SHS event, we quantified 1) the magnitude of stress relaxation, and 2) the magnitude of frictional healing obtained after each hold period. In the conventional methodology for SHS data processing (e.g. *Marone*, 1998a), the magnitude of frictional healing achieved after a hold time t_h is defined as the difference between the steady-state friction coefficient measured before and after the hold period ($\mu_{ss}^{pre} = \mu_{ss}^{post}$), and the peak frictional strength associated with reshearing (μ_{pk}). The magnitude of frictional relaxation ($\Delta\mu_c$) due to creep effects during the hold period is defined as the difference between μ_{ss}^{pre} and the minimum frictional strength (μ_{min}) attained during relaxation (Figure 5.2b). However, in some of our experiments, we observed marked changes in the pre- and post-hold steady-state friction coefficients, μ_{ss}^{pre} vs. μ_{ss}^{post}, across individual hold periods (Figure 5.3). This kind of behavior has been reported in only a few previous studies

(e.g. *Nakatani and Mochizuki*, 1996; *Yasuhara et al.*, 2005), and is not easily described using the conventional notation of *Marone* (1998a). Therefore, following the method recently developed by *Chen et al.* (*submitted,* Chapter 4), we use three parameters to describe frictional healing behavior – see Figure 5.2b. In this scheme, $\Delta\mu_{pk}$ is the transient peak strength due to healing, measured in terms of the difference $(\mu_{pk} - \mu_{ss}^{pre})$, which corresponds to the "healing" or "direct healing" effect (termed $\Delta\mu$) specified in the conventional definition (e.g. *Marone*, 1998a). By contrast, $\Delta\mu_w$ is the post-peak frictional weakening effect, measured as the difference $(\mu_{pk} - \mu_{ss}^{post})$. Lastly, $\Delta\mu_r$ is the residual healing-induced strengthening effect, measured as the difference $(\mu_{ss}^{post} - \mu_{ss}^{pre})$. Using these parameters, and taking into account the way in which they depend on hold time, this scheme allows definition of all possible categories of frictional healing behavior.

A few of the present experiments exhibited minor, near-linear slip hardening or weakening behavior in some of the velocity intervals employed in the various VS and SHS stages of the tests. These effects were corrected for using non-cumulative linear detrending of the data, following the standard approach introduced by *Blanpied et al.* (1995). Taking into account all errors in measuring internal shear stress, confining pressure and pore pressure (*Verberne et al.*, 2013b), and performing conventional error propagation analysis, the standard errors obtained for these quantities, are ± 0.15, ± 0.1 and ± 0.05 MPa, respectively. The error in the absolute friction coefficient values (μ) is ± 0.005 μ_{ss}, whereas for the frictional rate parameter (a–b), the standard error is ± 0.003μ_{ss} where μ_{ss} is the average steady-state coefficient for different loading rates. In the frictional healing and relaxation parameters, $\Delta\mu_{pk}$, $\Delta\mu_w$, $\Delta\mu_r$ and $\Delta\mu_c$, the standard error is ± 0.007μ_{ss}, where μ_{ss} is the average steady-state friction during sliding periods of the SHS sequences.

Lastly, compaction of the gouge layer in experiments on wet breccia-derived samples was estimated by dividing the pore fluid volume change, obtained from the high-precision volumetric pump, by the area of the gouge layer. This yielded thickness change vs. time data for the entire duration of each wet experiment, from which the compaction strain rate ($\dot{\varepsilon}$) was further calculated. We do not report compaction data for the gouge-derived samples because the resolution of the volumetric data obtained was not high enough, due to a later-discovered recording problem in these experiments. In addition, on-going shear deformation occurring during relaxation in "static" hold periods, allowed us to determine

shear strain rate ($\dot{\gamma}$) versus hold time from the stress relaxation data and machine stiffness. The approach used for this followed the classical method applied for example by *Rutter and Mainprice* (1978). By comparing the results obtained at different temperatures, activation energies for the operative compaction and relaxation creep processes were obtained by plotting $\ln \dot{\varepsilon}$ or $\ln \dot{\gamma}$ against $1/T$ (see appendix 5.A).

5.3. Experimental Results

5.3.1 Representative Results and General Features

Representative plots of frictional strength versus displacement for both the fault-gouge-derived and fault-breccia-derived samples are presented in Figure 5.3. Henceforth, we will refer to the two materials simply as gouge-derived and breccia-derived. All samples tested showed a rapid increase in friction coefficient in the first 0.3 to 0.5 mm of displacement, followed by macroscopic yield and gradual hardening towards a peak value of the apparent friction coefficient attained at around 1.0 mm of displacement. The frictional strength subsequently increased or decreased slightly in the VS-seq1, SHS-seq and VS-seq2 stages of each experiment, depending on imposed sliding velocity and/or hold time. A cumulative displacement of 5 – 6 mm was achieved in each test.

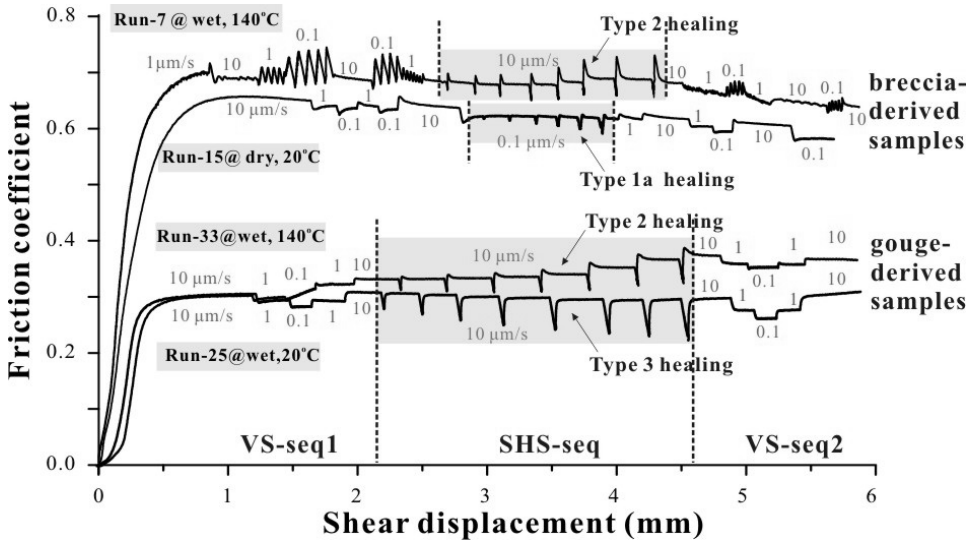

Figure 5.3. Representative friction versus displacement curves obtained from shearing experiments performed on powdered samples derived from carbonate-clay fault gouge and carbonate fault breccia. After a "run-in" at constant velocity, velocity stepping (VS) tests were employed to evaluate the rate dependence of frictional strength (VS-seq1). This was followed by a slide-hold-slide testing sequence (SHS-seq) and finally a second VS sequence

(VS-seq2). Effective normal stress was 50 MPa in all cases. Wet experiments were performed at a confining pressure of 65 MPa and a pore pressure of 15 MPa.

Generally speaking, peak friction values (μ_{max}), picked at ~ 1 mm displacement at a slip rate of 10 μm/s to roughly characterize the strength of the material, ranged from 0.30 to 0.34 for the gouge-derived samples (all wet), and from 0.64 to 0.72 for the breccia-derived samples (wet and dry). Dry gouge-derived samples tended to be slightly stronger than the wet ones (c.f. Figure 5.3). The strengths (μ_{max}) of all samples falling in Datasets 1–3 (Table 5.1) showed a tendency to increase with increasing temperature (Table 5.1). Focusing now on slip stability, the wet, gouge-derived samples showed stable sliding behavior at all temperatures investigated. By contrast, the breccia-derived samples showed stable sliding at 20 °C, transitioning to unstable slip (or stick-slip) at elevated temperatures, under both dry and wet conditions (Figure 5.3). During SHS testing, wet gouge- and breccia-derived samples showed a progressive increase in (quasi) steady-state friction upon reshearing, whereas dry breccia-derived samples showed more or less fixed steady-state strength throughout each SHS sequence (Figure 5.3).

5.3.2 Velocity Stepping Data

Representative velocity stepping or VS data obtained from the experiments performed on wet gouge-derived samples (Dataset 1), dry breccia-derived samples (Dataset 2) and wet breccia-derived samples (Dataset 3), are shown in Figure 5.4 (see also Table 5.1). For each dataset, we compare typical VS-seq1 and VS-seq2 data for experiments performed at 20, 80 and 140 °C. The (*a–b*) values obtained from all V-steps executed, in all experiments reported under Datasets 1–3, are plotted against temperature in Figure 5.5.

The wet gouge-derived samples showed stable, velocity strengthening sliding behavior in all velocity steps and at all temperatures investigated (Figure 5.4a). Further quantification of the velocity dependence of friction in terms of (*a–b*) showed that as temperature increases there is a systematic decrease in (*a–b*), from an average value of 0.0075 at 20 °C to 0.003 at 140 °C (Figure 5.5a). In addition, a slight increase in (*a–b*) is evident for V-steps (VS-seq2) performed after SHS testing relative to those performed before SHS testing (VS-seq1), as indicated in Figure 5.5a by the solid and dashed lines. This increase in (*a–b*) occurred for all individual V-steps (i.e. 0.1→1 μm/s, 1→10 μm/s, 1→0.1 μm/s and 10→1 μm/s), although the magnitude of the increase was close to the error in (*a–b*) (Figure 5.5a).

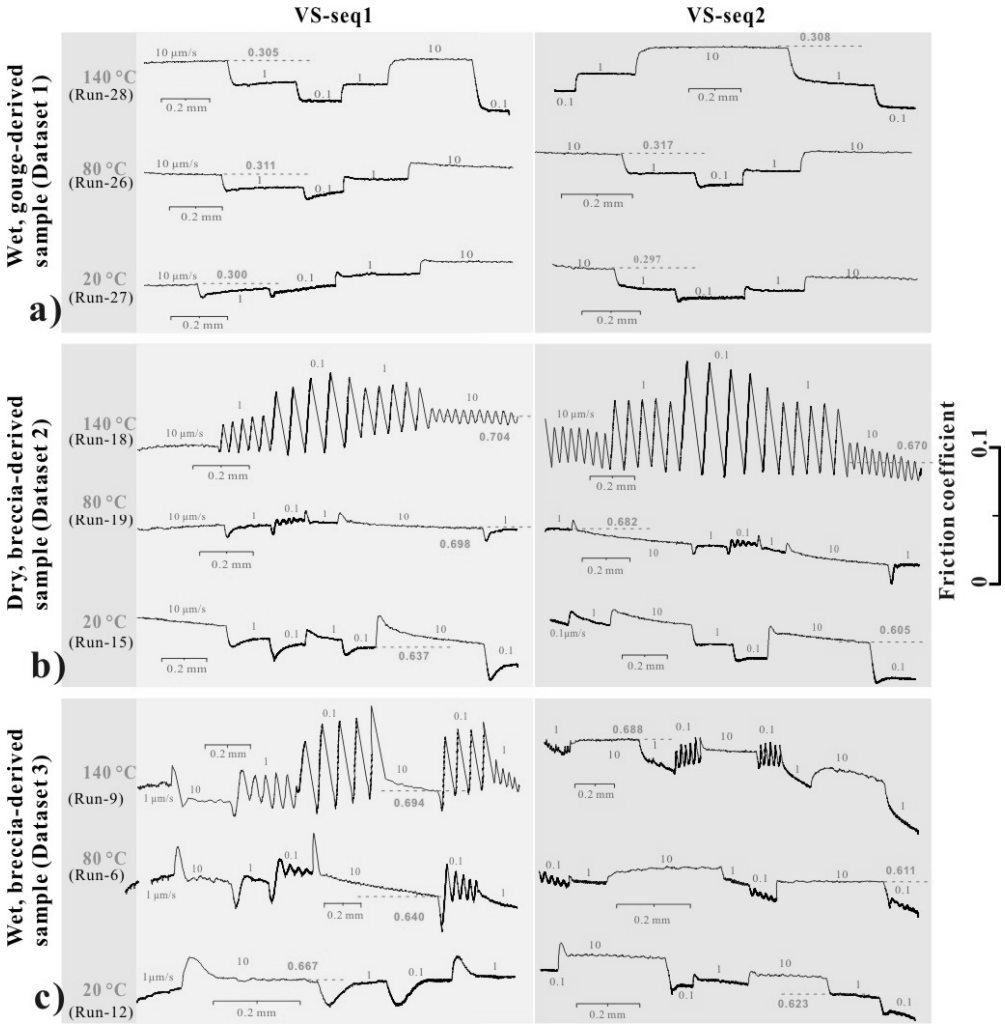

Figure 5.4.Velocity stepping data obtained in the VS-seq1 and VS-seq2 stages of representative experiments performed on(a) wet gouge-derived samples, (b) dry breccia-derived sample and (c) wet breccia-derived samples, at 20, 80 and 140 °C. Individual sample numbers from Table 5.1 are as indicated. Friction coefficient scale bar (right) applies to all data sets. The absolute frictional strength level of each curve is given in red. Velocities are indicated per step in µm/s.

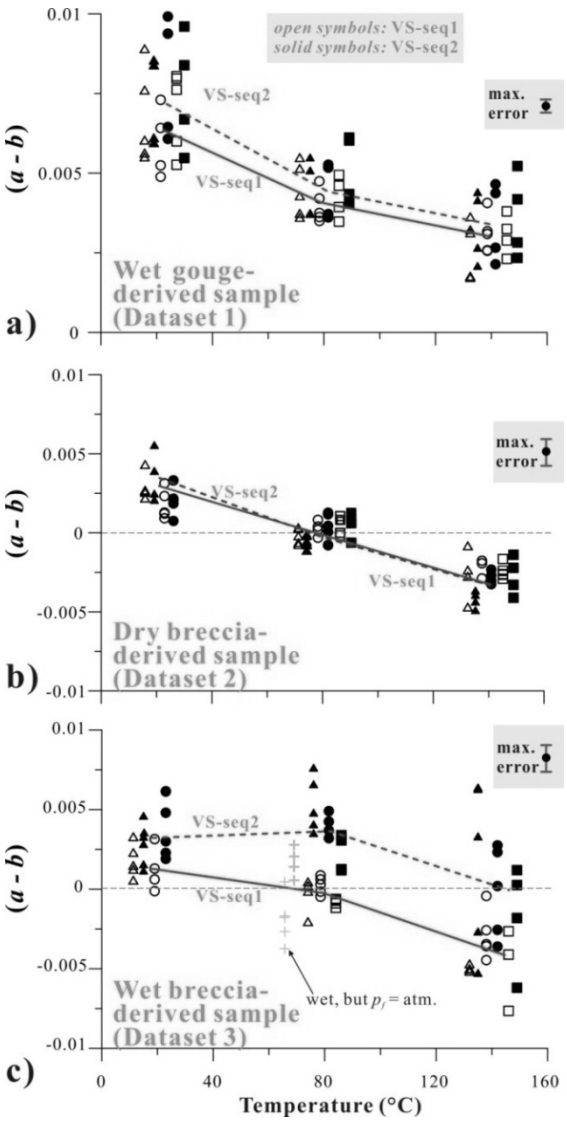

Figure 5.5. Temperature (T) dependence of the RSF rate dependence parameter (a–b), determined from the velocity-stepping sequences performed before (VS-seq1) and after (VS-seq2) SHS testing, for the sample materials shown. All experiments were performed at an effective normal stress of 50 MPa. Open and solid symbols represent (a–b) values obtained in VS-seq1 and VS-seq2, respectively. Circles, squares and triangles represent (a–b) values obtained in tests performed using re-shearing velocities of respectively 0.1, 1 and 10 μm/s in the SHS-stage (Table 5.1). Solid and dashed lines indicate the trends in average (a–b) with temperature, for the VS-seq1 and VS-seq2 data, respectively. Note that the (a–b) data obtained at each temperature (20, 80 and 140 °C) are plotted at T-values that are slightly displaced from the corresponding test temperature. This is done for plotting clarity.

The dry breccia-derived samples(Figure 5.4b) showed 1) stable sliding plus velocity strengthening at 20 °C, 2) velocity neutral or minor velocity weakening behavior at ~ 80 °C with oscillatory stick-slips at the lowest slip rate of 0.1 μm/s, and 3) velocity weakening at 140 °C with stick-slips at all velocities. In line with this, (*a–b*) decreases monotonically with increasing temperature over the full range of temperature investigated (Figure 5.5b), with a transition from velocity strengthening to velocity weakening occurring at ~ 80 °C. These samples showed no significant difference in the (*a–b*) values determined before versus after SHS testing. The only difference we found was that the stick-slips seen in the VS-seq2 stage of the experiments performed at 140 °C showed larger amplitude than in the VS-seq1 stage of the same experiments (Figure 5.4b).

For the wet breccia-derived samples, the first VS sequence (VS-seq1) showed similar behavior to that exhibited by the dry samples in VS-seq1 (or VS-seq2) at the same conditions (Figure 4c). Though slightly more scattered, the (*a–b*) values determined for the wet samples in VS-seq1 also showed a negative temperature dependence and a transition from velocity strengthening to velocity weakening slip at ~ 80 °C (Figure 5.5c). However, the second VS sequence (VS-seq2) showed higher, mostly positive (*a–b*) values, decreasing to more or less zero on average at 140 °C, implying a tendency for more stable slip behavior at all temperatures investigated (Figure 5.4c). This stabilization effect was also reflected by a decrease in stick-slip amplitude in the VS-seq2 stage of the experiments relative to the VS-seq1 stage (Figure 5.4c). Note that in the post-SHS sequences (VS-seq2), the higher (*a–b*) values and a slightly wider variability in (*a–b*), resulted in velocity weakening and marked stick-slips occurring only at 140 °C (Figure 5.4c and Figure 5.5c). The average increase in (*a–b*) values in VS-seq2 compared with VS-seq1, as indicated by the gap between the solid and dashed red lines in Figure 5.5c, was ~ 0.0042. This value is larger than the maximum error of ± 0.0017 in (*a–b*) displayed in Figure 5.5c, implying a true increase in (*a–b*) after SHS testing. This increase in (*a–b*) was evident in all V-steps.

Lastly, we examine the effect of sliding velocity on the friction rate parameter (*a–b*). All our data sets, i.e. the wet gouge-derived, dry breccia-derived and wet breccia-derived samples, showed similar effects of velocity, in both the VS-seq1 and VS-seq2 stages of the experiments. For plotting clarity, we illustrate the observed behavior for one experiment per sample type (i.e. for Datasets 1–3), focusing on the VS-seq1 data only– see Figure 5.6. The results demonstrate that the (*a–b*) values obtained for V-steps of 1–10 μm/s are always larger than that for V-steps of 0.1–1 μm/s with the same sense of stepping, i.e. upward or downward. This trend holds for all the three datasets (Figures 5.6a, 5.6b and 5.6c), suggesting that (*a–b*)

tends to increase with increasing load point velocity, with slopes ranging from 0.001 to 0.0035 per decade change in velocity.

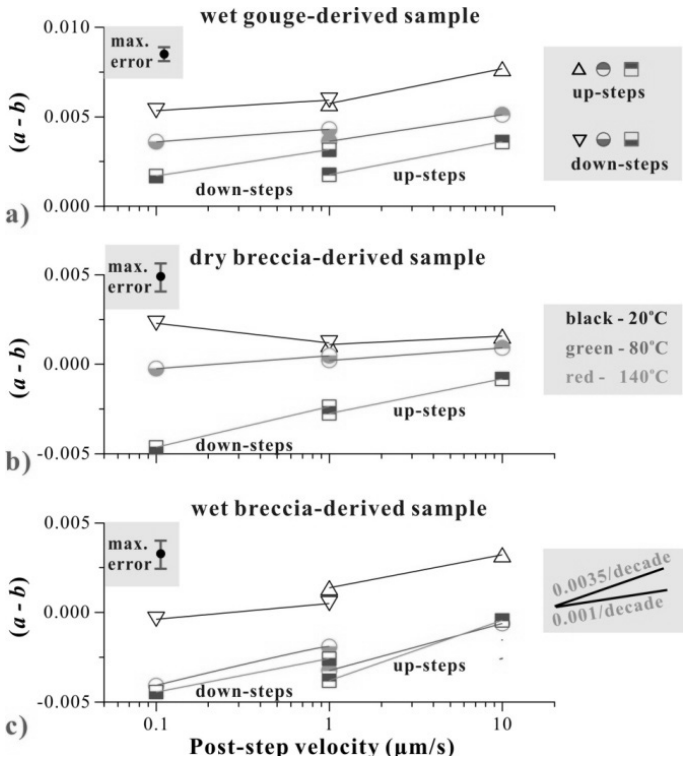

Figure 5.6. Velocity dependence of (a-b), determined from the velocity stepping data for a) wet gouge-derived, and b) dry and c) wet breccia-derived samples sheared at different temperatures. For each sample and each temperature (20, 80 and 140 °C), only (a–b) data from the VS-seq1 data are plotted. The legend and slope indicators (right) apply to all data sets.

5.3.3 Slide-hold-slide Data

5.3.3.1 Slide-hold-slide curves

The slide-hold-slide data obtained for the wet gouge-derived, dry breccia-derivedand wet breccia-derived samples (Datasets 1, 2 and 3, Table 5.1) are presented in Figures 5.7a, 5.7b and 5.7c, respectively. Broadly speaking, using the terminology of *Chen et al.* (submitted, Chapter 4) defined in section 5.2.4 (Figure 5.2b), and removing background slip weakening and strengthening trends, we observed three kinds of frictional healing behavior (Figure 5.7, Table 5.1):

1) Type 1a healing behavior with $\Delta\mu_{pk} = \Delta\mu_w > 0$ and $\Delta\mu_{pk} = \beta \cdot \log(1+t_h/t_c)$, where t_c is a

cutoff time on the order of 1 second. This is classical Dieterich-type healing behavior whereby $\beta = d(\Delta\mu_{pk})/d\log(t_h)$ is a constant, usually referred to as the healing rate (e.g. *Dieterich*, 1972). This type of behavior was typically exhibited by the dry breccia-derived samples (Figure 5.7b, Dataset 2), and wet breccia-derived samples sheared at 20 °C (Figure 5.7c).

2) Type 2 healing behavior with $\Delta\mu_{pk} > \Delta\mu_w > 0$. This is characterized by an increase in (quasi) steady-state friction coefficient after reshearing ($\Delta\mu_r > 0$). This type of healing behavior was observed in all of our wet experiments on both gouge- and breccia-derived samples (Datasets 1 and 3), sheared at elevated temperatures (Figures 5.7a and 5.7c).

3) Type 3 healing behavior with $\Delta\mu_{pk} = \Delta\mu_r < 0$ and $\Delta\mu_w = 0$. This is characterized by negative peak healing with zero post-peak weakening effect ($\Delta\mu_w = 0$), and corresponds to the healing behavior observed for wet gouge-derived samples deformed at 20 °C using V_{SHS} of 0.1 and 10 μm/s (Dataset 1, Figure 5.7a).

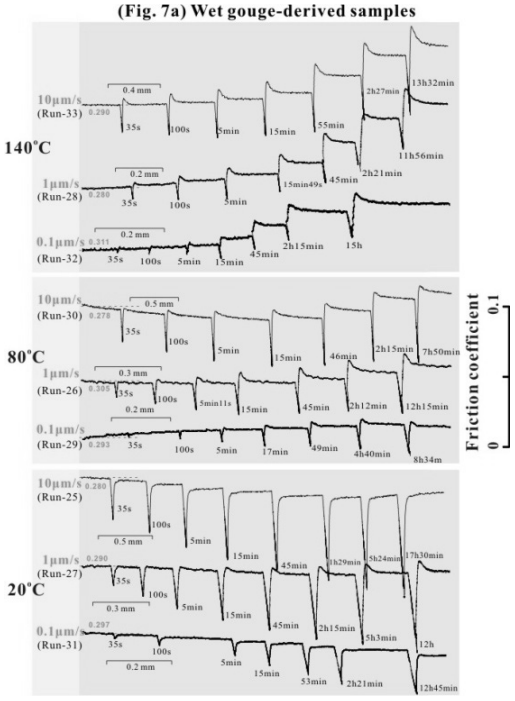

Figure 5.7a (to be continued)

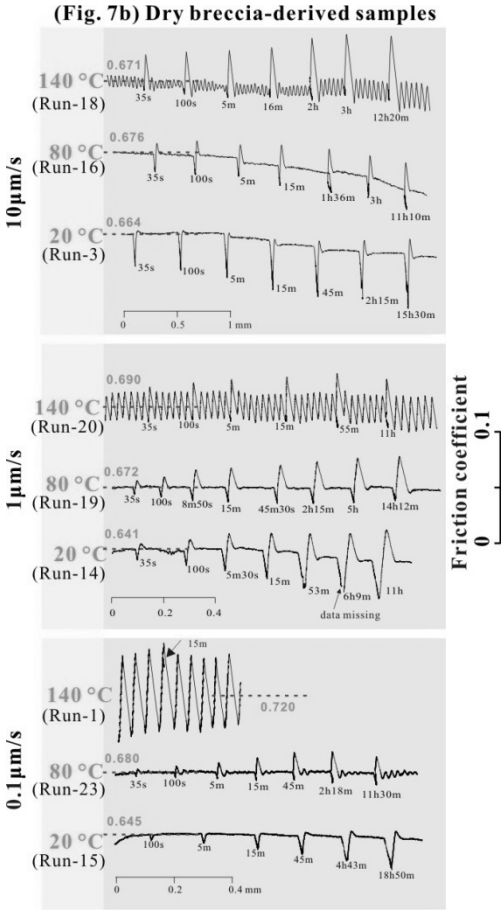

Figure 5.7b (to be continued)

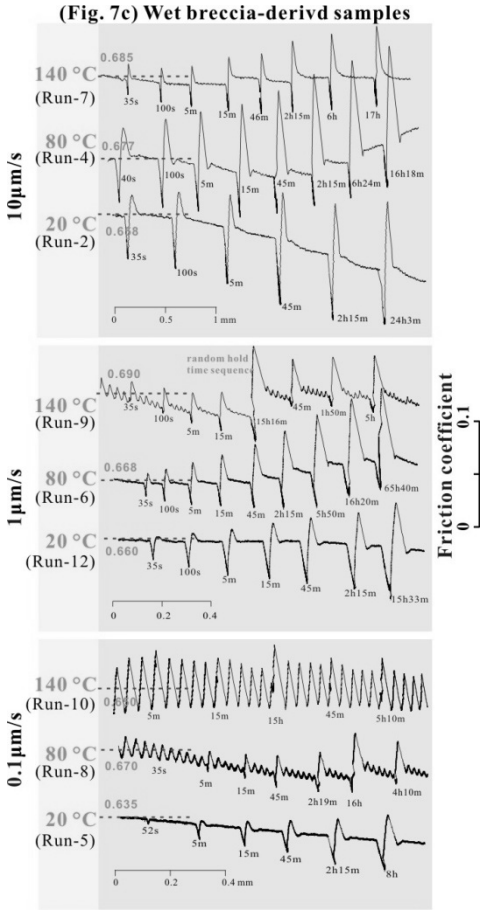

Figure 5.7. SHS results for a) the wet gouge-derived samples, b) dry breccia-derived samples, and c) wet breccia-derived samples. For each set of experiments, a range of temperatures (20, 80 and 140°C) and load point velocities (0.1, 1 and 10µm/s) was investigated. For optimum (internal) comparison, the results presented in (a) are categorized according to temperature and then sliding velocity, while for b) and c) they are categorized according to velocity and then temperature.

We now make use of this terminology and the associated parameters to describe the trends in healing behavior shown by samples falling in Datasets 1–3. First, we note that all experiments performed show that an increase in the magnitude of stress relaxation ($\Delta\mu_c$) with increasing V_{SHS} and increasing hold time t_h, and a decrease with increasing temperature (Figure 5.7). The wet breccia-derived samples relaxed more than the dry breccia-derived samples, but less than the wet gouge-derived samples at otherwise similar conditions. With continued reference to Figure 5.7, the behavior seen upon subsequent re-shearing can be

described as follows for each dataset.

1) Wet gouge-derived samples. At 20 °C and for V_{SHS} of 0.1 and 10 μm/s, these samples display Type-3 healing behavior with $\Delta\mu_{pk} = \Delta\mu_r < 0$ and $\Delta\mu_w = 0$. The sample tested with V_{SHS} of 1 μm/s (Run-27, Table 5.1) shows Type-1a healing behavior with $\Delta\mu_{pk} = \Delta\mu_w > 0$ and $\Delta\mu_r = 0$. No clear trends are visible in these few data at 20 °C (Figure 5.7a). By contrast, the samples tested at elevated temperatures (80 and 140 °C) all show Type-2 healing behavior ($\Delta\mu_{pk} > \Delta\mu_w$, Figure 5.7a), whereby the transient peak healing ($\Delta\mu_{pk}$) and post-peak weakening ($\Delta\mu_w$) parameters increase with increasing T, t_h and V_{SHS}. The healing-induced restrengthening ($\Delta\mu_r$) exhibited by these samples also increases with T and V_{SHS}, but no consistent trend is visible with hold time.
2) Dry breccia-derived samples. These show Dieterich-type (Type 1a) healing behavior, with $\Delta\mu_{pk} = \Delta\mu_w$ tending to increase with increasing T, t_h and V_{SHS} (Figure 5.7b). As seen in the VS data, stick-slips also occurred during the sliding portion of the SHS sequences performed on these samples at 140 °C.
3) Wet breccia-derived samples. At 20 °C, the wet breccia-derived samples display Dieterich-type (Type 1a) healing behavior with $\Delta\mu_{pk} = \Delta\mu_w > 0$ and $\Delta\mu_r = 0$. However, at elevated temperatures (80 and 140 °C), these samples exhibit Type-2 healing behavior, with $\Delta\mu_{pk}$ and $\Delta\mu_w$ increasing with increasing t_h and (crudely) with increasing shearing velocity V_{SHS} (Figure 5.7c). The corresponding $\Delta\mu_r$ values increase with t_h over the first few SHS events ($t_h < 60000$s), but then level off to finally cease changing over long hold periods (Figure 5.3 and Figure 5.7c). Note that the magnitude of healing ($\Delta\mu_{pk}$ and $\Delta\mu_w$) observed in the wet breccia-derived samples is always larger than in the dry equivalents ($\Delta\mu_{pk} = \Delta\mu_w$) at otherwise similar conditions, and that positive $\Delta\mu_r$ is only seen in the wet samples. Stick-slip occurred during the sliding portion of the SHS sequences performed on these samples at 140 °C for V_{SHS} of 1 and 0.1 μm/s, and at 80 °C for V_{SHS} of 0.1 μm/s.

5.3.3.2 Healing magnitude parameters versus log(t_h)

The healing magnitude parameters $\Delta\mu_c$, $\Delta\mu_{pk}$, $\Delta\mu_w$ and $\Delta\mu_r$, obtained from SHS testing are plotted against the logarithm of hold time in Figure 5.8. Specifically, the results for the wet gouge-derived, dry breccia-derived and wet breccia-derived samples are shown in Figures 5.8a, 5.8b and 5.8c, respectively. Comparison of these results shows that, in all cases, the magnitude of stress relaxation ($\Delta\mu_c$) increases more or less linearly with the logarithm of hold time (Figures 5.8a, 5.8b and 5.8c), with the effect being most marked in the wet, gouge-derived samples. The following observations emerge with respect to $\Delta\mu_{pk}$, $\Delta\mu_w$ and $\Delta\mu_r$.

1) Wet gouge-derived samples. These samples show a direct, near-linear relation between $\Delta\mu_w$ and $\log(t_h)$. By contrast, the transient peak healing and post-peak weakening parameters ($\Delta\mu_{pk}$ and $\Delta\mu_r$) generally show an increase with $\log(t_h)$ at relatively short hold periods (< 10^4 s), followed by a decrease at longer hold periods (Figure 5.8a). Where Type 3 healing behavior was encountered, i.e. in those samples deformed at 20 °C and showing negative $\Delta\mu_{pk}$, no clear trend in $\Delta\mu_r$ is visible (Figure 5.8a).
2) Dry breccia-derived samples. In these samples, the transient peak healing and post-peak weakening parameters ($\Delta\mu_{pk} = \Delta\mu_w$) increase roughly linearly with the logarithm of hold time (Figure 5.8b), confirming Type 1a or Dieterich-type healing.
3) Wet breccia-derived samples. Some samples show $\Delta\mu_{pk}$ being more or less linearly proportional to $\log(t_h)$, while others shows a poor correlation (Figure 5.8c). The $\Delta\mu_r$ data also show parallel trends. However, the post-peak weakening ($\Delta\mu_w$) displayed by these samples is mostly very well described by a linear relation versus $\log(t_h)$ (Figure 5.8c).

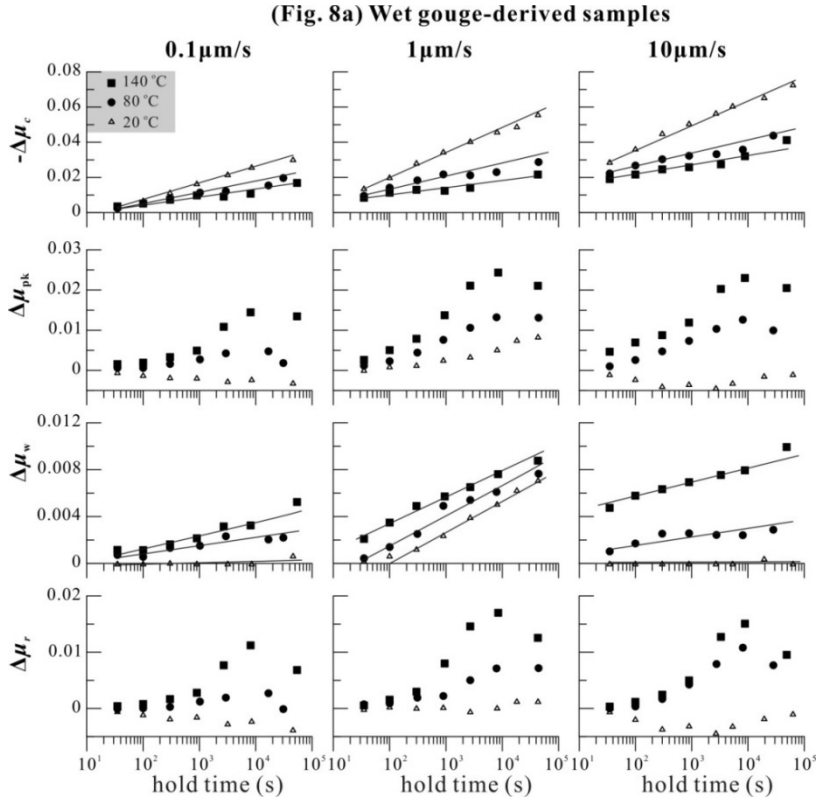

Figure 5.8a (to be continued)

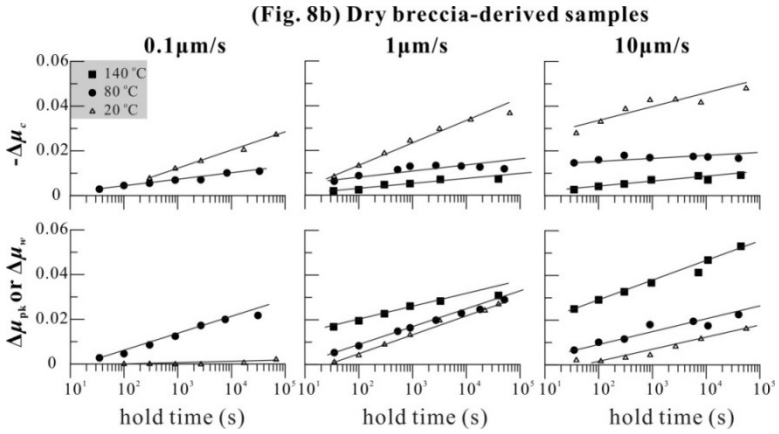

Figure 5.8b (to be continued)

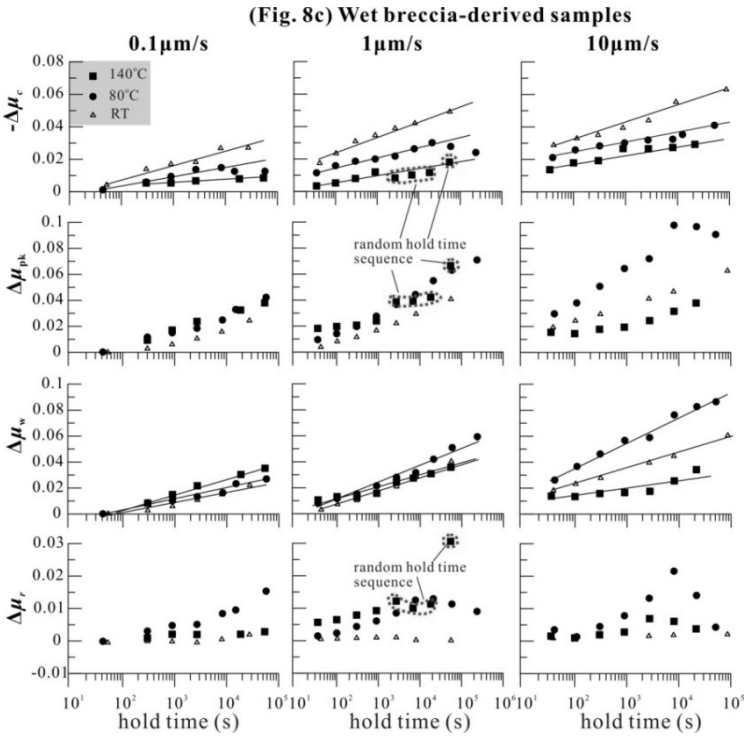

Figure 5.8.Frictional healing and relaxation parameters plotted as functions of the logarithm of hold time, for a) the wet gouge-derived, b) dry breccia-derived and c) wet breccia-breccia samples. For each material, we present the data obtained across the full range of temperatures and load point velocities investigated. Note that $\Delta\mu_c$ corresponds to shear stress relaxation, μ_{pk} to the transient peak healing, μ_w, to the post-peak frictional weakening, and μ_r to persistent, healing-induced strengthening.

In summary, our results on healing parameters versus $\log(t_h)$ demonstrate that the peak healing or re-strengthening effect ($\Delta\mu_{pk}$) observed in wet experiments on gouge- and breccia-derived samples, essentially comprises two components. These consist of a component $\Delta\mu_w$, which is linearly proportional to $\log(t_h)$ in a manner resembling Dieterich-type healing, plus a persistent increase in (quasi) steady-state friction coefficient $\Delta\mu_r$. The latter shows a maximum value at hold times of the order of 10^4 s (Figures 5.8a and 5.8c), except in the run we performed using a random hold time sequence (Run-9, Table 5.1 – Figure 5.8c plus Figure 5.7c for the SHS curve). Typical results explicitly illustrating this partitioning of $\Delta\mu_{pk}$ into $\Delta\mu_w$ and $\Delta\mu_r$, in the wet gouge- and breccia-derived samples are replotted from Figure 5.8 in Figures 5.9a and 5.9b, respectively. By contrast, the results obtained in our dry experiments on breccia-derived samples are characterized by $\Delta\mu_{pk} = \Delta\mu_w$ and $\Delta\mu_r = 0$, which corresponds to classical Dieterich-type healing.

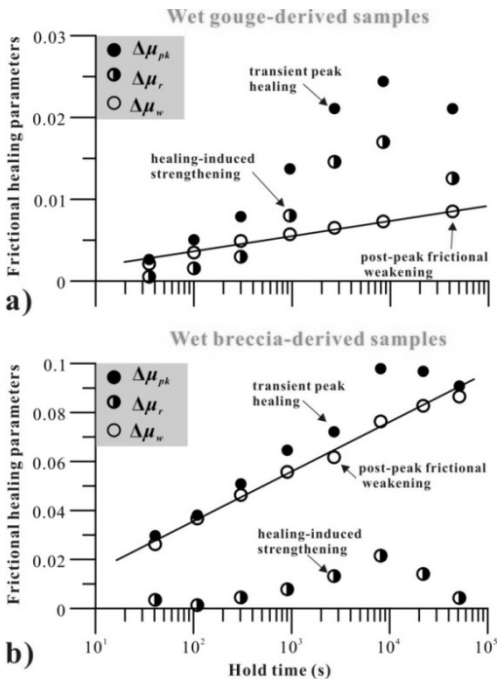

Figure 5.9. Typical frictional healing results for (a) wet gouge-derived and (b) wet breccia-derived samples, illustrating partitioning of healing seen in SHS stages. Data in a) are from Run-22 performed at 140 °C using V_{SHS} of 1 μm/s. Data in b) are from Run-4 performed at 80° Cusing V_{SHS} of 10 μm/s. In both cases, the peak healing ($\Delta\mu_{pk}$) observed essentially consists of two components, i.e. a persistent strengthening in dynamic friction ($\Delta\mu_r$-effect) plus a Dieterich component ($\Delta\mu_w$-effect).

5.3.3.3 Relaxation and healing rates

Shear stress relaxation rates during hold periods were obtained for all samples (Datasets 1-3), using the parameter defined as $\rho = d(-\Delta\mu_c)/d(\log_{10}(t_h))$, analogue to the definition of frictional healing rate. The values obtained lie in the ranges shown in Figure 5.10. For all SHS tests performed, ρ displayed a negative dependence on temperature and a positive dependence on V_{SHS} (Figure 5.10). For given values of V_{SHS} and T, wet breccia-derived samples always relaxed faster than dry breccia-derived samples, but more slowly than the wet gouge-derived samples (Figure 5.10).

Frictional healing rates occurring in the SHS stage of our experiments were quantified using the parameter $\beta_x = d(\Delta\mu_x)/d(\log_{10}(t_h))$, where the subscript "*x*" refers to either "*pk*" or "*w*". Note that some of the $\Delta\mu_{pk}$ data show a complex dependence on $\log_{10}(t_h)$ (see Figure 5.8). For consistency, β_{pk} fits are nonetheless added for comparison (grey symbols and grey dashed lines, Figure 5.10). For all SHS runs performed in this study, healing rate fits to our $\Delta\mu_w$ versus $\log_{10}(t_h)$ data yielded β_w values ranging from 0 to 0.0023/decade for the wet gouge-derived samples, from 0.0011 to 0.0086/decade for the dry breccia-derived samples ($\beta_w = \beta_{pk}$), and from 0.0097 to 0.0196/decade for the wet breccia-derived samples (Figure 5.10). The rate of transient peak healing β_{pk} was slightly (~ 1.1 times) higher than β_w for the wet breccia-derived samples at all temperatures investigated, while for the wet gouge-derived samples, β_{pk} values were much higher (~ 5 times at 80 °C and ~ 4 times at 140 °C) than β_w. For the dry breccia-derived samples, which showed classical Dieterich-type healing, β_w and β_{pk} values were of course equal, as indicated above. In general, β_{pk} and β_w increased with temperature, except in wet breccia-derived material between 80 °C and 140 °C. Even though the magnitude of healing ($\Delta\mu_{pk}$ and $\Delta\mu_w$) was always larger for higher V_{SHS}, the rate parameters β_{pk} and β_w do not show a consistent dependence on V_{SHS} for any sample type (Datasets 1–3).

We now consider the rate of development of $\Delta\mu_r$ during hold periods, for the samples that showed positive values of this parameter, i.e. the wet gouge- and wet breccia-derived samples at 80 and 140 °C (Figures 5.8a and 5.8c). Plotting $\Delta\mu_r$ against t_h or $\log(t_h)$ for these samples does not yield any systematic relationships such as those seen for $\Delta\mu_{pk}$ or $\Delta\mu_w$ (e.g. Figures 5.8 and 5.9). Rather, in the SHS sequences, the steady-state friction in some of these samples seems to become "saturated", causing $\Delta\mu_r$ to gradually approach zero in long hold periods – see Figures 5.7a, 5.7c, 5.8a, 5.8c and 5.9. In view of this, we examine the relationship between cumulative $\Delta\mu_r$ and cumulative hold time. Surprisingly, we found that the $\sum\Delta\mu_r$ data obtained in samples that show Type 2 healing behavior appear to approach an

asymptote with increasing cumulative hold time, regardless of T, V_{SHS} and hold time sequence. Figure 5.11 illustrates representative results for wet gouge- and breccia-derived samples at 80 °C. It is also apparent from Figure 5.11 that there is a positive dependence of $\sum\Delta\mu_r$ on V_{SHS}.

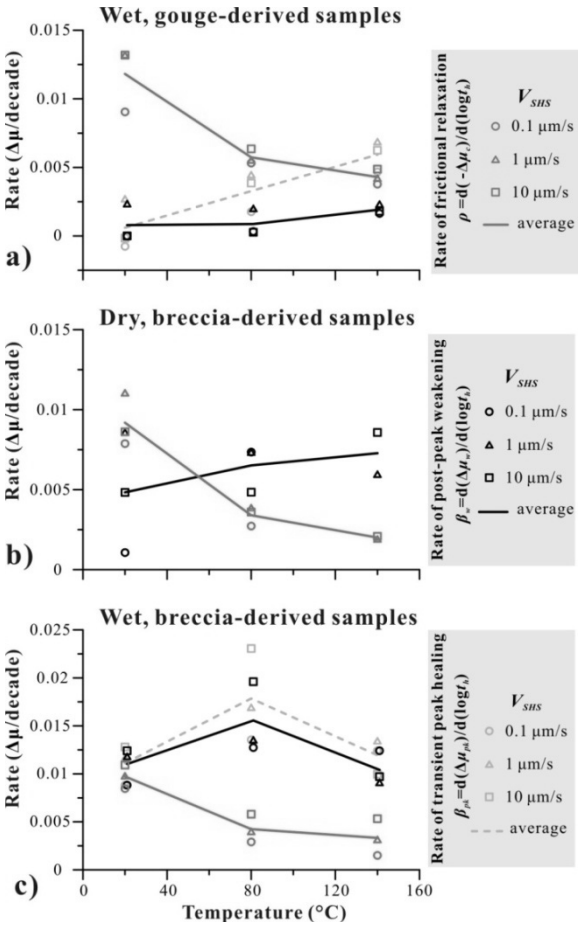

Figure 5.10. Frictional healing rates (β) and relaxation rates (ρ) plotted as a function of temperature, for a) wet gouge-derived, b) dry breccia-derived and c) wet breccia-derived samples. Blue, gray and black symbols indicate the rates of frictional relaxation ρ (-$\Delta\mu_c$/decade), frictional healing β_{pk} ($\Delta\mu_{pk}$/decade) and β_w ($\Delta\mu_w$/decade), respectively. The circular, triangular and square symbols represent imposed SHS velocities (V_{SHS}) of 0.1, 1 and 10 μm/s, respectively. The blue, gray and black lines represent trends in the average values of the corresponding rate parameter.

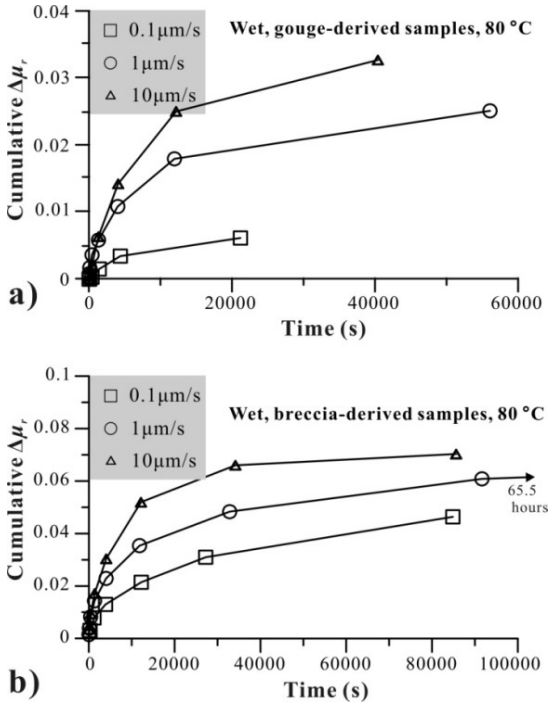

Figure 5.11.Cumulative healing-induced strengthening ($\sum\Delta\mu_r$) plotted as a function of cumulative hold time, for (a) the wet gouge-derived samples and (b) wet breccia-derived samples, sheared at 80 °C and at different load-point velocities (0.1, 1 and 10 μm/s).

5.3.4 Compaction data

Thickness change data, referred to here as compaction data since they are derived from pore volume change measurements, were obtained only for wet breccia-derived samples– see Figure 5.12a. These samples showed marked compaction in the first 200 – 300 s, or 0 – 1.5 mm of shear deformation, i.e. during initial hardening in the approach to macroscopic yield (c.f. Figure 5.3). Beyond this initial loading phase, the compaction curves exhibit a clear decrease in compaction rate with time (indicated by the decreasing slope in Figure 5.12a). For comparative purposes, friction coefficient and compaction versus displacement data are presented in the inset in Figure 5.12a, for a typical SHS testing sequence (Run-6) performed on wet breccia-derived samples at 80 °C. These data demonstrate an increase in gouge compaction with hold time, but no significant changes upon resliding or during sliding periods. Using the compaction (ΔL) and hold time (t_h) data obtained from the SHS phase of all experiments on wet, breccia-derived samples, we calculated the average compaction

strain rate for each hold period using the equation $\dot{\varepsilon} = \Delta L/(L_0 t_h)$, where L_0 is the initial sample thicknesses assumed to be 0.8 mm (see appendix 5.A). As shown in Figures 5.12b and 5.12c, the resulting compaction strain rates, calculated for all wet breccia-derived samples, show a decreasing trend with increasing temperature, and an increasing trend with increasing re-shearing velocity (V_{SHS}).

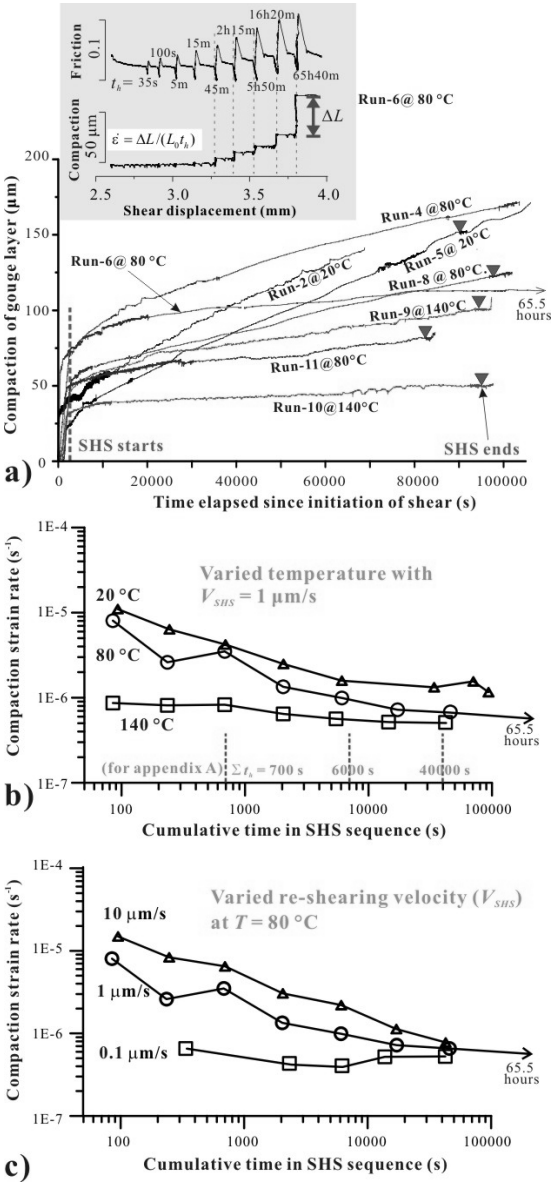

Figure 5.12. Gouge compaction and compaction strain rate data for the wet breccia-derived samples. a) Gouge compaction data for entire experiments (since the tough point). b) and c) Compaction strain rate vs. cumulative hold time during SHS testing phase. In (a), the black, blue and red lines indicate results from experiments performed at 20, 80 and 140 °C, respectively. The curves have been smoothed by averaging the original data obtained for every 100 data points (10 s). The inset graph in (a) illustrates gouge compaction/dilatation as a function of displacement during the SHS sequence, from which compaction strain rate was determined using the equation shown. In (b), calculated compaction strain rates are plotted as a function of the logarithm of time, for experiments performed at different temperatures (20, 80 and 140 °C), while (c) shows similar data plotted for different resliding velocities (0.1, 1 and 10 μm/s).

The total compaction of the gouge layer in each experiment (Datasets 1-3) was also obtained from the thickness change of the sample assembly before versus after the experiment. Since all samples were prepared with approximately the same initial thickness (1 ± 0.05 mm), the final thickness yields a direct indication of compaction magnitude, including any minor extrusion of material from the assembly during shear (Table 5.1). For the wet gouge-derived samples, and for the dry and wet breccia-derived samples, the mean compaction values calculated in this way, regardless of temperature, are 0.36, 0.31 and 0.15, respectively.

It should be noted here that the resolution of our volumetric measurements for monitoring sample thickness change was ~ 3 μm, which is much poorer than achieved for displacement measurement (*cf. Yashuhara et al.*, 2005). This means that only dynamic thickness changes bigger than this value, occurring in response to a long hold period, for example, can be reliably detected. For most of our SHS tests that have short hold period, i.e. $t_h < 10000$ s, dilatation upon reshearing was simply below the detection level (for details, see *Chen et al.*, *submitted*, Chapter 4).

5.3.5 Results of control runs on breccia-derived samples

The control experiments performed on breccia-derived samples using alternative pore fluids to sample-saturated water (Dataset 4, Table 5.1) yielded the following results. First, the use of phosphate solution yielded lower ($a–b$) and healing parameter values ($\Delta\mu_r$, $\Delta\mu_{pk}$ and $\Delta\mu_w$) compared with "normal" wet experiments in breccia-derived samples (Dataset 3). An increase in ($a–b$) in VS-seq2 relative to VS-seq1 also occurred in these runs. However, in view of the uncertainties in ($a–b$) (e.g. Figure 5.5), it is unclear how significant the apparent changes in ($a–b$) are compared with "normal" wet experiments (Dataset 3). Second, the experiments conducted using silicone oil as pore fluid showed behavior similar to dry

samples tested at similar conditions (i.e. Type-1a healing during SHS testing and no change in ($a–b$) between two VS-seqs), except for a few stress fluctuations occurring before reaching the macroscopic yield point. Finally, in the single experiment performed on a water-saturated, breccia-derived sample (Run-13) at atmospheric pore pressure, the ($a–b$) values obtained are systematically lower than "normal" wet experiments performed using pressurized pore fluid (Figure 5.5c). Nonetheless, an increase in ($a–b$) in VS-seq2 relative to VS-seq1 is still present (Figure 5.5c).

The control runs performed on wet breccia-derived samples but using non-standard SHS procedures (annotated with "b", "c" and "d" in Table 5.1) also showed interesting effects. Those employing an increasing hold time sequence followed by a decreasing sequence (Run-2 and Run-4) exhibited Type 2 healing behavior in both sequences. However, for the same duration of holds, $\Delta\mu_r$ obtained in the decreasing sequence was much smaller compared with that in the increasing sequence. In the run performed using randomly varied hold times (Run-9), the early long hold generated abnormally large $\Delta\mu_r$ and thus $\Delta\mu_{pk}$ compared with the "normal" tests (Figure 5.7c), though the $\Delta\mu_w$ data still showed a linear relation with $\log(t_h)$ (Figure 5.8c). Lastly, the experiment employing one hold period only (Run-11) also displayed positive $\Delta\mu_r$, as well as an increase in ($a–b$) immediately after the hold period.

5.4. Discussion

5.4.1. General features of the present experiments

The present results show frictional strengths (peak friction coefficients measured at 10 μm/s sliding velocity, Table 5.1) of 0.64 – 0.72 for the dry and wet breccia-derived samples studied, versus of 0.30 – 0.34 for wet gouge-derived samples. These values are in good agreement with previous results on carbonates and on clay-rich gouges obtained at room temperature (e.g. *Scuderi et al.*, 2013; *Verberne et al.*, 2013b; *Tembe et al.*, 2010; *Zhang and He*, 2013). Moreover, the frictional strengths for all samples tested showed a tendency to increase with increasing temperature within the range investigated (Figure 5.3 and Table 5.1). Positive temperature-dependent frictional strengths have also been previously observed in experiments on other material, for example on limestone (i.e. 20 – 150 °C, *Verberne et al.* (2013b)), on illite-quartz mixtures (100 – 600 °C, *den Hartog et al.* (2013)) and on biotite (25 – 600 °C, *Lu and He*, 2015).

We observed the same broad dependence of ($a–b$) on temperature in the experiments on dry and wet breccia-derived samples as reported for calcite-rich gouges by *Verberne et al.* (2013b) and by *Chen et al.* (submitted, Chapter 4), leading to a transition from velocity-strengthening to velocity-weakening slip with increasing temperature (Figures 5.4

and 5.5). By contrast, the gouge-derived samples exhibited stable, velocity strengthening slip at all the temperatures investigated, although a negative temperature dependence of (a–b) was present (Figure 5.5). We also observed a positive dependence of (a–b) on slip rate for all samples tested dry and with (sample-saturated) demineralized water (Datasets 1–3, Table 5.1), with (a–b) increasing at a rate of 0.001 – 0.0035 per decade change in velocity (Figure 5.6). All of these aspects of behavior are similar to previous findings for both carbonates and phyllosilicate-rich gouges (e.g. see discussions by *Weeks and Tullis*, 1985; *Ikari et al.*, 2009; *DenHartog et al.*, 2013; *Verberne et al.*, 2013a, b; *Zhang and He*, 2013).

In addition, we have found a variety of more unusual history effects made visible by the sequential application of VS, SHS and VS stages in the present experiments. Dry experiments on breccia-derived samples show classical Dieterich-type healing characterized by a transient peak in friction after each hold period, with no effects of SHS testing on velocity dependence. By contrast, the wet tests on breccia-derived samples show 1) an increase in steady-state friction upon resliding after a hold period, and 2) a pronounced increase in the velocity dependence parameter, (a–b), after the SHS stage. These effects are visible in our wet experiments performed at elevated temperatures, but are absent from experiments on either dry samples or wet samples tested at 20 °C (Figures 5.5, 5.7 and 5.8). These findings confirm our previous, preliminary data on the same sample breccia-derived gouge (*Chen et al.*, submitted, Chapter 4). Surprisingly, though, our results show that all of the unusual effects seen in the breccia-derived samples are also present in our experiments performed on gouge-derived samples at hydrothermal conditions (80 and 140 °C), despite the fact that these two gouge materials have quite different mineral compositions. Our healing partitioning analysis further demonstrates that the peak healing ($\Delta\mu_{pk}$) observed in all of our hydrothermal experiments can be essentially decomposed into a Dieterich-type ($\Delta\mu_w$) and a non-Dieterich-type ($\Delta\mu_r$) component (Figure 5.9).

In the following discussion, we will quantitatively analyze how the magnitudes and rates of the direct, peak frictional healing effect that we observed (i.e. $\Delta\mu_{pk}$) depend on the various factors investigated in this study, i.e. temperature, re-shearing velocity, mineral composition and the presence of pore fluid, and to what extent the different components (i.e. $\Delta\mu_w$ and $\Delta\mu_r$) contribute to the peak healing ($\Delta\mu_{pk}$). We go to discuss the possible mechanism(s) responsible for the observed behavior, and we consider the implications of our results for the Longmenshan fault zone (LFZ) that hosted the Wenchuan earthquake, and for faults in tectonically-active carbonates terrains in general. Finally, we compare our results with limited similar findings for other gouge materials (e.g. *Yasuhara et al.*, 2005) in an attempt to draw some broader conclusions.

5.4.2 Factors Influencing Frictional Healing

5.4.2.1 Effect of temperature

In the present experiments on wet and dry breccia-derived samples, and on wet gouge-derived samples, we observed a systematic increase in the magnitude of frictional healing (i.e. post-hold restrengthening, $\Delta\mu_{pk}$), and in healing rate (β_{pk}) with increasing temperature in the range 20 to 140 °C, expect in the case of wet breccia-derived material at 80 and 140 °C where the reverse trends were recorded (Figures 5.7 and 5.8). In particular, wet gouge-derived samples (Figure 5.10a) show an increase in average healing rate (β_{pk}) by ~ 10 times, from 0.0006/decade measured at 20 °C to 0.0059/decade at 140 °C. The average healing rate (β_{pk}) of dry breccia-derived samples increases monotonically from 0.0049/decade at 20 °C to 0.0072/decade at 140 °C (Figure 5.10b), while for wet breccia-derived samples, the β_{pk} value increases from 0.0111/decade at 20 °C to 0.0178/decade at 80 °C, and decreases to 0.0119/decade at 140 °C (Figure 5.10c).

Thermally-enhanced frictional healing, similar to that seen in all but wet breccia-derived samples at higher temperatures, has been observed in experiments on wet quartz gouge at 100 to 200 °C (e.g., *Nakatani and Scholz*, 2004), on dry feldspar gouge up to 600 °C (*Nakatani*, 2001), and on dry bare granite surfaces up to 550 °C (*Mitchell et al.*, 2012). Viewed in the framework of RSF laws, frictional healing rates (β_{pk}) are expected to scale with the evolution parameter b for long hold times (e.g. *Marone*, 1998a; *Beeler et al.*, 1994; *Baumberger et al.*, 1999). At the same time, theoretical analyses that assume friction is controlled by a thermally-activated mechanism indicate that b should be proportional to absolute temperature (*Bréchet and Estrin*, 1994; *Nakatani and Scholz*, 2004). Thus β_{pk} should increase in direct proportion to absolute temperature. Assuming a temperature change from 20 °C (293 K) near the surface, to 250 °C (523 K) at the base of the seismogenic zone for a carbonate fault (i.e. at 10 km depth), the implication is that healing rates across this range should roughly double. This is reasonably consistent with the variation in healing rates ($\beta_{pk} = \beta_w$) observed in our dry experiments on breccia-derived samples (Figure 5.10b). Similar sensitivities of healing rate (β_{pk}) to absolute temperature have also been reported for dry feldspar and wet quartz gouges (*Nakatani*, 2001; *Nakatani* and *Scholz*, 2004). However, the β_{pk} values observed in our wet experiments do not agree with this model prediction. In our runs on wet gouge-derived samples (Figure 5.10a), the increase in β_{pk} with temperature that we observed is far in excess of this model prediction, even though the temperature range investigated spanned only 20 to 140 °C. In addition, the β_{pk} data obtained for wet breccia-derived samples displayed an increase and then a decrease with increasing

temperature (Figure 5.10c). All this suggests that the direct effect of absolute temperature on healing embodied in previous models (*Bréchet and Estrin*, 1994; *Nakatani*, 2001; *Mitchell et al.*, 2012), though consistent with our results for dry breccia-derived samples, cannot (fully) account for the more rapid healing observed in our wet experiments on both gouges studied. This means that other effects must play a role. Lastly, we have to note that the peak healing ($\Delta\mu_{pk}$) observed in our hydrothermal experiments was decomposed into two components, i.e. $\Delta\mu_w$-effect and $\Delta\mu_r$-effect (Figure 5.9), and that our analysis indicates that the variations in both $\Delta\mu_w$ and $\Delta\mu_r$ with temperature show the same trends as the combing effect ($\Delta\mu_{pk}$) does (Figures 5.8a and 5.8c). This implies the two effects are related to both thermally-activated and non-thermally -activated mechanisms.

5.4.2.2 Effect of resliding velocity

Independently of temperature, our results for the wet gouge-derived samples, and for the dry and wet breccia-derived samples, show an increase in the magnitudes of frictional healing, i.e. in $\Delta\mu_{pk}$ and $\Delta\mu_w$, with increasing sliding velocity (V_{SHS}), as implemented in the SHS sequences (see Figure 5.8), except for a few wet tests run at between 1 and 10 μm/s (Runs 3, 16 and 25, Table 5.1). However, the healing rates (β_{pk} and β_w) obtained do not show a consistent trend with V_{SHS} (Figure 5.10). Previous experiments on dry quartz gouge and dry salt/salt interface, performed at room temperature, also report a strong increase in frictional healing ($\Delta\mu_{pk}$) with increasing SHS velocity, and a weak dependence of healing rate on reshearing velocity (*Marone*, 1998b; *Renard et al.*, 2012). These findings are thus broadly consistent with our results. The $\Delta\mu_r$ data obtained in our experiments at hydrothermal conditions, for both the gouge- and breccia-derived samples, do not suggest a systematic relationship with re-shearing velocity (Figures 5.8a and 5.8c). However, the cumulative values ($\sum\Delta\mu_r$) do show a tendency to increase with increasing re-shearing velocity (Figure 5.11).

Marone and Saffer (2015) recently carried out numerical modeling to investigate the effect of loading rate on frictional healing ($\Delta\mu$ or $\Delta\mu_w$ in our definition), based on a spring-slider model and the standard RSF equations. Their results show that the role of re-shearing velocity (V_{SHS}) in determining healing is the same as that of V-steps in determining the direct response to a velocity jump, with the magnitude of frictional healing being proportional to the logarithm of V_{SHS} implemented. This may explain the healing ($\Delta\mu_{pk} = \Delta\mu_w$) observed in our dry experiments or the Dieterich-type component of healing ($\Delta\mu_w$) found in our hydrothermal experiments. However, it cannot explain the total healing effect ($\Delta\mu_{pk}$) or the residual healing effect ($\Delta\mu_r$) observed in our runs showing Type 2 healing

behavior. The origin of healing-induced strengthening ($\Delta\mu_r$) and of its cumulative effect ($\sum\Delta\mu_r$) therefore remain unclear at this point. These healing effects, (i.e. the observed persistent change in frictional strength after a hold period), and the role of shearing rate are not readily embodied in the standard RSF laws. Alternative model(s) are therefore needed.

5.4.2.3 Presence of water in wet vs. dry breccia-derives samples

Comparison of our results for dry and wet breccia-derived samples clearly indicates that addition of water causes enhanced frictional healing (Figures 5.8b and 5.8c). Since the peak healing ($\Delta\mu_{pk}$) observed in the wet samples at elevated temperatures is essentially composed into two different components (i.e. $\Delta\mu_{pk} = \Delta\mu_w + \Delta\mu_r$), we thus interpret the difference between the peak healing ($\Delta\mu_{pk}$) observed in wet samples and dry samples at otherwise similar conditions (i.e. t_h, T and V_{SHS}) to be a combination of fluid-assisted effects influencing the Dieterich component ($\Delta\mu_w$) and producing the extra healing effect ($\Delta\mu_r$). As shown in Figure 5.10b, the healing rates (β_w) reported for the dry breccia-derived sample fall in range 0.0018–0.0085/decades (Figure 5.10b). However, the Dieterich component (β_w) reported here for the wet breccia-derived sample ranges from 0.0088 to 0.0196/decade. The healing rates are even higher (i.e., 0.0092 to 0.023/decade), if $\Delta\mu_r$ is taken into account (Figure 5.10c).

5.4.2.4 Effect of gouge composition (wet breccia- vs. gouge-derived samples)

As already discussed in section 5.3.3, the magnitudes ($\Delta\mu_{pk}$) and rates (β_{pk}) of peak healing measured for the wet breccia-derived samples are much higher than the wet gouge-derived samples at otherwise similar conditions (i.e. t_h, T and V_{SHS}). With reference to Figure 5.9, this is attributed to the fact that the Dieterich components ($\Delta\mu_w$) in the gouge-derived samples are only about one tenth of those for the breccia-derived samples. We infer that this is due to their distinct mineral compositions. The gouge-derived material has abundant phyllosilicate components (35 %, smectite-illite and chlorite). It is well documented that the presence of phyllosilicates in halite and silicate gouges can significantly inhibit the transient restrengthening processes in the presence of water (*Bos and Spiers*, 2002; *Carpenter et al.*, 2012), yielding healing rates much smaller than reported for pure quartz (e.g. by *Tesei et al.*, 2012; *Marone*, 1998b), presumably due to prevention of contact cementation/healing effects (*Tesei et al.*, 2012). Besides discrepant Dieterich component ($\Delta\mu_w$), we notice that the magnitudes of healing-induced strengthening ($\Delta\mu_r$) for these two sample types are more or less at the same level (cf. Figures 5.8a and 5.8c, or Figure 5.9a and 5.9b). The consequence is that for the gouge-derived samples, the peak healing observed in

our experiments was mostly (~ 90%) attributed to the healing induced strengthening ($\Delta\mu_r$), whereas for the breccia-derived samples, the contribution from $\Delta\mu_r$ was relatively small (< 20%). The quantities difference in $\Delta\mu_r$ and $\Delta\mu_w$ between these two samples also implies different origins of these two healing components.

5.4.3 The increase in (*a*–*b*) caused by SHS testing – the slip stabilization effect

We observed an increase in (*a*–*b*) after the SHS stages in our wet experiments on both the breccia- and gouge-derived samples. This stabilizing effect was absent in the dry breccia-derived samples (Figure 5.5). Previous studies (e.g., *Byerlee*, 1967; *Wong and Zhao*, 1990; *Voisin et al.*, 2007) have reported a similar transition from unstable stick-slip to stable sliding in experiments on initially bare surfaces made of granite or rock salt, attributed to continued wear with accumulated displacement (*Wong and Zhao*, 1990). However, almost all previous experiments on simulated fault gouge show the opposite, i.e. a transition from velocity-strengthening to -weakening with increasing shearing (e.g. *Beeler et al.*, 1996).

In our the control run (Run-11, Table 5.1), which involved a single long hold (5.5 hours) between two VS sequences, a large positive $\Delta\mu_r$ (Type 2 healing) and an increase in (*a*–*b*) immediately followed the hold period. These suggest that the "stabilization effect" observed in our wet experiments is unlikely to be due to accumulated displacement. As argued by *Chen et al.* (submitted, Chapter 4), strain localization/delocalization effects of the type, proposed by *Sleep et al.* (2000) also cannot explain the observed increase in (*a*–*b*), because theses affect only the frictional strength.

We note here that the stabilization effect seen in our wet experiments at elevated temperatures was always accompanied by Type 2 healing behavior, which was characterized by progressive increase in steady-state strength (i.e. in $\Delta\mu_r$) with sequential SHS events. As shown in Figure 5.11, the magnitude of $\Delta\mu_r$ also shows a positive dependence on sliding rate. On this basis, we propose the following conceptual model explaining how interseismic healing may cause an increase in (*a*–*b*).

First, let us write the (*a*–*b*) value prior to the healing stages

$$(a-b)\big|_{pre} = \frac{\mu_{ss}^{V_2} - \mu_{ss}^{V_1}}{\ln V_2 - \ln V_1} \tag{5.1}$$

Here $\mu_{ss}^{V_1}$ and $\mu_{ss}^{V_2}$ are the steady-state friction coefficients corresponding to velocities V_1 and V_2, used in velocity stepping. During any given SHS sequence, the steady-state friction coefficients increase by an amount corresponding to healing-induced strengthening, that is

$\Delta\mu_r^{V_1}$ and $\Delta\mu_r^{V_2}$ for V_1 and V_2, respectively. The (a–b) value after the healing stage will then be given as

$$(a-b)\Big|_{post} = \frac{(\mu_{ss}^{V_2} + \sum \Delta\mu_r^{V_2}) - (\mu_{ss}^{V_1} + \sum \Delta\mu_r^{V_1})}{\ln V_2 - \ln V_1} \tag{5.2}$$

Here, $\sum$ represents the cumulative healing obtained from different SHS events. From equations (5.1) and (5.2), the change in (a–b) caused by interim frictional healing should hence be given by

$$\Delta(a-b) = (a-b)\Big|_{post} - (a-b)\Big|_{pre} = \frac{\sum \Delta\mu_r^{V_2} - \sum \Delta\mu_r^{V_1}}{\ln V_2 - \ln V_1} \tag{5.3}$$

This implies that the change in (a–b) caused by SHS testing between VS sequences is determined by the difference in the cumulative healing-induced strengthening ($\sum\Delta\mu_r$) measured for different reshearing velocities. Substituting the $\sum\Delta\mu_r$ values for different velocities presented in Figure 5.11 into (5.3), yields $\Delta(a-b)$ values for the wet breccia-derived material of 0.0043 and 0.048 for velocity steps of 1–10 μm/s and 0.1–1μm/s, respectively. For gouge-derived samples, $\Delta(a-b)$ values are around 0.0043 and 0.0034 for velocity steps of 1–10 μm/s and 0.1–1μm/s, respectively. At the same time, the corresponding changes in (a–b) can be determined from the VS-sequences performed before and after SHS testing. As shown in Figure 5.5, the changes are around 0.004 and 0.001 for the breccia- and gouge-derived samples, respectively. Considering the errors in data processing, for example in calculating $\Sigma\Delta\mu_r$, these two sets of $\Delta(a-b)$ values, obtained independently from different data (VS-seq and SHS-seq), are reasonably consistent with one another, suggesting that the stabilization effect may indeed be due to the persistent healing-induced strengthening effect discussed above. However, this does not explain the stabilization effect seen at 20 °C, where $\Delta\mu_r$ is more or less zero. Further work is needed to resolve this issue.

5.4.4 Microphysical Mechanisms Controlling Healing

5.4.4. 1 Type 1a healing (dry breccia-derived samples)

At all temperatures investigated, the SHS stages of our experiments on dry breccia-derived samples (Dataset 2) showed Type 1a Dieterich-type healing behavior (Table 5.1), characterized by unchanged steady-state friction coefficient before vs. after individual hold events and by a log-linear relation between $\Delta\mu_{pk}$ and hold time t_h. This behavior is identical to that seen in previous experiments performed on dry quartz and dry granite gouge samples at similar conditions (e.g. *Marone*, 1998b; *Frye and Marone*, 2002). The healing rates obtained (0.005–0.0086/decade, with a slight temperature dependence) are similar to

those seen in dry quartz and granite gouges. Based on the microstructural observation on dry breccia-derived samples reported by *Chen et al.* (submitted, Chapter 4) and on the present thickness change data (Table 5.1) for these samples, we infer that cataclastic grain size reduction and grain rearrangement, leading to granular flow focused in shear bands found at the boundaries of the samples, were the dominant deformation mechanisms operating during active sliding periods. Though we have no direct evidence ourselves, from the conclusions of previous studies addressing Dieterich-type healing (*Dieterich*, 1979), it seems likely that the mechanisms controlling $\Delta\mu_{pk}$ in our dry SHS testing sequence, likely involved static growth or strengthening of solid-solid contact points during hold periods, due to indentation creep or surface diffusive transport.

5.4.4.2 Type 3 healing (wet gouge-derived material tested at 20 °C)

Type 3 healing, characterized by negative peak (or residual) healing and zero weakening effect ($\Delta\mu_{pk} = \Delta\mu_r < 0$ and $\Delta\mu_w = 0$), was seen only in the gouge-derived sample (Runs 25 and 31) sheared wet at 20 °C (Figure 5.7a). Similar healing behavior has been reported in many materials, for example for wet quartz gouge tested wet at 636°C (*Karner et al.*, 1997), and in experiments on a variety of dry phyllosilicate-rich gouges tested at room temperature (*Ikari et al.*, 2009; *Carpenter et al.*, 2012; *Tesei et al.*, 2012). Numerical fitting of standard RSF parameters to these results (by *Chester and Higgs*, 1992; *Karner et al.*, 1997) for quartz and phyllosilicate gouges revealed zero or negative values for the parameter *b*. Previous workers have proposed that near-zero healing effects may be caused by the saturation of contact area during hold-period compaction, and that the real area of contact does not evolve further upon reshearing (*Saffer and Marone*, 2003; *Ikari et al.*, 2009). The microstructural observations by *Chester and Higgs* (1992) indicated almost a complete loss of porosity, supporting contact saturation. Such a process may be promoted in our gouge-derived sample sheared at 20 °C because of 1) high pore compressibility of the gouge sample (*Chen et al.*, 2013b), and 2) the low intrinsic friction coefficient expected at clay-coated contacts, especially when wet (*Ikari et al.*, 2009).

5.4.4.3 Type 2 healing (breccia- and gouge-derived samples at hydrothermal conditions)

Type 2 healing, characterized by positive $\Delta\mu_r$, can be seen in the results obtained for both the breccia- and gouge-derived samples tested under hydrothermal conditions (80 and 140 °C, Table 5.1). One explanation that can be put forward for the $\Delta\mu_r$ effect after reshearing is the persistence of non-equilibrium pore pressure due to shear-induced dilatation/compaction. This cannot account for the observed positive value of $\Delta\mu_r$, because an

increase in steady-state friction implies lower pore pressure and thus higher porosity, which is inconsistent with the progressive compaction observed in the SHS stages (Figure 5.12a). A second possibility is that mineral transformations may have occurred during the long hold periods. This may explain the enhanced healing seen in the gouge-derived samples, but is unlikely to apply to the breccia-derived sample because they contain only 2% clay. A third possibility for explaining the Type 2 healing behavior ($\Delta\mu_r$) is strain localization/delocalization (c.f. *Sleep et al.*, 2000), which can cause changes in steady-state frictional strength by altering the strain rate in the active slip zone. However, the thickness change required by this mechanism makes it again unlikely in our experiments (see also *Chen et al.*, submitted, Chapter 4). A simple calculation indicates that a broadening of ~ 10–500 times would be needed to account for the observed increases in steady-state friction seen in the SHS events. Our wet breccia-derived samples show very similar shear band thicknesses, i.e. in the range 30 – 150 μm thick (*Chen et al.*, submitted, Chapter 4), to those reported for pure calcite samples subjected to velocity-stepping tests only (e.g. *Verberne et al.*, 2013b). Therefore, a Type 2 healing effect due purely to the combined effects of velocity weakening plus shear band delocalization can be eliminated. Finally, as explained by *Chen et al.* (submitted, Chapter 4), fluid-assisted deformation mechanisms causing asperity growth/strengthening due to fluid-enhanced indentation creep, or a static increase in cohesion (*Yasuhara et al.*, 2005; *Tenthorey and Cox*, 2006), or else by neck growth (e.g. *Hickman and Evans*, 1992; *Niemeijer et al.*, 2008) may explain the Dieterich component of healing ($\Delta\mu_w$), but are unlikely sources of the $\Delta\mu_r$ effect. This is because the enlarged contact area or increased cohesion would be immediately destroyed when reshearing the gouge layer.

5.4.4.3.1 Role of pressure solution in wet experiments

Several lines of evidence indicate that intergranular pressure solution (IPS) likely operated in our wet experiments, especially in the breccia-derived samples. Previous hydrostatic compaction experiments on calcite have shown that IPS is the dominant deformation mechanism in calcite under the P-T conditions investigated here (e.g. *Zhang X., et al.*, 2010; *Spiers et al.*, 2004). The most important evidence for IPS occurring in our wet experiments is the enhanced compaction and shear relaxation creep compared with the dry experiments. First, our thicknesses measurements on the breccia-derived samples showed much more compaction in the wet samples (~ 0.31 mm) than in the dry ones (~ 0.15 mm) (Table 5.1). Second, real-time compaction was evident from the pore fluid volume change (Figure 5.12a). Third, hold-time relaxation creep rates are higher for wet breccia-derived samples than for the dry samples at otherwise similar conditions (Figure 5.13a). Further

evidence comes from the sensitivity of compaction and relaxation to temperature during hold periods. As shown in Figures 5.12b and 5.13b, both gouge compaction and stress relaxation creep rates exhibit negative dependences on temperature, from which apparent activation energies can be derived (appendix 5.A). These fall in the range from –10.8 to –2.4 kJ/mol for compaction, and from –11.1 to –6.9 kJ/mol for shear relaxation creep, consistent with those obtained in hydrostatic experiments on calcite (–24 to –55 kJ/mol by *Liteanu et al.* (2012), –29.9 to –9.7 KJ/mol by *Zhang et al.,* (2010)). Following the arguments given by *Liteanu et al.* (2012), the negative sign is due to the decreasing solubility of calcite with increasing temperature. We have to note, however, that we could not find convincing microstructural evidence for pressure solution in wet breccia-derived samples, though we did find evidence for neck growth and sintering (*Chen et al.,* submitted, Chapter 4).

Though the calcite content is lower, we infer that the above IPS process was also likely to operate in the wet gouge-derived samples, which consists of almost equal proportions of clay, quartz and carbonate (mainly dolomite). Previous studies have inferred that pressure solution played a role in controlling the healing behavior of pure quartz gouge at temperatures as low as 65 °C (e.g. *Yasuhara et al.,* 2005). So far, no experimental studies have addressed IPS in dolomite. However, field evidence for IPS, such as stylolites and grain-to-grain sutures, are widespread in dolomitic limestone and dolomite units (e.g. *Wanless*, 1979). Moreover, data on the dissolution/precipitation kinetic of dolomite suggest that they would not be grossly different from calcite under the present conditions (*Pokrovsky et al.*, 2009). It seems reasonable then to infer then that dolomite may also undergo solution transfer effects similar to calcite in the present experiments on the wet breccia- and gouge-derived samples. On this basis, we infer that the Type 2 healing behavior ($\Delta\mu_r > 0$) observed in the wet gouge-derived samples at elevated temperatures is likely attributable to IPS or to surface energy driven solution transfer processes occurring in both calcite and dolomite, and possibly even in quartz, though solution transfer is known to be very slow in quartz at the present experimental conditions (e.g. *Spiers et al.*, 2004; *Van Noort et al.*, 2008).

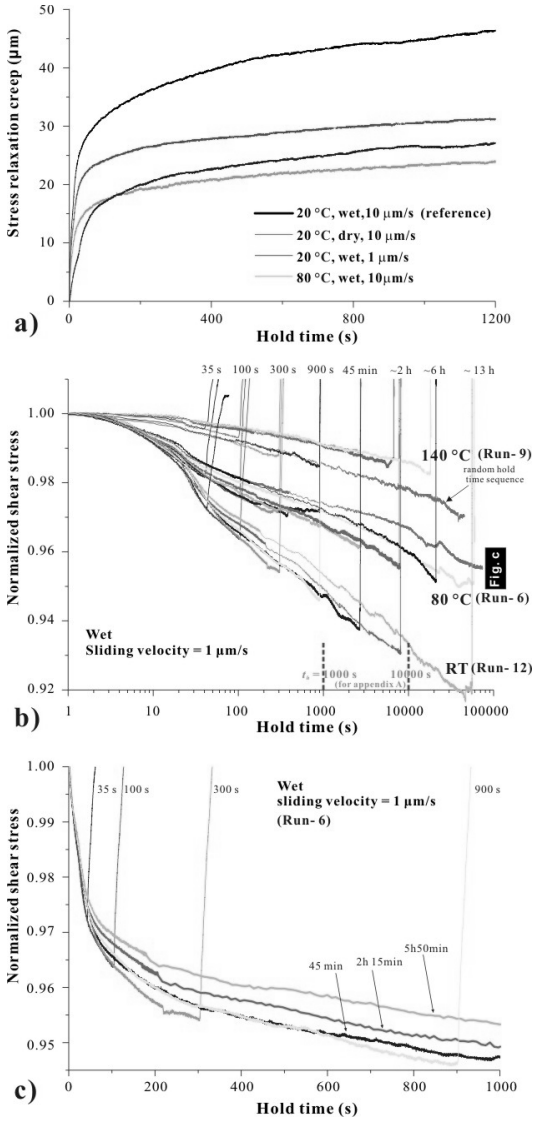

Figure 5.13. Representative data showing creep displacement and normalized stress relaxation occurring during hold periods in the present experiments on breccia-derived samples. a) Relaxation creep displacements vs. hold time (t_h) for the conditions shown. b) Normalized stress relaxation vs. log(t_h) data from individual SHS tests performed on wet samples at 20, 80 and 140 ℃, using a SHS velocity of 1 μm/s. (c) Normalized stress relaxation vs. t_h data from different SHS events within a single wet experiment (Run 6) performed at 80 ℃ and a SHS velocity of 1 μm/s.

The phyllosilicates present in the gouge-derived samples may have a variety of effects on healing involving solution transfer, possibly accelerating interfacial dissolution via

surface charge effects or accelerating intergranular diffusion (*Renard et al.*, 2001; *Greene et al.*, 2009; *Kristiansen et al.*, 2011). On the other hand, clay minerals have also been reported to inhibit healing by impeding intergranular neck growth processes, as reported in previous healing studies on salt–clay mixtures (*Bos and Spiers*, 2000). At the same time, we cannot eliminate the possibility that fluid-assisted subcritical crack growth played a role in the present wet experiments (*Atkinson and Meredith*, 1989; *Wong and Baud*, 1999). Hence it remains difficult to draw firm conclusions on what controls healing in the wet gouges we have studied. The main phyllosilicate components contained in our samples (chlorite and mixed smectite-illite) are relatively stable at the temperatures investigated (*Huang et al.*, 1993; *Chen et al.*, 2013b), so that any effects of transformations on healing in our experiments is very unlikely.

As a last piece of evidence, our control runs (Dataset 4) on breccia-derived samples indicate that fluid chemistry also plays an important role in determining the frictional healing behavior. The use of phosphate solution and silicon oil, both of which inhibit solution transfer in calcite (e.g. *Zhang and Spiers*, 2005), yielded a systematic decrease in the magnitude of stress relaxation ($\Delta\mu_r$) and frictional healing parameters ($\Delta\mu_{pk}$ and $\Delta\mu_w$) in these experiments. Once again this all points to pressure solution and fluid assisted neck growth or sintering processes contributing to healing in our wet experiments, and underscores the role that fluid chemistry may have in controlling healing of natural faults in carbonates.

5.4.4.3.2 Physical origin of $\Delta\mu_r$: irreversible compaction

Accepting that pressure solution and/or related processes were likely operative in our wet experiments showing Type 2 behavior, we now consider how IPS could be responsible for the increase in (quasi) steady-state frictional strength ($\Delta\mu_r$) observed in our SHS test sequences. As a starting hypothesis in line with the preceding discussion, we propose that positive $\Delta\mu_r$ observed in the SHS sequence of our wet experiments resulted from the increase in contact area due to ongoing, permanent porosity reduction, which was enhanced by the IPS processes. As shown in Figure 5.12a, the decrease in porosity that occurred during the hold periods, did not fully recover to the pre-hold state during the on-going reshearing. This implies that reshearing was accommodated in gouge material having persistently lower porosity and/or higher contact cohesion, hence persistently higher strength, than the active gouge zone prior to hold. Note that such an increase in contact area is distinct from the static growth of contact area by indentation creep, which would immediately diminish as slip is re-initiated on contacts, resulting in Type-1a, “Dieterich-type” healing.

As discussed by *Chen et al.* (*submitted*, Chapter 4), to achieve a persistent increase in

steady-state frictional strength ($\Delta\mu_r$) during post-hold re-shearing, two possible changes in microstructure can be envisaged. One possibility is permanent widening of the principal boundary shear band upon re-shearing (or the formation of a new, wider shear band). This would lead to lower shear band strain rates at a given velocity, and hence to more effective internal competition of compaction, by IPS, versus dilatation associated with cataclastic/granular shear flow. The result would be a lower steady-state porosity and higher strength. A second possibility is grain size reduction (i.e. grain breakage) occurring within the principal boundary shear upon post-hold re-shearing. This too would lead to an enhancement of compaction by IPS relative to dilatation by cataclastic/granular flow, since the rate of IPS compaction increases with decreasing grain size (*Zhang X., et al.*, 2010). We favor this explanation because of the extreme narrowness and submicron grain size of the boundary shear bands seen in our samples (*Chen et al.*, submitted; cf. *Verberne et al.*, 2013). Nonetheless, previous microphysical models, based on gouge deformation by granular flow plus pressure solution, predict increasing steady-state friction with both decreasing particle size and with increasing shear band thickness (*Niemeijer and Spiers*, 2007; *Den Hartog and Spiers*, 2014), so that either explanation seems viable. A quantitative model will be developed in a future paper.

Having identified possible origins for $\Delta\mu_r$, we propose that the remaining part of the direct healing effect ($\Delta\mu_{pk}$) observed in our wet experiments at elevated temperatures, i.e. $\Delta\mu_w = \Delta\mu_{pk} - \Delta\mu_r$, reflects changes in contact area and porosity, resulting from more or less reversible static contact growth and/or strengthening, as envisaged in the classical Dieterich model for healing. This is strongly supported by the Dieterich-type healing behavior exhibited by $\Delta\mu_w$ in our data (Figures 5.8 and 5.9). Hence, our favored interpretation of $\Delta\mu_{pk}$ in our experiments is that it consists of a Dieterich-type part ($\Delta\mu_w$) related to reversible contact growth and strengthening, plus a non-Dieterich-type part ($\Delta\mu_r$) related to pressure solution compaction, plus a concomitant irreversible increase in contact area in the actively shearing band, all enhanced by permanent grain size reduction and/or shear band broadening.

5.4.4.3.3 Remaining details of frictional healing data

Re-examining the details of our SHS data, we find that all aspects of the healing behavior seen in the wet experiments at 20 – 140 °C can be explained by the "irreversible compaction" mechanism put forward above. The fact that the shear relaxation creep was faster in early hold periods than in the later periods (Figure 5.13c), can be explained by a smaller contact area (corresponding to higher porosity) that supported the applied shear stress in the early holds. In the control runs performed with cycled hold time sequences

(Runs 2 and 4, Table 5.1), $\Delta\mu_c$ and $\Delta\mu_r$ measured in the increasing hold time sequence were much larger than in the subsequent decreasing sequence for the same hold times. This is consistent with the rate of IPS being smaller in the decreasing sequence owing to lower porosity. The increase in contact area led to a reduction in relaxation creep rates in the hold periods (Figures 5.12b and 5.12c), thereby lowering the magnitude of stress relaxation observed in a given hold time during the decreasing hold time sequence. Similar reasoning can also apply to the testing run with random hold times (Run 9, Table 5.1), in which the early long hold yielded an abnormally large $\Delta\mu_c$ and $\Delta\mu_r$ effects (Figures 5.7c and 5.8c).

5.4.5 Implications for Natural Earthquakes

5.4.5.1 Implications for seismicity in tectonically-active carbonates terrains.

As in several previous studies on quartz gouge (e.g. *Nakatani and Scholz*, 2004), the present experiments on carbonate fault rocks indicate that standard concepts of frictional healing, as embodied in the RSF laws (*Dieterich*, 1972), need to be modified to describe healing under hydrothermal conditions where thermally and chemically enhanced processes are active. In both the wet breccia- and gouge-derived samples studied here, we observed a positive temperature dependence of transient frictional healing (measured in terms of a direct effect $\Delta\mu_{pk}$), and a persistent healing-induced strengthening effect ($\Delta\mu_r$) at elevated temperatures. The latter effect did not occur in dry experiments on the breccia-derived sample. It has been long questioned whether lab-derived healing rates can be applied to natural fault zones (e.g. *Beeler et al.*, 2001; *Marone et al.*, 1995). Our interpretation for carbonate faults is that estimates of healing made by extrapolating dry, room temperature results may significantly underestimate both the magnitudes and rates of fault healing that apply to in-situ hydrothermal conditions, where thermally- and chemically-activated processes are expected to be active, leading to marked restrengthening of natural faults during interseismic periods (c.f. *Nakatani and Scholz*, 2004).

In particular, our results demonstrate that the gouge-derived sample subjected to hydrothermal conditions ($T > 80$°C) can heal at relatively high healing rates (β_{pk}) up to 0.0068/decade. This value is much larger than the rates (< 0.002/decade) typically seen in room temperature results for phyllosilicate/calcite gouges (*Tesei et al.*, 2012). Recent room temperature experiments have yielded zero or even negative healing rates for natural gouge materials collected from tectonically-active faults, such as the San Andreas fault (*Carpenter et al.*, 2012), the Alpine fault (*Boulton et al.*, 2012) and here the Longmenshan fault. This means that healing properties of upper-crustal faults often thought to deform predominantly by aseismic creep of phyllosilicate-rich gouge (e.g. *Bullock et al.*, 2014; *Lockner et al.*, 2011;

Tesei et al., 2012) need to be (re)examined via experiments conducted at in-situ conditions.

Our results provide new insights for understanding the earthquake dynamics of an active fault in carbonate terrains, such as the Apennines, Italy (*Bullock et al.*, 2014). Our results for both dry and wet breccia-derived samples revealed a transition in velocity dependence of friction coefficient from positive to negative with increasing temperature (depth), specifically at about 80 °C. Similar result has been reported previously for limestone and for pure calcite fault gouges (*Verberne et al.*, 2013b). Our results further showed after sequential healing stages involved in our experiments, the transition from velocity-strengthening to -weakening will shift to higher temperatures, resulting a negative (*a–b*) being first seen at ~ 140 °C (Figure 5.5). Assuming a typical geothermal gradient of 20 °C/km, the temperature of 140 °C suggests the onset of velocity weakening and thus possible seismogenesis at depth of ~ 7 km. These results can be expected to apply to the fault rocks represented at depths greater than 7 km on fault in carbonate terrains. This is because, at these depths, the phyllosilicate content of carbonate fault cores is expected to be low, and the carbonate content high, as it is only at shallow levels that some clay minerals (i.e. smectite, smectite-illite) can survive (*Pollastro*, 1993) and that mass removal is likely to concentrate phyllosilicates in the manner reported for the Longmenshan Fault, for example (*Chen et al.*, 2013a). Moreover, the present results for wet, clay-rich samples suggest that shallower, fault segments where a clay-rich carbonate gouge has developed will always be characterized by velocity strengthening behavior (Figure 5.5a). However, the enhanced healing effect reported here in both clay-rich and clay-poor gouges may help explain why relatively large aftershocks occur at shallow portions of faults in carbonate terrains ($M_L > 4$ at ~ 2 km, *Chiarabba et al.* (2009)).

Another key observation in this present study is that under water-saturated conditions, which probably represents the in-situ hydrological state of natural faults, a hold stage imposed between periods at stepped velocities, i.e. a simulated interseismic healing period, can cause an increase in (*a–b*). In our wet, breccia-derived samples, i.e. in wet clay-poor samples, this causes the transition temperature shifting to high temperatures, i.e. from about 80 to 140 °C (Figure 5.5). The implications is that interseismic frictional healing can stabilize rupture nucleation in carbonate-rich faults. If this is applicable to active fault in carbonate terrains, during long-term interseismic healing periods, this stabilization effect should result in the upper limit of the seismogenic zone tending to migrate to deeper crustal levels. In principal, this effect, combined with the enhanced frictional healing effects described above, will tend to promote the nucleation of progressively deeper earthquakes with increasing magnitude. However, we can find no evidence in natural earthquake records

to support the existence of such effects. This absence of such evidence may, of course, reflect preferred operation of other processes, such as initiation/activation of new, weaker fault planes as healing strengthens shallow fault segments (e.g. *Hou et al.*, 2013; *Fondriest et al.*, 2012; *Bullock et al.*, 2014) or else broadening of the original fault zone as deformation spreads into weaker marginal regions of the fault (*e.g. Collettini et al.*, 2014).

5.4.5. 2 Implications for the LFZ (the Wenchuan earthquake fault)

With respect to the 2008 Wenchuan earthquake, two principal asperity regions were associated with the main shock (*Zhang et al.*, 2009). One lies the vicinity of the hypocenter, which is inferred to be related to the Precambrian Pengguan complex (meta-volcanic and -intrusive rocks), and the other is ~ 100 km north (*Wang et al.*, 2011), a region where the coseismic rupture cut through extensive carbonate rocks (*Chen et al.*, 2013a; *Cao et al.*, 2011). The exposure studied here falls into the latter region. On the basis of geophysical inversion results (*Zhang et al.*, 2009; *Zhao et al.*, 2010), coseismic slip in this carbonate region predominantly occurred in the upper 10 km. High-precision relocation studies showed that strong aftershocks occurred in this area, characterized by magnitudes up to Ms 5.2 and focal depths of ~ 10 km (*Zhang et al.*, 2008; *Jia et al.*, 2010). Stratigraphic analysis showed the original thickness of the carbonate strata, which are from Sinian to Middle Triassic in age, to be about 4000 to 7000 m. Deep gas wells drilled in this areas also showed that carbonates dominate down to at least 7560 m (*Cao et al.*, 2011). Seismic reflection profiles further revealed that the sedimentary strata persist down to at least 9 km (*Jia et al.*, 2010; *Cao et al.*, 2011). All these pieces of evidence suggest that the extensive carbonate sequences seen at the surface may be present even at depth where rupture nucleated, and anyway hosted most of the trajectory followed by the rupture process. Against this background, our present study therefore offers relevant constraints on faulting dynamics in the carbonate cover affected by the Wenchuan earthquake rupture. We consider these cautiously below.

First, we have reported on high frictional healing rates (β_{pk}) for gouge samples prepared from carbonate breccia (up to 0.023/decade, Figure 5.10c). The values obtained are substantially higher than the healing rates reported for most other rock types (see a compilation by *Renard et al.* (2012)). Moreover, carbonate fault rocks are also strong, displaying a friction coefficient of typically ~ 0.7 (Table 5.1). The combined effects are consistent with the carbonate rocks present in the sampled segment of the LFZ at least contributing to the asperity associated with the Wenchuan earthquake on the northern part of the LFZ.

Second, as already discussed, our wet breccia-derived samples showed a transition from

velocity- strengthening to velocity-weakening slip above ~ 80 °C, corresponding to depths greater than 4 km. After a cumulative hold time of ~ 24 hours in our experiments, velocity weakening was first seen at ~ 140 °C, corresponding to depths greater than 7 km. Our results is thus consistent with available data from the Wenchuan earthquake, which suggests a focal depth of about 10 km (*Zhang et al.*, 2008), after a period without large earthquakes of at least 2700 years (*Zhang P. et al.*, 2010).

Third, we have found a significant positive dependence of (*a–b*) on load-point velocity, with a sensitivity of 0.001–0.0035 per decade change in velocity (Figure 5.6). On basis of this, we can crudely extrapolate the (*a–b*) values obtained in our experiments for displacement rates of 0.1 – 10 μm/s, to long term displacement rates in natural fault. Taking the breccia-derived sample for example which has a (*a–b*) value of –0.004 at slip rate of 1 μm/s and temperature of 140 °C (Figure 5.6c), this yields (*a–b*) values falling in the range from –0.01 to –0.02 for the cross-fault displacement rates of no more than 1 mm/yr on the LFZ prior to the Wenchuan earthquake (*Zhang P. et al.*, 2010). These values are more negative than the values reported for other rocks types that show velocity-weakening behavior (> – 0.009, see a compiled dataset by *Paterson and Wong* (2005)), suggesting significant potential for slip instability (c.f. *Wong and Zhao*, 1990; *Beeler et al.*, 2001; *He et al.*, 2003). At the same time, however, caution must be exercised when applying the lab-derived "seismicity criteria" to slowly-driven, long-reoccurrence faults, such as the Longmenshan fault (*Zhang et al.*, 2013).

5.4.6 Broader Comparison with Previous Work

Finally, we consider previous results that show behavior similar to the Type 2 healing behavior reported here ($\Delta\mu_r > 0$), and we assess if the healing parameters we have defined (Figure 5.2b) and the healing partitioning we have observed (Figure 5.9) in the present study apply to these previous data.

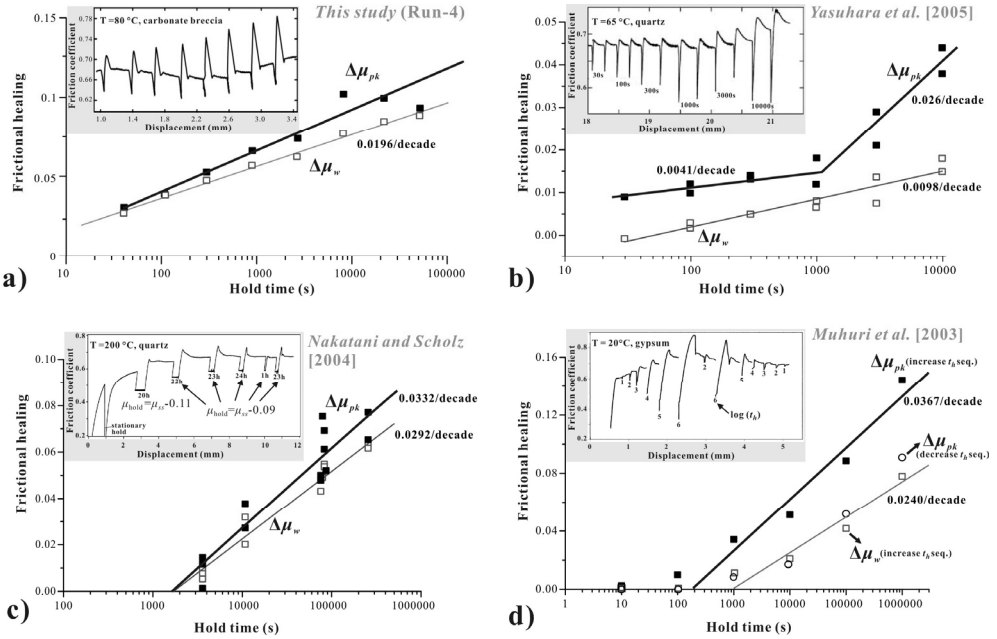

Figure 5.14. Comparison between a) a representative frictional healing experiment on wet carbonate breccia sample, with previous experiments on (b, and c) wet quartz, and on (d)wet gypsum gouges. The inset graphs in (b), (c) and (d) present the friction versus displacement results as given in Figure 2b of Yasuhara et al. (2005), in Figure 1a of Nakatani and Scholz (2004), and in Figure 1a of Muhuri et al. (2003), respectively. The frictional healing data presented ($\Delta\mu_{pk}$ and $\Delta\mu_w$) are derived from the "raw data" from these experiments using the definition (Figure 5.2b) and healing partitioning approach (Figures 5.9) developed in this study. In (b), the data points of $\Delta\mu_{pk}$ are relatively scattered and exhibit a change in slope with respect to log(t_h), with healing rates being shown separately for different intervals. However, the $\Delta\mu_w$ data obtained by subtracting $\Delta\mu_r$ from $\Delta\mu_{pk}$, converge together to yield a nice linear relation of $\Delta\mu_w$ versus log(t_h). In (c), after subtracting $\Delta\mu_r$ from $\Delta\mu_{pk}$, the $\Delta\mu_w$ data become less scattered compared with $\Delta\mu_{pk}$, and indicate more clearly a "Dieterich-type" healing behavior. In (d), the SHS tests were performed in first an increasing t_h sequence followed by the reverse sequence. The $\Delta\mu_{pk}$ data obtained in these two sequences deviated from one another. However, after subtracting $\Delta\mu_r$, the two sets of $\Delta\mu_w$ data converge together and show nice log-linear relation versus hold time.

We found three studies in literature that can be used. Two are on quartz gouges sheared at hydrothermal conditions (*Nakatani and Scholz* (2004) and *Yasuhara et al.* (2005)), and the other is on wet gypsum sheared at room temperature (*Muhuri et al.*, 2003). In all of these three studies, pressure solution was inferred to be the controlling mechanism responsible for the enhanced strengthening observed. As presented in Figure 5.14, the SHS results obtained

in these studies exhibited restrengthening effects in both the transient peak and steady-state frictional strengths. These feature were absent in the authors' wet, cold and dry experiments (not presented here). We applied our healing partitioning concept (Figure 5.9) to these previous data. Generally speaking, the "direct" healing values $\Delta\mu$ (or $\Delta\mu_{pk}$ in our definition), picked from the original data, are scattered and do not indicate clear linear relations with $\log(t_h)$ (Figure 5.14). However, after subtracting $\Delta\mu_r$, the residual portion ($\Delta\mu_w$=$\Delta\mu_{pk}$–$\Delta\mu_r$) for all three data sets yield a systematic linear relationship with the logarithm of hold time (see details in Figure 5.14). As a specific example, *Muhuri et al.* (2003) performed SHS tests with hold times administered first in an increasing sequence and then a decreasing one. They observed a marked $\Delta\mu_r$ effect in the first sequence and a minor effect in the reverse sequence. However, "$\Delta\mu_w$" data derived from the two sequences are consistent with one another and show a nice log-linear relation versus hold time (Figure 5.14c). These features are exactly as analogous with what we observed in our runs with in- and decreasing hold times (Run-2 and Run-4, Table 5.1).

Several other experiments also show increases in steady-state friction (positive $\Delta\mu_r$). *Fredrich and Evans* (1992), *Karner et al.* (1997), and *Tenthorey and Cox* (2006) performed so-called "hold-slide" experiments on quartz gouges at hydrothermal conditions, and observed strengthening in both peak and steady-state friction similar to Type 2 healing behavior. However, in these experiments, the gouges were "healed" at high temperature (636°C) prior to sliding at ~ 200 °C. The strengthening observed accordingly reflected the effects of lithification at high temperature by mineral precipitation (cementation) (*Karner et al.*, 1997), which was inferred to be different from the mechanism(s) operated during sliding.

Lastly, "low-stress" SHS experiments performed at dry, room temperature have shown that decreasing the shear stress to controlled values during the hold periods can lead to an increase in dynamic friction, and hence in peak friction upon resliding (*Nakatani and Mochizuki*, 1996; *Karner and Marone*, 2001). As evidenced by strong compaction observed in the hold periods (*Marone and Scholz*, 1989), the underlying mechanism for enhanced healing in these "low-stress" experiments was attributed to "tight packing" of the gouge due to particle rearrangement when reducing the shear stress. This tightening-up effect of unloading is to some extent similar to the irreversible compaction observed in our wet experiments, even though the deformation mechanisms are quite different.

By making a broad comparison with these previous results, we conclude that 1) our observations of Type-2 (non-Dieterich-type) healing behavior are not restricted to carbonate(-rich) rocks, but may apply to a wide variety of rock types, 2) it can be expected to occur preferentially under hydrothermal conditions where fluid-transfer processes are active,

and 3) in general, any deformation mechanism that facilitates "irreversible compaction" of active shear bands can help produce this behavior. All these previously proposed mechanisms, i.e. "pressure solution" (*Muhuri et al.*, 2003), "enhanced lithification" (*Karner et al.*, 1997), "tight-packing" (*Karner and Marone*, 2001) can to some extent lead to "irreversible compaction" of shear bands during the hold periods. In this point of view, these mechanisms can be classified into a general class of healing mechanism (the $\Delta\mu_r$ effect), not according to the specific microscopic processes, but according to the structures altered by whatever process.

5.5. Conclusions

We performed frictional experiments on simulated gouge samples prepared from carbonate(-rich) fault rocks collected from the YBF fault, a principal branch of the Longmenshan Fault Zone (LFZ) which hosted the 2008 Wenchuan Earthquake. Two sample materials were investigated, a carbonate- dominated breccia-derived sample representing a chemically-unaltered fault rock representing the composition expected at depth and a clay-rich gouge-derived sample representing fault core material characteristic of shallow portions of the fault (< 7 km). In our tests, we applied velocity-stepping (VS), slide-hold-slide (SHS) and a second VS testing sequences to dry and wet breccia-derived samples, and to wet gouge-derived samples, under conditions of 50 MPa effective pressure and 20 – 140 °C. We measured the frictional rate dependence and healing parameters, exploring the effects of temperature, sliding rate and hold times. The following conclusions can be drawn:

1) We found distinct frictional strengths for dry and wet breccia-derived samples versus for the wet gouge-derived samples. All sample types tested showed a negative temperature dependence of the friction rate parameter, (a–b). Dry and wet breccia-derived samples not subjected to healing display a transition from velocity-strengthening to -weakening at ~ 80 °C, while wet gouge-derived samples show velocity-strengthening slip at all temperatures investigated.
2) SHS tests on the dry breccia-derived samples showed typical Dieterich-type healing behavior, characterized by a linear relation between transient peak healing ($\Delta\mu_{pk}$) versus log hold time. However, in the SHS tests performed under hydrothermal conditions, both the gouge- and breccia-derived samples showed "non-Dieterich-type" healing behavior, characterized by an increase in (quasi) steady-state friction coefficient ($\Delta\mu_r > 0$) after the hold period. The transient peak healing ($\Delta\mu_{pk}$) observed in all our hydrothermal experiments consists of two components, i.e. a post-peak drop or

Dieterich component (the $\Delta\mu_w$-effect) plus a persistent strengthening in (quasi) steady-state friction (the $\Delta\mu_r$-effect).

3) Frictional healing rates of the dry breccia-derived samples display a tendency to increase with increasing temperature, consistent with previous results on quartz and feldspar gouges. The wet equivalents showed larger peak healing rates (β_{pk}) but with a more complex temperature dependence. By Contrast, wet gouge-derived samples show an increase in peak healing rate β_{pk} by ~ 10 times, from 0.0006/ decade at 20 °C to 0.0059/decade at 140 °C.
4) Mechanisms previously proposed to explain Dieterich-type healing (e.g. indentation creep, neck growth), cannot explain the positive $\Delta\mu_r$ observed in our wet experiments. We infer that the persistent restrengthening effect ($\Delta\mu_r$) is related to permanent, progressive porosity reduction during hold periods, probably due to intergranular pressure solution, modified in the case of the clay-rich gouge-derives samples by effects of the clay and quartz content.
5) Our experiments revealed that repeated SHS motion plus healing under wet conditions can lead to an increase in (a–b) and thus a tendency for slip stabilization in carbonate fault rocks. A conceptual model show this change in (a–b) is at least in part related to the persistent effect of healing- induced strengthening ($\Delta\mu_r$).
6) As for the Wenchuan earthquake, the carbonates present on the northern segment of the rupture zone are inferred to contribute to the asperity inferred in that region. For natural carbonate faults in general, our results indicate that a) where fluid-assisted processes such as pressure solution are an important healing mechanism, applying a log-linear trend will underestimate natural fault healing, and that quantitative models must account for fluid-assisted processes as inferred here, b) clay-rich fault rocks can heal at rates much higher than previously recognized from room temperature experiments, c) interseismic frictional healing can stabilize rupture nucleation in carbonate faults. This may result in the seismogenic zone migrating into deeper crustal levels with on-going fault activity.

Appendix 5.A: Derivation of activation energies from compaction and stress relaxation data

Numerous authors (*Lehner*, 1990; *Spiers and Schutjens*, 1990; *Spiers et al.*, 2004) have published theoretically derived IPS rate equations for both deviatoric and compaction creeps. Here, we assume the gouge compacts as an isotropic material in our frictional experiments, so that the effect of normal and shear stress on compaction and shear deformation occurring during hold periods in the present SHS testing sequences can be treated separately.

With reference to Figure 5.12a, the compaction strain rate during individual hold events can be estimated as $\dot{\varepsilon} = \Delta L/(L_0 t_h)$, where ΔL is the magnitude of compaction, t_h is the hold time over which the compaction took place, and L_0 is the initial thickness. Here, "initial" is defined as the start of a SHS sequence, with L_0 ranging from 0.7 to 0.85 mm, as estimated from the pore fluid volumetric data and the thickness change measurements made here (Table 5.1). We find that the main features of the calculation results are insensitive to L_0. For the sake of simplicity, we assume L_0 to be 0.8 mm for all cases. A generalized creep law of the form $\dot{\varepsilon} = A\exp(Q_1/RT)\sigma_n^m$ is used to describe normal compaction, where σ_n is effective normal stress, m is the stress sensitivity factor, Q_1 is activation energy, T is absolute temperature, R is gas constant (8.31 $\mathrm{Jmol^{-1}K^{-1}}$), and A is a temperature-independent constant. Considering σ_n was the same in all our runs, Q_1 can be determined by fitting $\log\dot{\varepsilon}$ against $1/T$. Figure 5.A1 plots representative results for the wet breccia-derived sample, and shows systematic linear relations. The activation energies obtained range from –21.1 to –2.4 KJ/mol.

Typical stress relaxation results are presented in Figure 5.13. At every moment of the hold period, the creep deformation accommodated by the gouge layer should be equal to the machine distortion. Time derivative of this relation can be expressed as

$$v_{el} = \dot{\gamma} L_t \tag{5.A1}$$

where v_{el} is velocity associated with distortion of loading system, and where $\dot{\gamma}$ and L_t are the shear strain rate and thickness of the gouge layer. The relaxation creep rate can be described using

$$\dot{\gamma} = B^* \tau^n \tag{5.A2}$$

where τ is shear stress, n is stress sensitivity factor, and B^* is a temperature-dependent term. At the same time, v_{el} can be expressed as $v_{el} = -\dfrac{d\tau}{Kdt}$, where K is stiffness of the loading frame. Combining 5.A1 and 5.A2, thus yields

$$\frac{d\tau}{dt} = -B^* K L_t \tau^n \tag{5.A3}$$

Integrating (5.A3) with the initial condition that $\tau = \tau_0$ at $t = 0$, the evolution of shear stress during a hold period can be calculated as

$$\left(\frac{\tau}{\tau_0}\right)^{1-n} = 1 + (n-1)\frac{t}{\lambda} \tag{5.A4}$$

where $\lambda = \tau_0^{1-n}/(B^* K L_t)$ is the characteristic relaxation time, and its reciprocal expresses stress attenuation rate. When t is not too small, (5.A4) can be rewritten as $\ln(\frac{\tau}{\tau_0}) = B^{\wedge} + \frac{\ln t}{1-n}$. Because the magnitude of stress relaxation was small in our experiments (< 6%, Figure 5.13b), using $\ln(1+x) \approx x$ for a small x, we get $\ln(\frac{\tau}{\tau_0}) = \frac{\tau - \tau_0}{\tau_0}$. Accordingly, (5.A4) is further reduced to

$$\tau / \tau_0 = c \ln(t) + c_0 \tag{5.A5}$$

Here c is $\log_{10}(e)$ times the slope of the curve of τ / τ_0 vs. $\log_{10}(t)$. As shown in Figure 5.13b, the slopes of these curves decrease with increasing temperature, and at each temperature the slopes are slightly different for individual SHS events. The curves for the latter SHS events are always gentler than the early ones. Taking the c values from Figure 5.13b, the shear strain rate can be calculated as

$$\dot{\gamma} = \frac{v_{el}}{L_t} = -\frac{d\tau}{K L_t dt} = -\frac{\tau_0 c}{K L_t t} \tag{5.A6}$$

which is proportional to the c value and is inversely proportional to hold time.

We now assume that relaxation creep follows a standard relation $\dot{\gamma} = B \exp(Q_2 / RT) \tau^n$, where Q_2 and B are the activation energy and pre-exponential constant for shear deformation (at given porosity). This equation is the expansion of (5.A2) to incorporate the temperature effect. Considering stress relaxation is small in our experiments, τ^n can be thus approximated as equal in all cases. Following the method used for compaction, the activation energy for relaxation (shear) creep can be determined (Figure 5.A1-b). In line with the compaction results, the shear strain rates obtained exhibit a decreasing trend with increasing temperature, with the activation energies obtained falling in the range from –11.1 to –6.9 KJ/mol.

Acknowledgements: We would like to thank Peter van Krieken and Gert Kastelein for their technical support in maintaining the testing machine. JC was funded by the Foundation of State Key Laboratory of Earthquake Dynamic (LED2010A03) and by the Netherlands Center for Solid Earth Science (ISES) grant 2013-103, while BAV was supported by ISES grant 2011-75.

Chapter 6

Rate and state frictional and healing behavior of carbonate fault gouge explained using microphysical model

Jianye Chen, and Christopher J. Spiers

Abstract

Classical rate-and-state friction (RSF) laws are widely applied in modeling earthquake dynamics, but generally using empirically determined parameters with little or no knowledge of, or quantitative account for, the controlling physical mechanisms. Here, a mechanism-based microphysical model is developed for describing the frictional behavior of carbonate fault gouge, assuming that the frictional behavior seen in lab experiments is controlled by competing processes of intergranular slip versus contact creep by pressure solution. By solving two controlling equations, derived from kinematic and energy/entropy balance considerations, and using standard creep equations for pressure solution, we simulate typical lab-frictional tests, namely "velocity stepping" and "slide-hold-slide" test sequences, for velocity histories and environmental conditions employed in previous experiments. The modeling results capture all of the main features and trends seen in the experimental results, including both steady-state and transient aspects of the observed behavior, with reasonable quantitative agreement. To our knowledge, ours is the first mechanism-based model that can reproduce RSF-like behavior without recourse to the RSF law. Since it is microphysically based, we believe our modeling approach can provide a much improved framework for extrapolating friction data to natural conditions.

6.1 Introduction

Rock friction data have been widely used as input for modeling the dynamics of rupture nucleation, slip and healing associated with natural earthquakes and with induced seismicity. Such data are usually described using the so called rate-and-state (RSF) friction law (*Dieterich*, 1979; *Ruina*, 1983), which expresses the rate (V) and state (θ) dependence of friction coefficient (μ), via the relation

$$\mu = \mu_0 + a\ln(\frac{V}{V^*}) + b\ln(\frac{V^*\theta}{D_c}) \tag{6.1}$$

where μ_0 is the steady-state friction coefficient at a reference slip rate V^*, a and b are empirical constants specifying the magnitude of the so-called "direct" and "evolution" effects that follow a stepwise increase in velocity from V^* to V, and D_c is the characteristic slip distance over which that evolution in μ takes place (*Dieterich*, 1979). Also embodied in the RSF constitutive framework is the concept that static fault restrengthening, following an active slip event, is expected to increase linearly with the logarithm of the healing or "hold" time (*Dieterich*, 1972; 1979), with the rate of restrengthening or healing (β) being expressed as

$$\beta = \frac{\partial(\Delta\mu_{pk})}{\partial \ln t_h} \tag{6.2}$$

where $\Delta\mu_{pk}$ is the magnitude of frictional healing (the transient increase in frictional strength upon reshearing) and t_h is the hold time over which healing occurs.

These equations were developed to provide a phenomenological description of the frictional and healing behavior typically observed in lab experiments (*Dieterich*, 1979), the parameters contained within them being generally obtained simply by fitting the equations to curves obtained from velocity stepping or slide-hold-slide friction experiments (e.g. *Marone*, 1998b). Though empirical in nature, it is widely agreed that RSF laws somehow reflect competition between contact creep vs. contact destruction within the relevant sliding interfaces (e.g. *Dieterich*, 1972). In response to a reduced slip rate or to a stationary hold, the contact area within the sliding surfaces is expected to increase owing to creep of the existing contacts. This means that when shearing switches to a faster rate or is resumed after a hold period, the resistance offered by the increased contact area offers an increased resistance to shear ("the direct effect"). After this transient response, the shear stress then evolves towards a new steady-state value, corresponding to a new population of contacts ("the evolution effect") determined by the effects of contact growth versus destruction. This evolution can lead either to an increase in steady state strength with increasing sliding velocity (velocity

strengthening) if the new contact population supports higher shear stress than the old, or to a decrease in strength (velocity weakening) if lower shear stress is supported.

The above RSF laws are widely used to model natural faulting phenomena, including earthquake nucleation (e.g. *Scholz*, 2002), aftershock activity (*Marone et al.*, 1995; *Chen and Lapusta*, 2009), slow slip (*Ampuero and Rubin*, 2008), and post-/interseismic fault creep and healing (*Marone*, 1998a; *Barbot et al.*, 2009; *Hetland et al.*, 2010). However, there are several critical discrepancies between seismological constraints on RSF behavior associated with earthquakes and lab-derived RSF parameters, in particular regarding the static stress drop and characteristic slip distance associated with seismic events (*Scholz*, 2002). Moreover, lab friction studies can address only limited fault topographies, displacements, experimental durations and P-T conditions, which means that scale issues, and especially processes like dilatation and fluid-rock interaction, cannot be fully taken into account. Without a basis for accounting for such effects, extrapolation of experimentally derived RSF data to other experimental conditions and to nature involves significant, often unknown uncertainties.

Besides these difficulties, it has been long recognized that the RSF laws have shortcomings in reproducing laboratory results (e.g. *Beeler et al.*, 1994; *Chester*, 1994; *Marone et al.*, 1995). For instance, at hydrothermal conditions where fluid-assisted mass transfer processes are active, frictional healing may be strongly promoted, with the healing rates measured lying far beyond the log-linear model used in RSF approaches (*Karner et al.*, 1997; *Nakatani and Scholz*, 2004; *Yasuhara et al.*, 2005; *Niemeijer et al.*, 2008). As one of the key parameters for earthquake nucleation and propagation, the velocity-dependence of friction, often expressed as ($a–b$), is revealed to be virtually velocity dependent in the low-velocity regime (*Shimamoto*, 1986; *Ikari et al.*, 2009; *den Hartog and Spiers*, 2013). This cannot be explained by the RSF laws and grave uncertainties hence exist when taking ($a–b$) as an indicator of slip in-/stability, considering the dynamic loading process of a tectonically-active fault.

We believe that the deficiencies stated above are at least in part due to the fact that RSF laws lack a fundamental physical basis (*Dieterich*, 1979; *Baumberger et al.*, 1999; *Nakatani*, 2001; *Rice et al.*, 2001), i.e. are based on a conceptual model of contact asperity growth and annihilation rather than on a microphysical description of the physical processes observed to operate in fault gouges (e.g., *Sleep et al.*, 2000; *Bos and Spiers*, 2002; *Niemeijer* and Spiers, 2006). In order to more reliably apply experimental results to natural fault zones, and notably to extrapolate lab data beyond laboratory pressure, temperature and velocity conditions, an understanding of the microphysical mechanisms governing fault frictional behavior is required. A better basis is needed to assess reliability and to underpin modeling of earthquake

phenomenon and induced seismicity. Some earlier efforts have succeeded in predicting steady-state frictional strengths of fault gouges, based on realistic, physical processes identified by means of microstructural analysis (*Bos and Spiers*, 2002; *Niemeijer and Spiers*, 2007; *den Hartog and Spiers*, 2014). However, these models have so far addressed only steady state friction, with transient frictional behavior, i.e. the response to a perturbation in sliding rate, not yet being considered. Ideally, of course, a single model based on the physical processes operating should be sought, which describes steady state, transient and healing behavior.

We recently reported frictional data on carbonate fault gouge (*Chen et al.*, submitted, Chapter 4) that demonstrate healing behavior characterized by a progressive increase in steady-state friction after static hold periods. Similar behavior has been reported by *Yasuhara* et al. (2005) for quartz gouge and *Muhuri et al.* (2003) for gypsum gouge. This type of behavior cannot be explained by the only transient healing effect embodied in classical RSF healing theory (equation 6.2). Our experimental data and microstructural observations point to granular/cataclastic flow and pressure solution as the dominant deformation mechanisms, with slip localization in boundary shears (though crystal plasticity may also play a role in the cataclastic grain size reduction process – *Verberne et al.* (2013a, b)). In this paper, we develop a model for friction and healing that is based on granular/cataclastic flow and pressure solution mechanisms. The modeled results capture all the main features of the frictional behavior observed in our lab experiments on carbonate gouge, and are consistent with the type of response expected using a classical RSF law. To the best of our knowledge, our model is the first based on a microphysical description of mechanisms inferred to operate via microstructural studies, which is able to produce "RSF-like" behavior without resorting to the RSF equations.

6.2 Frictional Behavior of Carbonate Gouges Under Hydrothermal Conditions

We first recap on our previous friction experiments on carbonate fault gouge (*Chen et al.*, *submitted*, Chapter 4). In that study, we employed a specially designed experimental strategy, consisting of sequential "velocity stepping", "slide-hold-slide" (SHS) and "velocity stepping" stages. The samples were sheared in a direct shear setup located in a triaxial testing machine at 20 – 140°C and 50 MPa effective normal stress. In experiments conducted wet, a (sample-saturated) pore fluid pressure of 15 MPa was used. As shown in Figure 6.1a, wet sample behavior at 80 – 140 °C is characterized by macroscopic yield, giving way to steady-state frictional sliding with $\mu_{ss} \approx 0.65$, plus unstable, velocity-weakening behavior in the first velocity stepping sequence (VS-1). Subsequent SHS testing is characterized by a

transient peak healing effect ($\Delta\mu_{pk}$) but also by a permanent increase in steady-state friction, referred to as the healing-induced strengthening ($\Delta\mu_r$) (Figure 6.1c). A pronounced increase in (a–b) can be seen in the second VS sequence (VS-seq2) after the SHS stage, leading, at 80 °C and above to a transition from velocity-weakening (seen in VS-seq1) to -strengthening (seen in VS-seq2). All of these features were absent in identical tests performed on dry samples. In the following, we focus on the results for wet samples.

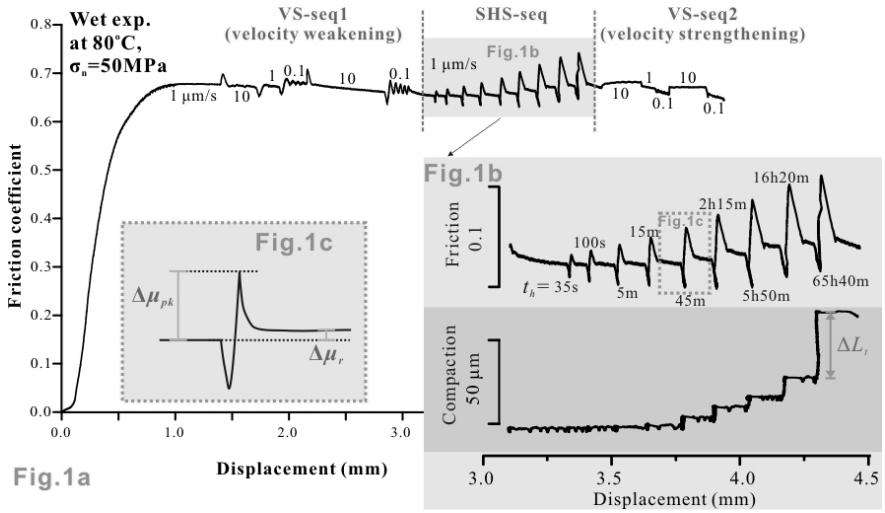

Figure 6.1. Representative experimental data on carbonate gouge sheared at hydrothermal conditions (compiled from Chen et al., submitted).

Based on the microstructural observations and enhanced gouge compaction seen in wet versus dry samples (*Chen et al.*, submitted, Chapter 4) intergranular pressure solution (IPS) was inferred to be an important deformation mechanism in our experiments. As shown in Figure 6.1b, marked gouge compaction was observed especially during the longer hold periods. Mean compaction strain rates calculated over such periods displayed a negative temperature dependence, in line with to the decrease in solubility of calcite seen with increasing temperature, and suggesting that grain boundary diffusion is the process controlling the rate of IPS (*Liteanu et al.*, 2012). The post-deformational gouge microstructure also revealed a well-developed cataclasite signature in both the bulk gouge and prominently developed boundary shears (Figure 6.2), indicating that brittle grain failure and granular flow were probably the most important shearing mechanisms in our experiments. For detailed mechanical data and an analysis of the active deformation

mechanisms, see *Chen et al., submitted* (Chapter 4).

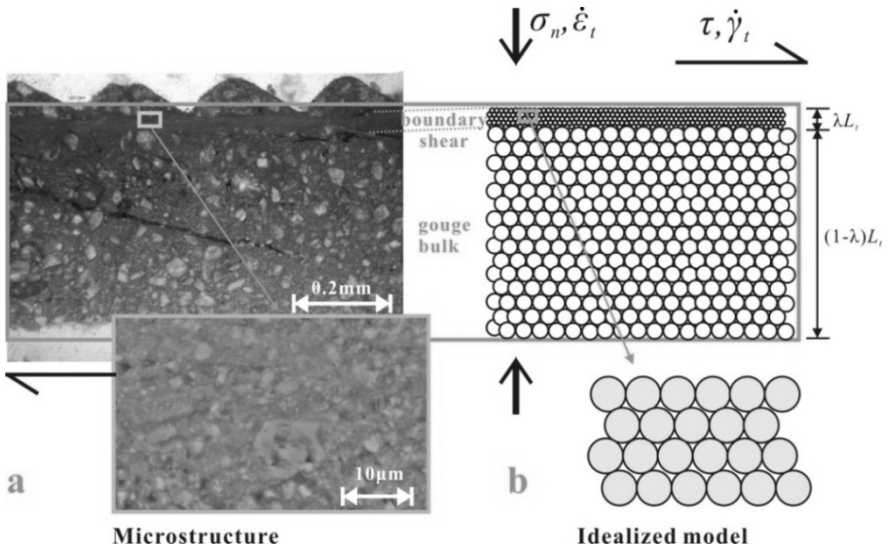

Figure 6.2. a) Representative microstructure of experimentally sheared carbonate gouge samples (Verberne et al., 2013; Chen et al., submitted) and b) the idealized microstructural model employed here. Note the impression of the tooth grips in the top surface of the experimentally sheared sample, immediately above the highly localized boundary shear in (a).

6.3 Microphysical Model Development

To develop a microphysical model, we start by constructing a microstructural model, based on the microstructure observed in our experiments on carbonate gouge, and by defining related microstructural state variables (i.e. porosity, average grain contact area and dilatancy angle). We proceed to derive a kinematic equation linking sample deformation/slip, machine distortion and imposed displacement at the "load point" (i.e. at the conceptual point of application of shear load to the apparatus or loading frame). Using an energy/entropy balance approach, we subsequently establish a second equation relating shear stress evolution to changing microstructure. Coupling these two equations leads to our final microphysical model, describing the frictional behavior of a granular fault gouge in response to any boundary condition imposed on it, including constant velocity sliding, velocity stepping, SHS testing or fixed boundary stresses.

6.3.1 Idealized Microstructural Model

Figure 6.2a shows a representative example of the microstructure exhibited by a wet

carbonate gouge sheared at 80 – 140 °C and 50 MPa effective normal stress. A fine-grained boundary shear zone measuring 20 – 40 μm in thickness is clearly developed at the upper sample interface (see also *Verberne et al.* (2013b) and *Chen et al.*, submitted). The bulk of the gouge layer is less deformed and shows a chaotic microstructure, with a particle size distribution similar to the starting material (average grain size 28 μm). Inclined Riedel shear bands (R1 shears, following the terminology of *Logan et al.* (1992)) can also be discerned locally. The boundary shear is characterized by extreme grain size reduction compared with the gouge bulk. Particles within this boundary shear band are poorly distinguishable or indistinguishable with an optical microscope. However, SEM images show a chaotic (no preferred orientation), granular microstructure similar to the gouge bulk, with grain sizes mainly in the range of 0.1 – 5 μm (Figure 6.2a).

On basis of the observed microstructure, we adopt the idealized microstructural model shown in Figure 6.2b, featuring a localized shear band developed at the margin of the bulk gouge. Both gouge zones are represented by densely packed cylinders or spheres, with different mean diameters per zone, representing the constituent grains (*Niemeijer and Spiers*, 2007). Imposed shear displacement is assumed to be accommodated mostly by the localized shear band, as observed in our experiments (*Verberne et al.*, 2013b; *Chen et al*, *submitted*). The thickness of the shear band is defined as λL_t, where L_t is the total thickness of the gouge layer and λ is taken as a constant defining relative shear band thickness ($\lambda \leq 1$).

6.3.2 Microstructural State Variables and Associated Relationships

Following the approach used by *Niemeijer and Spiers* (2007), shear deformation of both gouge zones is assumed to occur predominantly by granular flow with grain neighbors swapping occurring as grains slide over each other. Slip occurs on the inclined grain contacts, leading to dilatation with a dilatancy angle (ψ) (*Paterson*, 1995). Intergranular pressure solution (IPS) also occurs at grain contacts (each of area a_c), in response to the stresses transmitted across them, causing thermally activated (rate dependent) deformation in both the normal and shear directions. Figure 6.3 shows snapshots of the evolution of the microstructural model with increasing imposed sliding velocity. With increasing shear rate, Ψ becomes progressively smaller as dilatation becomes increasingly dominant over compaction by pressure solution, generating higher porosity φ and lower grain contact area a_c.

The microstructural state of the gouge material, in both gouge zones represented in Figure 6.2, is thus controlled by competition between compaction by IPS and dilatation due to granular flow. As explained by *Niemeijer and Spiers* (2007), this microstructural model is reasonable provided that competition between compaction and dilatation ensures that the

porosity remains below the maximum attainable (critical state) value.

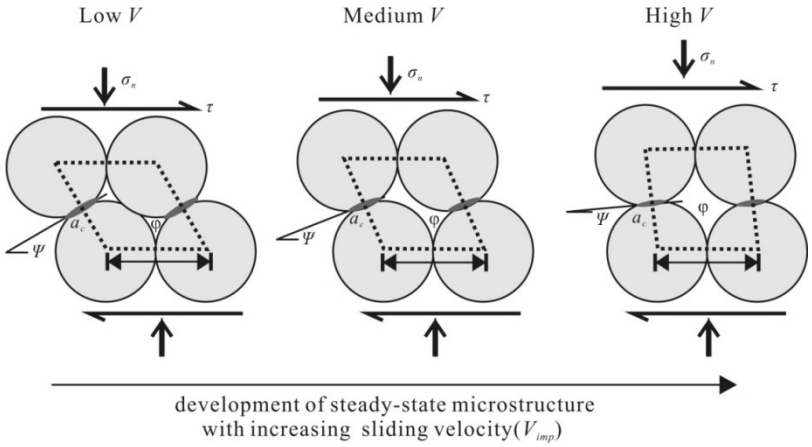

Figure 6.3. Conceptual model illustrating the evolution of the key microstructural state variables, i.e. dilatancy angle (ψ), porosity (φ) and average contact area (a_c), with increasing sliding velocity (V_{imp}).

To quantify the rate of change of volume due to the combined effects of granular flow and IPS during shearing and/or static healing, relations are required that link the above state variables, i.e. ψ, φ and a_c. Clearly, for any given grain packing geometry (e.g. a cubic pack of spherical grains of diameter d), ψ, a_c and φ are interdependent on one another (Figures 6.3 and 6.4). Following *Niemeijer and Spiers* (2007), ψ can be adequately related to φ by a function of the form

$$\tan\psi \approx H(q - 2\varphi) \tag{6.3}$$

where H and q are geometric constants, with H lying in the range $1/\sqrt{3}$ to $\sqrt{3}$ for 2-D grain pack, and q being two times the critical state porosity φ_c for granular flow, which when $\varphi = \varphi_c$ yields the extreme case that $\tan\psi$ equals zero. This function describes a monotonic decrease in ψ with increasing φ, in line with that observed during purely granular flow of particulate materials with a porosity less than the critical state value (e.g. *Campbell*, 2006). To describe how the mean grain-to-grain contact area a_c depends on φ, we assume that a_c is related to the surface area of a spherical grain via the average coordination number z, such that $a_c \rightarrow \pi d^2/z$ as $\varphi \rightarrow 0$, where d is grain diameter (Figure 6.4) (*Spiers et al.*, 2004; *Pluymakers and Spiers,* 2014). Analysis of the geometry of a simple cubic, or body-centered cubic pack of initially spherical grains compacted isotropically by pressure solution (*Renard et al.*, 1999; *Niemeijer and Spiers*, 2002) shows that the relation between contact area and porosity is then well approximated by the relation

$$a_c = \pi d^2 (q - 2\varphi) / z \tag{6.4}$$

for porosities down to ~ 5% (*Pluymakers and Spiers,* 2014). We use it here assuming that this relation holds for gouge material undergoing deformation in both the normal and shear directions. Hence, using (3) and (4), both a_c and ψ can be related to the key microstructural state variable φ.

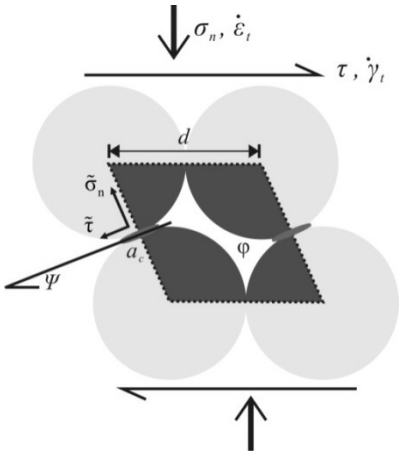

Figure 6.4. The unit cell characterizing the grain pack used in the present microstructure. Grain diameter is d, and grain-to-grain contact area per unit cell is a_c = 2 × ½ a_c.

6.3.3 Kinematic Relations for Gouge Deformation

6.3.3.1 Normal and Shear Strain Rate Components

In this analysis, we assume both the gouge bulk and boundary shear band deforms by two parallel processes, i.e. granular flow and pressure solution. Elastic deformation of the gouge is neglected. This allows us to write normal and shear strain rates ($\dot{\varepsilon}_t$ and $\dot{\gamma}_t$) in a representative volume of gouge as

$$\dot{\varepsilon}_t = \dot{\varepsilon}_{ps} + \dot{\varepsilon}_{gr} \tag{6.5a}$$

$$\dot{\gamma}_t = \dot{\gamma}_{ps} + \dot{\gamma}_{gr} \tag{6.5b}$$

Here compaction is taken as positive $\dot{\varepsilon}_t$, the subscript "*t*" indicates measured, total shear or compaction strain rate, and "*ps*" and "*gr*" represent deformation attributed to pressure solution and granular flow, respectively. Considering that compaction and shear deformation occur both within and outside the shear band (Figure 6.2), we further have

$$\dot{\varepsilon}_{ps} = \lambda \dot{\varepsilon}_{ps}^{sb} + (1-\lambda)\dot{\varepsilon}_{ps}^{bulk} \tag{6.6a}$$

$$\dot{\gamma}_{ps} = \lambda \dot{\gamma}_{ps}^{sb} + (1-\lambda)\dot{\gamma}_{ps}^{bulk} \tag{6.6b}$$

where the superscripts *sb* and *bulk* indicate the shear band and remaining bulk gouge, respectively. Since shearing is concentrated in the shear band, we assume that significant granular flow and dilation only occur in the shear band, that is $\dot{\varepsilon}_{gr}^{bulk} = 0$ and $\dot{\gamma}_{gr}^{bulk} = 0$. Following the classical soil mechanics approach to granular flow (*Paterson*, 1995), dilatation due to granular flow can be described using the relation $\dot{\varepsilon}_{gr}^{sb} = -(\tan\psi)\dot{\gamma}_{gr}^{sb}$. Using this relation, the compaction strain rate within the shear band, the bulk and entire gouge layer can hence be written as

$$\dot{\varepsilon}_{t}^{sb} = \dot{\varepsilon}_{ps}^{sb} - (\tan\psi)\dot{\gamma}_{gr}^{sb} \tag{6.7a}$$

$$\dot{\varepsilon}_{t}^{bulk} = \dot{\varepsilon}_{ps}^{bulk} \tag{6.7b}$$

$$\dot{\varepsilon}_{t} = \lambda\dot{\varepsilon}_{ps}^{sb} + (1-\lambda)\dot{\varepsilon}_{ps}^{bulk} - \lambda(\tan\psi)\dot{\gamma}_{gr}^{sb} \tag{6.7c}$$

Similarly, the shear strain rate within the shear band, the bulk and entire gouge layer can be given as

$$\dot{\gamma}_{t}^{sb} = \dot{\gamma}_{ps}^{sb} + \dot{\gamma}_{gr}^{sb} \tag{6.8a}$$

$$\dot{\gamma}_{t}^{bulk} = \dot{\gamma}_{ps}^{bulk} \tag{6.8b}$$

$$\dot{\gamma}_{t} = \lambda\dot{\gamma}_{ps}^{sb} + (1-\lambda)\dot{\gamma}_{ps}^{bulk} + \lambda\dot{\gamma}_{gr}^{sb} \tag{6.8c}$$

6.3.3.2 Rate of Compaction/Dilatation

To quantify the transient evolution of gouge layer porosity and strength in response to deformation, we now need a relation linking porosity of the material (φ) to normal strain rate ($\dot{\varepsilon}$). Assuming a closed elementary volume of gouge material with respect to solid species mass and volume, then the solid volume (V_s) will be constant at all times. The dynamic porosity is therefore related to the total volume of the gouge (V), $\varphi = 1 - V_s / V$. The time derivative of this then yields

$$\dot{\varphi} = \frac{V_s \dot{V}}{V^2} = \frac{(1-\varphi)\dot{V}}{V} \tag{6.9}$$

Here $\dot{V}/V$ is the volumetric strain rate measured in terms of dilatation normal to the shear plane. This is equal to the compaction strain rate but with the opposite sign, such that

$\dot{\varepsilon} = -\dot{V}/V$. Hence, (6.9) becomes

$$\dot{\varphi} = -(1-\varphi)\dot{\varepsilon} \tag{6.10}$$

Allowing now for dilatation and/or compaction to occur both within a boundary shear band and within the remainder of a bulk gouge layer, the dynamic porosity within the shear band (φ^{sb}), the bulk gouge layer (φ^{bulk}) can be expressed as

$$\dot{\varphi}^{sb} = -(1-\varphi^{sb})\dot{\varepsilon}_t^{sb} \tag{6.11a}$$

$$\dot{\varphi}^{bulk} = -(1-\varphi^{bulk})\dot{\varepsilon}_t^{bulk} \tag{6.11b}$$

6.3.3.3 Relationship between Gouge Shearing Rate and Load Point Velocity

To relate the instantaneous shear strain rate of the entire gouge layer ($\dot{\gamma}_t$) to the shear velocity imposed upon the loading system (V_{imp}), it is critical to note that V_{imp} is accommodated by (dynamic) elastic deformation of the loading system and by deformation of the sample. This relation can be expressed as

$$V_{imp} = V_{el} + \dot{\gamma}_t L_t \tag{6.12}$$

where V_{el} is the velocity due to elastic machine distortion caused by change in shear stress, given as

$$V_{el} = \dot{\tau}/K \tag{6.13}$$

Here K is the stiffness of the loading system and $\dot{\tau}$ is the time derivative of shear stress. In this equation, we neglect the elastic deformation of the gouge as well as the inertial term.

Combing equations (6.7a), (6.8c), (6.11a), (6.12) and (6.13), now yields the equation linking the imposed load point velocity, machine distortion rate and sample deformation rate, as follows

$$V_{imp} - \dot{\tau}/K = L_t[\lambda\dot{\gamma}_{ps}^{sb} + (1-\lambda)\dot{\gamma}_{ps}^{bulk}] + L_t\lambda[\dot{\varepsilon}_{ps}^{sb} + \dot{\varphi}^{sb}/(1-\varphi^{sb})]/\tan\psi \tag{6.14}$$

6.3.4 Energy/Entropy Balance and Dynamic Gouge Strength

6.3.4.1 Stresses Transmitted Across Grain Contacts

To formulate relations for the frictional resistance to sliding and the deformation rate accommodated by intergranular pressure solution at grain contacts, in either a boundary shear or bulk gouge layer, we need to quantify the stresses supported at grain-to-grain

contacts. This can be easily done with reference to the unit cell that describes (average) grain packing shown in Figure 6.4. For given externally applied effective normal and shear stresses (σ_n and τ), the horizontal and vertical forces on the unit cell are $F_h = \tau dd$ and $F_v = \sigma_n dd$, respectively. The force balance across grain contacts then requires that the intensified effective normal and shear stresses acting on the contacts ($\tilde{\sigma}_n$, $\tilde{\tau}$) are given by the relations

$$\tilde{\sigma}_n = (\sigma_n d^2 \cos\psi + \tau d^2 \sin\psi)/a_c \tag{6.15a}$$

$$\tilde{\tau} = (\tau d^2 \cos\psi - \sigma_n d^2 \sin\psi)/a_c \tag{6.15b}$$

During rapid shear deformation involving granular flow, frictional slip will occur on these inclined contacts. The stresses acting on individual contacts must then satisfy a grain boundary slip criterion, which we assume to be of Coulomb type given $\tilde{\tau} = \tilde{\mu}\tilde{\sigma}_n + \tilde{c}$, where $\tilde{\mu}$ is the intrinsic friction coefficient for contact sliding and $\tilde{c}$ is the cohesive strength of contacts. Assuming zero cohesion, combing the above equations, yields,

$$\tau = \frac{\tilde{\mu} + \tan\psi}{1 - \tilde{\mu}\tan\psi}\sigma_n \tag{6.16}$$

which is the same as the steady-state sliding-strength model given by *Niemeijer and Spiers* (2007), except for the cohesion term. This relation implies that during steady-state sliding, shear resistance depends only on state of the gouge material, as measured in terms of ψ and thus φ (via equation 6.3). Note that we assume zero cohesion here for simplicity and because $\tilde{c}$ is generally expected to be small (c.f. *Niemeijer and Spiers*, 2007). We also assume that the intrinsic friction coefficient for contact sliding is independent of grain contact sliding rate, though this can easily be modified in future.

6.3.4.2 Energy/Entropy Balance

The above equation derived from force balance considerations only holds under quasistatic conditions, i.e. at steady state. In the following, we consider more general situations using an energy/entropy balance approach. Following *Lehner* (1990) (see also *Lehner and Bataille* (1984)), the combined energy/entropy balance for unit volume of deforming fault gouge can be written as

$$\tau\dot{\gamma}_t + \sigma_n\dot{\varepsilon}_t = \dot{f} + \dot{\Delta} \tag{6.17a}$$

where $\dot{f}$ is the rate of change in Helmholtz free energy of the solid phase per unit volume of the gouge, and $\dot{\Delta}$ is the total dissipation per unit volume by the irreversible microscale processes operating. As a first approx, it is reasonable to suppose now that $\dot{f} \approx 0$, since

frictional stress changes typically associated with changes in slip velocity will generally cause negligible changes in the thermodynamic state (elastic or defect-stored energy) of the solid, though we note that grain size reduction (surface area increase) through cataclasis may cause changes in *f* that cannot be neglected. If the gouge deforms by frictional granular flow plus pressure solution, and assuming negligible dissipation due to viscous flow of the pore fluid phase compared to deformation of the gouge framework, the above equation can be rewritten as

$$\tau\dot{\gamma}_t + \sigma_n\dot{\varepsilon}_t = \dot{D}_{gr} + \dot{D}_{ps}^{comp} + \dot{D}_{ps}^{shear} \tag{6.17b}$$

where $\dot{D}_{gr}$ is the dissipation or energy release rate due to frictional sliding on grain contacts, and $\dot{D}_{ps}^{comp}$ and $\dot{D}_{ps}^{shear}$ represent dissipation due to deformation by IPS normal and parallel to the shear plane, respectively. Following *Niemeijer and Spiers* (2007), the dissipation due to contact friction can be written as $\dot{D}_{gr} = \dot{\Delta}_c N_c$, where $\dot{\Delta}_c = \tilde{\tau} a_c \tilde{v}_c$ is the dissipation rate per sliding contact, N_c is the number of contacts per unit volume of the deforming fault gouge, and $\tilde{v}_c$ is the average slip rate on the contacts. From the unit cell geometry (Figure 6.4), it is further apparent that $\tilde{v}_c = d\dot{\gamma}_{gr}$, and $N_c = 1/(d^3\cos\psi)$. Hence, the dissipation by granular flow is given as

$$\dot{D}_{gr} = \frac{\tilde{\tau} a_c \dot{\gamma}_{gr}}{d^2\cos\psi} \tag{6.18a}$$

Using the cohesion-free slip criterion for each contact ($\tilde{\tau} = \tilde{\mu}\tilde{\sigma}_n$) and force balance relation (6.15b), we now get

$$\dot{D}_{gr} = \tilde{\mu}\sigma_n\dot{\gamma}_{gr} + \tilde{\mu}\tau\tan\psi\dot{\gamma}_{gr} \tag{6.18b}$$

Assuming that all mechanical work done in causing deformation by pressure solution is fully dissipated through the microscale processes of mass dissolution, grain boundary diffusion and precipitation, and that the gouge deforms as an isotropic material, substituting (6.18b) into (6.17b) now, yields

$$\tau\dot{\gamma}_t + \sigma_n\dot{\varepsilon}_t = \tilde{\mu}\sigma_n\dot{\gamma}_{gr} + \tilde{\mu}\tau\tan\psi\dot{\gamma}_{gr} + \sigma_n\dot{\varepsilon}_{ps} + \tau\dot{\gamma}_{ps} \tag{6.19}$$

Using the kinematic relation that $\dot{\gamma}_t = \dot{\gamma}_{ps} + \dot{\gamma}_{gr}$, this equation can be rewritten as

$$\tau = \frac{\tilde{\mu} + \tan\psi}{1 - \tilde{\mu}\tan\psi}\sigma_n - \frac{1}{(1 - \tilde{\mu}\tan\psi)}\frac{\dot{\varepsilon}_t}{\dot{\gamma}_{gr}}\sigma_n \tag{6.20}$$

This is the energy balance equation, which holds at all times for granular fault gouge. Using the relation $\dot{\varepsilon}_{gr} = -(\tan\psi)\dot{\gamma}_{gr}$, along with equations (6.5a) and (6.10), the above equation finally modifies to

$$\tau = \frac{\tilde{\mu} + \tan\psi}{1 - \tilde{\mu}\tan\psi}\sigma_n + \frac{\tan\psi}{(1 - \tilde{\mu}\tan\psi)[1 + \dot{\varepsilon}_{ps}(1-\varphi)/\dot{\varphi}]}\sigma_n \tag{6.21}$$

At steady state ($\dot{\varepsilon}_t = 0$ or $\dot{\varphi} = 0$), the second term on the right hand side of (6.20) and (6.21) reduces to zero, and the whole expression returns to the same result as obtained from the static or steady state force balance (6.16). For a transient jump in velocity, let us say an up-step such as that imposed in a typical velocity stepping frictional test, equations (6.10) and (6.11) imply that the shearing material will dilate ($\dot{\varepsilon}_t < 0$ or $\dot{\varphi} > 0$) instantaneously and continuously but at decreasing dilation rate. Equation (6.21) then demonstrates that the shear stress supported will concomitantly rise abruptly, subsequently decreasing until a new steady state is reached ($\dot{\varepsilon}_t = 0$ or $\dot{\varphi} = 0$). By contrast, for an SHS test, when sliding is stopped, the gouge will compact immediately ($\dot{\varepsilon}_t > 0$ or $\dot{\varphi} < 0$) and will be accompanied by relaxation in shear stress due to the operation of pressure solution at grain contacts. As sliding resumes, the gouge will dilate, causing an instantaneous increase in strength followed by slip weakening until a new steady state is achieved.

6.3.5 Rate of Normal and Shear deformation by IPS

Numerous authors (e.g. *Rutter*, 1976; 1983; *Rai, 1982*; *Lehner*, 1990; *Shimizu*, 1995; *Spiers et al.*, 2004; *Pluymakers and Spiers,* 2014) have published theoretically derived rate equations for both deviatoric and compaction creep. Here, we assume that the gouge behaves like an isotropic material with respect to IPS, so that the effects of σ_n and τ on compaction and shear deformation by IPS can be treated separately (c.f. *Raj*, 1982). Against this background, compaction of the gouge normal to the shear plane can be modeled using a standard 1-D or uniaxial creep law for a regular pack of spherical grains (e.g. *De Meer and Spiers*, 1997; *Spiers* et al., 2004). Assuming grain boundary diffusion controlled IPS, as reported in compaction experiments on calcite by *Zhang et al.* (2010), the normal compaction strain rate under the effective normal stress σ_n, can hence be expressed as

$$\dot{\varepsilon}_{ps} = A_d \frac{DCS}{d^3}\frac{\sigma_n \Omega}{RT} f_d(\varphi) \tag{6.22}$$

Here A_d is a geometric constant, D is the diffusivity of the dissolved solid within the grain boundary fluid (m^2/s), C is the solubility of the solid in the fluid (m^3/m^3), S is the mean

thickness of the grain boundary fluid phase (m), Ω is the molar volume of the solid phase (m^3/mol), R is the universal gas constant (8.31 J.mol^{-1}K^{-1}), and T is the absolute temperature (K). The term $f_d(\varphi)$ is a dimensionless function of porosity that accounts for changes in grain contact area (hence contact stress magnitude) and transport path length, as porosity evolves. Following *Spiers et al.*, (2004) (see also *Pluymakers and Spiers*, 2014), for porosities in the range of 5–40 %, the geometry of a regular grain pack allows the approximation

$$f_d(\varphi) \approx 1/(q-2\varphi)^2 \tag{6.23}$$

Similarly, the shear strain rate accommodated by pressure solution can be expressed as

$$\dot{\gamma}_{ps} = B_d \frac{DCS}{d^3}\frac{\tau\Omega}{RT} f_d(\varphi) \tag{6.24}$$

where B_d is the geometric constant appropriate for shear deformation (c.f. *Rutter*, 1976; *Raj*, 1982; *Shimizu*, 1995). Note that these IPS equations can be applied to both the shear band and bulk portions of the gouge layer considered in our model.

6.3.6 Final Assembly of Controlling Equations

Coupling the full set of kinematic and energy/entropy equations given above (6.14 and 6.21) allows us to describe the frictional behavior of any granular fault gouge layer, either with a localized shear band (of relative thickness λ) or without a shear band (λ = 0). Here we rewrite the key results for a gouge with a localized shear band as follows,

$$V_{imp} - \dot{\tau}/K = L_t[\lambda\dot{\gamma}_{ps}^{sb} + (1-\lambda)\dot{\gamma}_{ps}^{bulk}] + L_t\lambda[\dot{\varepsilon}_{ps}^{sb} + \dot{\varphi}^{sb}/(1-\varphi^{sb})]/\tan\psi \tag{6.25a}$$

$$\tau = \frac{\tilde{\mu}+\tan\psi}{1-\tilde{\mu}\tan\psi}\sigma_n + \frac{\tan\psi}{(1-\tilde{\mu}\tan\psi)[1+\dot{\varepsilon}_{ps}^{sb}(1-\varphi^{sb})/\dot{\varphi}^{sb}]}\sigma_n \tag{6.25b}$$

These two equations (6.25a and 6.25b), combined with the compaction and shear creep laws for pressure solution (6.22 and 6.24), describe the frictional behavior of the carbonate fault gouge as represented in Figure 6.2. For the special case that shear deformation is uniformly distributed (no shear band), then putting λ =1 leads to

$$V_{imp} - \dot{\tau}/K = L_t\dot{\gamma}_{ps} + L_t[\dot{\varepsilon}_{ps} + \dot{\varphi}/(1-\varphi)]/\tan\psi \tag{6.26a}$$

$$\tau = \frac{\tilde{\mu}+\tan\psi}{1-\tilde{\mu}\tan\psi}\sigma_n + \frac{\tan\psi}{(1-\tilde{\mu}\tan\psi)[1+\dot{\varepsilon}_{ps}(1-\varphi)/\dot{\varphi}]}\sigma_n \tag{6.26b}$$

6.4 Model Implementation

6.4.1 Solution Method

In order to compute the frictional behavior implied by our model, the governing equations above must be solved numerically. We used the solvers embedded in the finite element package COMSOL to do this. For easy programming, we rewrite (6.25) in the form of two coupled partial differential equations, specifying the rates of change of shear stress (τ) and porosity (φ) (i.e. defining strength and state changes) as follows,

$$\dot{\tau} / K = V_{imp} - L_t[\lambda\dot{\gamma}_{ps}^{sb} + (1-\lambda)\dot{\gamma}_{ps}^{bulk}] - L_t\lambda\dot{\varepsilon}_{ps}^{sb}\frac{\sigma_n}{\sigma_n(\tilde{\mu} + 2\tan\psi) - \tau(1-\tilde{\mu}\tan\psi)} \tag{6.27a}$$

$$\dot{\varphi}^{sb} = \frac{\tau(1-\tilde{\mu}\tan\psi) - \sigma_n(\tilde{\mu} + \tan\psi)}{\sigma_n(\tilde{\mu} + 2\tan\psi) - \tau(1-\tilde{\mu}\tan\psi)}\dot{\varepsilon}_{ps}^{sb}(1-\varphi^{sb}) \tag{6.27b}$$

Shear Stress (τ) and porosity (φ) evolution were computed by numerical integrating with respect to time. In each time step employed, all variables were iterated sequentially until an accurate solution was found (within a relative tolerance of $1{:}10^6$). To simulate our lab experiments, which consisted of sequential velocity stepping and SHS testing phases (Figure 6.1), we entered load point velocity at fixed temperature (T = 80°C) and effective normal stress (σ_n = 50 MPa) as input to our model, obtaining shear strength and porosity as a function of time (or displacement) as output.

6.4.2 Input Parameters

The input parameters used in obtaining reference case solutions to our model are listed in Table 6.1 and described below. Based on the microstructure observed in our experiments (Figure 6.2, see also *Chen et al., submitted*, Chapter 4), we use λ = 0.0625 and L_t = 0.8 mm, implying a 50-μm-thick shear band. The average grain sizes in the bulk gouge and shear band are taken as 20 μm and 2 μm, respectively. The initial porosity of the bulk gouge is set to be 32%, as estimated from the mass and grain density of the experimental gouge (2.4 g with density of 2700 kg/m^3). For the shear band, we allow the model to find a steady-state porosity for a given imposed velocity, and then use this porosity as the initial porosity for subsequent transient modeling. The parameter q reflects the critical state porosity φ_c for pure granular flow, and plays its role via the term ($q - 2\varphi$). Here, we take q to be 0.8 for the bulk gouge, following the values used by *Niemeijer and Spiers* (2007) and *Pluymakers and Spiers* (2014) for similar grain size material. To account for the effect of the wider range in (log) grain size observed in the shear bands, which generally reduces q and hence dilatancy angle at given porosity (e.g. *Al Hattamleh et al.*, 2013), we use q = 0.4 for the shear band. Regarding the stiffness (K) of the testing machine used in our experiments, this was calibrated at systematically varied confining pressures and temperatures. For the

experimental conditions modeled here (65 MPa and 80°C), the appropriate value of K is 5.993×10^{10} Pa/m. The intrinsic grain contact friction coefficient for carbonate fault gouge is set at a constant value of 0.60, consistent with the overall level of frictional strength typically exhibited by calcite gouges (*Verberne et al.*, 2013b). In reality, this parameter presumably reflects normal-stress-dependent, and possibly velocity-dependent, nanoscale asperity or surface force interactions occurring in grain boundaries. We treat it as constant as little is yet known about such interactions.

Table 6.1. List of Parameters and Reference Case Values used in the Present Model [a]

Para.	Description (unit)	Value (range)	Data source and additional information [b]
σ_n	effective normal stress (Pa)	5×10^7	experimentally applied value
T	Temperature (K)	353	experimental temperature
K	machine stiffness (Pa/m)	5.993×10^{10} [c]	calibrated machine value
V_{imp}	load point velocity (m/s)	$0.1–10\times10^{-6}$	experimentally applied values
L_t	thickness of the gouge layer (m)	8×10^{-4}	value from experiments
λ	localization degree	0.0625 (0.0125–0.188)	value observed in experiments
φ_0^{bulk}	initial porosity of bulk gouge	0.32	experimentally observed value
d^{sb}	average grain size of shear band (m)	2×10^{-6} (1×10^{-7}–5×10^{-6})	middle range of observed values
d^{bulk}	average grain size of the bulk gouge (m)	2×10^{-5}	mean value of the observed range
q^{sb}	2× critical porosity for shear band	0.4	assumed here
q^{bulk}	2× critical porosity for bulk gouge	0.8	assumed here
z	grain coordination number	6	*Spiers et al.* (2004)
H	geometrical parameter	0.577(0.36–1.73)	assumed following *Niemeijer and Spiers*
A_d	geometric constant for compaction by IPS	30.6	value for uniaxial compaction (*Pluymaker and Spiers*, 2014)
B_d	geometric constant for shear by IPS	30.6	as above
DS	Product of diffusion coefficient D times mean grain boundary fluid thickness S (m^3/s)	2×10^{-20} (10^{-19}–10^{-20})	*Nakashima* (1995); *Renard et al.* (1997); *Zhang et al.* (2010); *Koelemeijer et al.* (2012)
C	solubility of the solute in fluid film (m^3/m^3)	3.95×10^{-6} [c]	*Plummer and Busenberg* (1982)
Ω	molar volume of solid phase (m^3/mol)	3.69×10^{-5}	*Plummer and Busenberg* (1982)
$\tilde{\mu}$	intrinsic grain contact friction coefficient	0.6	assumed here

[a] *Other symbols used are explained in the text;*

[b] *All experimentally derived values were obtained from Chen et al., submitted, except where stated.*

[c] *These parameters are temperature dependent, and here we use the values at 80 °C.*

Some parameters are poorly constrained in our model. The geometric parameter H falls in the range of $1/\sqrt{3}$ to $\sqrt{3}$ as specified earlier for a 2-D grain pack (*Niemeijer and Spiers*, 2007), but can be as low as 0.36 in a 3-D model. For our reference case calculations, we used $H = 1/\sqrt{3}$ (Table 6.1). The geometric constants A_d and B_d are taken to be equal, with values varying from 30.6 for uniaxial compaction to 183 for isotropic 3-D compaction (*Pluymakers and Spiers*, 2014). Lastly, compaction and shear strain rates due to diffusion-controlled IPS are determined by the magnitude of *DCS* (see equations 6.22 and 6.24). From the empirical equation given by *Plummer and Busenberg* (1982), the solubility of calcite at the conditions modeled is 3.95×10^{-6} m^3/m^3. Note that unlike most other minerals, the solubility of calcite (C) decreases with increasing temperature. The product DS was estimated directly from pressure solution experiments on calcite (*Zhang et al.*, 2010; see also halite - *Koelemeijer et al.*, 2012), but can also be evaluated from independent estimates of D (*Nakashima*, 1995) and S (*Renard et al.*, 1997), giving values in the range 10^{-19} – 10^{-20} m^3/s (Table 6.1).

6.5 Modeling Results and Comparison with Experiments

6.5.1 Steady-state Shearing and Parametric Sensitivity Analysis

We start with modeling steady state shearing behavior of the shear band, in which the time derivatives of shear stress ($\dot{\tau}$) and porosity ($\dot{\varphi}^{sb}$) are zero. Equations 6.27a and 6.27b accordingly become

$$V_{imp} = L_t \lambda \dot{\varepsilon}_{ps}^{sb} / \tan\psi_{ss} \tag{6.28a}$$

$$\tau = \frac{\tilde{\mu} + \tan\psi_{ss}}{1 - \tilde{\mu}\tan\psi_{ss}} \sigma_n \tag{6.28b}$$

These imply that, at steady state, the sliding velocity and the IPS-induced compaction rate in the shear band ($\dot{\varepsilon}_{ps}^{sb}$) decide the state of the internal gouge material, measured in terms of ψ or φ, and hence the shear resistance (τ) offered by the band. Using the reference case parameter values given in Table 6.1, we calculated the steady-state friction coefficient ($\mu_{ss} = \tau_{ss}/\sigma_n$) as a function of load point velocity (V_{imp}). As shown in Figure 6.5, μ_{ss} decreases with increasing velocity, indicating velocity weakening behavior. The corresponding values of $(a - b) = \Delta\mu_{ss}/\Delta\ln(V)$ increase with increasing velocity, and lie between –0.015 and –0.002, for velocity steps imposed in the range of velocities investigated in our lab experiments (0.1

– 10 μm/s). All these features are consistent with the trends seen in our experimental data for carbonate gouge sheared in VS mode at 80 – 140 °C and σ_n = 50 MPa (*Verberne et al.*, 2013b; *Chen et al.*, *submitted*), and are in order-of-magnitude agreement quantitatively (refer Figure 6.5). Given the straight-forward basis for choosing the values of the parameters used, we consider this to be acceptable agreement.

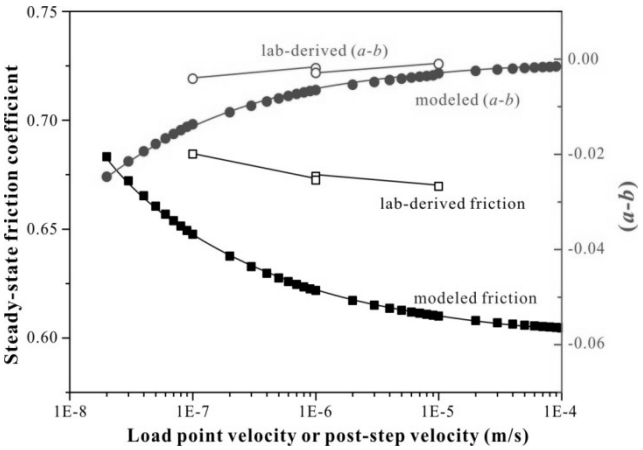

Figure 6.5. Modeling results for steady-state friction coefficient and (a – b) as a function of load point velocity, obtained using the reference state parameter values given in Table 6.1. The lab-derived data reported by Chen et al., submitted for wet carbonate gouge sheared at the same T-σ_n conditions (T = 80 °C and σ_n = 50 MPa) are added for comparison.

To gain insight into the properties of the model, we performed a parametric analysis to investigate the sensitivity of the computed behavior to the parameters used (i.e. to H, λ, d^{sb}, DS, $\tilde{\mu}$ and q^{sb}), varying these parameters in realistic ranges. As shown in Figure 6.6a, the modeling results exhibit a weak dependence on the geometric constant (q^{sb}), but a strong dependence on grain size (d^{sb}), the geometric factor (H), the grain contact friction coefficient ($\tilde{\mu}$), the extent of slip localization (λ), and the grain boundary diffusivity product (DS). In particular, variations in $\tilde{\mu}$ vertically translate the model predictions of steady-state strength (Figure 6.6a). The model also predicts significantly lower steady-state strength for larger grain size and more localized slip, with these effects becoming more pronounced at lower velocities. By adjusting $\tilde{\mu}$ and other parameter(s) such as d^{sb} within small, reasonable ranges, the modeled frictional strength can be fit quantitatively to the experimental results (Figure 6.6b). Good agreement between modeled and measured frictional strength and ($a - b$) values can be obtained, for example, by choosing an intrinsic grain contact friction

coefficient $\tilde{\mu}$ of 0.65 – 0.67 (specifically 0.664) and a shear band grain size d^{sb} of 4 μm – see Figure 6.6b. Purely varying H or λ cannot predict the observed frictional strength. However, doing so in combination with small variations in DS and/or d^{sb} yields close agreement between the model- and lab-derived μ_{ss} and ($a - b$) values, within the sliding velocity investigated (0.1 – 10 μm/s) (Figure 6.6b). We note, however, that manipulating these (or the many other) parameters to produce a good fit has little value other than to demonstrate that the model offers a viable (but not necessarily unique) explanation for the steady state frictional behavior observed in our experiments.

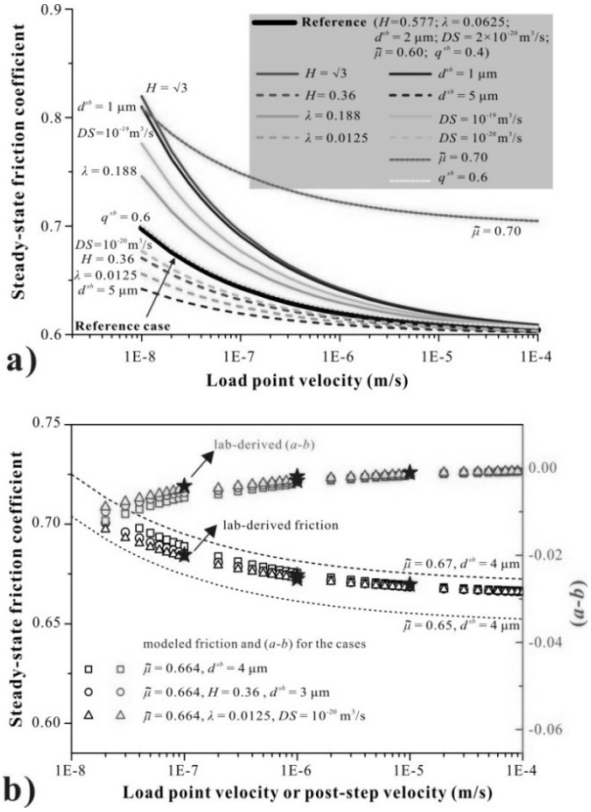

Figure 6.6. a) Sensitivity of computed steady-state friction coefficient to variation in parameter values (H, λ, d^{sb}, $\tilde{\mu}$ and q). Note that the reference case (solid black line) employs the parameter values H = 1, λ = 0.0625, d^{sb} = 2 μm, DS = 2×10^{-20} m^3/s; $\tilde{\mu}$ = 0.6 and q^{sb} = 0.4. All parameter values used are listed in Table 6.1. b) Good fit of the model to the lab data, for both μ_{ss} and (a – b), obtained using parameter values adjusted in reasonable ranges from the reference case, as described in the main text. The experimental data for gouge sheared at the reference T-σ_n conditions (Chen et al., submitted) are included for comparison.

6.5.2 Transient Response to Velocity Stepping

For comparison with our lab-experiments (VS-seq1, Figure 6.1), we modeled a velocity stepping sequence employing individual velocity steps of 1→10→1→0.1→1μm/s, taking T = 80 °C and σ_n = 50 MPa (Figure 6.7a), and using the reference case parameter values employed in the steady state calculations presented in Figure 6.5. The results show a transient frictional strength response that is closely similar to the experimental observations for VS-seq1 (see Figures 6.1a and 6.7b) and consistent with the type of response obtained using a classical RSF law. For each velocity step, the frictional strength exhibits first a "direct" effect and then evolves to a new steady state, consistent with velocity weakening behavior (Figure 6.7b). The characteristic displacement associated with the modeled evolution effect is around 0.15 mm compared with ~ 0.18 mm in our experiments. For down-steps in sliding velocity from 1 to 0.1 μm/s, small fluctuations occur before attaining the new steady state. All of these features are seen in our lab experiments (Figure 6.1a, Figure 6.7b). Moreover, alongside the transient changes in shear strength towards lower and higher values, our model results show that the active shear band dilates or compacts respectively, causing small increases and decreases in porosity of the shear band (Figure 6.7c). To compare with the macroscopic volumetric changes measured in our experiments, we calculate the total compaction of the sample, with the rate being expressed as $\dot{\varepsilon}_t = \lambda\dot{\varepsilon}_t^{sb} + (1-\lambda)\dot{\varepsilon}_t^{bulk}$. Integration of this expression gives the net cumulative compaction for the whole sample as a function of time or displacement. As shown in Figure 6.7d, the predicted gouge compaction exhibits stepped variations between adjacent V-steps, with trends similar to that observed for the whole gouge layer in our experiments, though the magnitude is much smaller. The discrepancy can be attributed either to the underestimate of shear band thickness in our reference modeling case (50 μm and can be as wide as 150 μm, Table 6.1), or to the dilatant response of the bulk gouge which is inhibited in the present model.

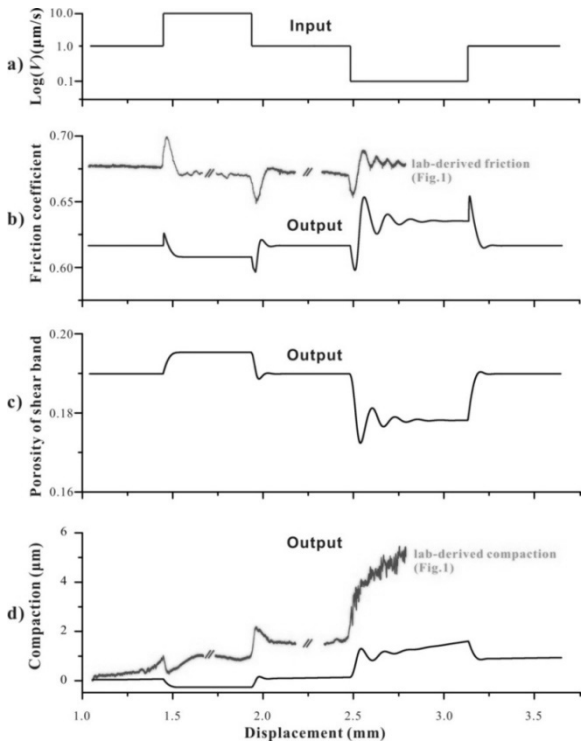

Figure 6.7. Modeling results for velocity stepping sequences, replicating the conditions of our VS experiments (VS-seq1) performed on wet carbonate gouge at T = 80 °C and σ_n = 50 MPa (see Chen et al, submitted). a) Velocity step sequence entered as input to the model, b) frictional response, c) shear band porosity, and d) total compaction of the gouge layer. Typical experimental data are added to (b) and (d) for comparison (VS-seq1, Figure 6.1). Note that for sake of comparison, the curves of experimental data vs displacement are laid out with breaks, since the displacements of individual V-steps imposed in our experiments are smaller than those of the modeled steps.

6.5.3 Response to Slide-hold-slide Testing

Again replicating the procedure and conditions employed in our lab-experiments (Figure 6.1a, 6.b), we modeled a SHS test sequence consisting of eight individual SHS events with hold times increasing from 3 to 2700 s in three-fold jumps (Figure 6.8a), again using the reference case parameter values given in Table 6.1. Plots showing the evolution of frictional strength, shear band porosity and total compaction predicted by our model are shown in Figure 6.8b-6.8d. The following main features of the computed friction-displacement curve are consistent with classic SHS test results (e.g. *Marone*, 1998a) and with our lab data (Figure 6.1b). First, our model predicts stress relaxation during hold periods, followed by an instantaneous increase in shear resistance on reloading and by a

subsequent gradual decay to steady state. Second, the magnitudes of each stress relaxation event and of each subsequent transient peak healing ($\Delta\mu_{pk}$) event increase with hold time. Our model predicts that the shear band will compact during individual hold periods and dilate upon reshear, especially after long hold periods (Figure 6.8c). The predicted cumulative sample compaction (bulk plus shear band) during the hold time is qualitatively consistent with our lab data (Figure 6.8d).

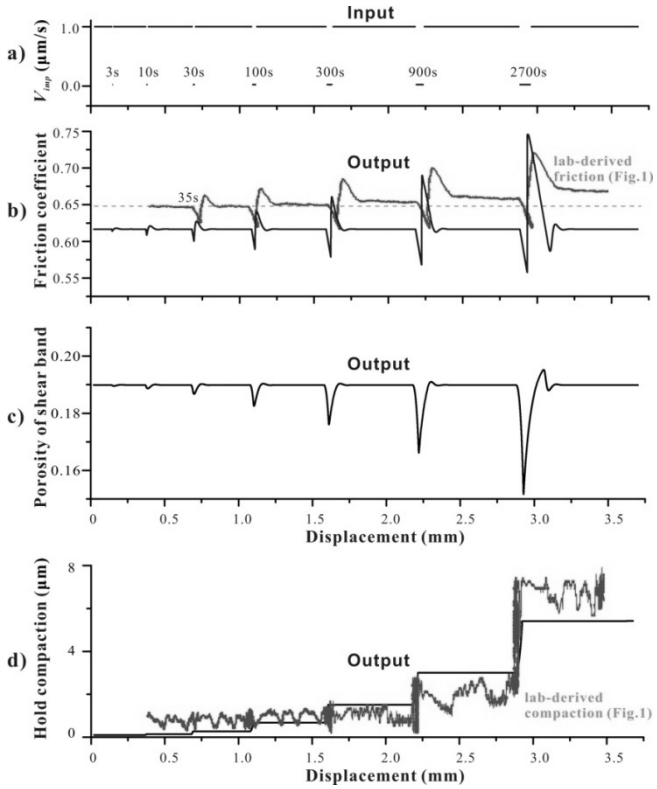

Figure 6.8. Modeling results for a slide-hold-slide testing sequence as executed in our experiments on carbonate gouge at T = 80 °C and σ_n = 50 MPa (see Chen et al, submitted). a) Input sliding velocities and hold times. b) Friction coefficient vs. displacement. c) Shear band porosity vs. displacement. d) Cumulative hold-time compaction of the whole-sample. Experimental results from Figure 6.1 are added to b) and d) for comparison.

Despite this broad agreement between our model and experimental results on SHS response, a clear difference is also visible, namely in relation to the stepwise increase in steady-state friction coefficient that occurs after each reshearing event in our experiments. In our modeling results, no such increase in steady-state friction occurs. Rather, the steady-state

frictional strength before and after each SHS event remains the same (Figure 6.8b), while the shear band porosity returns to the original steady-state level upon reshearing (Figure 6.8c). As shown in Figure 6.8d, our model predicts that progressive compaction of the whole sample during hold periods causes a reduction in total porosity. However, in the present model this is not expected to affect shear strength, as that is determined by the shear band. It follows, then, from our parametric analysis (Figure 6.5) that the increase in steady-state friction seen in our SHS sequence can likely be attributed to stepwise changes in shear band grain size (d^{sb}), shear localization degree (λ), or the sensitivity of shear band dilatation to porosity (H) occurring during relaxation or upon reshearing during SHS testing.

On the basis of microstructural examination of our experimental samples, we can immediately eliminate changes in the degree of shear localization at the sample boundary from the above list of possibilities. This is because our model shows that a broadening of 10 times would be needed to account for the observed increases in steady-state friction coefficient per SHS event. No such broadening is seen in experimentally deformed samples subjected to SHS testing compared to velocity stepping only (*Chen et al., submitted*, Chapter 4). We likewise eliminate purely packing-related changes in the parameter H as causing the observed increase in steady-state strength, because the compaction strains (porosity reduction) occurring in the shear band, as predicted by our model for stress relaxation during hold periods, are far too small to significantly change the granular packing microstructure (Figure 6.8c).

Let us therefore consider the possibility of reduction in the mean, shear band grain size (d^{sb}) in more detail. Feasible mechanisms for this include cataclasis occurring within the boundary shear band during reshearing, or perhaps mass removal from the shear band by diffusion as the shear band compacts by IPS during relaxation. Such effects could conceivably also lead to a permanent increase in H in active shear bands. To crudely incorporate grain size reduction within the shear band into our model, we make the assumption that the extent of grain size reduction ($\Delta d/d$) by either cataclasis (due to restrengthening) or mass removal (by diffusion during relaxation) will be directly related to the extent of IPS compaction occurring during relaxation. To capture such a relation in the simplest possible way, we assume that $\Delta d/d = c\Delta\varepsilon^{sb}$, where ε^{sb} is the compaction strain prediction predicted to occur in the shear band by our model in each hold period and where c is a constant of order 1. Including this in our model calculation (measuring $\Delta\varepsilon^{sb}$ with respect to shear band thickness before SHS testing), produces the results shown in Figure 6.9. These agree more favorably with our experimental data supporting grain size reduction as a possible explanation of the increase in μ_{ss} seen our SHS tests (Figure 6.9b).

Making use of the modeling results plotted in Figure 6.9, i.e. incorporating the grain size reduction effect on reshearing, we now examine the predicted shear stress relaxation results for different SHS events (Figure 6.10a). These show that the average modeled relaxation and hence creep rate is much higher in the early, shorter hold periods than that in the later, longer holds. This reflects a systematic decrease in evolution effect with increasing hold time and relaxation strain. In our model, this is caused by the decrease in porosity that occurs due to compaction of the static shear band by IPS during each hold (refer equations 6.22 and 6.24). Similar results have been observed in our experiments (Figure 6.10b) and in other studies where pressure solution was thought to be active (e.g. *Niemeijer et al.*, 2008).

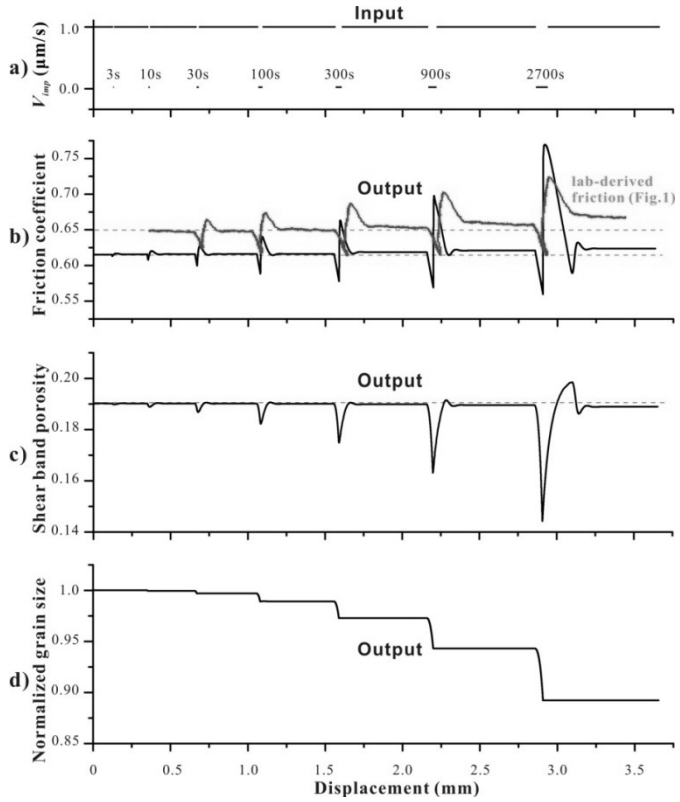

Figure 6.9 Modeling results for slide-hold-slide testing allowing for grain size reduction Δd/d during each hold-reshearing event, occurring in proportion to the compactional strain (Δε) accumulated in the shear band during the hold period (i.e. such that Δd/d = cΔε where c ≈ 1). a) Input sliding velocity and hold times. b) Calculated friction coefficient vs. displacement. c) Calculated shear band porosity vs. displacement; d) Calculated normalized grain size (Δd/d) vs. displacement. Lab-derived friction coefficients are added to b) for comparison (see Figure 6.1 and Chen et al., submitted).

Finally, we derive the frictional healing parameters (Figure 6.1c) from our modeling predictions of Figure 6.9, for SHS behavior with grain size reduction upon reshearing. The results (Figure 6.11) indicate a non-linear increase in transient restrengthening or peak healing ($\Delta\mu_{pk}$) with logarithm of hold time. Similar "non-Dieterich type" frictional healing behavior (i.e. not fitting equation 6.2) occurred in our experiments (Figure 6.1) and has also been observed in SHS experiments on both quartz and halite, where it was attributed to contact area growth through pressure solution (*Nakatani and Schloz*, 2004; *Yasuhara et al.*, 2005; *Niemeijer et al.*, 2008). In our model, the effect is due to shear band compaction by pressure solution during hold periods, resulting in an increase in dilation angle (refer equation 6.3). Our modeling results allowing for grain size reduction upon reshearing also show a non-linear increase in healing-induced residual strengthening ($\Delta\mu_r$) with $\log(t_h)$ (Figure 6.11). However, in our lab experiments, the $\Delta\mu_r$ showed this increase only after the early holds, and then leveled off after longer, later holds (Figure 6.1b, see also *Chen et al.*, *submitted*, Chapter 4). In our modeling to date, the maximum hold time investigated is 2700 s, so that the effect of long hold times has not yet been explored.

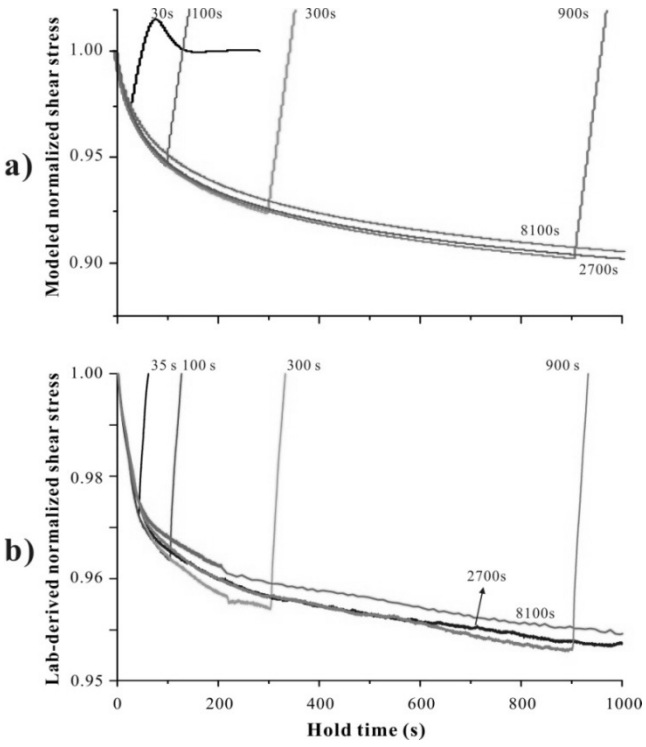

Figure 6.10. a) Calculated versus b) lab-derived curves showing the shear stress supported during stress relaxation as a function of hold time for individual holds periods, plus the abrupt increase in strength during subsequent reloading. All shear stresses are normalized with respect to the steady state stress supported immediately prior to initiating the corresponding hold.

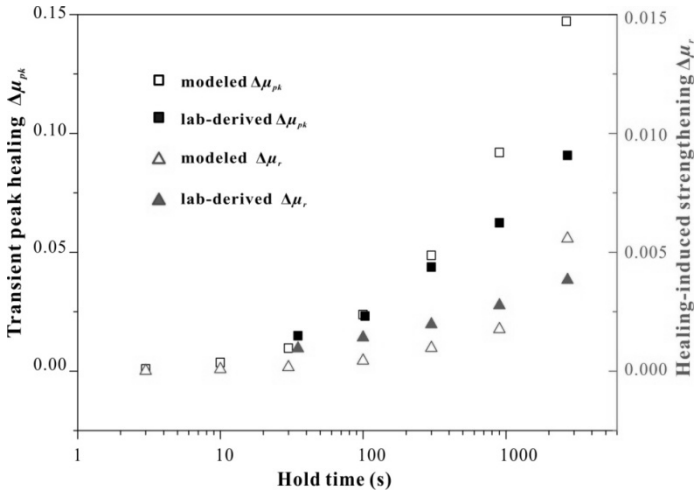

Figure 6.11. Frictional healing ($\Delta\mu_{pk}$ and $\Delta\mu_r$) calculated as a function of the logarithm of hold time, as derived from the modeled SHS results shown in Figure 6.9. Data derived from experimental result shown Figure 6.1 are added for comparison (also see Chen et al., submitted).

6.6 Discussion and Conclusions

Building upon the microphysical modelling work of *Niemeijer and Spiers* (2007) and *den Hartog et al.* (2014), who addressed steady-state friction, we have established a microphysical theory and numerical model describing both the transient and steady-state frictional behavior of a monomineralic, velocity weakening, granular fault gouge composed of a solid phase capable of undergoing IPS. We have compared the predictions of this model with lab experiments on wet carbonate gouge as reported by *Chen et al., submitted* (Chapter 4). As demonstrated by this comparison (Figures 6.5 to 6.11), our modeling results successfully capture all of the main features and trends by our lab experiments, by rock friction experiments in general, and by classical RSF models, including the "direct effect", "evolution effect", "stress relaxation" and "restrengthening".

In a broader sense, our theoretical analysis provides governing equations (6.25 or 6.27) that describe the frictional behavior of any granular fault gouge deforming by granular flow

plus a grain scale creep mechanism. A key condition required for the model to be applied is that a finite amount of porosity must exist in the gouge material, or can be created and modified by dilatation due to shearing. The present model predicts velocity weakening behavior, which originates from competition between shear-induced dilatancy and compaction by pressure solution. In the extreme case that porosity is near-zero, our model will translate into a velocity-strengthening flow law for grain-scale creep, though this has not been explicitly addressed in the present paper. Actually, at the slip rates (0.1 – 10 μm/s) and temperature (T = 80 °C) investigated in our experiments and model, the shear component of IPS at grain contacts in the localized shear band is negligible relative to the imposed sliding rates ($\dot{\gamma}_{ps}^{sb} << \dot{\gamma}_t$). According to our modeling results, at a slip rate of 0.1 μm/s, the shear component of IPS in the shear band contributes to only 2.5% the applied slip rate, while at a slip rate of 0.01 μm/s, this value increases to 5 %. Our model further predicts that, as the slip rate decreases to 3.2×10^{-10} m/s (10 mm/yr), the porosity of the shear band approaches zero and the deformation within the shear band will be fully controlled by contact creep (note that in this case, dilatant granular flow of the bulk gouge might be activated, depending the strength of the bulk gouge vs. the shear band). Similar transition from friction law to flow law with decreasing sliding rate has been previously observed in halite (*Shimamoto*, 1986), and the resultant change in friction rate dependence (i.e. from velocity-weakening to -strengthening) has also been more recently observed and predicted by *Niemeijer and Spiers* (2006) and by *den Hartog et al.* (2014). This reminds us that caution is needed when extrapolating lab-derived ($a-b$) values to natural seismogenic zones, where the fault slip rates are of the order of typical plate velocities of ~ 10^9 m/s or even less, and are thus 3–5 orders of magnitude lower than typically imposed in lab experiments.

Besides carbonate fault rocks, our model can be applied to a wide variety of materials sheared under a broad range of conditions. The extra information needed is to choose the most appropriate deformation mechanism and corresponding creep law to describe grain contact creep, especially if pressure solution is not dominant. Information on intrinsic grain contact frictional strength is also needed. We can then apply the model to predict the steady-state frictional strength and transient evolution thereof for any fault material in response to any imposed boundary conditions. Recognizing that other grain-scale deformation mechanisms can be incorporated in the model as an alternative creep process, we believe that our model embodies the key physics underlying the RSF-type behavior and the RSF law, though several issues still need to be clarified and refinements made, notably to describe the true nature of intrinsic grain contact friction, as well as velocity strengthening

slip. As mentioned above, when the dilation rate is slow, e.g. at low slip rates, or compaction is fast, e.g. at high temperatures, porosity will be eliminated and velocity-strengthening creep deformation will result. On the other hand, if a microphysical model for intrinsic grain contact friction $\tilde{\mu}$ is included, for example along the lines of the velocity-strengthening model proposed by *Rice et al.* (2001), velocity-strengthening behavior will also result at high velocities and/or low temperatures, where dilation produces critical state granular flow.

To our knowledge, our theory is the first to be able to model full RSF type behavior in terms of realistic, microstructurally-verifiable processes and state variables (such as porosity), without using the RSF law (note that *Sleep et al.* (2000) incorporated the strain de-/localization hence porosity changes into a classical RSF law, in a phenomenological sense, in order to describe the evolution of the state variable but with no mechanistic basis). It can accordingly provide a significantly improved basis for extrapolation of lab-derived friction data to natural conditions. However, many further improvements still need to be made. These include 1) analytical derivation of the RSF parameters a, b, $(a–b)$, D_c and β, as well the slip instability parameters such as critical stiffness K_c and reoccurrence wavelength L_c; 2) incorporation of other creep mechanisms for grain- and contact-scale creep besides pressure solution; 3) incorporation of the effects of increasingly important shear creep behavior at low or zero porosity, resulting in velocity strengthening at high temperature and/or low load point velocity; 4) incorporation of a more realistic friction law for contact slip (e.g. $\tilde{\mu}=f(\tilde{v}_c)$), which will cause velocity strengthening at low temperature or high load point velocity. Moreover, the present model only applies to grain-supported granular materials, and needs further modification to be applicable to matrix-supported materials. Some of these advances have already been initiated in steady-state models (*den Hartog and Spiers*, 2014), but they need extending to the transient case. In a future paper, we will derive analytical expressions for a, b, $(a–b)$, D_c and β in terms of evolving state variables from the present model, and we will apply our model to extrapolate our lab data on carbonate gouge to examine the implications for the seismic cycle on active faults in limestone terrains, including the middle-northern portion of the Longmenshan fault.

Acknowledgements

Jianye Chen was funded by the China NSF (41372202) and by Grant 2013-103 awarded by the Netherlands Research Centre for Integrated Solid Earth Science (ISES).

Chapter 7

General conclusions and suggestions for future research

This thesis has reported experimentally based study aimed at determining the compositional, transport and mechanical properties of carbonate fault rocks collected from surface exposures located on the northern, limestone-dominated segment of Longmenshan fault zone (LFZ), specifically at Beichuan and Pingwu in Sichuan Province, China. The work is relevant not only to understanding the seismic cycle of this portion of the LFZ, which hosted the largest surface rupture associated with the 2008 Wenchuan Earthquake, but to the seismic cycle of fault in limestone terrains in general. In this sense, the work can be regarded as a case study. On the basis of the results obtained, I reach the main conclusions outlined below. Questions which remain unanswered are then identified, with suggestions being made for future research.

7.1 Main findings

7.1.1 General structure, mineralogical and geochemical patterns within the LFZ

Fault zone structure: The exposures studied revealed a typical fault zone structure consisting of a carbonate fault breccia zone, a clay-rich fault core and a second fault breccia zone across the transects. The internal structure of the fault zone is relatively simple. For both exposures studied, the fault core is about 20−40 cm thick, consisting of a 2cm-thick gray gouge zone and a thin (< 7 mm) balck gouge zone in the center, and the surrounding highly-crushed fault breccias. Mineralogical analysis showed that there is an enrichment in smectite towards the fault core, with the gray gouges having the largest content. The balck gouges are depleted in smectite compared with the grey gouges.

Large volume loss: Mineralogical and geochemical profiles along with the Isocon diagrams, as well as isotopic results, consistently demonstrate that pervasive fluid infiltration occurred and altered the chemical architecture of the fault segments studied. Enrichment/depletion patterns, elements partitioning and the large volume loss (> 90 vol.%) characterizing the carbonate-rich fault zones investigated are quite different from those characterizing granitic and clastic sedimentary fault zones. This can be explained by a mass removal model, involving long term, interseismic dissolution and transport of carbonate components by fluid phases migrating through and/or along the fault zone, with mass transfer likely being enhanced by pressure solution creep.

Fluid origin: An increasing enrichment in smectite towards the gray gouge zone observed in the fault core of the exposures studied, plus a high abundance of fluid-related minerals and elements, as well as the depletion in heavy isotopes (^{13}C), consistently suggest activity of fluids of hydrothermal origin. Stable isotope compositions ($\delta^{13}C$ and $\delta^{18}O$) obtained from precipitated vein material and cements indicate continuous equilibration

between protolith-derived breccia fragments and the percolating fluids.

Coseismic illitization: The black, smectite-depleted gouge found in the fault core at the exposures studied, is inferred to be the material having accommodated most of the displacement during the Wenchuan Earthquake, i.e. to represent the principal slip zone. Illitization caused by frictional heating has occurred within it. I propose that coseismic frictional heating effects, along with the action of post-seismic hydrothermal fluids, controlled the formation, transformation and distribution of smectite and illite within the fault core of the LFZ. The dehydration of smectite, formed in interseismic periods, by subsequent coseismic frictional heating is expected to have been most extensive at depth, where effective normal stress are initially high. Preliminary numerical modeling, using rock properties data obtained on material sampled from the exposure studied, indicates that the excess pore pressures generated purely by semetite dehydration can significantly assist dynamic slip weakening during the Wenchuan Earthquake.

7.1.2 Importance of thermochemical pressurization in Wenchuan earthquake

Coseismic slip associated with the Wenchuan earthquake was systematically investigated via combined experimental and modeling work, taking into account the effects of a range of thermal-hydrological-mechanical-chemical processes within the principal slip zone.

Thermal pressurization (TP) in high-velocity wet experiments: High-velocity friction experiments, performed at coseismic velocity of 1.3 m/s on both fault breccia and central fault gouge samples collected from the exposure studied revealed low steady-state frictional strength (apparent friction coefficient of 0.08−0.11). All wet experiments showed rapid slip weakening and lower friction than the dry experiments, suggesting that friction-induced heating and associated fluid pressurization occurs in thin layers of wet gouges. Numerical modeling of the high-velocity friction experiments confirmed the feasibility of this mechanism.

Low-permeability slip zone: Amongst the materials investigated from the exposures studied, the grey gouge samples from the fault core show the lowest permeability ($< 10^{-21}$ m^2 at 165 MPa effective pressure) and generally low lowest porosity, compared with the fault rocks, such as breccias, from the surrounding damaged zone. The intact country rocks also have low permeability, even below the detection limit ($<10^{-22}$ m^2) of the experimental configuration used. The permeability profile across the fault zone thus exhibits a typical “conduit/barrier” (or binary) structure, with fluid flow being constrained to occur in the highly damaged zone on each side of the central gouge.

Thermochemical pressurization modeling: Numerical modeling of coseismic slip using the measured fault rock properties and seismological data on slip rate and displacement, indicated that thermochemical pressurization played an important role during the Wenchuan earthquake, with dynamic stress reduction being strongly enhanced by the liberation of water by smectite dehydration and further increase inpore pressure due to frictional heating. The calculated slip-weakening distance resulting from these effects is strikingly consistent with the seismologically-inferred value for the Wenchuan earthquake. The model results indicate that overshooting of lithostatic pressure by pore pressure generation might have occurred at depth, limiting temperature development to values less than 600 °C. Fluid pressurization within the slip zone can help explain the large coseismic displacement and slip acceleration observed in the portions of the LFZ studied. The results obtained indicate that it is essential to consider thermal and thermochemical pressurization phenomena in future seismic-hazard assessment, at least for the LFZ but presumably more generally also. In this context, it is important to note that the present results show that there exists a critical thickness of the co-seismic slip band, W_{cr}, which is approximately equal to 2 times the characteristic hydrological diffusion length. If the coseismic slip band is thicker than W_{cr}, major TP weakening is possible.

Some speculation on "hydrological asperities": On the basis of the model results, I speculate that locations where localized or branching slip occurs may allow thermally pressurized fluids to leak out of a propagating rupture on one branch, producing a strong portion of the fault that may act as a seismic asperity.

7.1.3 Frictional healing behavior in carbonate(-rich) rocks

I investigated the frictional healing behavior of simulated fault gouges prepared from 1) a carbonate breccia sample, and 2) a sample of clay-rich, fault core gouge, both taken from the exposures of the LFZ discussed above. The breccia-derived samples were under dry and wet conditions, while the gouge-derived smaples were tested wet. A direct shear set up, located in a triaxial testing machine, was used, operating at temperatures in the range 20–140 °C, and at low sliding velocities 0.1–10 μm/s. The main finding were follows.

Unusual healing behavior: Slide-hold-slide or SHs tests on the dry breccia-derived samples showed typical Dieterich-type healing behavior, characterized by unchanged steady-state frictional strength and by a linear relation between the transient peak healing ($\Delta\mu_{pk}$) measured upon reshearing and log hold time. However, in the SHS tests performed under hydrothermal conditions (wet, 80–140°C), both the gouge- and breccia-derived samples showed "non-Dieterich-type" healing behavior, characterized by an increase in

(quasi) steady-state friction coefficient ($\Delta\mu_r > 0$) seen after the hold period and transient peak healing ($\Delta\mu_{pk}$). This Transient peak healing ($\Delta\mu_{pk}$), observed in the hydrothermal experiments, was found to consist of two components, namely 1) a persistent increase in dynamic friction ($\Delta\mu_r$-effect: non-Dieterich) plus 2) a Dieterich component ($\Delta\mu_w$-effect) exhibiting the classical linear relation with log hold time. Both effects exhibit a positive temperature dependence and to some extent a positive dependence on the sliding rate imposed during SHS testing.

Water-enhanced healing rates: For the breccia-derived samples, the frictional healing rates ($\beta_{pk} = \beta_w$, defined as $d(\Delta\mu_{pk})/d(\log_{10}(t_h))$ and $d(\Delta\mu_w)/d(\log_{10}(t_h))$, respectively) of the dry samples increase with increasing temperature, consistent with previous results on quartz and feldspar gouges. The wet samples showed larger healing rates (β_{pk}) but increasing and then decreasing with temperarure. By contrast, wet gouge-derived samples show an increase in β_{pk} by ~ 10 times, from 0.0006/ decade at 20 °C to 0.0059/decade at 140 °C. Healing partitioning analyses indicate this is mostly related to the contribution by $\Delta\mu_r$, which increases remarkably with temperature.

Proposed healing mechanism: The mechanism of indentation creep and grain contact cementation or neck growth previously proposed to explain Dieterich-type healing, i.e. healing characterized by the classtical log-linear relation and near constant steady-state friction values, cannot explain the positive $\Delta\mu_r$ observed in our wet experiments. This is because such processes are expected to be "undone" upon reshearing healed samples. I infer that this effect is instead related to permanent, progressive porosity reduction during hold periods, attributed to intergranular pressure solution. Multiple arguments exist to support the operation of this mechanism in the breccia-derived sample (containing 97% carbonate minerals). However, in the gouge-derived samples, extra/reduced contribution from quartz and clay should be considered.

7.1.4 Velocity dependence of friction strength: (a–b) in carbonate(-rich) rocks

The above experiments also provided valuable and surprising results on the effects of healing on the velocity dependence of steady-state friction in carbonate-rich fault rocks.

Temperature and velocity dependence: Frictional strengths (peak friction coefficients measured at 10 μm/s) of 0.64–0.72 were measured for dry and wet breccia-derived samples, versus 0.30–0.34 for the wet gouge-derived samples. All experiments showed a negative temperature dependence of friction rate parameter, (a–b). Dry and wet breccia-derived samples not subjected to healing, displayed a decrease in (a–b) from ~ +0.003 at 20 °C to –0.004 at 140°C, becoming velocity-neutral at about 80 °C, in agreement with previous

reports (*Verberne et al.*, 2013a; 2013b). The data obtained for wet gouge-derived samples show velocity-strengthening slip at all temperatures investigated, with (a–b) decreasing from ~ 0.007 at 20 °C to 0.003 at 140 °C. We also observed a positive dependence of (a–b) on slip rate for all samples tested dry and with sample-saturated demineralized water, with asensitivity of 0.001–0.0035 per decade change in velocity.

Effect of interseismic healing: The experiments revealed that repeated SHS motion plus healing under wet conditions leads to an increase in (a–b) and thus to slip stabilization in carbonate fault rocks. The experiments on wet calcite gouge seem to be the first to show that interseismic healing can cause changes in slip stability. After the healing stages implemented in the present experiments, (a–b) increased by ~ 0.004 for the breccia-derived smples and by 0.001 for the gouge-derived samples. A simple conceptual model indicates that this change in (a–b) can be accounted for in terms of the persistent, healing- induced strengthening ($\Delta\mu_r$-effect) observedin the SHS runs performed on wet samples.

Implications of (a-b) data: The implications of the above results on frictional strength, healing and the effects of healing on (a–b) for the Wenchuan earthquake are: a) the carbonate rocks found along the northern portion of the LFZ are strong enough to provide an asperity function; b) the carbonate rocks studied tend to show velocity-weakening slip at the hypocentral depth of the north segment of the LFZ, especially if they are extrapolated to tectonically-driven slip rates. At those rates, (a–b) is expected to be negative enough to cause unstable slip, potentially. For faults in carbonate terrains in general, our results indicate that a) assuming fluid-assisted processes such as pressure solution are active, then applying a Dieterich-type log-linear law will underestimate natural fault healing rates, b) to be generally applicable, quantitative models for healing must account for fluid-assisted processes as inferred here, c) clay-rich fault rocks can heal at rates much higher than previously recognized from room temperature experiments, and d) interseismic frictional healing can stabilize rupture nucleation in carbonate faults. This may result in the seismogenic zone migrating nto deeper crustal levels in successive seismic cycles.

7.2 A microphysical model for friction and healing behavior of granular fault gouge

In an attempt to develop a mechanistic basis for extrapolating laboratory friction and healing data on carbonate gouges to natural conditions, I established a microphysical theory and numerical model. This describes both the transient and steady-state frictional behavior of a velocity weakening, granular fault gouge composed of a solid phase capable of undergoing intergranular pressure solution (IPS), assuming that deformation occurs on the grain scale by frictional intergranular sliding plus pressure solution. The model basically

consists of two governing equations derived from energy/entropy balance considerations and the kinematic relations that apply to a granular fault gouge undergoing shear and dilatation/compaction. These two equations can be written as

$$\dot{\tau} / K = V_{imp} - L_t[\lambda \dot{\gamma}_{ps}^{sb} + (1-\lambda)\dot{\gamma}_{ps}^{bulk}] - L_t \lambda \dot{\varepsilon}_{ps}^{sb} \frac{\sigma_n}{\sigma_n(\tilde{\mu} + 2\tan\psi) - \tau(1 - \tilde{\mu}\tan\psi)} \quad (7.1)$$

$$\dot{\varphi}^{sb} = \frac{\tau(1-\tilde{\mu}\tan\psi) - \sigma_n(\tilde{\mu} + \tan\psi)}{\sigma_n(\tilde{\mu} + 2\tan\psi) - \tau(1 - \tilde{\mu}\tan\psi)} \dot{\varepsilon}_{ps}^{sb}(1 - \varphi^{sb}) \quad (7.2)$$

They describe the evolution of shear stress (τ) and shear band porosity (φ^{sb}) in response to any boundary conditions imposed (for definition of all symbols see Chapter 6).

By solving these two controlling equations , and using standard creep equations to describe gouge compaction by pressure solution, typical lab-frictional tests were simulated, namely “velocity stepping” and “slide-hold-slide” test sequences, using velocity histories and environmental conditions employed in the experiments summarized above. The modeling results capture all of the main features and trends seen in the experimental data, including both steady-state and transient aspects of the observed behavior, with reasonable quantitative agreement. The model is the first mechanism-based model that I am aware of that can reproduce RSF-like behavior without recourse to the RSF law. Since it is microphysically based, the approach adopted should help provide a much improved framework for extrapolating friction data to natural conditions.

7.3 Remaining problems and suggestions for further research

The results given in this thesis leave behind a number of unsolved questions and new problems. The main ones are summarized below and suggestions are mad on how these issues may be addressed in future.

Limitations related to the study of isolated fault zone exposures: Using lab data obtained from a single surface exposure of the LFZ as input, numerical modeling of coseismic slip weakening was performed including the effects of thermal presssurization of pore fluids (TP) and mineral decomposition. The results indicate that fluid pressurization played an important role during the Wenchuan earthquake at the exposure sites studied, with dynamic stress reduction being strongly enhanced by increase of pore pressure due to frictional heating and smectite dehydration. The implication is that all aspects of TP should be considered in future seismic-hazard assessment. However, the presentwork was based only on the one surface exposure. To confirm the conclusions drawn, similar work on different locations along the LFZ should be performed, seeking correlations between computed thermochemical effects and rupture parameters (e.g. slip weakening distance)

obtained from seismological and other geophysical data for validation purposes. Moreover, the fault rock compositions used in the modeling conducted here were of course surface compositions. If it is possible, studies of fault rocks derived from depth should be performed in future. Such studies should be repeated not only on the LFZ of course, but for other active fault zones in carbonate terraines.

High-velocity experiments on wet fault gouge: As in some previous studies (e.g. *Faulkner et al.*, 2011), our high-velocity wet experiments suffer from the same technical problem that the Teflon sleeve used to confine the sample has poor sealing capacity. As a result, in this type of experiment, water, CO_2 and other volatiles inevitably escape during the experiments so that the evolving pore fluid pressure is moderated. This causes a poor reproducibility and the lack of a systematic relationship between the measured critical slip distance d_c and the applied normal stress for the wet data. Actually knowing the applied effective stress and fluid pressure are highly problematic. Further experiments, preferably within a pressure vessel, and/or at least with well constrained boundary conditions on normal stress and fluid pressure are needed (e.g. *Violay et al.*, 2013). This requires significant technical developments, many of which are being considered at present (*Ma et al.*, 2014). Moreover, numerical modeling of the wet experiments is also very challenging due to vapourization of water. This must be considered in further work.

Generality of "non-Dieterich-type" healing and its stabilizing effect: The "non-Dieterich-type" healing observed in the present study on wet carbonates is in part similar to the healing behavior reported in friction experiments on wet quartz (*Nakatani and Scholz*, 2004; *Yasuhara et al.*, 2005), though the increase in (a-b) caused by repeated SHS events has not been previously seen. I inferred in Chapter 5, that the "non-Dieterich-type" healing and its stabilizing effect, as seen in the present experiments, may be not limited to carbonates, but likely apply in any material where pressure solution or similar fluid-assisted deformation/healing processes can operate to produce time-dependent gouge compaction during the hold period. To confirm this, and to assess the broader implications, experiments on other minerals should be done in the future, under wet and dry conditions and at extended ranges of pressure and temperature. Also needing further investigation is the issue of the microphysical mechanism(s) responsible for the stabilization effect. This effect, seen in all the present wet experiments at elevated temperatures, was always accompanied by "non-Dieterich-type" behavior, characterized by a permanent increase ($\Delta\mu_r$) in dynamic steady-state friction. However, the microphysical process causing the $\Delta\mu_r$ effect, and whether this effect is indeed responsible for the increase in (a–b) caused by SHS testing, remains to be clarified, especially as the increase in (a–b) is also seen at

room temperature where no $\Delta\mu_r$ effect was observed (see Chapter 5).

Extension and application of the microphysical model: To our knowledge, while the work by *Niemeijer and Spiers* [2007] and by *Den Hartog and Spiers* [2014] addressed steady state friction, our theory is the first to be able to model full, steady state and transient, RSF-type behavior in terms of realistic, microstructurally-verifiable processes and state variables (such as porosity), without using the RSF law. It accordingly has the potential to provide a significantly improved basis for extrapolation of lab-derived friction data to natural conditions. However, many further improvements still need to be made. These include

a. Analytical derivation of the RSF parameters, namely a, b, $(a–b)$, D_c and β, as well the slip instability parameters such as critical stiffness K_c and reoccurrence wavelength L_c (in so far that analytical solutions can be obtained).
b. Incorporation of other creep mechanisms for grain- and contact-scale creep besides pressure solution.
c. Incorporation of the effects of increasingly important shear creep behavior at low velocities and high temperatures, resulting in low porosity and velocity strengtheningbehaviour.
d. Incorporation of a more realistic friction law for contact slip (e.g. $\tilde{\mu}=f(\tilde{v}_c)$), which can account for the velocity strengthening observed in the present and in previous experiments (e.g. *Marone*, 1998b) at low temperatures and or high slip rates (see also *den Hartog* and *Spiers*, 2014).
e. The present model is only applied for constant normal stress. Extension of the model to variable normal stress conditions (e.g. normal stress oscillation) is needed (c.f. the extended RSF law by *Linker and Dieterich*, 1992).
f. The present model only applies to grain-supported granular materials, and needs further modification to be applicable to matrix-supported materials. Some of these advances have already been initiated in steady-state models (*den Hartog and Spiers*, 2014), but they need extending to the transient case.

In the present model, it is assumed that the granular (dilatational) flow is dominant in the shear band localized at the sample boundary. This is a reasonable assumption, but we do not address why localized shear band(s) form. While the reasons have been discussed in literature (e.g. *Logan et al.*, 1992; *Marone*, 1998a; *Sleep et al.*, 2000; *Rice et al.*, 2014), a complete model should address this too. Also needed in future is application of the present model to extrapolate the experimental data obtained on carbonate rocks to examine the implications for the seismic cycle on active faults in limestone terrains, including the carbonate segment of the Longmenshan fault.

Bibliography

Agosta, F. and A. Aydin (2006), Architecture and deformation mechanism of a basin bounding normal fault in Mesozoic platform carbonates, Central Italy, *Journal of Structural Geology*, 28, 1445-1467.

Al Hattamleh, O. H., H. H. Al-Deeky, and M. N. Akhtar (2013), The consequence of particle crushing in engineering properties of granular materials, *International Journal of Geosciences*, 4, 1055-1060.

Ampuero, J.-P., and A. M. Rubin (2008), Earthquake nucleation on rate-and-state faults: aging and slip laws, *J. Geophys. Res.*, *113*, B01302, doi:10.1029/2007JB005082.

Atkinson, B. K., and R. G. Meredith (1989), The theory of subcritical crack growth with applications to minerals and rocks, *Fracture mechanics of rock*, 111-166.

Ballentine, C., and R. K. O'Nions (1994), The use of natural He, Ne, and Ar isotopes to study hydrocarbon-related fluid provenance, migration and mass balance in sedimentary basins, in *Geofluids: Origin, Migration, and Evolution of Fluids in Sedimentary Basins*, edited by J. Parnell, Geological Society Special Publication, vol. 78, pp. 347-361.

Barbot, S., Y. Fialko, and Y. Bock (2009), Postseismic deformation due to the Mw 6.0 2004 Parkfield earthquake: Stress driven creep on a fault with spatially variable rate-and-state friction parameters, *J. Geophys. Res.*, *114*, B07405, doi:10.1029/2008JB005748.

Bar-Sinai, Y., R. Spatschek, E. A. Brener, and E. Bouchbinder (2014), On the velocity-strengthening behavior of dry friction, *J. Geophys. Res.*, *119*, doi:10.1002/2013JB010586.

Baumberger, T., P. Berthoud, and C. Caroli (1999), Physical analysis of state- and rate-dependent friction law, II. Dynamic friction, *Phys. Rev. B*., *60*(6), 3928–3939

Bayer, G. (1973), Thermal expansion anisotropy of oxide compounds, *Proc. Br. Ceram. Soc.*, *22*, 39–53.

Beeler, N. M., S. H. Hickman, and T.-f. Wong (2001), Earthquake stress drop and laboratory-inferred interseismic strength recovery, *J. Geophys. Res.*, *106*, 30,371– 30,713.

Beeler, N. M., T. E. Tullis, and J. D. Weeks (1994), The roles of time and displacement in the evolution effect in rock friction, *Geophys. Res. Lett.*, *21*, 1987–1990.

Beeler, N. M., T. E. Tullis, and J. D. Weeks (1996), Frictional behavior of large displacement experimental faults, *J. Geophys. Res.*, *101*, 8697–8715.

Bernabé, Y., U. Mok, and B. Evans (2006), A note on the oscillating flow method for measuring rock permeability, *Int. J. Rock Mech. Min. Sci.*, 43, 311–316.

Bernabé, Y., U. Mok, B. Evans, and F. J. Herrmann (2004), Permeability and storativity of binary mixtures of high- and low-permeability materials, *J. Geophys. Res.*, *109*, B12207, doi:10.1029/2004JB003111.

Bernard, J. E., W. Hubert, and M. Diraison (2006), Seismicity wedge beneath the Upper Rhine Graben due to backwards Alpine push? , *Tectonophysics*, *428*, 49–64.

Billi, A. (2005), Gain size distribution and thickness of breccias and gouge zones form thin (<1m) strike-slip fault cores in limestone, *J. Struc. Geol.*, *27*, 1823–1837.

Billi, A., and F. Storti (2004), Fractal distribution of particle size in carbonate cataclastic rocks from the core of a regional strike-slip fault zone, Tectonophysics, 384, 115– 128.

Birch, F. (1966), Compressibility: elastic constants, in *Handbook of Physical Constants*, edited by D. P. Jr. Clark, *Geol. Soc. Amer. Mem*., *97*, 97–174.

Bizzarri, A., and M. Cocco (2006), A thermal pressurization model for the spontaneous dynamic rupture propagation on a three-dimensional fault: 1. Methodological approach, *J. Geophys. Res.*, *111*, B05303, doi:10.1029/2005JB003862.

Blanpied, M. L., D. A. Lockner, and J. D. Byerlee (1995), Frictional slip of granite at hydrothermal conditions, *J. Geophys. Res.*, *100*, 13045–13064.

Bos, B., and C. J. Spiers (2002), Fluid-assisted healing processes in gouge bearing faults: Insights from experiments on a rock analogue system, *Pure Appl. Geophys.*, *159*, 2537–2566, doi: 10.1007/s00024-002-8747-2.

Boullier, A. M., K. Fujimoto, T. Ohtani, G. Roman-Ross, E. Lewin, H. Ito, P. Pezard, and B. Ildefonse (2004), Textural evidence for recent co-seismic circulation of fluids in Nojima fault zone, Awaji Island, Japan, *Tectonophysics*, 378, 165-181.

Boulton, C., B. M. Carpenter, V. Toy, and C. Marone (2012), Physical properties of surface outcrop cataclastic fault rocks, Alpine Fault, New Zealand, *Geochem. Geophys. Geosyst.*,*13*, Q01018, doi:10.1029/2011GC003872.

Brace, W. F., and J. D. Byerlee (1966), Stick-slip as a mechanism for earthquakes, *Science*, *153*, 990-992.

Brace, W. F., J. B. Walsh, and W. T. Frangos (1968), Permeability of granite under high pressure, *J. Geophys. Res.*, *73*, 2225-2236.

Brantut, N., A. Schubnel, J. Corvisier, and J. Sarout (2010), Thermochemical pressurization of faults during coseismic slip, *J. Geophys. Res.*, *115*, B05314, doi:10.1029/2009JB006533.

Brantut, N., A. Schubnel, J.-N. Rouzaud, F. Brunet, and T. Shimamoto (2008), High-velocity frictional properties of a clay-bearing fault gouge and implications for earthquake mechanics, *J. Geophys. Res.*, *113*, B10401, doi:10.1029/2007JB005551.

Brantut, N., R. Han, T. Shimamoto, N. Findling, and A. Schubnel (2011), Fast slip with inhibited temperature rise due to mineral dehydration: Evidence from experiments on gypsum, *Geology*, *39* (1), 59-62.

Bray, H. J., and S. A. T. Redfern (1999), Kinetics of dehydration of Ca-montmorillonite, *Phys. Chem. Miner.*, *26*, 591-600, doi:10.1007/s002690050223.

Bréchet, Y., and Y. Estrin (1994), The effect of strain rate sensitivity on dynamic friction of metals, *Scr. Metall. Mater.*, 30, 1449– 1454.

Brindley, G. W. (1952), Structural mineralogy of clays, *Clays and Clay Minerals*, *1*, 33-43.

Bullock, R. J., N. De Paola, R. E. Holdsworth, and J. Trabucho-Alexandre (2014), Lithological controls on the deformation mechanisms operating within carbonate-hosted faults during the seismic cycle, *Journal of Structural Geology*, 58, 22–42.

Byerlee, J. D. (1967), Frictional characteristics of granite under high confining pressure, *J. Geophys. Res.*, *72*, 3639–48

Byerlee, J. D. (1978), Friction of rocks, *Pure Appl. Geophys.*, *116*, 615–626.

Caine, J. S., J. P. Evans, and C. B. Forster (1996), Fault zone architecture and permeability structure, *Geology*, *24*, 1025-1028.

Campbell, C. S. (2006), Granular material flows–An overview, *Powder Technol.*, *162*, 208–229, doi:10.1016/j.powtec.2005.12.008

Cao, J.X.，S.G. Liu, R.F. Tian, X.J. Wang, and X.Y. He (2011), Seismic prediction of carbonate reservoirs in the deep of Longmenshan foreland basin, *Acta Petrologica Sinica*, *27*(8), 2423－2434. (in Chinese with English abstract)

Carpenter, B. M., C. Marone, and D. M. Saffer (2011), Weakness of the San Andreas Fault revealed by samples from the active fault zone, *Nature Geoscience*, *4*, 251–254, doi:10.1038/ngeo1089.

Carpenter, B. M., D.M. Saffer, and C. Marone (2012), Frictional properties and sliding stability of the San Andreas fault from deep drill core, *Geology*, *40* (8), 759–762,doi:10.1130/G33007.1

Cello, G., S. Mazzoli, and E. Tondi (1998), The crustal fault structure responsible for the 1703 Earthuqake sequence of central Italy, *J. Geodynamics*, 26(2-4), 443-460.

Chen, J., and X. Yang (2012), The permeability of earthquake fault, *Earth science frontiers*, *19* (4), 30 - 40. (in Chinese with English abstract)

Chen, J., X. Yang, J. Dang, C. He, Y. Zhou, and S. Ma (2011), Internal structure and permeability of Wenchuan earthquake fault, *Chinese J. of Geophys*, *54* (7), 1805-1916. (In Chinese with an English abstract)

Chen, J., X. Yang, S. Ma, and C. J. Spiers (2013a), Mass removal and clay mineral de/re-hydration in carbonate-rich portions of the Wenchuan earthquake fault: Geochemical evidence and implications for fault zone evolution and coseismic slip, *J. Geophys. Res.*, *118*, doi:10.1002/jgrb.50089.

Chen, J., X. Yang, Q. Duan, T. Shimamoto, and C. J. Spiers (2013b), Importance of thermochemical pressurization in the dynamic weakening of the Longmenshan Fault during the 2008 Wenchuan earthquake: Inferences from experiments and modeling, *J. Geophys. Res.*, 118, 4145–4169, doi:10.1002/jgrb.50260.

Chen, L., and P. Talwani (1998), Reservoir-induced seismicity in China, *Pure and Applied Geophysics*, 153, 133-149.

Chen, T., and N. Lapusta (2009), Scaling of small repeating earthquakes explained by interaction of seismic and aseismic slip in a rate and state fault model, *J. Geophys. Res.*, *114*, B01311, doi:10.1029/2008JB005749.

Chen, W-M. D., H. Tanaka, H-J. Huang, C-B. Lu, C-Y Lee, and C-Y. Wang (2007), Fluid infiltration associated with seismic faulting: Examining chemical and mineralogical compositions of fault rocks from the active Chelungpu fault, *Tectonophysics*, *443*, 243-254.

Chester, F. M. (1994), Effects of temperature on friction: Constitutive equations and experiments with quartz gouge, *J. Geophys. Res.*, *99*, 7247– 7261.

Chester, F. M., and N. G. Higgs (1992), Multimechanism friction constitutive model for ultrafine quartz gouge at hypocentral conditions, *J. Geophys. Res.*, *97*, 1859–1870.

Chester, F. M., J. P. Evans, and R. L. Biegel (1993), Internal Structure and Weakening Mechanisms of the San Andreas Fault, *J. Geophys. Res.*, *98*(B1), 771–786, doi:10.1029/92JB01866.

Chiarabba, C., A. Amato, M. Anselmi, et al. (2009), The 2009 L'Aquila (central Italy) MW6.3 earthquake: main shock and aftershocks, *Geophys. Res. Lett.*, *36* (18), 1–6.

Chiaraluce, L. (2012), Unravelling the complexity of Apenninic extensional fault systems: a review of the 2009 L'Aquila earthquake (Central Apennines, Italy), J. Struct. Geol., 42, 2–18.

Collettini, C., B.M. Carpenter, C. Viti, et al. (2014), Fault structure and slip localization in carbonate-bearing normal faults: an example from the northern Apennines of Italy, *Journal of Structural Geology*, *67*, 154 – 166.

Collettini, C., C. Viti, T. Tesei, and S. Mollo (2013), Thermal decomposition along natural faults during earthquakes, *Geology*, *41*, 927-930.

Coulomb, C. A. (1785), The´orie des machines simples, Me´m. Math. Phys. Acad. Sci., 10, 161– 331.

Criado, J. M., M. Gonzalez, J. Malek, and A. Ortega (1995), The effect of the CO_2 pressure on the thermal decomposition kinetics of calcium carbonate, *Thermochim. Acta*, *254*, 121-127.

Dang, J., Y. Zhou, L. Hang, C. He, J. Chen, X. Dang, and X. Yang (2012), Fault gouge in carbon mudstone at outcrops of Bajiaomiao and Shenxigou in Hongkou, *Seismology and Geology*, *34*(1), 17-27. (in Chinese with English abstract)

David, C., T-f. Wong, W. Zhu, and J. Zhang (1994), Laboratory measurement of compaction- induced permeability change in porous rocks: Implications for the generation and maintenance of pore pressure excess in the crust, *Pure Applied Geophysics*, 143, 425-456.

de Lorenzo, S., and M. Lpddo (2010), Effect of frictional heating and thermal advection on pre-seismic sliding: a numerical simulation using a rate-, state- and temperature-dependent friction law, *Journal of Geodynamics*, *49* (1),1-13.

de Meer, S., and C. J. Spiers (1997), Uniaxial compaction creep of wet gypsum aggregates, *J. Geophys. Res.*, *102*(B1), 875-891, doi:10.1029/96JB02481.

De Paola, N., G. Chiodini, T. Hirose, C. Cardellini, S. Caliro, and T. Shimamoto (2011), The geochemical signature caused by earthquake propagation in carbonate-hosted faults, *Earth and Planet. Sci. Lett.*, *310*, 225-232.

De paola, N., T. Hirose, and T. Mitchell (2011), Fault lubrication and earthquake propagation in thermally unstable rocks, *Geology*, *39* (1), 35-38.

Den Hartog, S., and C. J. Spiers (2014), A microphysical model for fault gouge friction applied to subduction megathrusts, *J. Geophys. Res.*, *119*, 1510–1529, doi:10.1002/2013JB010580.

Den Hartog, S.A.M., A.R. Niemeijer, and C.J. Spiers (2013), Friction on subduction megathrust faults: Beyond the illite-muscovite transition, *Earth Planet. Sci. Lett.*, *373*, 8-19.

Di Toro, G., D. Goldsby, and T. E. Tullis (2004), Friction falls towards zero in quartz rock as slip velocity approaches seismic rates, *Nature*, *427*, 436-439.

Di Toro, G., R. Han, T. Hirose, N. De Paola, S. Nielsen, K. Mizoguchi, F. Ferri, M. Cocco, and T. Shimamoto (2011), Fault lubrication during earthquakes, *Nature*, *471*, 493-499.

Dieterich, J. H. (1972), Time-dependent friction in rocks, *J. Geophys. Res.*, *77*, 3690–3697

Dieterich, J. H. (1979), Modeling of rock friction: 1. Experimental results and constitutive equations, *J. Geophys. Res.*, *84*(B5), 2161–2168.

Famin, V., S. Nakashima, A-M. Boullier, K. Fujimoto, and T. Hirono (2008), Earthquakes produce carbon dioxide in crustal faults, *Earth Planet. Sci. Lett.*, *265* (3-4), 487-497.

Faulkner, D. R., A. C. Lewis, and E. H. Rutter (2002), On the internal structure and mechanics of large strike-slip fault zones: field observations of the Carboneras fault in southeastern Spain, *Tectonophysics*, *367*, 235-251.

Faulkner, D. R., and E. H. Rutter (2000), Comparison of water and argon permeability in natural clay-bearing fault gouge under high pressure at 20 °C, *J. Geophys. Res.*, 105, 16415-16427.

Faulkner, D. R., T. M. Mitchell, J. Behnen, T. Hirose, and T. Shimamoto (2011), Stuck in the mud? Earthquake nucleation and propagation through accretionary forearcs, *Geophys. Res. Lett.*, 38, L18303, doi:10.1029/2011GL048552.

Ferri, F., G. Di Toro, T. Hirose, and T. Shimamoto (2010), Evidence of thermal pressurization in high-velocity friction experiments on smectite-rich gouges, *Terra Nova*, *00*(0), 1-7.

Fine, R. A., and F. J. Millero (1973), Compressibility of water as a function of temperature and pressure, *J. Chem. Phys.*, *59*(10), 5529–5536, doi:10.1063/1.1679903.

Fischer, G. J., and M. S. Paterson (1992), Measurement of permeability and storage capacity in rocks during deformation at high temperature and pressure, in *Fault Mechanics and Transport Properties of Rocks*, edited by B. Evans and T-F. Wong, pp. 187-211, Academic Press, New York.

Fondriest, M., S. A. F. Smith, G. Di Toro, D. Zampieri, and S. Mittempergher (2012), Fault zone structure and seismic slip localization in dolostones, an example from the Southern Alps, Italy, *J. Struc. Geol.*, *45*, 52-67.

Fondriest, M., S. A. F. Smith, T. Candela, S. B. Nielsen, K. Mair, and G. Di Toro (2013). Mirror-like faults and power dissipation during earthquakes, Geology 41, 1175-1178.

Fredrich, J. T., and B. Evans (1992), Strength recovery along simulated faults by solution transfer, Proc. U.S. *Rock Mech. Symp.*, *33*, 121–130.

Frye, K. M., and C. Marone (2002), Effect of humidity on granular friction at room temperature, *J. Geophys. Res.*, *107*(B11), 2309, doi:10.1029/2001JB000654.

Fu, B., P. Wang, P. Kong, G. Zheng, G. Wang, and P. Shi (2008), Preliminary study of coseismic fault gouge occurred in the slip zone of the Wenchuan Ms 8.0 earthquake and its tectonic implications, *Acta Petrologica Sinica*, *24*(10), 2237-2243. (In Chinese with an English abstract)

Goddard, J. V., and J. P. Evans (1995), Chemical changes and fluid-rock interaction in faults of crystalline thrust sheets, northwestern Wyoming, U.S.A., *J. Struct. Geol.*, *17*, 533-547.

Goldsby, D. L., and T. E. Tullis (2011), Flash heating leads to low frictional strength of crustal rocks at earthquake slip rates. *Science*, *334*, 216-218.

Grant, J. A. (1986), The isocon diagram-a simple solution to Gresens' equation for metasomatic alteration. *Econ. Geol.*, *81*, 1976-1982.

Gratier, J.-P., J. Richard, F. Renard, S. Mittempergher, M.-L. Doan, G. Di Toro, J. Hadizadeh, and A.-M. Boullier (2011), Aseismic sliding of active faults by pressure solution creep: Evidence from the San Andreas-Fault Observatory at Depth, *Geology*, *39*, 1131-1134.

Greene, G. W., K. Kristiansen, E. E. Meyer, J. R. Boles, J. N. Israelachvili (2009), Role of electrochemical reactions in pressure solution, *Geochimica et Cosmochimica Acta*, *73*, 2862-2874.

Hamada, Y., T. Hirono, W. Tanikawa, W. Soh, and S.-R. Song (2009), Energy taken up by co-seismic chemical reactions during a large earthquake: An example from the 1999 Taiwan Chi-Chi earthquake, *Geophys. Res. Lett.*, *36*, L06301, doi:10.1029/2008GL036772.

Han, L., Y. Zhou, J. Chen, S. Ma, X. Yang, C. He, and J. Dang (2010), Structural characters of co-seismic fault gouge in bed rocks during the Wenchuan Earthquake, *Quaternary Science*, *30*(4), 746 -758. (In Chinese with an English abstract)

Han, R., T. Hirose, and T. Shimamoto (2010), Strong velocity weakening and powder lubrication of simulated carbonate faults at seismic slip rates, *J. Geophys. Res.*, *115*, B03412, doi:10.1029/2008JB006136.

Han, R., T. Shimamoto, T. Hirose, J. Ree, and J. Ando (2007), Ultralow friction of carbonate faults caused by thermal decomposition, *Science*, *316*, 878–881.

Hausegger, S., W. Kurz, R. Rabitsch, E. Kiechl, and F-J. Brosch (2010), Analysis of the internal structure of a carbonate damaged zone: Implications for the mechanisms of fault breccia formation and fluid flow, *J. Struc. Geol.*, *32*(9), 1349-1362.

Hawkins, R. K., P. A. Egelstaff (1980), Interfacial water structure in montmorillonite from neutron diffraction experiments, *Clays and Clay Minerals*, *28*, 19-28.

He, C., T.-f. Wong, and N. M. Beeler (2003), Scaling of stress drop with recurrence interval and loading velocity for laboratory derived fault strength relations, *J. Geophys. Res.*, 108(B1), 2037, doi:10.1029/2002JB001890.

He, C., Z. Wang, and W. Yao (2007), Frictional sliding of gabbro gouge under hydrothermal conditions, *Tectonophysics*, *445*, 353–362.

Hellings, L., F. Dehairs, M. Tackx, E. Keppens, and W. Baeyens (1999), Origin and fate of organic carbon in the freshwater part of the Scheldt Estuary as traced by stable carbon isotope composition, *Biogeochemistry*, *47*(2), 167-186.

Hetland, E.A., M. Simons, and E.M. Dunham (2010), Post-seismic and interseismic fault creep I: model description, *Geophys. J. Int.*, *181*, 81-98.

Hickman, S. H., and B. Evans (1992), Growth of grain contacts in halite by solution-transfer: Implications for diagenesis, lithification, and strength recovery, in *Fault Mechanics and Transport Properties of Rocks*, edited by B. Evans and T.-F. Wong, pp. 253– 280, Elsevier, New York.

Hickman, S., R. Sibson, and R. Bruhn (1995), Introduction to special section: Mechanical involvement of fluids in faulting, *J. Geophys. Res.*, *100*(B7), 12,831–12,840, doi:10.1029/95JB01121.

Hirono, T., et al. (2006), Evidence of frictional melting from disk-shaped black material, discovered within the Taiwan Chelungpu fault system, *Geophys. Res. Lett.*, *33*, L19311, doi:10.1029/2006 GL027329.

Hirono, T., et al. (2007), A chemical kinetic approach to estimate dynamic shear stress during the 1999 Taiwan Chi-Chi earthquake, *Geophys. Res. Lett.*, *34*, L19308, doi:10.1029/2007GL030743. (Correction, *Geophys. Res. Lett.*, *35*, doi:10.1029/2007GL032512, 2008.)

Hirono, T., et al. (2008), Clay mineral reactions caused by frictional heating during an earthquake: An example from the Taiwan Chelungpu fault, *Geophys. Res. Lett.*, *35*, L16303, doi:10.1029/2008 GL034476.

Hirose, T., and M. Bystricky (2007), Extreme dynamic weakening of faults during dehydration by coseismic shear heating, *Geophys. Res. Lett.*, *34*, L14311, doi:10.1029/2007GL030049.

Hirose, T., and T. Shimamoto (2005), Growth of molten zone as a mechanism of slip weakening of simulated faults in gabbro during frictional melting, *J. Geophys. Res.*, *110*, B05202, doi:10.1029/2004JB003207.

Hou, L., S. Ma, T. Shimamoto, J. Chen , J. Yao, X. Yang, and Y. Okimura (2012), Internal structures and high-velocity frictional properties of a bedding-parallel carbonate fault at Xiaojiaqiao outcrop activated by the 2008 Wenchuan earthquake, *Earthquake Science*, 25, 197–217.

Hu, J., Z. Duan, C. Zhu, and I.-M. Chou (2007), PVTx properties of the CO_2-H_2O and CO_2-H_2O-NaCl systems below 647 K: Assessment of experimental data and thermodynamic models, *Chemical Geology*, *238* (3-4), 249-267.

Huang, W. L., J. M. Longo, and D. R. Pevear (1993), An experimentally derived kinetic model for smectite-to-illite conversion and its use as a geothermometer, *Clays and Clay Minerals*, *41*, 162-177.

Huang, W. L., W. A. Bassett, and T. C. Wu (1994), Dehydration and hydration of montmorillonite at elevated temperatures and pressures monitored using synchrotron radiation, *American Mineralogist*, *79*, 683-691.

Ikari, M. J., C. Marone, D.M. Saffer, and A. J. Kopf (2013), Slip weakening as a mechanism for slow earthquakes, *Nature Geoscience*, doi: 10.1038/NGEO1818.

Ikari, M. J., D. M. Saffer, and C. Marone (2009), Frictional and hydrologic properties of clay-rich fault gouge, *J. Geophys. Res.*, *114*, B05409, doi:10.1029/2008JB006089.

Ikehara, M., et al. (2007), Low total and inorganic carbon contents within the Chelungpu fault, *Geochemical Journal*, *41*, 391-396.

Isaacs, A. J., J. P. Evans, S-R. Song, and P. T. Kolesar (2007), Structural, Mineralogical, and Geochemical Characterization of the Chelungpu Thrust Fault. Taiwan, *Terr. Atmos. Ocean. Sci.*, *18*(2), 183-221.

Ishikawa, T., et al. (2008), Coseimic fluid-rock interations at high temperatures in the Chelungpu fault, *Nature geosciences*, *1*, 679-683.

Jacobsen, S. D., J. R. Smyth, R. J. Swope, and R. T. Downs (1998), Rigid-body character of the SO4 groups in celestine, anglesite, and barite, *Can. Mineral.*, *36*, 1053-1060.

Janssen, C., R. L. Romer, A. Hoffmann-Rothe, B. Mingram, P. Dulski, P. Moller, and H. Al-Zubi (2005), The role of fluid in faulting deformation: a case study from the Dead Sea Transform (Jordan), *Int. J. Earth Sci.*, *94*, 243-255.

Jia, D., Y. Li, A. Lin, M. Wang, W. Chen, X. Wu, Z. Ren, Y. Zhao, and L. Luo (2010), Structural model of 2008 Mw 7.9 Wenchuan earthquake in the rejuvenated Longmen Shan thrust belt, China, *Tectonophysics*, *491*, 174–184.

Johnson, K. M., A. E. King, and J. M. Sieburth (1985), Coulometric TCO_2 analyses for marine studies; an introduction, *Marine Chemistry*, *16* (1), 61-82.

Kanamori, H. (1994), Mechanics of earthquakes, *Ann. Rev. Earth Planet. Sci.*, *22*, 207-237.

Karner, S. L., and C. Marone (2001), Frictional restrengthening in simulated fault gouge: effect of shear load perturbations, *J. Geophys. Res.*, *106* (B9), 19,319–19,337.

Karner, S. L., C. Marone, and B. Evans (1997), Laboratory study of fault healing and lithification in simulated fault gouge under hydrothermal conditions, *Techtonophysics*, *277*, 41– 55.

Karner, S. L., and C. Marone (2000), Effects of loading rate and normal stress on stress drop and stick-slip recurrence interval. Geocomplexity and the physics of earthquakes, *Geophysical Monograph*, *120*, 187–198.

Kerr, P. F. (1952), Formation and occurrence of clay minerals, *Clays and Clay Minerals*, *1*, 19-32.

Kerrich, R., T. E. La Tour, and L. Willmore (1984), Fluid Participation in Deep Fault Zones: Evidence From Geological, Geochemical, and $^{18}O/^{16}O$ Relations, *J. Geophys. Res.*, *89*(B6), 4331-4343, doi:10.1029/JB089iB06p04331.

King, D. S. H., C. Marone (2012), Frictional properties of olivine at high temperature with applications to the strength and dynamics of the oceanic lithosphere, *J. Geophys. Res.*, *117*, B12203, doi:10.1029/2012JB009511.

Kirschner, D. L., and L. A. Kennedy (2001), Limited syntectonic fluid flow in carbonate-hosted thrust faults of the Front Ranges, Canadian Rockies, inferred from stable isotope data and structures, *J. Geophys. Res.*, 106(B5), 8827-8840, doi:10.1029/2000JB900414.

Ko, S.-c., D. L. Olgaard, and T.-f. Wong (1997), Generation and maintenance of pore pressure excess in a dehydrating system, 1 Experimental and microstructural observations, *J. Geophys. Res.*, *102*, 825-839.

Koelemeijer, P. J., C. J. Peach, and C. J. Spiers (2012), Surface diffusivity of cleaved NaCl crystals as a function of humidity: Impedance spectroscopy measurements and implications for crack healing in rock salt, J. Geophys. Res., 117, B01205, doi:10.1029/2011JB008627.

Kranz, R. L., J. S. Saltzman, and J. D. Blacic (1990), Hydraulic diffusivity measurements on laboratory rock samples using an oscillating pore pressure method, *Int. J. Rock Mech. Min. Sci.*, *27*, 345-352.

Kristiansen, K., M. Valtiner, G. W. Greene, J. R. Boles, and J. N. Israelachvili (2011), Pressure solution – The importance of the electrochemical surface potentials, *Geochimica et Cosmochimica Acta*, *75*, 6882–6892.

Kuo, L.-W., S.-R. Song, E.-C. Yeh, and H.-F. Chen (2009), Clay mineral anomalies in the fault zone of the Chelungpu Fault, Taiwan, and their implications, *Geophys. Res. Lett.*, 36, L18306, doi:10.1029/2009GL039269.

Labaume, P., E. Carrio-Schaffhauser, J.-F. Gamond, and F. Renard (2004), Deformation mechanisms and fluid-driven mass transfers in the recent fault zones of the Corinth Rift (Greece), *C. R. Geoscience*, *336*, 375-383.

Lachenbruch, A. H. (1980), Frictional Heating, Fluid Pressure, and the Resistance to Fault Motion, *J. Geophys. Res.*, *85* (B11), 6097-6112.

Lehner, F. K. (1990), Thermal dynamics of rock deformation by pressure solution, in *Deformation Processes in Minerals, Ceramics and Rocks*, edited by D. J. Barber and P. G. Meredith, pp. 296–333, Unwin Hyman, London.

Lehner, F. K., and J. Bataille (1985), Nonequilibrium thermodynamics of pressure solution, *Pure Appl. Geophys.*, *122*, 53-85.

Li ,Y., et al. (2006), Elimination efficiency of different reagents for the memory effect of mercury using ICP-MS. *J. Anal. At. Spectrom.*, *21*, 94-96.

Li, Y., Z. Yan, S. Liu, et al. (2014), Migration of the carbonate ramp and sponge buildup driven by the orogenic wedge advance in the early stage (Carnian) of the Longmen Shan foreland basin, China, *Tectonophysics*, *619-620*, 179-193.

Li, C.-Y., Z.-Y.Wei, J.-Q. Ye, Y.-B. Han, and W.-J. Zheng (2010), Amounts and styles of coseismic deformation along the northern segment of surface rupture, of the 2008 Wenchuan Mw 7.9 earthquake, China, *Tectonophysics*, *491* (1-4), 35-58.

Li, Y.-G., J. E. Vidale, S. M. Day, D. D. Oglesby, and E. Cochran (2003), Postseismic fault healing on the rupture zone of the 1999 M 7.1 Hector Mine, California, earthquake, *Bull. Seismol. Soc. Am.*, *93*, 854– 869.

Lin, X., F. Ying, and N. Zheng (1992), Techniques of X-ray Diffraction Analysis and Its Geological Application, pp. 119-131, Petroleum Industry Press, Beijing. (in Chinese with an English abstract)

Linker, M.F., and J. H. Dieterich (1992), Effects of Variable Normal Stress on Rock Friction: Observations and Constitutive Equations, *J. Geophys. Res.*, *97*(B4), 4923-4940.

Liteanu, E., A. Niemeijer, C. J. Spiers, C. J. Peach, and J. H. P. de Bresser (2012), The effect of CO2 on creep of wet calcite aggregates, *J. Geophys. Res.*, *117*, B03211, doi:10.1029/2011JB008789.

Liu, B. Y., and B. P. Shi (2011), The state of stress of the M_s 8.0 Wenchuan earthquake faulting and its implication to the aftershock hazard, *Chinese J. Geophys.*, *54* (4), 1002-1009. (in Chinese with English abstract)

Liu, C.-W., and W.-S. Lin (2005), A smectite dehydration model in a shallow sedimentary basin: model development, *Clays and Clay minerals*, *53*(1), 55-70.

Liu, J., J. M. Walter, and K. Weber (2002), Fluid-enhanced low-temperature plasticity of calcite marble: Microstructures and mechanisms, Geology, 30 (9), 787 – 790.

Lockner, D. A., C., Morrow, D., Moore, and S. Hickman (2011), Low strength of deep San Andreas Fault gouge from SAFOD core, *Nature*, *472*, 82-85.

Logan, J. M., C. A. Dengo, N. G. Higgs, and Z. Z. Wang (1992), Fabrics of experimental fault zones: their development and relationship to mechanical behavior. In *Fault mechanics and transport properties of rocks*, ed. B. Evans and T.f. Wong, pp. 33–67. London, Academic.

Lu, R., D. He, J. Suppe, Y. Ma, B. Liu, and Y. Chen (2012), Along-strike variation of the ftontal zone structural geometry of the Central longmen Shan thrust belt revealed by seismic reflection profiles, *Tectonophysics*, *580*, 178-191.

Lu, Z., and C. He (2014), Frictional behaviour of simulated biotite fault gouge under hydrothermal conditions, *Tectonophysics*, 622, 62 – 80.

Luo, L., L. Tang, Z. Xu, H. Li (2010), Monitor and characteristics of fluid during Chinese Wenchuan Fault Scientific Drilling, American Geophysical Union, Fall annual meeting, San Francisco, Abstract T53E-05.

Ma, K.-F., et al. (2006), Slip zone and energetics of a large earthquake from the Taiwan Chelungpu-fault Drilling Project, *Nature*, *444*, 473 -476.

Ma, S., T. Shimamoto, L. Yao, T. Togo, and H. Kitajima (2014), A rotary-shear low to high-velocity friction apparatus in Beijing to study rock friction at plate to seismic slip rates, *Earthquake Science*, *27*(5),469-497.

Ma, W., X. Xu, G. Yu, J. Yuan, C. Xu, and R. Lin (2012), Assess the reservoir-induced seismic harzard in the Hubei section of the three gorges reservoir using gray clustering method, *Seismology and Geology*, *34* (4), 726-738.

MaCaig, A. M. (1988), Deep fluid circulation in fault zone, *Geology*, *16*(10), 867-870.

Marone, C. (1998a), Laboratory-derived friction laws and their application to seismic faulting, *Annu. Rev. Earth Planet. Sci.*, *26*, 643 – 696, doi:10.1146/annurev.earth.26.1.643.

Marone, C. (1998b), The effect of loading rate on static friction and the rate of fault healing during the earthquake cycle, *Nature*, *391*, 69 – 72.

Marone, C., and C. H. Scholz (1989), Particle-size distribution and microstructures with in simulated fault gouge, *J. Struct. Geol.*, *11*(7), 799-814.

Marone, C., and D. M. Saffer (2014/2015). The mechanics of frictional healing and slip instability during the seismic cycle, *Treatise on Geophysics*, TGP2: 00092

Marone, C., C.B. Raleigh, and C.H. Scholz (1990), Frictional behavior and constitutive modeling of simulated fault gouge, J. Geophys. Res., 95, 7007–7025.

Marone, C., J. E. Vidale, and W. Ellsworth (1995), Fault healing inferred from time dependent variations in source properties of repeating earthquakes, *Geophys. Res. Lett.*, *22*, 3095–98

Marone, C., M. Cocco, E. Richardson, and E. Tinti (2009), The critical slip distance for seismic and aseismic fault zones of finite width, in Fault-zone Properties and Earthquake Rupture Dynamics, edited by E. Fukuyama, International Geophysics Series, 94, 135-162, Elsevier.

Mase, C., and L. Smith (1985), Pore-fluid Pressure and frictional heating on a fault surface, *Pageoph, Pure Appl. Geophys.*, *122*, 583- 607.

Mirabella, F., M. Barchi, A. Lupattelli, E. Stucchi, and M.G. Ciaccio (2008) Insights on the seismogenic layer thickness from the upper crust structure of the Umbria-Marche Apennines (central Italy), *Tectonics*, *27*, TC1010, doi:10.1029/2007TC002134.

Mishima, T., T. Hirono, W. Soh, and S.-R. Song (2006), Thermal history estimation of the Taiwan Chelungpu fault using rock-magnetic methods, *Geophys. Res. Lett.*, 33, L23311, doi:10.1029/2006GL028088.

Mitchell, E. K., Y. Fialko, and K. M. Brown (2012), Temperature dependence of frictional healing of Westerly granite: experimental observations and numerical simulations, *Geochem. Geophys. Geosyst.*, *14*, 567–582, doi:10.1029/2012GC004241.

Mizoguchi, K., and T. Shimamoto (2008), A combined thermal pressurization and high-velocity behavior Nojima fault gouge to infer slip-weakening of a fault. *AOGS annual meeting*, Abstract, 58-SE-A1507.

Mizoguchi, K., T. Hirose, T. Shimamoto, and E. Fukuyama (2007), Reconstruction of seismic faulting by high-velocity friction experiments: An example of the 1995 Kobe earthquake, *Geophys. Res. Lett.*, *34*, L01308, doi:10.1029/2006GL027931.

Mizoguchi, K., T. Hirose, T. Shimamoto, and E. Fukuyama (2008), Internal structure and permeability of the Nojima fault, southwest Japan, *J. Struct. Geol.*, *30*, 513-524.

Molli, G., et al. (2010), Fault zone structure and fluid-rock interaction of a high angle normal fault in Carrara marble (NW Tuscany, Italy), *J. Struc. Geol.*, *32*, 1334-1348.

Mori, J. J. (2010), Temperature Measurements in the WFSD-1 Borehole Following the 2008 Wenchuan earthquake, *American Geophysical Union*, *fall annual meeting*, San Francisco, T53E-03.

Morrow, C., B. Radney, and J. Byerlee (1992), Frictional strength and the effective pressure law of montmorillonite and illite clays, in *Fault Mechanics and Transport Properties of Rocks*, Int. Geophys. Ser., vol. 51,edited by B. Evans and T.-F. Wong, pp. 69– 88, Academic, London.

Morrow, C.A., D.A. Lockner, D.E. Moore, and S. Hickman (2014), Deep permeability of the San Andreas Fault from San Andreas Fault Observatory at Depth (SAFOD) core samples, Journal of Structural Geology, 64, 99–114.

Muhuri, S. K., T. A. Dewers, T. E. Scott Jr., and Z. Reches (2003), Interseismic fault strengthening and earthquake-slip instability: Friction or cohesion?, *Geology*, *31*, 881–884, doi:10.1130/G19601.1.

Nakashima, S. (1995), Diffusivity of ions in pore water as a quantitative basis for rock deformation rate estimates, *Tectonophysics*, *245*, 185-203.

Nakatani, M. (2001), Conceptual and physical clarification of rate and state friction: Frictional sliding as a thermally activated rheology, *J. Geophys. Res.*, *106*(B7), 13,347-13,380.

Nakatani, M., and C. H. Scholz (2004), Frictional healing of quartz gouge under hydrothermal conditions: 1. Experimental evidence for solution transfer healing mechanism, *J. Geophys. Res.*, *109*, B07201, doi:10.1029/2001JB001522

Nakatani, M., and H. Mochizuki (1996), Effects of shear stress applied to surfaces in stationary contact on rock friction, *Geophys. Res. Lett.*, *23*, 869–872.

Niemeijer, A. R., and C. J. Spiers (2006), Velocity dependence of strength and healing behaviour in simulated phyllosilicate-bearing fault gouge, *Tectonophysics*, *427*, 231– 253.

Niemeijer, A. R., and C. J. Spiers (2007), A microphysical model for strong velocity weakening in phyllosilicate-bearing fault gouges, *J. Geophys. Res.*, *112*, B10405, doi:10.1029/2007JB005008.

Niemeijer, A., C. Marone, and D. Elsworth (2008), Healing of simulated fault gouges aided by pressure solution: Results from rock analogue experiments, *J. Geophys. Res.*, *113*, B04204, doi:10.1029/2007JB005376.

Noda, H., and T. Shimamoto (2005), Thermal pressurization and slip weakening distance of a fault: An example of the Hanaore fault, southwest Japan, *Bull. Seismol. Soc. Am.*, *95*(4), 1224-1233, doi:10.1785/0120040089.

Noyan, H., M. O¨nal, and Y. Sarikaya (2008), Thermal deformation thermodynamics of a smectite mineral, *J. Therm. Anal. Calorim.*, *91*, 299–303, doi:10.1007/s10973-007-8260-z.

O'Hara, K. (1988), Fluid flow and volume loss during mylonitization: an origin for phyllonite in an overthrust setting, North Carolina U.S.A., *Tectonophysics*, *156*(1-2), 21-36.

O'Neil, J. R., R. N. Clayton, and T. K. Mayeda (1969). Oxygen isotope fractionation in divalent metal carbonates, *J. Chem. Physics.*, *51*, 5547-5558.

Olivieri, M., and G. Ekström (1999), Rupture depths and source processes of the 1997-1998 Earthquake Sequence in Central Italy, *Bulletin of the Seismological Society of America*, *89* (1), 305-310.

Ohnaka, M., and L.-F. Shen (1999), Scaling of the rupture process from nucleation to dynamic propagation: implications of geometric irregularity of the rupturing surfaces, *J. Geophys. Res.*, *104*, 817-844.

Ohomoto, H., and R. O. Rye (1979), Isotopes of sulfur and Carbon, in *Geochemistry of hydrothermal ore deposits*, edited by H. L. Barnes, pp. 509-567, Wiley, New York.

Olsen, M.P., C.H. Scholz, and A. Le´ger (1998), Healing and sealing of a simulated fault gouge under hydrothermal conditions: Implications for fault healing, *J. Geophys. Res.*, *103*, 7421– 7430.

Olsson, W. A. (1974), Effect of temperature, pressure and displacement rate on the frictional characteristics of a limestone, *Int. J. Rock Mech. Min. Sci. &Geomech. Abst*, *11*, 267-278.

Paterson, M. S. (1995), A theory for granular flow accommodated by material transfer via an intergranular fluid, *Tectonophysics*, *245*, 135–151.

Paterson, M. S., and T.-F. Wong (2005), Experimental rock deformation – The brittle field, 2nd ed., Springer-Verlag. Berlin Heidelberg.

Pili, E., B. M. Kennedy, M. E. Conrad, and J.-P. Gratier (2011), Isotopic evidence for the infiltration of mantle and metamorphic CO_2-H_2O fluids from below in faulted rocks from the San Andreas Fault System, *Chem. Geol.*, *281*(3-4), 242-252.

Pili, E., F. Poitrasson, and J. P. Gratier (2002), Carbon-oxygen isotope and trace element constraints on how fluids percolate faulted limestones from the San Andreas Fault system: partitioning of fluid sources and pathways, *Chem. Geol.*, *190*, 231-250.

Plummer, L. N., and E. Busenberg (1982), The solubilities of calcite, aragonite and vaterite in CO_2-H_2O solutions between 0 and 900 °C, and an evaluation of the aqueous model for the system $CaCO_3$-CO_2-H_2O, *Geochim. Cosmochim. Acta, 46*, 1011-1040.

Pluymakers, A. M. H., and C. J. Spiers (2014), Compaction creep of simulated anhydrite fault gouge by pressure solution: theory v. experiments and implications for fault sealing, in *Rock Deformation from Field, Experiments and Theory: A Volume in Honour of Ernie Rutter,* ed. D.R. Faulkner, E. Mariani, and J. Mecklenburgh, Geological Society, London, Special Publications *409,* doi:10.1144/SP409.6.

Pokrovsky, O.S., S.V. Golubev, J. Schott, and A. Castillo (2009), Calcite, dolomite and magnesite dissolution kinetics in aqueous solutions at acid to circumneutral pH, 25 to 150 °C and 1 to 55 atm pCO_2: New constraints on CO_2 sequestration in sedimentary basins, *Chemical Geology*, *265*, 20–32.

Pollastro, R. M. (1993), Considerations and applications of the illite/smectite geothermometer in hydrocarbon-bearing rocks of Miocene to Mississippian age, *Clay and Clay minerals*, *4* (2), 119-133.

Rao, T. G., and P. K. Govil (1995), Merits of using Barium as a heavy absorber in major element analysis of rock samples by XRF: New data on ASK-1 and ASK-2 reference samples, *Analyst*, *120*, 1279 -1282.

Reches, Z., and D. A. Lockner (2010), Fault weakening and earthquake instability by power lubrication, *Nature*, 467, 452-455.

Renard F., Park A., P. Ortoleva, and J. P. Gratier (1999), A transitional pressure solution model, *Tectonophysics*, *312*, 97-115.

Renard, F., D. Dysthe, J. Feder, K. Bjorlykke, and B. Jamtveit (2001), Enhanced pressure solution creep rates induced by clay particles: experimental evidence in salt aggregates, *Geophys. Res. Lett. 28*(7), 1295–1298.

Renard, F., P. Ortoleva, and J. P. Gratier (1997), Pressure solution in sandstones: influence of clays and dependence on temperature and stress, *Tectonophysics*, *280*, 257-266.

Renard, F., S. Beauprêtre, C. Voisin, D. Zigone, T. Candela, D. K. Dysthe, and J.-P. Gratier (2012), Strength evolution of active frictional interface is controlled by the dynamics of contacts and chemical effects, *Earth Planet. Sci. Lett.*, *341-344*, 20-34.

Rice, J. R. (1999), Flash heating at asperity contacts and rate-dependent friction, *Eos Trans. AGU*, *80*(46), Fall Meet. Suppl., F681.

Rice, J. R. (2006), Heating and weakening of faults during earthquake slip, *J. Geophys. Res.*, *111*, B05311, doi:10.1029/2005JB004006.

Rice, J.R., N. Lapusta, and K. Ranjith (2001), Rate and state dependent friction and the stability of sliding between elastically deformable solids, *J. Mech. Phys. Solids*, *49*(9), 1865-1898.

Rice J. R., J. W. Rudnicki, and J. D. Platt (2014), Stability and localization of rapid shear in fluid-saturated fault gouge: 1. Linearized stability analysis, *J. Geophys. Res.*, *119*, 4311–4333, doi:10.1002/2013JB010710.

Richardson, E., and C. Marone (1999), Effects of normal stress vibrations on frictional healing, *J. Geophys. Res.*, 104 (B12), 28,859 – 28878.

Roland, P., and K. Ola (1996), Physico/chemical stability of smectite clays, *Engineering Geology*, *41*, 73-85.

Rowe, C. D., Å. Fagereng, J. A. Miller, and B. Mapani (2012), Signature of coseismic decarbonation in dolomitic fault rocks of the Naukluft Thrust, Namibia, *Earth and Planetary Science Letters*, *333-334*, 200-210.

Ruina, A. (1983), Slip instability and state variable friction laws, *J. Geophys. Res.*, *88*, 10359– 10370.

Rutter, E. H., and D. H. Mainprice (1978), The effect of water on the stress relaxation of faulted and unfaulted sandstone, *Pure Appl. Geophys.*,*116*, 634-54.

Sabirzyanov, A. N., R. A. Shagiakhmetov, F. R. Gabitov, A. A. Tarzimanov, and F. M. Gumerov (2003), Water Solubility of Carbon Dioxide under Supercritical and Subcritical Conditions, Theoretical Foundation of Chemical Engineering, 37 (1), 51-53, Doi: 10.1023/A:1022256927236.

Saffer, D. M., and C. Marone (2003), Comparison of smectite- and illite-rich gouge frictional properties: Application to the updip limit of the seismogenic zone along subduction megathrusts, *Earth Planet. Sci. Lett.*, *215*, 219-235.

Samuelson, J., and C. J. Spiers (2012), Fault friction and slip stability not affected by CO_2 storage: Evidence from short-term laboratory experiments on North Sea reservoir sandstones and caprocks, *Int. J. Greenhouse Gas Control*, *11*, S78-S90.

Sawai, M., T. Shimamoto, and T. Togo (2012), Reduction in BET surface area of Nojima fault gouge with seismic slip and its implication for the fracture energy of earthquakes, *J. Struct. Geol.*, *38*, 117-138.

Schleicher, A. M., S. N. Tourscher, B. A. van der Pluijm, and L. N. Warr (2009), Constraints on mineralization, fluid-rock interaction, and mass transfer during faulting at 2–3 km depth from the SAFOD drill hole, J. Geophys. Res., 114, B04202, doi:10.1029/2008JB006092.

Scholz, C. H. (2002), The Mechanics of Earthquakes and Faulting (2ndedition), New York, Cambridge Univ. Press., Cambridge, 471pp.

Scuderi, M. M., A. R. Niemeijer, C. Collettini, and C. Marone (2013), Frictional properties and slip stability of active faults within carbonate–evaporate sequences: The role of dolomite and anhydrite, *Earth Planet. Sci. Lett.*, *369-370*, 220-232.

Segall, P., and J. R. Rice (2006), Does shear heating of pore fluid contribute to earthquake nucleation? *J. Geophys. Res.*, *111*, B09316, doi:10.1029/2005JB004129.

Sheppard, S. M., and H. P. Schwarcz (1970), Fractionation of carbon and oxygen isotopes and magnesiumbetween coexisting metamorphic calcite and dolomite, *Contrib. Mineral. Petrol.*, *26* (3), 161-198.

Shi, Y., and C. Y. Wang (1986), Pore pressure generation in sedimentary basins: overloading versus aquathermal, *J. Geophys. Res.*, 91(B2), 2153-2162.

Shieh, Y. N., and H. P. Taylor (1969), Carbon and hydrogen isotope studies at contact metamorphism in the Santa Rosa Range, Nevada and other areas, *Contrib. Mineral. Petrol.*, *20*, 306-356.

Shimamoto T. (1986), Transition between frictional slip and ductile flow for halite shear zones at room temperature, *Science*, *231*, 711-714.

Sibson, R. H. (1973), Interaction between temperature and pore-fluid pressure during earthquake faulting-A mechanism for partial or total stress relief, *Nature*, *243*, 66-68.

Sibson, R. H. (1975), Generation of pseudotachylyte by ancient seismic faulting, *Geophys. J. Int.*, *43*(3), 775.

Sibson, R. H. (1977), Fault rocks and fault mechanisms, *Journal of the Geological Society*, *133*, 191-213.

Sibson, R. H. (1982), Fault zone models, heat flow, and the depth distribution of earthquakes in the continental crust of the United States, *Bull. Seismol. Soc. Am.,72*(1), 151–163.

Sibson, R. H. (1990), Conditions for fault-valve behavior. *Geological Society*, London, Special Publications, *54*, 15-28.

Sibson, R. H., and V. Toy (2006), The habitat of fault-generated pseudotachylyte: Presence vs. absence of friction-melt, in *Radiated energy and the physics of faulting*, *Geophysical Monograph Series*, *vol. 170*, edited by R. Abercrombie et al., pp. 153–166, AGU, Washington, D. C.

Sibson, R. H., F. Robert, and K. H. Poulsen (1988), High-angle reverse faults, fluid-pressure cycling, and mesothermal gold-quartz deposits, *Geology*, *16*(6), 551-555.

Siman-Tov, S., E. Aharonov, A. Sagy, and S. Emmanuel (2013), Nanograins from carbonate "fault mirrors", *Geology*, *41*, 703-706.

Sleep, N. H., E. Richardson, and C. Marone (2000), Physics of strain localization in synthetic fault gouge, *J. Geophys. Res.*, 105(B11), 25,875–25,890.

Smith, S. A. F., A. Billi, G. Di Toro, and R. Spiess (2011), Principal slip zones in limestone: Microstructural characterization and implications for the seismic cycle (Tre Monti fault, central Apennines, Italy), *Pure and Applied Geophysics*, *168*, 2365-2393.

Solum, J. G., B. A. van der Pluijm, D. R. Peacor, and L. Warr (2003), Influence of phyllosilicate mineral assemblages, fabrics, and fluids on the behavior of the Punchbowl Fault, Southern California, *J. Geophys. Res.*, *108*, doi: 10.1029/2002JB001781.

Solum, J. G., S. H. Hickman, D. A. Lockner, D. E. Moore, B. A. van der Pluijm, A. M. Schleicher, and J. P. Evans (2006), Mineralogical characterization of protolith and fault rocks from the SAFOD Main Hole, *Geophys. Res. Lett.*, *33*, L21314, doi:10.1029/2006GL027285.

Spiers, C. J., S. De Meer, A. R. Niemeijer, and X. Zhang (2004), Kinetics of rock deformation by pressure solution and the role of thin aqueous films, in *Physicochemistry of Water in Geological and Biological Systems*, edited by S. Nakashima et al., pp.129 – 158, Univ. Acad. Press, Inc., Tokyo.

Sulem, J., and V. Famin (2009), Thermal decomposition of carbonates in fault zones: Slip-weakening and temperature limiting effects, *J. Geophys. Res.*, *114*, B03309, doi:10.1029/2008JB006004.

Sulem, J., I. Vardoulakis, H. Ouffroukh, and V. Perdikatsis (2005), Thermoporo-mechanical properties of the Aigion fault clayey gouge – application to the analysis of shear heating and fluid pressurization, *Soils Found.*, *45*(2), 97–108.

Sulem, J., I. Vardoulakis, H. Ouffroukh, M. Boulon, and J. Hans (2004), Experimental characterization of the thermo-poro-mechanical properties of the Aegion fault gouge, *C. R. Geosci.*, *336*(4– 5), 455– 466.·

Sulem, J., P. Lazar, and I. Vardoulakis (2007), Thermo-poro-mechanical properties of clayey gouge and application to rapid fault shearing, *Int. J. Numer. Anal. Meth. Geomech.*, *31*, 523-540.

Syunnan, S. (1981), Clay mineralogy, Translated by S. Yan, W. Liu and K. Jia, Beijing: Geological Publishing House, 230pp.(In Chinese)

Tanaka, H., K. Fujimoto, T. Ohtani, and H. Ito (2001), Structural and chemical characterization of shear zones in the freshly activated Nojima fault, Awaji Island, southwest Japan, *J. Geophys. Res.*, 106(B5), 8789–8810, doi:10.1029/2000JB900444

Tanaka, H., W. M. Chen, C. Y. Wang, K. F. Ma, N. Urata, J. Mori, and M. Ando (2006), Frictional heat from faulting of the 1999 Chi-Chi, Taiwan earthquake, *Geophys. Res. Lett.*, *33*, L16316, doi:10.1029/2006GL026673.

Tanikawa, W., H. Mukoyoshi, O. Tadai, T. Hirose, A. Tsutsumi, and W. Lin (2012), Velocity dependence of shear-induced permeability associated with frictional behavior in fault zones of the Nankai subduction zone, *J. Geophys. Res.*, *117*, B05405, doi:10.1029/2011JB008956.

Tanikawa, W., M. Sakaguchi, T. Hirono, W. Lin, W. Soh, and S.-R. Song (2009), Transport properties and dynamic processes in a fault zone from samples recovered from TCDP Hole B of the Taiwan Chelungpu Fault Drilling Project, *Geochem. Geophys. Geosyst.*, *10*, Q04013, doi:10.1029/2008GC002269.

Tanikawa, W., T. Mishima, T. Hirono, W. Lin, T. Shimamoto, W. Soh, and S.-R. Song (2007), High magnetic susceptibility produced in high-velocity frictional tests on core samples from the Chelungpu fault in Taiwan, *Geophys. Res. Lett.*, 34, L15304, doi:10.1029/2007GL030783.

Tembe, S., D. A. Lockner, and T.-f. Wong (2010), Effect of clay content and mineralogy on frictional sliding behavior of simulated gouges: Binary and ternary mixtures of quartz, illite, and montmorillonite, *J. Geophys. Res.*, 115, B03416, doi: 10.1029/2009JB006383.

Tenthorey, E., and S. F. Cox (2006), Cohesive strengthening of fault zones during the interseismic period: An experimental study, *J. Geophys. Res.*, *111*, B09202, doi:10.1029/2005JB004122.

Tenthorey, E., S. F. Cox, and H. F. Todd (2003), Evolution of strength recovery and permeability during fluid-rock reaction in experimental fault zones, *Earth Planet. Sci. Lett.*, *206*, 161-172.

Tesei, T., C. Collettini, B. M. Carpenter, C. Viti, and C. Marone (2012), Frictional strength and healing behavior of phyllosilicate-rich faults, *J. Geophys. Res.*, *117*, B09402, doi: 10.1029/2012JB009204.

Tesei, T., C. Collettini, C. Viti, and M.R. Barchi (2013), Fault architecture and deformation mechanisms in exhumed analogues of seismogenic carbonate-bearing thrusts, Journal of Structural Geology, 55, 167-181.

Togo, T., T. Shimamoto, S. Ma, and T. Hirose (2011), High-velocity frictional behavior of Longmenshan fault gouge from Hongkou outcrop and its implications for dynamic weakening of fault during 2008 Wenchuan earthquake, *Earthquake Science*, *24*, 267- 281.

Tsutsumi, A., T. Shimamoto (1997), High-velocity frictional properties of gabbro, *Geophys. Res. Lett.*, *24*(6), 699-702.

Tullis, T.E., and J. D. Weeks (1986), Constitutive behavior and stability of frictional sliding of granite, Pure Appl. Geophys., 124, 383–414.

Ujiie, K., A. Tsutsumi, and J. Kameda (2011), Reproduction of thermal pressurization and fluidization of clay-rich fault gouges by high-velocity friction experiments and implications for seismic slip in natural faults. in *Geology of the earthquake source: a volume in honor of Rick Sibson*, edited by A. Fagereng et al., 359, 267 -285, Geological Society, London.

Ujiie, K., A. Yamaguchi, and S. Taguchi (2008), Stretching of fluid inclusions in calcite as an indicator of frictional heating on fault, Geology, 36 (2), 111-114.

Valoroso, L., L. Chiaraluce, D. Piccinini, R. Di Stefanp, D. Schaff, and F.Waldhauser (2013), Radiography of a normal fault system by 64,000 high-precision earthquake locations: the 2009 L'Aquila (central Italy) case study, J. Geophys. Res., doi:10.1002/jgrb.50130.

van Noort, R., C. J. Spiers, and G. M. Pennock (2008), Compaction of granular quartz under hydrothermal conditions: Controlling mechanisms and grain boundary processes, J. Geophys. Res., 113, B12206, doi:10.1029/2008JB005815.

Verberne, B. A., C. He, and C. J. Spiers (2010), Frictional properties of sedimentary rocks and natural fault gouge from the Longmenshan Fault Zone, Sichuan, China, *B. Seismol. Soc. Am.*, *100*, 2767–2790.

Verberne, B. A., J. H. P. De Bresser, A. R. Niemeijer, C. J. Spiers, D. A. M. De Winter, and O. Plümper (2013a), Nanocrystalline slip zones in calcite fault gouge show intense crystallographic preferred orientation: Crystal plasticity at subseismic slip rates at 18–150 °C, *Geology*, *41*, 863–866.

Verberne, B. A., C. J. Spiers, A. R. Niemeijer, J. H. P. De Bresser, D. A. M. De Winter, and O. Plümper (2013b), Frictional properties and microstructure of calcite-rich fault gouges sheared at sub-seismic sliding velocities, *Pure Appl. Geophy.*, doi: 10.1007/s00024-013-0760-0

Verberne, B.A, Plümper, O., De Winter, D.A.M., and Spiers, C. J. (2015), Superplastic nanofibrous slip zones control seismogenic fault friction. Science, doi: 10.1126/science.1259003

Violay, M., S. Nielsen, B. Gibert, et al. (2013), Effect of water on the frictional behavior of cohesive rocks during earthquakes, *Geology*, doi:10.1130/G34916.1

Viti, C., C. Collettini, and T. Tesei (2014), Pressure solution seams in carbonatic fault rocks: mineralogy, micro/nanostructures and deformation mechanism, *Contributions to Mineralogy and Petrology*, 167:970, doi: OI 10.1007/s00410-014-0970-1

Voisin, C., F. Renard, and J.-R. Grasso (2007), Long term friction: From stick-slip to stable sliding, *Geophys. Res. Lett.*, *34*, L13301, doi:10.1029/ 2007GL029715.

Vredevoogd, M. A., D. D. Oglesby, and S. K. Park (2007), Fluid pressurization due to frictional heating on a fault at a permeability contrast, *Geophys. Res. Lett.*, *34*, L18304, doi:10.1029/2007GL030754.

Vrolijk, P., and B. van der Pluijm (1999), Clay gouge, *J. Struc. Geol.*, *21*, 1039 - 1048.

Wang, P.-L., J.-J. Wu, E.-C. Yeh, S.-R. Song, Y.-G. Chen, and L.-H. Lin (2010), Isotopic constraints of vein carbonates on fluid sources and processes associated with the ongoing brittle deformation within the accretionary wedge of Taiwan, *Terra Nova*, *22*, 251-256.

Wang, Q., X. Qiao, Q. Lan, et al. (2011), Rupture of deep faults in the 2008 Wenchuan earthquake and uplift of the Longmen Shan, *Nature Geoscience*, *4*, 634-640.

Wanless, H. R. (1979), Limestone response to stress; pressure: solution and dolomitization, *Journal of Sedimentary Petrology*,*49* (2), 437–462.

Weeks, J. D., and T. E. Tullis (1985), Frictional sliding of dolomite: a variation in constitutive behavior, *J. Geophys. Res.*, 90(B9), 7821–7826.

Wibberley, C. A. J. (2002), Hydraulic diffusivity of fault gouge zones and implications for thermal pressurization during seismic slip, *Earth Planets Space*, *54*, 1153-1171.

Wibberley, C. A. J., and T. Shimamoto (2003), Internal structure and permeability of major strike-slip fault zones: the Median Tectonic Line in Mie Prefecture, Southwest Japan, *Journal of Structural Geology*, *25*, 59-78.

Wibberley, C. A. J., and T. Shimamoto (2005), Earthquake slip weakening and asperities explained by thermal pressurization, *Nature*, *436*, 689 - 692.

Wintsch, R. P., R. Christoffersen, and A. K. Kronenberg (1995), Fluid-rock reaction weakening of fault zones, *J. Geophys. Res.*, 100(B7), 13,021–13,032, doi:10.1029/94JB02622.

Wong, T.-f, and Y. Zhao (1990), Effects of load point velocity on frictional instability behavior, *Tectonophysics*, *175*, 177–195.

Wong, T.-f., and P. Baud (1999), Mechanical Compaction of Porous Sandstone, *Oil & Gas Sci. and Tech. - Rev. IFP*, *54*(6), 715–727.

Wong, T-F., S-C. Ko, and D. L. Olgaard (1997), Generation and maintenance of pore pressure excess in a dehydrating system 2. Theoretical analysis, *J. Geophys. Res.*, *102* (B1), 841 - 852.

Xu, X., X., Wen, G. Yu, G. Chen, Y. Klinger, J. Hubbard, and J. Shaw (2009), Coseismic reverse- and oblique-slip surface faulting generated by the 2008 Mw 7.9 Wenchuan earthquake, China, *Geology*, *37*(6), 515-518.

Xu, Z., and H. Li (2010), New Results from the Wenchuan Earthquake Fault Scientific Drilling Project (WFSD), American Geophysical Union, fall annual meeting, San Francisco, Abstract T53E-01.

Xue, L., H. Li, and E. E. Brodsky (2013), Continuous permeability measurements record healing inside the Wenchuan earthquake fault zone, Science, 340, 1555-1559.

Yamaguchi, A., et al. (2011), Progressive illitization in fault gouge caused by seismic slip propagation along a megasplay fault in the Nankai Tough, *Geology*, *39* (11), 995-998.

Yang, T., J. Chen, H. Wang, and H. Jin (2012), Rock magnetic properties of fault rocks from the rupture of the 2008 Wenchuan earthquake, China and their implications: Preliminary results from the Zhaojiagou outcrop, Beichuan County (Sichuan), *Tectonophysics*, *530*, 331-341.

Yao, L., S. Ma, T. Shimamoto, and T. Togo (2013), Structures and high-velocity frictional properties of the Pingxi fault zone in the Longmenshan fault system, Sichuan, China, activated during the 2008 Wenchuan earthquake, *Tectonophysics*, 10.1016/j.tecto.2013.04.011.

Yao, L., T. Shimamoto, S. Ma, J. Chen, and T. Togo (2011), Internal structures and High-velocity (HV) frictional properties of Longmenshan fault zone at Pingxi outcrop, Sichuan, China, AOGS annual meeting, Taibei, Abstract SE83-A028.

Yasuhara, H., C. Marone, and D. Elsworth (2005), Fault zone restrengthening and frictional healing: The role of pressure solution, J. Geophys. Res., 110, B06310, doi:10.1029/2004JB003327.

Zhang, L., and C. He (2013), Frictional properties of natural gouges from Longmenshan fault zone ruptured during the Wenchuan Mw7.9 earthquake, *Tectonophysics*, 594,149-164.

Zhang, P. (2013), Beware of slowly slipping faults, *Nature Geoscience*, *6*, 323-324.

Zhang, P., X. Wen, Z. Shen, and J. Chen (2010), Oblique, high-angle, listric reverse faulting and associated development of strain: The Wenchuan earthquake of May 12, 2008, Sichuan, China, *Annu. Rev. Earth Planet. Sci.*, *38*, 353–382.

Zhang, R. Q., Q. J. Wu, Y.H. Li, Z.F. Ding, and R.S. Zeng (2008), Focal depths for moderate-sized aftershocks of the WenchuanMs8.0 earthquake and their implications, *Science in China* (D series),*51* (12), 1694-1702, doi:10.1007/s11430-008-0140-2

Zhang, X., and C. J. Spiers (2005), Effects of phosphate ions on intergranular pressure solution in calcite—An experimental study, *Geochim. Cosmochim. Acta*, *69*(24), 5681–5691.

Zhang, X., C.J. Spiers, and C.J. Peach (2010), Compaction creep of wet granular calcite by pressure solution at 28 °C to 150 °C, *J. Geophys. Res.*, 115, B09217, doi:10.1029/2008JB005853.

Zhang, Y., W. Feng, L. Xu, C. Zhou, and Y. Chen (2009), Spatio-temporal rupture process of the 2008 great Wenchuan earthquake, *Science in China* (Series D: Earth Sciences), *52*(2), 145–154.

Zhao, C. P., Z.L. Chen, Q.L. Zhou, Z.X. Li, and Y. Kang (2010), Rupture process of the 8.0 Wenchuan earthquake of Sichuan, China: the segmentation feature, *Chinese Sci. Bull.*, *55*(3), 284–292, doi: 10.1007/s11434-009-0425~7 (in Chinese with English abstract)

Zhao, G., D. R. Peacor, and S. D. McDowell (1999), "Retrograde Diagenesis" of clay minerals in the Precambrian Freda sandstone, Wisconsin, *Clays and Clay Minerals*, *47*(2), 119-130.

Zheng, Y. F., and J. Hoefs (1993), Carbon and oxygen isotopic covariations in hydrothermal calcites, *Mineralium Deposita*, *28*, 79-89.

Zhou, X. (1993), Hydrogeochemical characteristics and formation of subsurface brines of deep aquifers in Longnu temple brine-bearing structure, Sichuan Basin, *Geoscience*, *7*(1), 83-92. (in Chinese with English abstract)

Zhou, X., et al. (2010), Geochemistry of soil gas in the seismic fault zone produced by the Wenchuan Ms 8.0 earthquake, southwestern China, *Geochemical Transactions*, *11*(5), 1-10.

Zhou, Y., and C. He (2009), The rheological structures of crust and mechanics of high-angle reverse fault slip for Wenchuan Ms 8.0 earthquake, *Chinese J. Geophys.*, *52*(2), 474-484. (in Chinese with English abstract)

Samenvatting

Destructieve aardbevingen vinden veelvuldig plaats in tektonisch actieve gebieden gedomineerd door carbonaatgesteente. Een voorbeeld is de catastrofale Wenchuan aardbeving in Sichuan, China. Talrijke studies hebben zich gericht op het karakteriseren van silicaatrijk breukgesteente, met name op de compositionele, transport- en mechanische eigenschappen. Dergelijke studies hebben geleid tot modellen voor dynamische breuk- en wrijvingsprocessen. Gegevens over carbonaatrijk breukgesteente, daarentegen, zijn tot op heden schaars. In dit proefschrift rapporteer ik de eigenschappen van breukgesteenten afkomstig van twee carbonaatrijke ontsluitingen waar de breuk geassocieerd met de Wenchuan aardbeving aan het oppervlak komt. De belangrijkste conclusies zijn als volgt:

1. De geobserveerde elementpartitionering, verrijkings/verarmingspatronen en het daaruit afgeleide volumeverlies (> 90%) voor de breukgesteenten ten opzichte van het moedergesteente verschillen van die voor breuken in granietische- en siliciklastische gesteenten, en kunnen worden verklaard door een massaverwijderingsmodel waarin mineraaloplossing en advectie versterkt worden door drukoplossing. Een toename van de smectiet-verrijking richting het principiële schuifvlak werd waargenomen. Beide types ontsluitingen lieten illitisatie van de breukmelen van het principiële schuifvlak zien. Deze illitisatie is het gevolg van een coseismische temperatuurstoename door wrijving. De resultaten impliceren dat coseismische ontwateringsreacties waarschijnlijk significant zijn op diepte en mogelijk helpen bij het genereren van hoge porievloeistofdrukken waardoor dynamische verplaatsingsverzwakking kon plaatsvinden tijdens de Wenchuan aardbeving.
2. Wrijvingsexperimenten uitgevoerd op hoge snelheid hebben laten zien dat natte breukmelen een grotere verplaatsingsverzwakking laten zien dan droge breukmelen, wat inderdaad op thermische drukvorming wijst. Het breukmeel afkomstig uit de kern van de breuk heeft een zeer lage permeabiliteit ($<10^{-21}$ m^2 op 165 MPa) en is omringd door breukbreccie met een permeabiliteit van 10^{-19} tot 10^{-17} m^2, wat overgaat in gebroken moedergesteente met een lagere permeabiliteit. Er is dus sprake van een doorgang/barrière structuur van de breukzone. We hebben de coseismische verplaatsingsverzwakking numeriek gemodelleerd, gebaseerd op de gemeten eigenschappen. De resultaten laten zien dat thermochemische drukvorming een sleutelrol speelt in het veroorzaken van dynamische verplaatsingsverzwakking en een aannemelijke verklaring vormt voor de grote coseismische verplaatsing in het bestudeerde gebied.
3. Nucleatie van verplaatsing en interseismisch herstel van de sterkte langs carbonaatbreuken is gesimuleerd door middel van experimenten die inzicht geven in de

wrijvingsseigenschappen op lage snelheid en de helingseigenschappen. Droge experimenten laten klassiek of Dieterich-type helingsgedrag zien. Hydrothermale testen, daarentegen, laten “non-Dieterich-type” helingsgedrag zien, gekarakteriseerd door: 1) een toename van de schijnbare tijdsonafhankelijke (“*steady-state*”) wrijving bij het hervatten van schuiven na een periode van stilstand (een *SHS* fase) en 2) een duidelijke toename van (*a*-*b*) na de *SHS* fase. Verdere analyse suggereert dat deze aspecten van “non-Dieterich-type” helingsgedrag gerelateerd waren aan versterkte oplossing verplaatsingsprocessen die tijdens de periode van stilstand plaatsvonden. Onze bevindingen suggereren dat onder hydrothermale condities, interseismische water-gefaciliteerde deformatieprocessen het aansterken gunstig beinvloeden en het schuiven stabiliseren.

4. Een microfysisch model gebaseerd op de onderliggende mechanismes is ontwikkeld. We hebben typische laboratorium wrijvingsexperimenten (snelheids-stap testen en schuif-halt-schuif of *SHS* testen) weten te simuleren door twee bepalende vergelijkingen - afgeleid van een beschouwing van de kinematica en energie/entropie balans – op te lossen, en daarbij standaard vergelijkingen voor drukoplossing te gebruiken. Voor zover we weten is ons model het eerste model dat op mechanismen gebaseerd is dat het volledige snelheids-staat-wrijvings (”*rate and state friction”* of *RSF*) achtig gedrag kan reproduceren zonder gebruik te maken van de *RSF* wetten. Onze aanpak van modelleren kan een sterk verbeterd kader bieden voor het extrapoleren van laboratorium-wrijvingsdata naar natuurlijke omstandigheden.

Acknowledgements

Here I am at the end, writing the part of thesis which I think it is as important as the main chapters, as it gives me the chance to express my appreciation to many persons I enjoyed working with.

First of all, a big thanks to my supervisors!

I would like to thank my promoter, Prof. Chris Spiers of Utrecht University, for accepting me as a joint PHD student to visit the HPT lab for one year, also for encouraging me to complete the PHD degree at Utrecht. Chris, I have learned a tremendous amount from you, especially your creative, clear, scientific thinking, and it is always a pleasure to work with you. The discussion with you are encouraging because often when I thought some data were not helping at all, you somehow knew how to turn them into a useful outcome and I gained new inspiration…I want to thank my second promotor, Prof. Xiaosong Yang, in the Institute of Geology, China Earthquake Administration (CEA), for introducing me to this field of research and for always being a to-the-point discussion partner.

I fell the HPT group to be like a big family, being one of which I worked in with pleasure in my every day spent at Utrecht. I thank all the HPTers for the group you have been developing over the years. A positive attitude is always in the group, and of course the good science. I really enjoyed every moment of my stay in the group. I like to thank Hans de Bresser, Colin Peach and Andre Niemeijer for their constructive comments on my research. Much appreciated! I owe Berend A. Verberne much for guiding me using the apparatus and helping me with the microscopic analysis. Magda Mathot-Martens is thanked for taking care of me in management and organizing many things. On the technical support, I want to thank Peter van Krieken, Gert Kastelein and Eimert de Graaff for their support. I would like to thank the rest of the HPT team, Jon, Suzanne, Sander, Amir, Sabine, Loes, Tim, Anne, Nawaz, Ross, Elisenda and Miao. I had great times in the lab working with you, and enjoyed the many discussions and laughs we had.

I also want to thank my colleagues at CEA, Prof. Shengli Ma, Prof. Toshihiko Shimamoto, Prof. Changrong He, Prof. Yongsheng Zhou, Yutao Ji, Lu Yao, Lei Zhang, and the students, Ping Zhou, Xiaobing Yan, Guoling Zhang, Man Wu, Yongxin Yang, Qingbao Duan, Jingyu Chen, Liang Hang, Li Luo and Ali Miao. Prof. Shengli Ma is specially thanked for leading me on the first field trip to the study area, Toshi for being a critical co-author on some of my papers and for helping me build the fluid-flow apparatus, and Lu Yao for guiding me use the high-velocity frictional apparatus.

I would like to thank many of the journal reviewers that have contributed to imporving my paper and hence the chapters in this theisis, namely Teng-fong Wong, Chris Marone, Dan Faulkner, Brett Carpenter, and several anonymous reviewers for the constructive comments and suggestions.

Finally I am grateful to my family. It is difficult to express the support from them in English, but I will give a try in Chinese. 特别感谢我的妻子杨巧凤。从相识，相恋，结婚到如今，刚好对应于博士学习这几年。感谢她一直以来对我工作的理解，在生活上对我无微不至的关怀。在我困难的时候她总是默默的和我在一起；在我开心时，她总是争着要第一个和我分享。虽然你不说，我知道你一直以我为荣。我会继续努力，和你一起谱写我们未来更加美好的“章节”。特别感谢我的父母，你们总是无条件的支持我，鼓励我，你们永远是我精神上最宁静的港湾。也要感谢我的外婆，我的岳父母和其他长辈们，感谢我的兄弟姐妹们。谢谢你们！我爱你们！

Curriculum vitae

Jianye Chen (jychen@ies.ac.cn)

19-09-1983: Born in Songzi, Hubei Province, China

2002-2006: B.Sc. Earth Sciences, China University of Geoscience, Wuhan, Hubei, China

2006-2009: M.Sc. Structural Geology, Institute of Geology, China Earthquake Administration, Beijing, China

2011-present: Researcher, State Key Laboratory of Earthqquake Dynamics, Institute of Geology, China Earthquake Administration, Beijing, China

2010-2014: Ph.D. Experimental Rock Deformation, Utrecht University, The Netherlands